HZDR-078

Wissenschaftlich-Technische Berichte
HZDR-078 2017 · ISSN 2191-8708

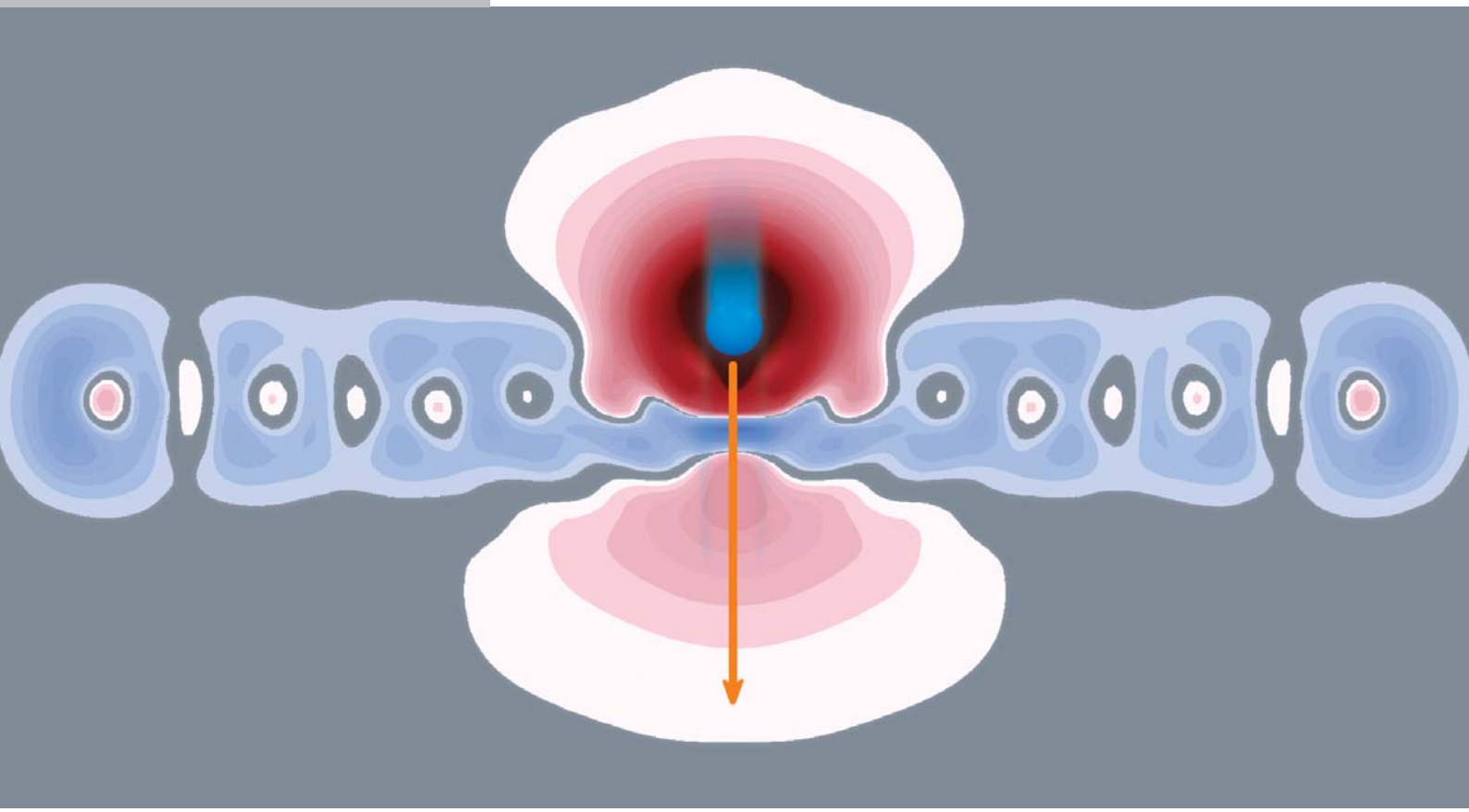

# ANNUAL REPORT 2016

## INSTITUTE OF ION BEAM PHYSICS AND MATERIALS RESEARCH

HZDR

HELMHOLTZ ZENTRUM DRESDEN ROSSENDORF

Wissenschaftlich-Technische Berichte
**HZDR–078**

# Annual Report 2016

## Institute of Ion Beam Physics and Materials Research

Editors

J. Fassbender, V. Heera,
M. Helm, P. Zahn

HZDR

HELMHOLTZ ZENTRUM DRESDEN ROSSENDORF

**Cover Picture**

The cover picture shows a snapshot of the induced changes of the electron charge density in a graphene sheet while the incoming highly charged ion projectile traverses the layer from the top. The polarization of the layer due to the ion's electric field and the excitation of the graphene layer while and after the crossing of the ion are clearly visible.

The width of the figure covers a length of two nanometers.

Image: © HZDR / M. Voigt (WERKSTATT X)

For further information see:
E. Gruber et al., Nature Communications **7**, 13948 (2016),
reprinted at pp. 26 – 32 of this Annual Report.

Print edition: ISSN 2191-8708
Electronic edition: ISSN 2191-8716

urn:nbn:de:bsz:d120-qucosa-220503
www.hzdr.de/publications/Publ-25256
Published by Helmholtz-Zentrum Dresden - Rossendorf e.V.

This report is also available at https://www.hzdr.de/FWI.

Helmholtz-Zentrum Dresden - Rossendorf e.V.
Institute of Ion Beam Physics and Materials Research
Bautzner Landstraße 400
01328 Dresden
Germany

| | | |
|---|---|---|
| Directors | Prof. Dr. M. Helm | Prof. Dr. J. Faßbender |
| Phone | + 49 (351) 260 2260 | + 49 (351) 260 3096 |
| Fax | + 49 (351) 260 3285 | + 49 (351) 260 3285 |
| Email | m.helm@hzdr.de | j.fassbender@hzdr.de |

www.hzdr.de/FWI

# Preface by the directors

After having allocated a tremendous amount of time to the integration into the Helmholtz Association, the initiation of collaborative research with other Helmholtz centers, and the Helmholtz program oriented funding evaluation, we could focus more on research again in 2016. This was very successful and we are particularly delighted in view of the numerous publications in high-impact journals, including ACS Nano, Advanced Materials, Applied Physics Review, Nano Letters, Nature Communications and Nature Nanotechnology, which have been published by scientists from the Institute. You will find a few of these highlight publications on the subsequent pages, demonstrating the broad range of science the Institute is addressing. Important results have been achieved in our already well established areas of interaction of highly charged ions with solids, THz spectroscopy and magnetization dynamics. The potential of our recently installed semiconductor molecular beam epitaxy system was demonstrated by growing epitaxial GaAs nanowires on Si at CMOS-compatible temperatures.

In addition, also users of our Ion Beam Centre (IBC) were very productive. Most notably users of our DREsden Accelerator Mass Spectrometry (DREAMS) facility within the IBC were able to publish their results in the most prestigious journals Science and Nature. We would like to congratulate them and would be happy to welcome more users from this area of science which is rather new to our Institute.

Excellent research is only possible, if there is a critical mass of people working cooperatively together. In order to further increase the number of scientists, the acquisition of external funds is inevitable. Also in this respect 2016 was a very successful year. In addition to the two already running EU-projects we have received funding for two new collaborative projects funded by the European Union. In one of them, Dr. Gregor Hlawacek further exploits the use of Helium Ion Microscopy for the characterization of nanoparticles. In the other, an FET-Open project which in total had only 4 % of funding probability, Dr. Alina Deac and her team will extend the communication characteristics of spin torque resonators to the Terahertz regime. Also three of our young investigators, Dr. Rantej Bali, Dr. Alexei Pashkin and Dr. Richard Wilhelm, successfully applied for projects from the Deutsche Forschungsgemeinschaft.

A major achievement in 2016 was to attract Prof. Dr. Olav Hellwig, who had been working for more than a decade in California on magnetic storage media for IBM, Hitachi GST and Western Digital, to a joint appointment between TU Chemnitz and HZDR. Prof. Hellwig started his professorship with TU Chemnitz and will, in addition to his Chemnitz group, be able to establish a second group at our Institute, working on functional magnetic materials due to a special grant he received from the Helmholtz Association. We wish him a quick start off and look forward to the new expertise we gain in magnetic thin film growth and characterization.

With the end of 2016 the division on structural materials led by Dr. Eberhard Altstadt and Dr. Cornelia Heintze left the Institute and is now part of the Institute of Resource Ecology. This move was necessary to better integrate their research into the Helmholtz programme “Nuclear Safety” which is mainly operated by the Institute of Resource Ecology. We thank all members of this division for their contributions to our Institute and wish them a good reception and working environment in their new Institute.

Last but not least, we recently received the information that our Emmy Noether group leader Dr. Helmut Schultheiß will receive the prestigious Walter Schottky Prize 2017 from the Deutsche Physikalische Gesellschaft for his contributions to the understanding of spin wave propagation phenomena in nanostructures and their application in new functional devices. We sincerely congratulate him on this excellent achievement.

Finally we would like to cordially thank all partners, friends, and organizations who supported our progress in 2016. Special thanks are due to the Executive Board of the Helmholtz-Zentrum Dresden-Rossendorf, the Minister of Science and Arts of the Free State of Saxony, and the Ministers of Education and Research, and of Economic Affairs and Energy of the Federal Government of Germany. Numerous partners from universities, industry and research institutes all around the world contributed essentially, and play a crucial role for the further development of the institute. Last but not least, the directors would like to thank again all IIM staff for their efforts and excellent contributions in 2016.

Prof. Manfred Helm

Prof. Jürgen Fassbender

# Contents

## Selected Publications



## Statistics

# Selected Publications

Image: ressourcenmangel dresden

# Copyright remarks

The following journal articles are reprinted with kind permission from:

Wintz, S.; Tiberkevich, V.; Weigand, M.; Raabe, J.; Lindner, J.; Erbe, A.; Slavin, A.; Fassbender, J.
**Magnetic vortex cores as tunable spin-wave emitters**
Manuscript

Published in Nature Nanotechnology, Vol. 11, pp. 948 – 953
DOI: 10.1038/NNANO.2016.117

Wagner, K.; Kákay, A.; Schultheiss, K.; Henschke, A.; Sebastian, T.; Schultheiss, H.
**Magnetic domain walls as reconfigurable spin-wave nanochannels**
Manuscript

Published in Nature Nanotechnology, Vol. 11, pp. 432 – 436
DOI: 10.1038/NNANO.2015.339

Gruber, E.; Wilhelm, R. A.; Pétuya, R.; Smejkal, V.; Kozubek, R.; Hierzenberger, A.; Bayer, B. C.; Aldazabal, I.; Kazansky, A. K.; Libisch, F.; Krasheninnikov, A. V.; Schleberger, M.; Facsko, S.; Borisov, A. G.; Arnau, A.; Aumayr, F.
**Ultrafast electronic response of graphene to a strong and localized electric field**
Nature Communications Vol. 7, 13948

DOI: 10.1038/ncomms13948

Balaghi, L.; Tauchnitz, T.; Hübner, R.; Bischoff, L.; Schneider, H.; Helm, M.; Dimakis, E.
**Droplet-Confined Alternate Pulsed Epitaxy of GaAs Nanowires on Si Substrates down to CMOS-Compatible Temperatures**
Nano Letters, Vol. 16, pp. 4032 – 4039

DOI: 10.1021/acs.nanolett.6b00527

Melkhanova, S.; Haluska, M.; Hübner, R.; Kunze, T.;Keller, A.; Abrasonis, G.; Gemming, S.; Krause, M.
**Carbon:nickel nanocomposite templates – predefined stable catalysts for diameter-controlled growth of single-walled carbon nanotubes**
Nanoscale, Vol. 8, pp. 14888-14897

DOI: 10.1039/c5nr06972f

König-Otto, J. C.; Mittendorff, M.; Winzer, T.; Kadi, F.; Malic, E.; Knorr, A.; Berger, C.; de Heer, W. A.; Pashkin, A.; Schneider, H.; Helm, M.; Winnerl, S.
**Slow Noncollinear Coulomb Scattering in the Vicinity of the Dirac Point in Graphene**
Physical Review Letters, Vol. 117, 087401

DOI: 10.1103/PhysRevLett.117.087401

NATURE NANOTECHNOLOGY | VOL 11 | pp. 948 – 954 | NOVEMBER 2016 | DOI: 10.1038/NNANO.2016.117

# Magnetic vortex cores as tunable spin-wave emitters

Sebastian Wintz[1,2,*], Vasil Tiberkevich[3], Markus Weigand[4], Jörg Raabe[5], Jürgen Lindner[1], Artur Erbe[1], Andrei Slavin[3] and Jürgen Fassbender[1,2]

**The use of spin waves as information carriers in spintronic devices can substantially reduce energy losses by eliminating the ohmic heating associated with electron transport. Yet, the excitation of short-wavelength spin waves in nanoscale magnetic systems remains a significant challenge. Here, we propose a method for their coherent generation in a heterostructure composed of antiferromagnetically coupled magnetic layers. The driven dynamics of naturally formed nanosized stacked pairs of magnetic vortex cores is used to achieve this aim. The resulting spin-wave propagation is directly imaged by time-resolved scanning transmission X-ray microscopy. We show that the dipole-exchange spin waves excited in this system have a linear, non-reciprocal dispersion and that their wavelength can be tuned by changing the driving frequency.**

Spin waves in ferromagnetic materials have been studied since the beginning of the twentieth century[1] (Fig. 1). The corresponding subfield of magnetism is now known as 'magnonics', named after the quasiparticle of spin-wave excitations, the magnon[1-3]. In general, spin waves propagate much more slowly than electromagnetic waves, which makes their wavelengths $\lambda$ up to five orders of magnitude smaller (~$1 \times 10^{-6}$ m) than those of electromagnetic waves (~$1 \times 10^{-1}$ m) of the same microwave frequency ($f \approx$ 1-10 GHz)[4]. This property stimulated interest in the application of spin waves as information carriers in microwave signal processing, which would allow for the development of miniature devices with large and easily controllable time delays.

Besides energy, spin waves also carry spin angular momentum. They can therefore be used in nanoscale spintronic signal-processing devices[5-9], where the information is coded with the spin orientation. Spin waves as information carriers are very flexible, because they can propagate in both magnetic conductors and insulators, and their dispersion relations can be 'tailored to order' by applying external magnetic bias fields[4]. Finally, their propagation is not associated with the motion of charge, so ohmic losses are avoided, and the power consumption for information processing can be reduced substantially.

A major challenge for the use of spin waves in nanosized spintronic devices is the requirement to excite propagating spin waves with nanoscale wavelengths. The traditional method of linear spin-wave excitation using spatially confined oscillating magnetic fields (with dimension on the order of the smallest achievable λ) is difficult to implement because of technological restrictions in fabricating nanoscale transducers and matching their impedance to that of conventional transmission lines[10]. Only recently has the challenge of generating short spin waves been partly solved by reducing the wavelength after the generation process[11]. The second well-known method of spin-wave excitation is parametric pumping, which involves the creation of spatially uniform double frequency oscillating magnetic fields[4,12]. However, this method suffers from a relatively low excitation efficiency, non-locality and poor control of the excited wavelengths.

Another recently developed method of spin-wave excitation utilizes spin-transfer torques, which are induced via spin-polarized[13-15] direct currents in magnetic nanocontacts. This method allows one to excite propagating spin waves, predominantly in the case

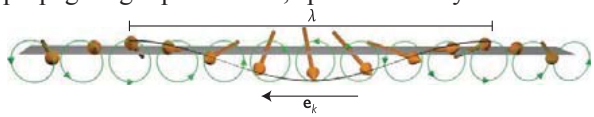


**Figure 1 | Schematics of a spin wave propagating along $\mathbf{e}_k$.** Magnetic moments (orange arrows) precess with a periodic spatial phase difference, determining the spin-wave wavelength $\lambda$.

where the oscillating magnetic layer is magnetized out of plane[5,16-18], which at the same time requires rather large external magnetic bias fields. For in-plane magnetization, which can be excited in smaller fields, spin waves resulting from spin-transfer torques are typically localized near the nanocontact[5,18-20]. Therefore, such locally generated spin waves can only be used for the transmission of microwave signals when they are coupled into waveguides that provide a specific

[1]Helmholtz-Zentrum Dresden-Rossendorf, 01328 Dresden, Germany. [2]Technische Universität Dresden, 01069 Dresden, Germany. [3]Oakland University, Rochester, Michigan 48309, USA. [4]Max-Planck-Institut für Intelligente Systeme, 70569 Stuttgart, Germany. [5]Paul Scherrer Institut, 5232 Villigen, Switzerland. *e-mail: s.wintz@hzdr.de

NATURE NANOTECHNOLOGY | VOL 11 | pp. 948 – 954 | NOVEMBER 2016 | DOI: 10.1038/NNANO.2016.117

propagation channel for them[21].

**Vortex core spin-wave emitters**

Here, we experimentally realize a new method for the excitation of short-wavelength propagating spin waves in layered magnetic structures. For this purpose we use the driven rotational dynamics of naturally formed nanosized magnetic vortex cores in an antiferromagnetically coupled trilayer without magnetic bias fields. The nanoscale size of the vortex cores ensures the excitation of spin waves with sufficiently small wavelengths. Meanwhile, the driven vortex core rotation, together with the rather linear spin-wave dispersion in the antiferromagnetically coupled trilayer, provides linear tunability of the excited wavelength by varying the driving frequency.

Magnetic thin-film elements in a certain size range exhibit a magnetization (**M**) ground state of a flux-closing, planar vortex with a nanoscale core of perpendicular magnetization in the centre (Fig. 2a)[22-24]. Such magnetic vortices possess a non-trivial topological structure, characterized by their unique winding number of +1 and their binary core polarity of $p = \pm 1$ (ref. 25). Here, $p = +1$ corresponds to an upwards pointing core magnetization. Another vortex state parameter is the circulation $c = \pm 1$, where positive circulation $c = +1$ corresponds to an anticlockwise rotation of the static magnetization in the vortex plane. The magnetodynamic excitation spectrum of a vortex under the influence of laterally oscillating magnetic fields includes the gyration of the vortex core around its equilibrium position[26-30], as well as standing radial and rotating azimuthal dipolar spin-wave modes[31-33]. A pair of stacked vortices can be confined into a trilayer element, in which two ferromagnetic layers are separated by a non-magnetic spacer (Fig. 2b,c). For such a vortex pair there may be four non-degenerate configurations with respect to the relative circulations and polarities[35-36].

We used vortex pairs with opposite circulations $c_1c_2 = -1$ and parallel cores $p_1p_2 = +1$ as emitters of propagating spin waves. In our first experimental sample (sample 1), the vortex pair was confined into a square-shaped element patterned with a lateral size of 4 μm, made of a Co/Ru/$Ni_{81}Fe_{19}$ (47.8/0.8/42.8 nm) trilayer stack. We chose two different ferromagnetic materials (Co and NiFe) to allow for layer-selective X-ray measurements. The Ru interlayer supports strong antiferromagnetic interlayer exchange coupling between these two ferromagnetic layers[37], which makes opposite vortex circulations energetically favourable[35]. The pair configuration was verified by direct imaging of the magnetic orientation $\mathbf{m} = \mathbf{M}/M$ using scanning transmission X-ray microscopy[38,39]. Figure 2 shows the planar circulations (Fig. 2d) and perpendicular cores (Fig. 2e) of both layers (Co and NiFe). Note that, instead of a continuous curl, square-shaped elements exhibit a discrete circulation via four uniform domains that are intersected by 90 ° domain walls. From a topological point of view, however, both types of vortices are equivalent.

The vortex pair in sample 1 was excited by an in-plane sinusoidal magnetic field $H_y = H_0\sin(\omega t)$. The excitation frequency $f = \omega/2\pi$ was varied between 1 and 4 GHz with amplitudes of the order of $\mu_0 H_0 \approx 1$ mT. Within this interval of driving frequencies it was possible to excite an 'anti-phase' gyration of the vortex cores[36,40], for which the eigenfrequency is strongly dependent on the inter-core distance[40,41].

We used time-resolved scanning transmission X-ray microscopy to directly image the magnetic response of the system. Figure 3 shows the resulting perpendicular magnetic deviation $\Delta m_z(t)$ from the average state $\langle m_z(t)\rangle_T$ at fixed times. The response to an excitation of $f = 1$ GHz is displayed separately for the NiFe layer (Fig. 3a) and the Co layer (Fig. 3b). Obviously, both layers exhibit a radially coherent wave

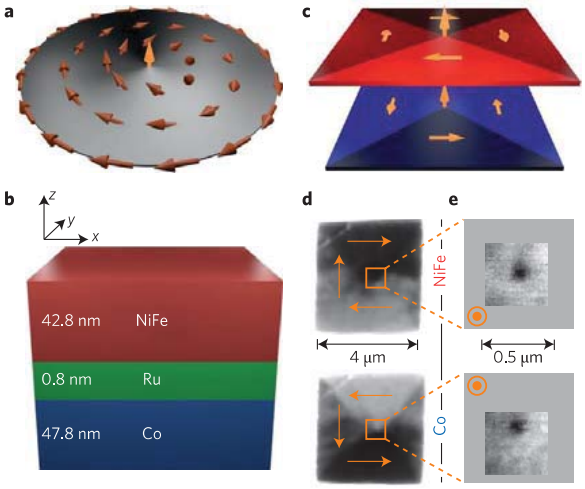


**Figure 2 | Sketches and scanning transmission X-ray microscopy images of magnetic vortices. a**, Disk with continuous planar magnetization circulation ($c = -1$, anticlockwise) and perpendicular core ($p = +1$, upwards along $\mathbf{e}_z$). **b**, Trilayer stack consisting of Co/Ru/NiFe layers. **c–e**, Vortex pair in a square-shaped trilayer element (sample 1), with discrete antiferromagnetic circulations ($m_x$-sensitivity; triangular domains) (**d**) and parallel cores ($m_z$-sensitivity; black dots) (**e**).

pattern with a characteristic wavelength of $\lambda = 365 \pm 20$ nm. Because this pattern is congruent between NiFe and Co ($m_z^{NiFe}(\mathbf{r},t) \sim m_z^{Co}(\mathbf{r},t)$), it represents a collective spin-wave mode of the trilayer stack.

The underlying wave propagation is depicted by $\Delta m_z$ line profiles for different excitation times $t = 0$, 250 ps and 500 ps (excitation phases ~0, π/2 and π) in Fig. 3c. Subsequent profiles are shifted by $\lambda/4 \approx 90$ nm, which corresponds to a spin-wave phase shift of $\Phi = \pi/2$. The temporal evolution of the excited

NATURE NANOTECHNOLOGY | VOL 11 | pp. 948 – 954 | NOVEMBER 2016 | DOI: 10.1038/NNANO.2016.117

wave pattern is best visualized by means of animated experimental image sequences (Supplementary Movies 1–4). These movies clearly show spin waves that are propagating from the centre to the edge of the sample in a spiralling manner.

Wave patterns corresponding to three different excitation frequencies (1, 2 and 4 GHz) are shown enlarged for the sample centre in Fig. 3d. All three panels show the same kind of spiralling spin-wave emission and propagation, but the resulting wavelength decreases when the excitation frequency is increased

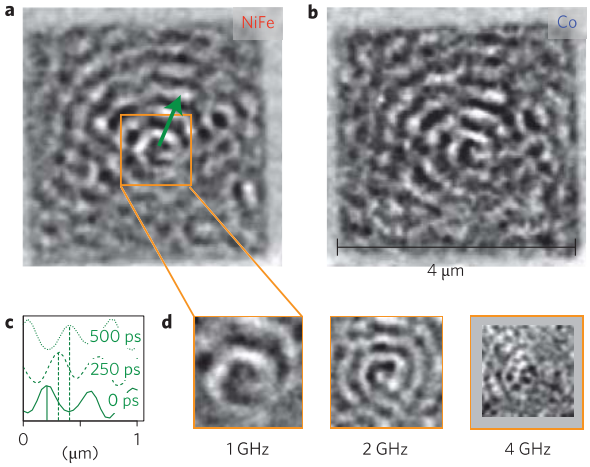


**Figure 3 | Time-resolved scanning transmission X-ray microscopy images of spin-wave emission from magnetic vortex cores (sample 1).** **a**,**b**, Normalized $\mathbf{m}_z$ contrast for NiFe (**a**) and Co (**b**) under lateral field excitation with $\mu_0 H_0 \approx 1$ mT at 1 GHz. **c**, Radial spin-wave line profile along the green arrow in a, for different response times of 0, 250 and 500 ps. **d**, Normalized NiFe $m_z$ contrast of spin-wave emission at 1, 2 and 4 GHz in the central part of the sample, as indicated in **a** by the orange box.

(Supplementary Movies 5–10). Starting from $\lambda = 365 \pm 20$ nm at $f = 1$ GHz, a decrease to $\lambda = 200 \pm 20$ nm at $f = 2$ GHz and eventually to $\lambda = 125 \pm 10$ nm at $f = 4$ GHz is observed. We estimate the corresponding phase velocities $V(f)$ by $V = \omega/k$, with wavenumber $k = 2\pi/\lambda$, to be $V(1\text{ GHz}) = 365$ ms$^{-1}$, $V(2\text{ GHz}) = 400$ ms$^{-1}$ and $V(4\text{ GHz}) = 500$ ms$^{-1}$. The experiments clearly show that the wave-length of the excited spin-wave mode scales almost linearly with the excitation frequency. Therefore, stacked pairs of magnetic vortices confined into trilayer elements can be used as tunable emitters of propagating spin waves with nanoscale wavelengths.

### Collective spin-wave dispersion relation

To obtain a clear understanding of the spin waves observed, we investigated their properties by means of analytic calculations. Our experiments show that we are looking at a layer-collective spin-wave mode propagating perpendicularly to the circulating magnetization of an anti-ferromagnetically coupled vortex pair. This situation is similar to the propagation of a quasi-Damon–Eshbach mode[42] in a trilayer where two ferromagnetic films,

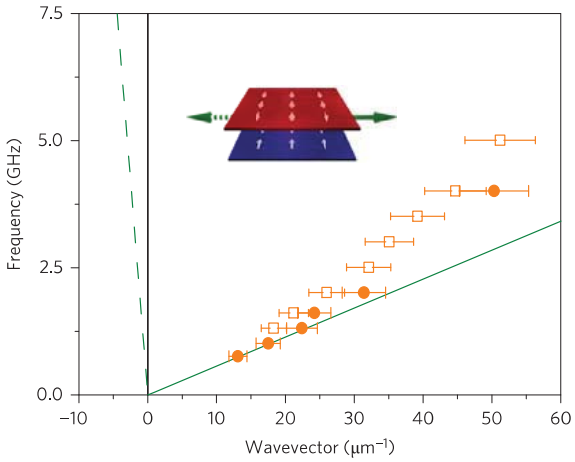


**Figure 4 | Dispersion $f(k)$ of collective spin waves propagating perpendicular to the direction of static magnetization in a trilayer where two in-plane ferromagnetic layers are antiferromagnetically coupled via a non-magnetic interlayer.** Solid and dashed green lines correspond to the calculated dispersions for the 'slow' and 'fast' spin-wave branches, respectively. Inset: Schematic showing the directions of static magnetization in the two ferromagnetic layers (white arrows) and the propagation direction for the 'slow' and 'fast' spin-wave branches (solid and dashed green arrows, respectively). Experimental results obtained by exciting vortex pair sample 1 with laterally oscillating magnetic fields are shown by filled orange circles, and the results of micromagnetic modelling are shown by open orange squares. Error bars indicate the uncertainty of wavelength determination.

separated by a non-magnetic spacer, are magnetized into opposite in-plane directions. The dispersion of such magnetostatic waves (neglecting exchange) was calculated in the pioneering work of Grünberg[43]. In our case, however, the exchange interaction cannot be ignored and thus we had to generalize the results of propagating perpendicularly to the circulating magnetization of an antiferromagnetically coupled vortex pair. This situation is similar to the propagation of a quasi-Damon–Eshbach mode[42] in a trilayer where two ferromagnetic films, separated by a non-magnetic spacer, are magnetized into opposite in-plane directions. The dispersion of such magnetostatic waves (neglecting exchange) was calculated in the pioneering work of Grünberg[43]. In our case, however, the exchange interaction cannot be ignored and thus we had to generalize the results of ref. 43 for the case of dipole-exchange spin waves. For this purpose, we start from a pair of coupled Landau–Lifshitz equations[44] for the

NATURE NANOTECHNOLOGY | VOL 11 | pp. 948 – 954 | NOVEMBER 2016 | DOI: 10.1038/NNANO.2016.117

magnetizations $\mathbf{M}_j$ ($i,j = 1,2$) of the two ferromagnetic layers:

$$\frac{\partial \mathbf{M}_j}{\partial t} = \gamma\left[\mathbf{B}_{ji} \times \mathbf{M}_j\right] \quad (1)$$

where γ is the modulus of the gyromagnetic ratio and $\mathbf{B}_{ji}$ is the effective magnetic field in the $j$th layer, which is assumed to contain only inhomogeneous exchange ($\propto \nabla^2\mathbf{M}_j$) and magneto-dipolar ($\mu_0\mathbf{H}_{ji}$) contributions:

$$\mathbf{B}_{ji} = \frac{2A}{M_s^2}\nabla^2\mathbf{M}_j + \mu_0\mathbf{H}_{ji} \ . \quad (2)$$

Here $A$ is the exchange constant, $M_s$ is the saturation magnetization, $\mu_0$ is the permeability in vacuum, and $\mathbf{H}_{ji}$ is the dipolar magnetic field that couples the magnetizations of the two ferromagnetic layers. It can be shown that the antiferromagnetic interlayer exchange coupling between the ferromagnetic layers – which is ignored in equation (2) – does not noticeably change the dispersion of the considered spin-wave mode. A detailed analytical solution of the problem formulated by equations (1) and (2) is presented in Supplementary Section 7.

For the model case of identical ferromagnetic layers in the long-wavelength limit (when $|\mathbf{k}| = k \to 0$), we found that the dipole-exchange spectrum of an antiparallel bilayer contains a spin-wave mode with linear dispersion and no frequency gap:

$$\omega(\mathbf{k}) = V(\phi_k)k \ , \quad (3)$$

where $\Phi_k$ is the angle between the spin-wave wavevector $\mathbf{k}$ and the in-plane direction of the static magnetization in the ferromagnetic layers (in our case $\Phi_k = \pm\pi/2$), while the velocity $V(\Phi_k)$ of the spin-wave mode is given by:

$$V(\phi_k) = \omega_M d\left[\sqrt{\frac{\lambda_{ex}^2}{d^2} + \frac{1}{12}\left[4 + 6\frac{d_s}{d} - F\left(\frac{\lambda_{ex}}{d}\right)\right]}\sin^2\phi_k - \frac{1}{2}\sin\phi_k\right]. \quad (4)$$

Here $\omega_M = \gamma\mu_0 M_s$, $\lambda^2_{ex} = 2A/\mu_0 M_s^2$ (exchange length), $d$ is the thickness of the ferromagnetic films, $d_s$ is the separation between the films, and the function $F(u)$ is given by

$$F(u) = 1 - 12u^2 + 24u^3\tanh\left(\frac{1}{2u}\right). \quad (5)$$

The fact that the spin-wave dispersion relation (3) depends on the sign of $\sin\Phi_k$ means that this spin-wave mode is non-reciprocal; that is, the velocities of spin waves propagating in opposite directions are substantially different. In our experimental conditions, when $d_s \ll d$ and $\lambda^2_{ex} \ll d^2$, expression (4) can be simplified to

$$V(\phi_k) \cong \omega_M d\left[\frac{1}{\sqrt{3}} + \frac{1}{2}sign(\sin\phi_k)\right]\left|\sin\phi_k\right| \ . \quad (6)$$

---

Thus, in our case of $\mathbf{k} \perp \mathbf{M}$, the velocities of spin waves propagating in opposite directions are much different—$V(\Phi_k = +\pi/2)/V(\Phi_k = -\pi/2) \simeq 14$.

Using equation (6), one can estimate the velocity of the 'slow' spin-wave branch $V(\Phi_k = -\pi/2)$ for the conditions of our experiment, assuming $\omega_M d \simeq (\omega_{M1}d_1 + \omega_{M2}d_2)/2$ to $V(\Phi_k = -\pi/2) \simeq 360$ ms$^{-1}$, which is rather close to the measured value at small wavenumbers. The wavelength of the 'fast' spin-wave branch with a velocity of $V(\Phi_k = +\pi/2) \simeq 5{,}000$ ms$^{-1}$, however, will be of the order of the lateral size of our sample, which would make it difficult to observe the 'fast' branch in our experiment. In particular, the formation of standing wave patterns involving counter-propagating 'slow' and 'fast' wave branches is practically suppressed. For this reason, and because of the smaller amplitudes expected for the 'fast' branch (Supplementary Section 4), only the 'slow' spin-wave branch was observed in our experiment, as shown in Fig. 3. The corresponding experimental dispersion relation $f(k)$ is plotted in Fig. 4 as filled orange dots. In addition, the dispersion curves of the 'slow' and 'fast' spin waves, calculated using equation (6) are shown as solid and dashed green lines, respectively.

From Fig. 4 it is clear that the 'slow' spin-wave branch calculated from our planar symmetric model system in equation (6) essentially describes the experimentally

NATURE NANOTECHNOLOGY | VOL 11 | pp. 948 – 954 | NOVEMBER 2016 | DOI: 10.1038/NNANO.2016.117

observed dispersion of a propagating mode in the vortex pair state with opposite circulations and asymmetric layers. Only for higher wavenumbers do the experimental frequencies of the 'slow' branch start to deviate from the theoretical line. This deviation can be attributed to an increasing effect of the exchange interaction, which presumably will eventually lead to a *k*-quadratic dispersion relation for high wavenumbers[44].

**Spin-wave generation mechanism**

To reveal the origin of the observed spin-wave generation process, we carried out micromagnetic simulations for a vortex-state magnetic trilayer[45]. The results of these simulations, shown for the 'slow' spin-wave branch by open orange squares in Fig. 4, are in excellent agreement with the experimental data. The spiralling spin-wave emission patterns obtained from these simulations (Supplementary Section 5) are also very similar to the experimentally measured spin-wave profiles.

It also follows that the origin of the observed spin-wave emission is a field-driven, small-amplitude vortex core gyration around the equilibrium position of the parallel cores. This core gyration is accompanied by the formation of a similarly gyrating perpendicular magnetization 'dip' of opposite sign that has already been observed for single-layer vortices[46] (Supplementary Section 5). Cores and 'dips' then act as perpendicular magnetic perturbations travelling laterally on the gyration orbit. These perturbations thus give rise to a local $m_z$-collective magnetization precession, that is, a source for spin waves, with a continuous azimuthal phase shift along the gyration orbit. The azimuthal precession phase shift essentially leads to the formation of a spiralling wave pattern instead of a concentric one. In a certain way, this spin-wave excitation mechanism can also be seen as an analogue to an orbiting stirrer in a fluid system, which leads to a similar pattern of spiralling wave propagation. Note that the mechanism of coherent spin-wave generation identified here is fundamentally different from that of the incoherent spin-wave emission predicted for dynamic vortex core switching[25,47,48].

**Non-reciprocal spin-wave propagation**

As follows from both analytical theory and from our micromagnetic simulations, the spin-wave mode observed in our experiments belongs to the 'slow' branch of the dipole-exchange dispersion relation (3). For the vortex pair shown in Fig. 2d ($c_{1(Co)} = +1$, $c_{2NiFe} = -1$), this 'slow' branch corresponds to outwards-propagating spin waves. Obviously, when both circulations are reversed ($c_{1(Co)} = -1$, $c_{2NiFe} = +1$), the 'slow' branch should also experience a reversal of its propagation direction and should therefore become inwards-propagating. Note that this effect is independent of the mean circulation of the vortex pair given by the higher magnetic moment of the Co layer, and only depends on the handedness of the pair circulations (Supplementary Section 4).

To evaluate this property experimentally, we measured a further trilayer sample containing a vortex pair with $c_{1(Co)} = -1$ and $c_{2NiFe} = +1$ (sample 2). Sample 2 is a circular Co/Ru/$Ni_{81}Fe_{19}$ (47.8/0.8/42.8 nm) disk with a diameter of 2 μm (Supplementary Section 2). Given this sample, we were able to compare the excitation of spin waves in vortex pairs with $c_{1(Co)} = +1$, $c_{2(NiFe)} = -1$ (sample 1) and $c_{1(Co)} = -1$, $c_{2(NiFe)} = +1$ (sample 2) using time-resolved scanning transmission X-ray microscopy. To exclude any stroboscopic artefacts, the samples were now driven by in-plane magnetic field pulses ($\mu_0 H_y \approx 1$ mT) of 500 ps length at a repetition rate of 5 ns. The results from this experiment are presented in Fig. 5, where the image contrast corresponds to the perpendicular magnetic deviation $\Delta m_z(t)$ in the respective NiFe layers of sample 1 (left image series) and sample 2 (right image series). Each series of four images spans an observation time of $\Delta t = 1.43$ ns, which covers the significant temporal changes in the spin-wave patterns observed (see Supplementary Movies 11–16 for the full 5 ns interval).

In sample 1, following the application of the driving pulse, a spin-wave train is formed at the centre of the sample, which then successively propagates outwards to the sample periphery, eventually reaching the outer edge of the field of view after ~1.4 ns. This pulse-driven spin-wave generation and propagation is similar to that of spin waves excited by a sinusoidal driving signal (as shown in Fig. 3).

The spin-wave propagation following pulsed excitation in sample 2 is crucially different. Here, the spin-wave train first appears at the outer edge of the field of view, propagates inwards, and eventually disappears at the centre of the sample. This behaviour confirms our prediction of two strongly non-reciprocal spin-wave branches ('slow' and 'fast'). The rotating vortex cores can only excite spin waves that propagate outwards from the centre. For sample 2, such outward-propagating spin waves correspond to the 'fast' branch, which cannot be directly observed in the experiment. However, once the 'fast' spin waves have reached the outer edge of the sample, they are reflected backwards, transforming into the observable inward-propagating 'slow' branch. Because there is only a very short delay (<280 ps) between the application of the driving pulse and the appearance of the observable spin waves at the outer edge of the sample, we conclude from this experiment that the 'fast' spin-wave branch is propagating much faster (at least ten times) than the 'slow' spin-wave branch. Complementary micromagnetic simulations

NATURE NANOTECHNOLOGY | VOL 11 | pp. 948 – 954 | NOVEMBER 2016 | DOI: 10.1038/NNANO.2016.117

(Supplementary Movie 19) were used to directly estimate the group velocity of the 'fast' branch as ~4 × $10^3$ $ms^{-1}$, which is close to the calculated value of ~5 × $10^3$ $ms^{-1}$. These findings therefore substantially support our theoretical prediction of the strongly non-reciprocal character of spin-wave propagation in antiferromagnetically coupled trilayers.

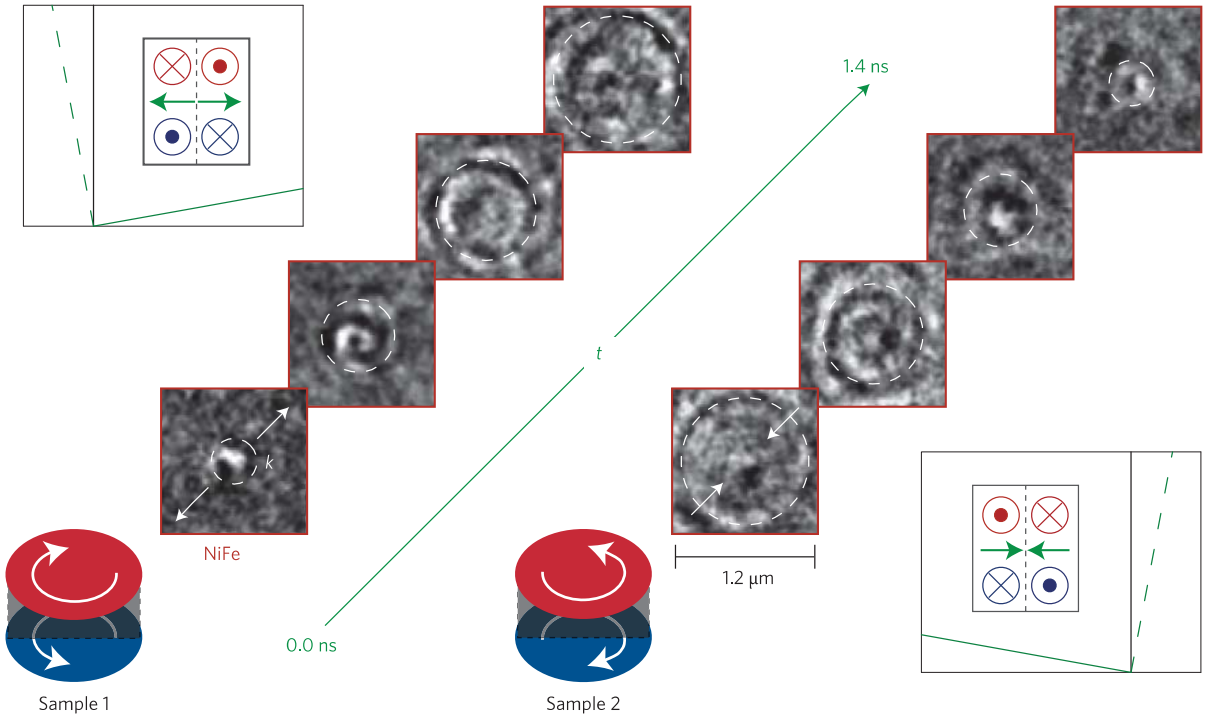


**Figure 5 | Pulsed excitation of spin waves in the two samples containing magnetic vortex pairs with opposite circulations.** The left series of images corresponds to sample 1 ($c_{1(Co)} = +1$, $c_{2(NiFe)} = -1$), supporting an outwards-propagating 'slow' spin-wave branch, and the right series corresponds to sample 2 ($c_{1(Co)} = -1$, $c_{2(NiFe)} = +1$), supporting an inwards-propagating 'slow' spin-wave branch. The image series consists of time-resolved scanning transmission X-ray microscopy images showing the $\Delta m_z$ contrast of the NiFe layer for different delay times. The phase fronts of excited spin-wave trains are highlighted by dashed white circles. The vortex circulations in the two ferromagnetic layers (blue, Co; red, NiFe) are indicated by white arrows in the adjacent schematics. The upper left and lower right insets show the dispersion curves for the 'slow' (solid green lines) and 'fast' (dashed green lines) spin-wave branches in samples 1 and 2, respectively. In these insets, green arrows indicate the propagation directions of the 'slow' spin-wave branch.

## Conclusions

We have found a highly agile mechanism for the coherent generation of propagating spin waves, whose nanoscale wavelengths are linearly tunable by the frequency of the driving signal. This generation mechanism overcomes the bandwidth limitations of conventional spin-wave generation methods, which are determined by the patterning size. In our case, spin-wave excitation stems from the driven gyration of naturally formed magnetic vortex cores that have sizes on the order of the exchange length of the sample material. We used time-resolved scanning transmission X-ray microscopy to directly image such propagating spin waves with wavelengths down to 100 nm and frequencies up to ~4 GHz. We found that – at relatively small wavenumbers – the excited spin-wave mode has a linear dispersion without a frequency gap. Moreover, this mode is strongly non-reciprocal; that is, waves travelling in opposite directions exhibit propagation velocities that are more than one order of magnitude different. Apart from the fundamental importance of the phenomena observed, we believe that the obtained results will open a way for the development of new and efficient bias-free non-reciprocal microwave signal-processing devices, such as isolators, circulators, unidirectional conduits, phase shifters and controlled switches.

submitted 12 August 2015; accepted 27 May 2016;

NATURE NANOTECHNOLOGY | VOL 11 | pp. 948 – 954 | NOVEMBER 2016 | DOI: 10.1038/NNANO.2016.117

published online 18 July 2016

## References


1. Bloch, F. Zur Theorie des Ferromagnetismus. *Z. Phys.* **61**, 206–219 (1930).
2. Holstein, T. & Primakoff, H. Field dependence of the intrinsic domain magnetization of a ferromagnet. *Phys. Rev.* **58**, 1098–1113 (1940).
3. Dyson, F. J. General theory of spin wave interactions. *Phys. Rev.* **102**, 1217–1230 (1956).
4. Gurevich, A. G. & Melkov, G. A. *Magnetization Oscillations and Waves* (CRC, 1996).
5. Demidov, V. E., Urazhdin, S. & Demokritov, S. O. Direct observation and mapping of spin waves emitted by spin-torque nano-oscillators. *Nature Mater.* **9**, 984–988 (2010).
6. Madami, M. *et al.* Direct observation of a propagating spin wave induced by spin-transfer torque. *Nature Nanotech.* **6**, 635–638 (2011).
7. Voigt, K. *et al.* Realization of a spin-wave multiplexer. *Nature Commun.* **5**, 3727 (2014)
8. Yu, H. *et al.* Omnidirectional spin-wave nanograting coupler. *Nature Commun.* **4**, 2702 (2013)
9. Macià, F., Backes, D. & Kent, A. D. Stable magnetic droplet solitons in spin- transfer nanocontacts. *Nature Nanotech.* **9**, 992–996 (2014).
10. Stancil, D. D. *Theory of Magnetostatic Waves* Ch. 5 (Springer, 1993).
11. Demidov, V. E. *et al.* Excitation of short-wavelength spin waves in magnonic waveguides. *Appl. Phys. Lett.* **99**, 082507 (2011).
12. Demokritov, S. O. *et al.* Bose–Einstein condensation of quasi-equilibrium magnons at room temperature under pumping. *Nature* **443**, 430–433 (2006).
13. Slonczewski, J. C. Current-driven excitation of magnetic multilayers. *J. Magn. Magn. Mater.* **159**, L1–L7 (1996).
14. Berger, L. Emission of spin waves by a magnetic multilayer traversed by a current. *Phys. Rev. B* **54**, 9353–9358 (1996).
15. Tsoi, M. *et al.* Generation and detection of phase-coherent current-driven magnons in magnetic multilayers. *Nature* **406**, 46–48 (2000).
16. Slonczewski, J. C. Exitation of spin waves by an electric current. *J. Magn. Magn. Mater.* **195**, L261–L268 (1999).
17. Hoefer, M. A., Silva, T. J. & Stiles, M. D. Model for a collimated spin-wave beam generated by a single-layer spin torque nanocontact. *Phys. Rev. B* **77**, 144401 (2008).
18. Bonetti, S. *et al.* Experimental evidence of self-localized and propagating spin wave modes in obliquely magnetized current-driven nanocontacts. *Phys. Rev. Lett.* **105**, 217204 (2010).
19. Slavin, A. & Tiberkevich, V. Spin wave mode excited by spin-polarized current in a magnetic nanocontact is a standing self-localized wave bullet. Phys. Rev. Lett. **95**, 237201 (2005).
20. Demidov, V. E. *et al.* Magnetic nano-oscillator driven by pure spin current. *Nature Mater.* **11**, 1028–1031 (2012).
21. Urazhdin, S. *et al.* Nanomagnonic devices based on the spin-transfer torque. *Nature Nanotech.* **9**, 509–513 (2014).
22. Kittel, C. Physical theory of ferromagnetic domains. *Rev. Mod. Phys.* **21**, 541 (1949).
23. Feldtkeller, E. & Thomas, H. Struktur und energie von blochlinien in dünnen ferromagnetischenen schichten. *Phys. Kondens. Materie* **4**, 8–14 (1965).
24. Shinjo, T., Okuno, T., Hassdorf, R., Shigeto, K. & Ono, T. Magnetic vortex core observation in circular dots of permalloy. *Science* **289**, 930–932 (2000).
25. Tretiakov, O. A. & Tchernyshyov, O. Vortices in thin ferromagnetic films and the skyrmion number. *Phys. Rev. B* **75**, 012408 (2007).
26. Guslienko, K. Y. Magnetic vortex state stability, reversal and dynamics in restricted geometries. *J. Nanosci. Nanotech.* **8**, 2745–2760 (2008).
27. Thiele, A. A. Steady-state motion of magnetic domains. *Phys. Rev. Lett.* **30**, 230–233 (1973).
28. Völkel, A. R., Wysin, G. M., Mertens, F. G., Bishop, A. R. & Schnitzer, H. J. Collective-variable approach to the dynamics of nonlinear magnetic excitations with application to vortices. *Phys. Rev. B* **50**, 12711–12720 (1994).
29. Choe, S.-B. *et al.* Vortex core-driven magnetization dynamics. *Science* **304**, 420–422 (2004).
30. Vansteenkiste, A. *et al.* X-ray imaging of the dynamic magnetic vortex core deformation. *Nature Phys.* **5**, 332–334 (2009).
31. Buess, M. *et al.* Fourier transform imaging of spin vortex eigenmodes. *Phys. Rev. Lett.* **93**, 077207 (2004).
32. Perzlmaier, K. *et al.* Spin-wave eigenmodes of permalloy squares with a closure domain structure. *Phys. Rev. Lett.* **94**, 057202 (2005).
33. Kammerer, M. *et al.* Magnetic vortex core reversal by excitation of spin waves. *Nature Commun.* **2**, 279 (2011).
34. Buchanan, K. *et al.* Magnetic remanent states and magnetization reversal in patterned trilayer nanodots. *Phys. Rev. B* **72**, 134415 (2005).
35. Wintz, S. *et al.* Control of vortex pair states by post-deposition interlayer exchange coupling modification. *Phys. Rev. B* **85**, 134417 (2012).
36. Guslienko, K. Y. u., Buchanan, K. S., Bader, S. D. & Novosad, V. Dynamics of coupled vortices in layered magnetic nanodots. *Appl. Phys. Lett.* **86**, 223112 (2005).
37. Grünberg, P., Schreiber, R., Pang, Y., Brodsky, M. B. & Sowers, H. Layered magnetic structures: evidence for antiferromagnetic coupling of Fe layers across Cr interlayers. *Phys. Rev. Lett.* **57**, 2442–2445 (1986).
38. Nolle, D. *et al.* Unique characterization possibilities in the ultra high vacuum scanning transmission X ray microscope (UHV-STXM) 'MAXYMUS' using a rotatable permanent magnetic field up to 0.22 T. *Rev. Sci. Instrum.* **83**, 046112 (2012).
39. Raabe, J. *et al.* PolLux: a new facility for soft X-ray spectromicroscopy at the Swiss light source. *Rev. Sci. Instrum.* **79**, 113704 (2008).
40. Cherepov, S. S. *et al.* Core–core dynamics in spin vortex pairs. *Phys. Rev. Lett.* **109**, 097204 (2012).
41. Hänze, M., Adolff, C. F., Velten, S., Weigand, M. & Meier, G. Two-body problem of core-region coupled magnetic vortex stacks. *Phys. Rev. B* **93**, 054411 (2016).
42. Damon, R. W. & Eshbach, J. R. Magnetostatic modes of a ferromagnetic slab. *J. Phys. Chem. Solids* **19**, 308–320 (1961).
43. Grünberg, P. Magnetostatic spin-wave modes of a heterogeneous ferromagnetic double layer. *J. Appl. Phys.* **52**, 6824 (1981).
44. Landau, L. & Lifshitz, E. On the theory of the dispersion of magnetic permeability in ferromagnetic bodies. *Phys. Z. Sowjetunion.* **8**, 153–169 (1935).
45. Scheinfein, M. R. LLG Micromagnetics Simulator; http://llgmicro.home. mindspring.com
46. Kravchuk, V. P., Gaididei, Y. & Sheka, D. D. Nucleation of a vortex–antivortex pair in the presence of an immobile magnetic vortex. *Phys. Rev. B* **80**, 100405(R) (2009).
47. Lee, K. S. & Kim, S. K. Radiation of spin waves from magnetic vortex cores by their dynamic motion and annihilation processes. *Appl. Phys. Lett.* **87**, 192502 (2005).
48. Hertel, R., Gliga, S., Fähnle, M. & Schneider, C. M. Ultrafast nanomagnetic toggle switching of vortex cores. *Phys. Rev. Lett.* **98**, 117201 (2007).


## Acknowledgements

The authors thank A. Puzic, K.W. Chou and M.-Y. Im for their contributions to the preparation of this work, C. Quitmann, H. Stoll, G. Schütz, M. Curcic, R. Mattheis, J. McCord, S. Gemming, V. Sluka, K. Schultheiss and R. Hübner for their support and discussions, as well as V. Kühn, J. Kerbusch and K. Kirsch for their assistance in sample fabrication. Most experiments were performed at the Maxymus endstation at BESSY2, HZB (Berlin, Germany). The authors acknowledge HZB for the allocation of synchrotron radiation beam time. Some experiments were performed at the Pollux endstation at SLS, PSI (Villigen, Switzerland). Pollux is financed by BMBF under contracts nos. 05KS4WE1/6 and 05KS7WE1. Technical support by M. Bechtel and B. Sarafimov at the scanning transmission X-ray microscopy set-ups is gratefully acknowledged. This work was supported in part (V.T. and A.S.) by a grant from DARPA MTO/MESO (nos. N66001-11-1-4114), grant no. ECCS-1305586 from the National Science Foundation, and by contracts from the US Army TARDEC, RDECOM. V.T. and A.S. acknowledge the Center for NanoFerroic

NATURE NANOTECHNOLOGY | VOL 11 | pp. 948 – 954 | NOVEMBER 2016 | DOI: 10.1038/NNANO.2016.117

Devices (CNFD) and the Nanoelectronics Research Initiative (NRI) for partial support of this work.

## Author contributions

S. W., M. W. and J. R. performed the experiments. S. W. fabricated the samples and performed the simulations. V. T. and A. S. calculated the dispersion relations. S. W. and A. S. wrote the manuscript. All authors discussed the data and commented on the manuscript.

## Additional information

Supplementary information is available in the online version of the paper. Reprints and permissions information is available online at www.nature.com/reprints. Correspondence and requests for materials should be addressed to S.W.

## Competing financial interests

The authors declare no competing financial interests.

## Methods

**Sample fabrication.** The samples were fabricated on X-ray-transparent silicon-nitride membrane substrates with a thickness of 100 nm. The patterning of microelements was achieved by a sequence of electron-beam lithography, multilayer deposition and liftoff processing. A positive poly(methyl methacrylate) (PMMA) resist was first spun onto the substrate. In the second step, circular and square-shaped elements with base sizes between 2 and 4 μm were exposed by means of electron-beam lithography and then subsequently developed for 30 s in a methyl isobutyl ketone:isopropyl alcohol (MIBK:IPA) mixture (1:3 volume ratio). A Co/Ru/$Ni_{81}Fe_{19}$/Al multilayer was then deposited by magnetron sputter deposition, with Al serving as a capping layer for oxidation protection. The resulting layer thicknesses were determined by transmission electron microscopy (TEM) to be 47.8, 0.8, 42.8 and 5 nm (Supplementary Section 1). For the chosen Ru thickness, antiferromagnetic interlayer exchange coupling is expected to occur between the two ferromagnetic layers; that is, antiparallel magnetic alignment between the two layers is energetically preferred. This coupling was quantitatively estimated by fitting an extended Stoner-Wolfarth model on the magnetization reversal signal measured by magneto-optic Kerr effect (Supplementary Section 1), resulting in a bilinear coupling constant of $J_L = -0.35$ mJ m$^{-2}$ and biquadratic coupling constant of $J_Q = -0.07$ mJ m$^{-2}$. This type of coupling leads to the formation of spin vortex pairs with antiparallel circulations in microelements of the given sizes and materials. Oscillating magnetic fields can be applied to the sample via electric currents flowing through a copper strip fabricated on top of the elements. The patterning of the strip was carried out analogously to the microelements, but a bilayer copolymer/polymer resist was used instead and the development time was increased to 120 s. The coppert hin film was deposited with a nominal thickness of 200 nm by means of evaporation, together with a 5-nm-thick aluminium cap layer. The patterned microstrip had a width of 5 μm. Based on this, the resulting magnetic field was estimated to be $\mu_0 H = 4\pi \times 10^{-2}$ mT mA$^{-1}$.

**Time-resolved scanning transmission X-ray microscopy.** The magnetization distribution of the vortex pair structure was imaged by means of synchrotron-based scanning transmission X-ray microscopy[38,39]. This method uses a Fresnel zone plate to focus a monochromatic X-ray beam onto the sample. The sample was then raster-scanned through this beam, and the transmitted intensity, collected by a point detector, yielded a two-dimensional image with ~25 nm lateral resolution. By the application of circularly polarized photons, X-ray magnetic circular dichroism (XMCD)[49] was used to acquire a magnetic signal. Because XMCD is only relevant at the resonant absorption edges of a specific element, the two ferromagnetic layers of the Co/Ru/NiFe stack could be separately addressed by tuning the incident X-ray energy to different absorption edges, in this case the Ni $L_3$ edge ($E \approx 853$ eV) and the Co $L_3$ edge ($E \approx 778$ eV), respectively. The achieved magnetic contrast is proportional to the projection of the magnetic orientation $\mathbf{m} = \mathbf{M}/M$ onto the photon propagation direction $\mathbf{e}_k$. Therefore, a normal incidence set-up is sensitive to perpendicular magnetization components, whereas additional in-plane sensitivity can be gathered when the sample normal is inclined versus $\mathbf{e}_k$. The dynamic response of the vortex pair to an alternating magnetic field excitation was stroboscopically imaged by means of time-resolved scanning transmission X-ray microscopy. This method employs the specific time structure of the incoming synchrotron radiation, that is, X-ray flashes of an approximate temporal width of 100 ps at a 2 ns repetition rate. The transmitted intensity is on the order of a single photon per flash and is recorded by a fast avalanche photodiode. The result of each probing event (photon or no photon transmitted) is routed to a specific counting register of a periodic register set by a field-programmable gate array. Here, the integer total amount of registers has to be commensurable with the single-cycle (non-stroboscopic) measurement duration divided by 2 ns. Furthermore, the electronic excitation sources are required to be synchronized to the repetition rate of the X-ray flashes. The excitation signal (current in the stripline) is evaluated before and after the sample by means of two – 20 dB pick-off tees that provide pick-off signals to an oscilloscope.

**Micromagnetic simulations.** Micromagnetic simulations based on time integration of the Landau–Lifshitz–Gilbert equation[50] were carried out using the 'LLG Micromagnetic Simulator' environment[45]. At first, the initial state of a Co/NiFe vortex pair with antiparallel circulations and parallel cores was simulated using an artificially high Gilbert damping constant of $\alpha = 1$, allowing for relatively fast relaxation of the system. Once the residual relative torque decreased below $1 \times 10^{-6}$ in all simulation cells, the system was assumed to have reached its equilibrium state. The time evolution of the system was simulated with a damping constant of $\alpha = 0.01$ following excitation by a laterally alternating sinusoidal magnetic field. The simulated material parameters were set to the following values: $M_s^{Co} = 1{,}273$ kAm$^{-1}$, $M_s^{NiFe} = 740$ kAm$^{-1}$, $d^{Co} = 47.8$ nm and $d^{NiFe} = 42.8$ nm as measured by a superconducting quantum interference device (SQUID) and TEM[35], and $A^{Co} = 3.05 \times 10^{-11}$ Jm$^{-1}$, $A^{NiFe} = 1.05 \times 10^{-11}$ Jm$^{-1}$ and $d^{IL} = 0.8$ nm, as taken from refs 35 and 45. For simplicity, we neglected the small intrinsic anisotropies of the ferromagnetic layers and we assumed that the interlayer possesses vacuum permeability. The interlayer exchange coupling constants were set to $J_L = -0.35$ mJ m$^{-1}$ and $J_Q = -0.07$ mJ m$^{-2}$ (ref. 35). The underlying simulation body was a square-shaped element with an edge length of 1 μm that was discretized into 128 × 128 uniform orthogonal cells, corresponding to lateral cell dimensions of approximately (7.8 nm)$^2$. For symmetry reasons, this structure was reduced to a circular element with a diameter of 1 μm. Vertically, a non-uniform discretization was chosen, attributing five cells each to the ferromagnetic layers (9.56 nm, Co; 8.56 nm, NiFe) and a single cell (0.8 nm) for the interlayer, respectively.

### References

49. Schütz, G. *et al.* Absorption of circularly polarized X rays in iron. *Phys. Rev. Lett.* **58**, 737–740 (1987).
50. Gilbert, T. L. A phenomenological theory of damping in ferromagnetic materials. *IEEE Trans. Magn.* **40**, 3443–3449 (2004).

NATURE NANOTECHNOLOGY | VOL 11 | pp. 432 – 437 | NOVEMBER 2016 | DOI: 10.1038/NNANO.2015.339

# Magnetic domain walls as reconfigurable spin-wave nano-channels

K. Wagner,[1] A. Kákay,[1] K. Schultheiss,[1] A. Henschke,[1] T. Sebastian,[1] and H. Schultheiss[1,2]
[1)] *Helmholtz-Zentrum Dresden - Rossendorf, Institute of Ion Beam Physics and Materials Research, Bautzner Landstraße 400, 01328 Dresden, Germany*
[2)] *Technische Universität Dresden, D-01062 Dresden, Germany*

(Dated: 7 March 2017)

**In the research field of magnonics[1–7], spin waves are envisioned to be used as information carriers promoting operations based on their wave properties. However, the field still faces major challenges: To become fully competitive, novel schemes for an energy-efficient control of spin-wave propagation in 2D have to be realised on much smaller length scales than used before. In this letter, we address these challenges by the experimental realisation of a novel approach to guide spin waves in reconfigurable, nano-sized magnonic waveguides. For this purpose, we make use of two inherent characteristics of magnetism: the nonvolatility of magnetic remanence states and the nanometre dimensions of domain walls formed within these magnetic landscapes. We present the experimental observation and micromagnetic simulations of spin-wave propagation *inside* nano-sized domain walls and realise a first step towards a reconfigurable domain-wall based magnonic nano-circuitry.**

Spin waves are the dynamic eigen-excitations of a magnetically ordered medium with their quanta being referred to as magnons. In the last years, the scientific community in the field of magnonics made huge efforts to realise concepts to use these spin waves for data processing. Quite recently, remarkable progress has been made by the demonstration of prototype building blocks of a future spin-wave based logic[8–10]. Despite this progress, most concepts are based on very similar sample layouts that are limited regarding the further optimisation of existing devices. Previous studies on spin-wave propagation on the nanoscale relied on confinement in geometrically patterned waveguides[11] that lack any flexibility for manipulating the spin-wave propagation path as required for flexible, reprogrammable devices. On the microscale, this dynamic control of spin waves in two-dimensional structures has been realised but is based on the continuous application of external fields or currents and has been achieved at the cost of very high energy consumption. In the following, we will present a possible way to overcome these challenges.

Spin waves impinging on a domain wall are either reflected or experience a phase shift when transmitted, depending on the spin-wave wavelength and the type of domain wall[12–16]. Additional studies were devoted to the investigation of the domain dynamics itself that were found in the very low MHz frequency range on the order of 10 MHz[17]. However, the possibility to send spin waves *along* a domain wall has only recently been addressed in a numerical study for a material with out-of-plane magnetisation that is difficult to handle in experimental scenarios[18]. Here, we experimentally explore the intrinsic spin-wave eigenmodes that are quantised across the width of a domain wall and yet possess a well-defined wave vector along the wall that enable information transport and processing. Targeting this class of still widely unknown spin-wave modes, we focus on the potential of utilising domain walls as nanometre-scaled spin-wave channels that open new perspectives for the energy-efficient control of spin-wave propagation in 2D.

The top panel in Fig. 1a shows a schematic illustration of a 180° Néel wall. The magnetic moments rotate within the sample plane, giving rise to magnetic volume charges – defined as the divergence of the magnetisation $\nabla \cdot \mathbf{M}$ – with opposite signs on the two sides of the domain-wall centre. The red curve in Fig. 1a illustrates these volume charges calculated via micromagnetic simulations. The charges generate a strong magnetostatic field $\mathbf{H}_{\mathrm{demag}}$ (blue curve in Fig. 1a) oriented antiparallel to the magnetisation direction in the centre of the domain wall resulting in a locally decreased effective magnetic field. Since the spin-wave dispersion depends on this effective field, field gradients form potential wells for spin waves[19,20]. In the actual case, a potential well for spin waves is created across the domain wall with a width of only a few ten nanometres. The exact width of a domain wall strongly depends on various parameters of magnetic materials and can be tuned towards even smaller sizes. In this letter, we demonstrate experimentally and numerically that such a potential well leads to spin-wave modes which are strongly localised to the domain-wall width and yet travel freely along the wall. Moreover, and in contrast to the vast majority of experimentally realised scenarios, no energy-consuming external bias fields are needed to promote spin-wave propagation in the preferred geometry[10] along the domain wall within the magnetic remanence state.

Figure 1b shows a scanning electron micrograph of the structure that was used in the experiment. A 40-nm-thick $Ni_{81}Fe_{19}$ (Permalloy, Py) film is patterned into a spin-wave waveguide that is 5-$\mu$m wide at the top end, then gradually broadens until it reaches a constant width of 10 $\mu$m. The variable width stabilises the desired remanence state. A gold microwave antenna is positioned at the beginning of the 10-$\mu$m wide part of the waveguide. Oscillating magnetic fields $h_{\mathrm{rf}}$ generated by the application of microwave currents to this antenna allow for the local excitation of spin waves with well defined frequencies.

NATURE NANOTECHNOLOGY | VOL 11 | pp. 432 – 437 | NOVEMBER 2016 | DOI: 10.1038/NNANO.2015.339

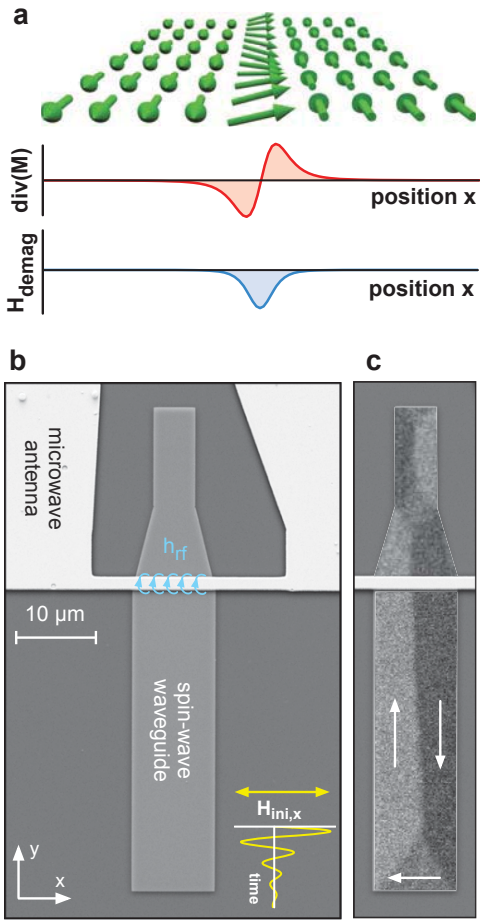


FIG. 1. **Channelling principle, sample geometry and magnetisation configuration. a**, Schematic illustration of a 180° Néel wall carrying a spin wave. The divergence of the magnetisation $\nabla \cdot \mathbf{M}$ across the width of the wall shows opposite sign on the two sides of the domain wall centre and results in a strong magnetostatic field $\mathbf{H}_{\mathrm{demag}}$ oriented antiparallel to the magnetisation direction. This potential well confines the spin-wave propagation into the narrow region of the wall. **b**, Scanning electron micrograph of the investigated Py structure and the microwave antenna for the external excitation of spin dynamics. The inset on the lower right shows the magnetic field sweep that is used to initialize the domain configuration. **c**, The black-white contrast of the Kerr-microscopy image confirms the formation of a Landau-like domain pattern. The arrows indicate the magnetisation direction in the domains.

In order to reproducibly prepare the aforementioned remanence state with the domain wall parallel to the long axis of the waveguide, we applied a sinusoidal, exponentially decaying magnetic field $H_{\mathrm{ini,x}}$ parallel to the short axis of the waveguide as depicted by the inset in Fig. 1b. We used magneto-optical Kerr microscopy to confirm the magnetic state of the waveguide. The overlay in Fig. 1c shows an exemplary Kerr image with the black-white colour code representing the magnetisation component along the y-direction. A Landau-like domain pattern is formed with a 180° Néel wall in the centre of the waveguide separating two domains with opposite magnetisation. The arrows indicate the magnetisation direction in the domains. Additional micromagnetic simulations (discussed below) confirm the Néel-type character of the domain wall with the magnetic moments rotating in the sample plane as is expected for the material parameters and thickness of the Py film[21].

Experimentally, the propagation of spin waves was studied by micro-focus Brillouin light scattering (BLS) spectroscopy[22]. To analyse the spectrum in the different areas of the domain pattern, we measured the spin-wave intensity as a function of the excitation frequency at two different positions: inside the domain wall and in the domains. These measurements were performed in the 10-$\mu$m wide bottom part of the waveguide at a distance of 1-$\mu$m from the antenna. Figure 2a summarizes the results of the measurements and clearly shows two distinct spectra depending on the probing position: inside the domain wall (squares), the maximum spin-wave intensity was observed at the lowest possible detection frequency of 500 MHz whereas in the domains (triangles) highest intensities can be found at much higher frequencies around 2.8 GHz. The existence of a strongly localised mode inside the domain wall is a remarkable observation supporting our assumption of spin waves trapped in a potential well.

To analyse the nature of the different spin-wave modes within the wall and the domains, we detected their intensity profile across the width of the waveguide. These measurements were carried out at the excitation frequencies where maximum intensity was observed within the wall and the domain. Fig. 2b illustrates the results of these line scans. The detected modes show a clear spatial separation with one mode strongly confined in the centre of the waveguide at the position of the domain wall (squares). In contrast, the higher-frequency mode (triangles) is spread throughout the domains at both sides of the wall whereas it almost vanishes at the domain-wall position. Thus, the potential well formed by the domain wall can be used to confine spin waves in a certain frequency range on the nanoscale.

The slightly different intensity profiles detected at 2.8 GHz in the two domains are attributed to the fact that the domain wall is not perfectly centred in the waveguide. This asymmetry leads to different lateral confinement conditions in the two domains and, consequently, to a relative shift of the corresponding excitation spectra. However, quantisation due to confinement in micron-sized waveguide structures has already been studied extensively[22–24].

Here, we focus on the spin-wave mode inside the nanochannel formed by the domain wall that can be selectively excited by choosing the proper microwave frequency. The localisation becomes even more evident from the two-dimensional BLS measurement presented

NATURE NANOTECHNOLOGY | VOL 11 | pp. 432 – 437 | NOVEMBER 2016 | DOI: 10.1038/NNANO.2015.339

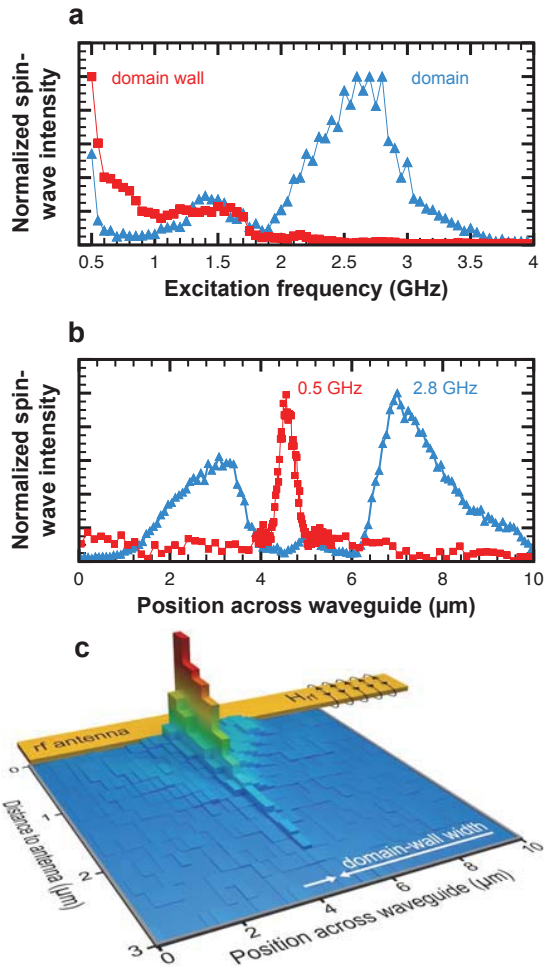


FIG. 2. **Excitation spectra and spin-wave mode profiles. a**, Spin-wave spectrum measured by BLS microscopy inside the domain wall (squares) and the domains (triangles), respectively. The measurement clearly shows different excitation spectra depending on the probing position. **b**, Line scans of the spin-wave intensity across the width of the Py waveguide for the two excitation frequencies that yielded maximum spin-wave intensity inside the domain wall (squares) and in the domain (triangles). The data exhibit two spatially separated spin-wave modes with the low-frequency mode strongly localised at the domain wall position. **c**, Two-dimensional intensity distribution of spin waves propagating along the nano-channel formed by the domain wall in the centre of the waveguide.

in Fig. 2c. Solely at the position of the domain wall, the signal of a spin-wave mode propagating away from the antenna is detected revealing the channelling character of the nano-sized domain wall.

To get a deeper insight in the propagation characteristics within the domain wall, micromagnetic simulations were carried out[25]. The studied system was a 5-$\mu$m long, 1-$\mu$m wide and 10-nm thick Py rectangle and, thus, smaller than the experimentally observed structure. This reduction of size allowed for a sufficiently fine discretisation required to simulate the nano-sized domain wall without affecting its character which is mainly determined by the material parameters and not by the different dimensions. Therefore, a direct comparison between experiment and simulation is still possible for the spin-wave modes within the domain wall. Figure 3a shows the static equilibrium magnetisation configuration. The red-blue colour codes the in-plane magnetisation component $m_x$ parallel to the short axis of the rectangle and the arrows display the magnetisation direction. The microstructure exhibits a flux-closure Landau-like domain pattern with a 180° Néel wall separating two large domains with opposite magnetisation.

The magnitude of the effective magnetic field calculated from this remanence state is presented in Fig. 3b with the red-blue colour representing the in-plane field component $H_x$ along the short axis of the rectangle. The data clearly show strong effective fields along the domain walls that are oriented anti-parallel to the magnetisation direction and, thus, form potential wells for spin waves.

Starting from the Landau-type magnetisation configuration, an out-of-plane field pulse is applied locally at the domain-wall position at 1.6-$\mu$m distance from the bottom edge to excite spin dynamics (see green dot in Fig. 3c). This pulsed excitation and subsequent analysis as discussed in the method section yields the spin-wave spectrum and dispersion relation, which is discussed in the next paragraph. For displaying the mode profiles of the spin-wave resonances we simulated the response to a continuous microwave excitation at four different frequencies. In Fig. 3c the normalized z-component of the magnetization ($m_z$) is plotted for a given time once the system reached a steady state. The time evolution of the spin-wave amplitudes showing their propagating nature are available as supplementary material for two distinct frequencies. For the lower frequencies of 0.52 GHz, 1.28 GHz and 2.16 GHz, the spin-wave modes are strongly localized inside the domain wall. However, a general trend in Fig. 3c is that the strong localisation within the domain wall gets weaker for increasing frequency. For modes with high frequencies, *e.g.* 5.68 GHz, the clearly visible radiation from the wall indicates the onset of the spin-wave band in the domains and, thus, the loss of the channelling effect. While the strong localisation of the low-frequency spin waves inside the domain wall is in good accordance to the experiment, the domain modes appear at higher frequencies in the simulation. In general, the spin-wave eigenmodes shift to higher frequencies when reducing the domain size which, therefore, allows guiding of spin waves inside the wall even for higher frequencies and smaller wavelength.

In addition to the spatial and spectral characteristics of the investigated spin-wave modes, the micromagnetic simulations also shed light on the spin-wave dispersion. The spin-wave wavelength for a given frequency - as illustrated by the green bars in Fig. 3c - can be determined

NATURE NANOTECHNOLOGY | VOL 11 | pp. 432 – 437 | NOVEMBER 2016 | DOI: 10.1038/NNANO.2015.339

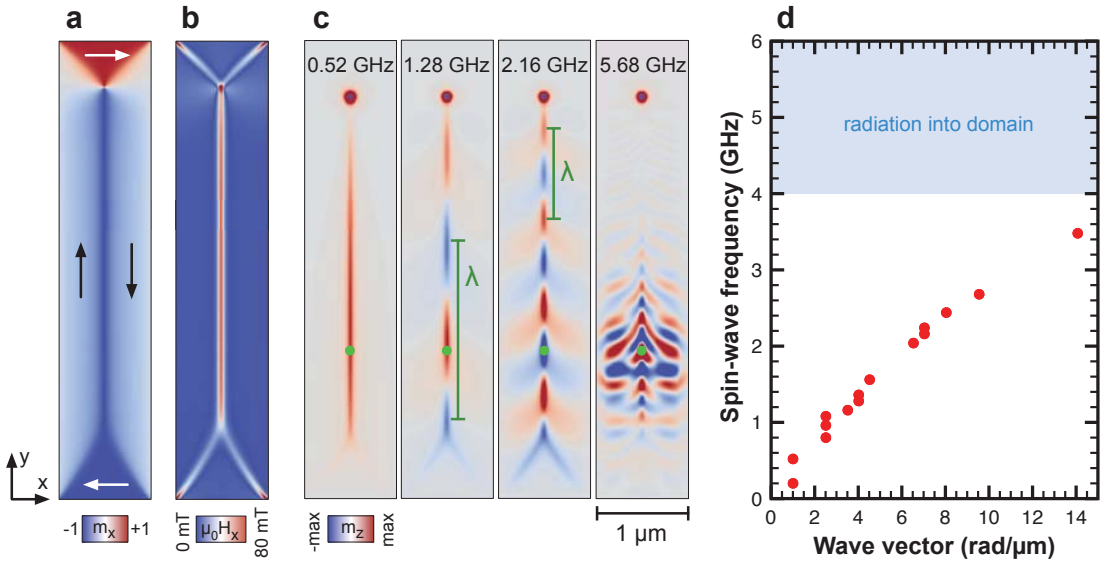


FIG. 3. **Magnetisation, effective magnetic field, spin-wave modes and dispersion. a**, Simulated domain configuration of the rectangular Py thin-film element. The red-blue colour represents the in-plane magnetisation component $m_x$ parallel to the short axis of the rectangle, the arrows display the net magnetisation direction in the domains. **b**, $x$-component of the resulting effective field. The image clearly shows that strong fields are present along the domain walls. **c**, Amplitude profiles of different spin-wave modes excited locally at the position indicated by the green dot. The red-blue colour represents the out-of-plane component of the magnetisation $m_z$. The green bars indicate the spin-wave wavelengths that can be extracted from the data. **d**, Dispersion relation for spin waves mostly confined to the domain wall.

by a Fourier analysis of the dynamic magnetisation along the domain wall. Figure 3d shows the resulting dispersion relation and reveals a positive dispersion that enables the transport of information via spin waves propagating within the domain wall. **Even though the spin waves are confined transverse to the wall on a length scale given by the domain wall width, the dispersion is mainly dominated by dipolar energy. For the first three modes shown in Fig. 3c the dynamic part of the dipolar energy originating from the spin waves is by a factor 3-5 larger than the dynamic exchange energy.** The observation of well-defined wave vectors along the propagation path is a crucial pre-condition for numerous concepts that rely on the interference of spin waves[12,26,27]. Therefore, this observation highlights the potential of utilising domain walls in sophisticated magnonic circuits for information transport and data processing.

To evaluate the localisation of the numerically calculated spin-wave modes, we extract a line profile of the spin-wave intensity excited at 0.52 GHz across the domain wall. The result is shown by the black dashed line in Fig. 4 yielding a signal with a full width at half maximum (FWHM) of about 40 nm. Additionally, we also plot the line profile of the effective magnetic field $H_{\mathrm{eff}}$ (blue solid line) extracted for the same position as the dynamic magnetisation. The direct comparison of the two curves shows the strong confinement of the spin precession to the area of the potential well and, hence, to the position of the domain wall.

Furthermore, we analysed the lateral spin-wave localisation from the experimental results shown in Fig. 2. The experimental data is plotted by red squares in Fig. 4 and is well reproduced by a Gaussian fit (red dotted line) with a FWHM of 340 nm. To compare this value to the simulation, we have to take into account that the detected BLS signal does not directly reflect the spatial distribution of the observed spin-wave mode but is the convolution of the actual spin-wave signal with the shape of the probing laser spot. In fact, the FWHM extracted from the data is already on the order of the focal spot size that is expected for the confocal microscope used in our study and, thus, confirms the strong lateral confinement revealed by micromagnetic simulations.

In a final step we go beyond these mere observations and demonstrate the intriguing flexibility of spin-wave nano-channels based on domain walls by actually controlling the spin-wave propagation path. In contrast to waveguides based on geometric confinement that cannot be modified after patterning, a domain wall can be easily manipulated by several means like magnetic fields, charge or spin currents. These manipulations of domain walls open a new perspective to control spin-wave transport in two-dimensional nanostructures and towards reconfigurable magnonic circuits and logic devices.

In the actual experimental scenario, we controlled the position of the domain wall by applying small external magnetic fields along the long axis of the waveguide. De-

NATURE NANOTECHNOLOGY | VOL 11 | pp. 432 – 437 | NOVEMBER 2016 | DOI: 10.1038/NNANO.2015.339

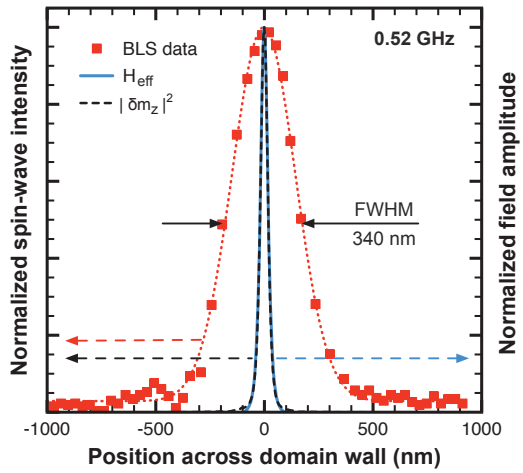


FIG. 4. **Spin-wave localisation.** Spin-wave intensity across the domain-wall width determined from experiment (squares) and simulation (dashed line) for 0.52 GHz. The dotted line represents a Gaussian fit to the measured data that is the convolution of the actual spin-wave signal with the focal spot size of the BLS microscope. This fit with a FWHM of 340 nm mainly reflects the spot size that is expected to be on the same order for confocal microscopes and, thus, suggest a confinement of several tens of nanometres. In accordance to this consideration, the micromagnetic simulation shows a strong lateral confinement of 40 nm for the spin-wave modes within the wall. The solid blue line is the magnitude of the effective magnetic field indicating the width of the potential well for the simulated magnetisation configuration.

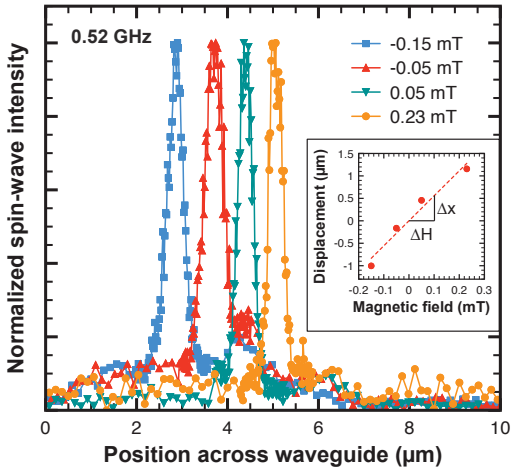


FIG. 5. **Steering spin waves with small fields.** Spin-wave intensity measured across the waveguide for different external magnetic fields applied parallel to the long axis of the waveguide for 0.52 GHz. The measurements show that the domain wall can be easily shifted with small applied fields over $\mu$m distances in both directions, therefore allowing for a fine control of the spin-wave channel position. The inset illustrates the displacement of the spin-wave propagation path as a function of the applied field and yields a proportionality constant of 5.57 $\mu$m/mT.

pending on the polarity of the applied field, the growth of either the left or the right domain is favoured and results in a shift of the domain wall. Figure 5 shows BLS line scans across the width of the waveguide at four different small magnetic fields of -0.15 mT, -0.05 mT, 0.05 mT, and 0.23 mT. The measurements clearly show that the detected spin-wave mode is shifted together with the domain wall by the applied field. The observed left-right asymmetry of the domain-wall shift versus the field is attributed to the initial displacement of the domain wall even in the absence of any external magnetic fields.

In fact, the position of the domain wall and, thus, the spin-wave propagation path can be moved with nanometre precision over a distance of about 2 $\mu$m within a field range of only $\Delta H = 0.38$ mT. The inset in Fig. 5 illustrates this displacement as a function of the applied field and yields a proportionality constant of 5.57 $\mu$m/mT. These data already establish a novel mechanism to control spin-wave transport in 2D. Moreover, they pave the way for a potential reconfigurable but non-volatile magnonic nano-circuitry. In future scenarios, artificial pinning centres - for instance induced by ion implantation[28,29] - might be used to enable switching between several stable remanence states with different domain-wall configurations that act as pre-defined nano-channels to guide spin-wave propagation in logic devices. **Furthermore, multiple domain walls can form in materials with a perpendicular magnetic anisotropy with a separation of a few tens of nanometers[18], which allows for an even higher integration density of these spin-wave nano channels.**

In summary, we experimentally demonstrated the channelling of spin-waves in nanometre-wide magnetic domain walls with a width of about 40 nm. Micromagnetic simulations allowed for further analysis of the propagation characteristics. The spin-wave modes propagating inside domain walls exhibit a well-defined wave vector along their propagation path and a positive dispersion enabling information transport as well as data processing based on the interference of waves. Finally, we demonstrated a major advantage of domain-wall based magnonic waveguides over geometric patterning: manipulating the domain configurations with tiny, external fields well below 1 mT allowed us to actually shift the spin-wave propagation path over the distance of several micrometres. These observations pave the way for the realisation of reconfigurable, yet non-volatile magnonic circuitry by switching between different remanence states and, thus, for the realisation of energy-efficient and programmable spin-wave logic devices on the nanoscale.

NATURE NANOTECHNOLOGY | VOL 11 | pp. 432 – 437 | NOVEMBER 2016 | DOI: 10.1038/NNANO.2015.339

## METHODS

**Sample Preparation.** A bilayer of 3 nm Ti for adhesion and 40 nm Py was deposited on a $SiO_2$ substrate using electron-beam evaporation. Employing electron-beam lithography and lift-off techniques, micron-sized spin-wave waveguides were patterned. Their major part has a width of 10 $\mu$m which is gradually reduced to 5 $\mu$m towards one side to form a nucleation pad for a magnetic domain wall. In a second step, a 100-nm thick and 1.6-$\mu$m wide gold antenna is positioned at the beginning of the 10-$\mu$m wide part of the waveguide utilising electron-beam lithography, electron-beam evaporation and subsequent lift-off. A microwave current flowing through the antenna generates an oscillating magnetic field that couples to the magnetization and allows for the excitation of spin waves with well defined frequencies.

**BLS microscopy.** The spin-wave intensity is locally recorded by means of BLS microscopy at room temperature. BLS is the inelastic scattering of photons and magnons. Light from a continuous wave, single-frequency 532-nm solid-state laser is focused on the sample surface using a high numerical aperture microscope lens yielding a spot that can be approximated by a Gaussian profile with a FWHM of about $320 \pm 50$ nm.

The frequency shift of the inelastically scattered light is analysed using a six-pass Fabry-Perot interferometer TFP-2 (JRS Scientific Instruments) providing an accessible frequency range from 500 MHz to a few hundred gigahertz.

**Micromagnetic simulations.** The magnetisation dynamics is described by the Landau-Lifshitz-Gilbert equation of motion:

$$\frac{1}{\gamma}\frac{d\mathbf{m}}{dt} = -\frac{1}{1+\alpha^2}(\mathbf{m}\times\mathbf{H}_{\text{eff}}) - \frac{\alpha}{1+\alpha^2}\mathbf{m}\times(\mathbf{m}\times\mathbf{H}_{\text{eff}}), \quad (1)$$

where $\gamma$ is the gyromagnetic ratio, $\mathbf{m} = \mathbf{M}/M_S$ the normalised magnetisation vector, $\alpha$ the Gilbert damping parameter, and $\mathbf{H}_{\text{eff}}$ the total effective field comprising the exchange, anisotropy, magnetostatic, and external magnetic fields. The simulations are performed by numerically solving equation 1 using the GPU accelerated code MuMax3[25].

Simulations were performed for a rectangular element that is 5-$\mu$m long, 1-$\mu$m wide and 10-nm thick. This structure is discretised by cells with edge lengths $\Delta x = 2.44$ nm, $\Delta y = 1.90$ nm, and $\Delta z = 10$ nm, respectively. The following material parameters for Py are used: saturation magnetisation $M_S = 830$ kA/m, exchange constant $A = 1.3 \times 10^{-11}$ Jm$^{-1}$, and zero crystalline anisotropy $K = 0$ Jm$^{-3}$. The Gilbert damping parameter is set to $\alpha = 0.007$.

The magnetisation dynamics is excited by an out-of-plane field pulse of Gaussian shape with 20-nm FWHM that is applied inside the domain wall at 1.6$\mu$m distance from the bottom edge of the rectangular element. The time evolution of the field pulse is a *sinc* function chosen such that the cut-off frequency in the Fourier transform is 40 GHz. The Fourier transform of the magnetisation dynamics was calculated over a period of 25 ns for each cell. The sum over all nodes provides the integral spectrum of the given configuration. The mode profiles of the individual resonances are determined by a backward windowed Fourier transform to deduce the dispersion relation.

## REFERENCES


[1] Kruglyak, V. V. & Hicken, R. J. Magnonics: experiment to prove the concept. *J. Magn. Magn. Mater.* **306**, 191 (2006).
[2] Neusser, S. & Grundler, D. Magnonics: spin waves on the nanoscale. *Adv. Mater.* **21**, 2927 (2009).
[3] Khitun, A., Bao, M. & Wang, K. L. Magnonic logic circuits. *J. Phys. D: Appl. Phys.* **43**, 264005 (2010).
[4] Kruglyak, V. V., Demokritov, S.O. & Hillebrands, B. Magnonics. *J. Phys. D: Appl. Phys.* **43**, 264001 (2010).
[5] Lenk, B., Ulrichs, H., Garbs, F. & Münzenberg, M. The building blocks of magnonics. *Phys. Rep.* **507**, 107 (2011).
[6] Grundler, D. Reconfigurable magnonics heats up. *Nat. Phys.* **11**, 438-441 (2015).
[7] Chumak, A. V., Vasyuchka, V. I. & Hillebrands, B. Magnon spintronics. *Nat. Phys.* **11**, 453-461 (2015).
[8] Vogt, K., Schultheiss H., Jain S., Pearson J. E., Hoffmann A., Bader S. D. & Hillebrands B. Spin waves turning a corner. *Appl. Phys. Lett.* **101**, 042410 (2012).
[9] Chumak, A. V., Serga, A. A. & Hillebrands, B. Magnon transistor for all-magnon data processing. *Nat. Comm.* **5**, 4700 (2014).
[10] Vogt, K., Fradin F. Y., Pearson J. E., Sebastian T., Bader S. D., Hillebrands B., Hoffmann A. & .Schultheiss H. Realization of a spin-wave multiplexer. *Nat. Comm.* **5**, 3727 (2014).
[11] Urazhdin, S., Demidov V. E., Ulrich H., Kendziorczyk T., Kuhn T., Leuthold J., Wilde G. & Demokritov S. O. Nanomagnonic devices based on the spin-transfer torque *Nat. Nano.* **9**, 509-513 (2014).
[12] Hertel, R., Wulfhekel, W. & Kirschner, J. Domain-wall induced phase shifts in spin waves. *Phys. Rev. Lett.* **93**, 257202 (2004).
[13] Bayer, C., Schultheiss, H., Hillebrands, B. & Stamps, R. Phase shift of spin waves traveling through a 180° Bloch-domain wall *IEEE T. Magn.* **41**, 3094-3096 (2005).
[14] Kim, S.-K., Choi S., Lee K. S., Han D. S., Jung D. E. & Choi Y. S. Negative refraction of dipole-exchange spin waves through a magnetic twin interface in restricted geometry. *Appl. Phys. Lett.* **92**, 212501 (2008).
[15] Macke, S. & Goll, D. Transmission and reflection of spin waves in the presence of Néel walls. *J. Phys.: Conf. Ser.* **200**, 042015 (2010).
[16] Pirro, P., Koyama T., Brächer T., Sebastian T., Leven B. & Hillebrands B. Experimental observation of the interaction of propagating spin waves with Néel domain walls in a Landau domain structure. *Appl. Phys. Lett.* **106**, 232405 (2015).
[17] Saitoh E., Miyajima H., Yamaoka T. & Tatara G. Current-induced resonance and mass determination of a single magnetic domain wall. *Nature* **432**, 203 (2004).
[18] Garcia-Sanchez, F., Borys P., Soucaille R. Adam J. P., Stamps R. L. & Kim J. V. Narrow magnonic waveguides based on domain walls. *Phys. Rev. Lett.* **114**, 247206 (2015).
[19] Jorzick J., Demokritov S.O., Hillebrands B., Bailleul M., Fermon C., Guslienko K. Y., Slavin A. N., Berkov D. V. & Gorn N. L., Spin Wave Wells in Nonellipsoidal Micrometer Size Magnetic Elements. *Phys. Rev. Lett.* **88**, 047204 (2002).
[20] Sebastian T., Brächer T., Pirro P., Serga A.A., Hillebrands B., Kubota T., Naganuma H., Oogane M., & Ando Y. Nonlinear emission of spin-wave caustics from an edge mode of a microstruc-

NATURE NANOTECHNOLOGY | VOL 11 | pp. 432 – 437 | NOVEMBER 2016 | DOI: 10.1038/NNANO.2015.339

tured $Co_2Mn_0.6Fe_0.4Si$ waveguide. *Phys Rev Lett.* **110**, 067201 (2013).
[21]Rave W. & Hubert A., Magnetic ground state of a thin-film element *IEEE T. Magn.* **36**, 3886 (2000).
[22]Sebastian, T., Schultheiss, K., Obry, B., Hillebrands, B. & Schultheiss, H. Micro-focused Brillouin light scattering: imaging spin waves at the nanoscale. *Front. Phys.* **3**, 35 (2015).
[23]Demidov V. E., Demokritov S. O., Rott K., Krzysteczko P. & Reiss G., Self-focusing of spin waves in Permalloy microstripes. *Appl. Phys. Lett.* **91**, 252504 (2004).
[24]Schultheiss H., Schäfer S., Candeloro P., Leven B., Hillebrands B. & Slavin A. Observation of coherence and partial decoherence of quantized spin waves in nanoscaled magnetic ring structures. *Phys Rev Lett.* **100**, 047204 (2008).
[25]Vansteenkiste, A., Leliaert J., Dvornik M., Helsen M., Garcia-Sanchez F. & van Waeyenberge B. The design and verification of MuMax3. *AIP Advances* **4**, 107133 (2014).
[26]Lee K. S. & Kim S.K. Conceptual design of spin wave logic gates based on a MachZehnder-type spin wave interferometer for universal logic functions. *J Appl Phys.* **104**, 053909 (2008). doi: 10.1063/1.2975235
[27]Schneider T., Serga A. A., Hillebrands B. & Kostylev M. Spin-wave ferromagnetic film combiner as a NOT logic gate. *J Nanoelectron Optoe.* **3**, 69 (2008).
[28]Fassbender J., Ravelosona D. & Samson Y., Tailoring magnetism by light-ion irradiation. *J. Phys. D Appl. Phys.* **37**, R179 (2004).
[29]Fassbender J. & McCord J. Magnetic patterning by means of ion irradiation and implantation. *J. Magn. Magn. Mater.* **320**, 579 (2008).

## ACKNOWLEDGMENTS

Financial support by the Deutsche Forschungsgemeinschaft is gratefully acknowledged. K.S. acknowledges funding from the Helmholtz Postdoc Programme. A.K. would like to thank Prof. Claus M. Schneider for supporting the transfer of the GPU machines to the HZDR, on which the micromagnetic simulations were partially performed.

## AUTHOR CONTRIBUTIONS

K.W., T.S., A.H. and H.S. designed the experiment. K.W. and T.S. prepared the samples. K.W. performed the BLS microscopy measurements and analysed the experimental. K.W. and A.K. performed and evaluated the micromagnetic simulations. All authors interpreted and discussed the results and co-wrote the manuscript.

## ADDITIONAL INFORMATION

The authors declare no competing financial interests. Reprints and permission information is available online at http://www.nature.com/reprints. Correspondence and requests for materials should be addressed to H.S.

nature COMMUNICATIONS

ARTICLE

Received 17 Sep 2016 | Accepted 15 Nov 2016 | Published 21 Dec 2016

DOI: 10.1038/ncomms13948 OPEN

# Ultrafast electronic response of graphene to a strong and localized electric field

Elisabeth Gruber[1], Richard A. Wilhelm[1,2], Rémi Pétuya[3], Valerie Smejkal[1], Roland Kozubek[4], Anke Hierzenberger[4], Bernhard C. Bayer[5], Iñigo Aldazabal[6], Andrey K. Kazansky[3,7], Florian Libisch[8], Arkady V. Krasheninnikov[2], Marika Schleberger[4], Stefan Facsko[2], Andrei G. Borisov[9], Andrés Arnau[3,6,10] & Friedrich Aumayr[1]

The way conduction electrons respond to ultrafast external perturbations in low dimensional materials is at the core of the design of future devices for (opto)electronics, photodetection and spintronics. Highly charged ions provide a tool for probing the electronic response of solids to extremely strong electric fields localized down to nanometre-sized areas. With ion transmission times in the order of femtoseconds, we can directly probe the local electronic dynamics of an ultrathin foil on this timescale. Here we report on the ability of freestanding single layer graphene to provide tens of electrons for charge neutralization of a slow highly charged ion within a few femtoseconds. With values higher than $10^{12}$ A cm$^{-2}$, the resulting local current density in graphene exceeds previously measured breakdown currents by three orders of magnitude. Surprisingly, the passing ion does not tear nanometre-sized holes into the single layer graphene. We use time-dependent density functional theory to gain insight into the multielectron dynamics.

[1] TU Wien, Institute of Applied Physics, 1040 Vienna, Austria. [2] Helmholtz-Zentrum Dresden-Rossendorf (HZDR), Institute of Ion Beam Physics and Materials Research, 01328 Dresden, Germany. [3] Donostia International Physics Centre (DIPC), 20018 Donostia-San Sebastian, Spain. [4] Universität Duisburg-Essen, Fakultät für Physik and Cenide, 47048 Duisburg, Germany. [5] University of Vienna, Faculty of Physics, Boltzmanngasse 5, 1090 Vienna, Austria. [6] Centro de Fisica de Materiales (CFM), Centro Mixto CSIC-UPV/EHU - MPC, 20018 Donostia-San Sebastian, Spain. [7] IKERBASQUE, Basque Foundation for Science, 48013 Bilbao, Spain. [8] TU Wien, Institute for Theoretical Physics, 1040 Vienna, Austria. [9] CNRS-Université Paris Sud, Institut des Sciences Moléculaires d'Orsay - UMR 8214, 91405 Orsay Cedex, France. [10] Departamento de Fisica de Materiales UPV/EHU, Facultad de Quimica, 20018 Donostia-San Sebastian, Spain. Correspondence and requests for materials should be addressed to E.G. (email: egruber@iap.tuwien.ac.at) or to F.A. (email: aumayr@iap.tuwien.ac.at) or to A.G.B (email: andrei.borissov@u-psud.fr) or to A.A. (email: andres.arnau@ehu.es) or to M.S. (email: marika.schleberger@uni-due.de).

Its exceptionally high carrier mobility[1] makes graphene a promising material for future electronic applications. The linear Dirac-like dispersion and the associated constant high carrier velocity promise the realization of ultrafast devices in electronics[2], optics[3] or even q-bits based on nitrogen vacancies[4]. The ultra-short timescales involved, $<1$ ps, provide stringent requirements on material properties. Direct current measurements on supported single layer graphene (SLG) reveal breakdown currents due to Joule heating larger than in copper, with densities of about $10^8$–$10^9$ A cm$^{-2}$ (refs 5–8). Note that these measurements include substrate and finite size effects, which may increase the breakdown current as compared with pristine freestanding graphene. Indeed, heat dissipation via the substrate seems essential to achieve these numbers[9,10]. Photoexcitation measurements reveal efficient excited carrier relaxation within a few hundred femtoseconds[11,12] yet probe the lattice on the length scale of the optical wavelength. Moreover, large electric fields[13,14] and collisions with energetic particles[15–28], which allow for tuning the properties of graphene, further modify the response of the material. A reliable tool to locally probe the timescales of the electronic response of pristine graphene to large fields is thus urgently needed.

One way to measure the short-time response of materials is the irradiation with highly charged ions (HCIs), which results in an extremely large, local external field: the Coulomb field of an approaching HCI. A charge state of $q_{in}=35$ implies a local electric field strength of $1.8\times10^{11}$ V m$^{-1}$ at 5 Å distance from it. Achieving the same local field strength using laser fields would require power densities above $10^{17}$ W cm$^{-2}$, a field strength where non-destructive measurements become challenging. Previous work on scattering of HCI from solid surfaces or their transmission through freestanding carbon membranes reported unexpectedly large charge capture within 5–30 fs (refs 29–34).

In this contribution, we take the final step and present the results for the ultimately thin carbon target, a freestanding single layer of graphene. Measurements of the charge state and energy of the transmitted ions and time-dependent density functional theory (TDDFT) calculations show that large number of electrons are extracted from a very small surface area, which implies a high local surface current density. We identify a multielectron process and estimate the relevant timescales for charge transfer along the graphene layer. For example, while passing through SLG, the HCI with initial charge state $q_{in}=30$ captures $\sim25$ electrons on a timescale of a few fs. Based on the experimental data, a lower bound for the current densities reached locally within a nm$^2$ area is at least $10^{12}$ A cm$^{-2}$ exceeding the breakdown current densities reported so far[5–8] by three orders of magnitude.

## Results

**Exit charge state analysis**. The amount of charge transferred to the HCI can be estimated by measuring the distribution of exit charge states $q_{out}$ and the energy of highly charged Xe ions after transmission through SLG (for details of sample preparation, see Supplementary Note 1). Initial ion charge states of $10\leq q_{in}\leq35$ and velocities below 0.5 nm fs$^{-1}$ were used. Ions are transmitted through SLG under normal incidence and analysed with respect to their charge state and kinetic energy by an electrostatic analyser (Fig. 1c). Typical transmission spectra (Fig. 1a) show a distribution of different exit charge states, with a mean value $\bar{q}_{out}$ shifted towards smaller exit charge states for slower ions. To extract the abundances and widths of every single peak, the spectra have to be deconvoluted with the analyser function, since the spectra are broadened by the design of the electrostatic analyser (details on the data evaluation can be found in ref. 35). The corrected abundances follow a symmetric Gaussian function with a full width at half maximum of three to five electrons as a result of final de-excitation processes. From these Gaussian fits the mean value $\bar{q}_{out}$ is extracted. Even for the smallest velocities (largest interaction times) used in our experiment ($v_{min}=0.13$ nm fs$^{-1}$), $\bar{q}_{out}$ remains considerably larger than the equilibrium charge state of a Xe ion in a solid target ($q_{eq}\sim1$)[36], indicating incomplete neutralization.

Depending on the initial charge state the HCI captures and stabilizes between 20 and 30 electrons during its transmission through graphene (Fig. 1e). The experimentally observed average electron capture is extracted from the mean exit charge state of each transmission spectrum. The transmission time through graphene can be defined by $\tau=d_{eff}/v$, where $v$ is the ion velocity. The effective interaction length $d_{eff}$ corresponds to the projectile-surface distance where the electron transfer processes between the HCI and graphene take place. The values of $d_{eff}$ can be obtained from the TDDFT calculations which yield for $q_{in}=20$ a value of $d_{eff}\simeq9$ Å. This is in good agreement with predictions of the classical over the barrier model[37].

The number of captured and stabilized electrons (they are not reemitted due to autoionization processes) as function of interaction time is shown in Fig. 1e. The data can be well fitted by the simple expression

$$\bar{q}_{out}=q_{in}\left(1-e^{-\tau/\tau_n^{exp}}\right) \quad (1)$$

with an effective $q_{in}$-neutralization time constant $\tau_n^{exp}$. Using $d_{eff}=9$ Å we obtain $\tau_n^{exp}=2.1$ fs for $q_{in}=35$, and $\tau_n^{exp}=1.4$ fs for $q_{in}=20$, respectively. The performed TDDFT study (for details, see Supplementary Note 2 and Supplementary Fig. 4) shows a multielectron character of the charge transfer that can explain the experimentally observed strong reduction of the charge state of the HCI. We calculate that HCIs with initial charge states $q_{in}=10$, 20 and 40 capture $\sim9$, $\sim17$ and $\sim34$ electrons during the passage through the graphene layer, respectively.

Since at least $q_{in}-\bar{q}_{out}$ electrons are transferred from the graphene sheet to the HCI during the interaction, the lower bound for the electron transfer rate is given by $(q_{in}-\bar{q}_{out})/\tau$, which corresponds to $10^{16}$ electrons per second as can be estimated from the experimental data. This corresponds to a local current of $I\gtrsim1.5$ mA. The TDDFT study shows on the one hand that the charge is extracted from the graphene area with lateral radius $R=5$ Å around the impact point that we can define as an interaction region (Figs 1b and 2), and on the other hand that the electron flow along the graphene layer compensates the electron extraction by the HCI on the timescale of the collision (fs), otherwise the neutralization of the projectile would be stopped by the local charging of the target. The latter is in accord with experimental data that shows the absence of the post-collisional defects that would result from Coulomb explosion (see the section Transmission electron microscopy results). The electrons moving along graphene enter the interaction region crossing the surface $S=2\pi Rh$ ($h=3.4$ Å is the width of the graphene layer that we estimate from the interlayer spacing of graphite[38]). Thus, a time averaged electron current density $J=I/S$ in the graphene plane exceeding $\sim6\times10^{11}$ A cm$^{-2}$ is reached. This value, however, is just a lower limit because it only accounts for the electrons captured by the projectile. Indeed, because of the interaction with HCI $N_{vac}$ electrons will also be emitted into vacuum. We calculate that for each captured electron approximately one additional electron is emitted. $N_{vac}$ can be even larger if one accounts for Auger processes involving tightly bound electronic shells of the projectile. Estimations as high as $N_{vac}\approx3\times q_{in}$ (ref. 39) have been reported.

NATURE COMMUNICATIONS | DOI: 10.1038/ncomms13948 ARTICLE

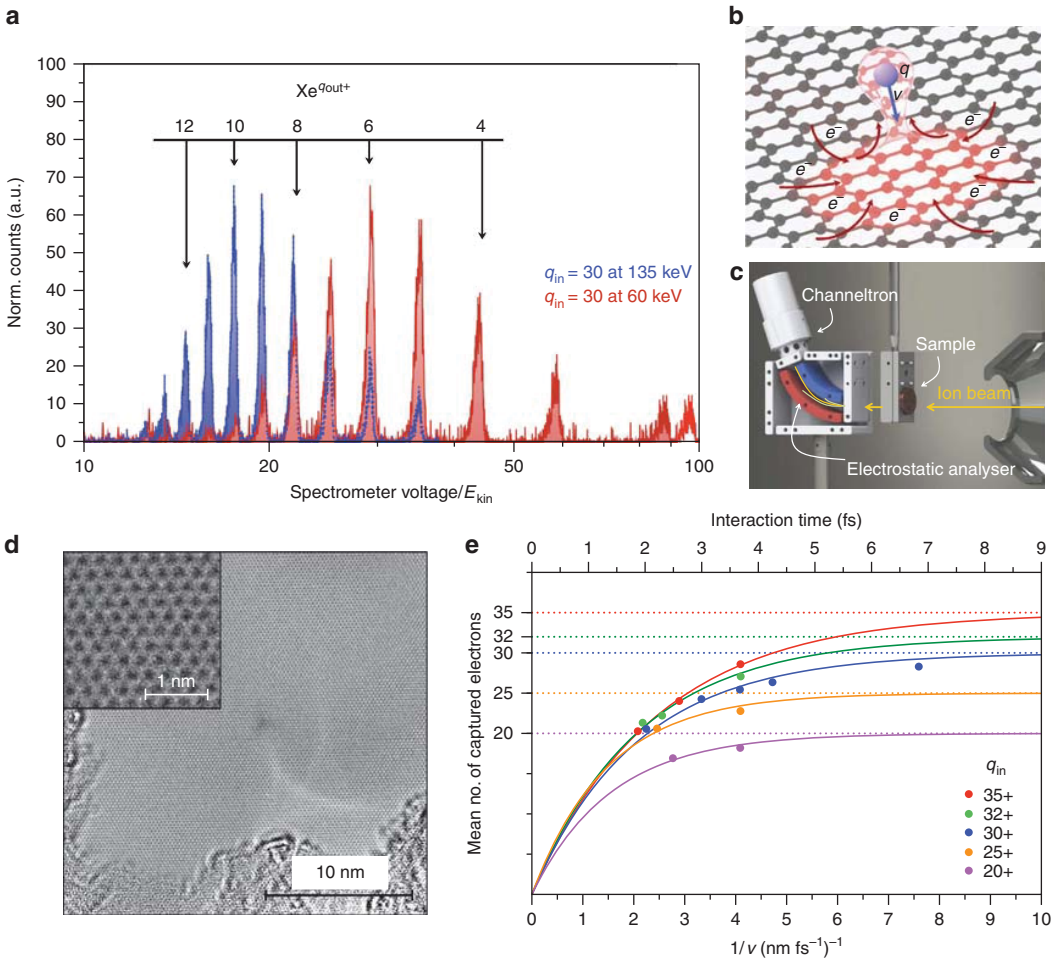


**Figure 1 | Experimental scheme and results.** (**a**) Measured spectra of a $Xe^{30+}$ beam at kinetic energies of 135 and 60 keV (blue and red, respectively) transmitted through a freestanding SLG sheet. Exit charge states $q_{out}$ are calculated from the spectrometer voltage of the electrostatic analyser. The exit charge state distribution shifts towards smaller average exit charge $\bar{q}_{out}$ for slower ions. (**b**) Schematic of the interaction process between freestanding SLG and an approaching highly charged ion (HCI). The HCI extracts a lot of charge from a very limited area on the femtosecond time scale leading to a temporary charge-up of the impact region. (**c**) Sketch of the experimental set-up with the target holder and electrostatic analyser. (**d**) TEM image of a freestanding monolayer of graphene after irradiation with $Xe^{40+}$ ions at 180 keV with an applied fluence of $10^{12}$ ions per $cm^2$ (about six impacts on the shown scale). No holes or nanosized topographic defects could be observed. The inset shows the intact hexagonal structure of graphene. (**e**) Average number of captured and stabilized electrons ($q_{in} - \bar{q}_{out}$) after transmission of $Xe^{q_{in}+}$ ions through a single layer of graphene as a function of the inverse projectile velocity for different incident charge states. Fits to the experimental data points assume a continuous neutralisation following an exponential function. Neutralisation time constants of a few femtoseconds can be extracted.

**Transmission electron microscopy results**. Failure to sufficiently resupply the lost charge and to dissipate the absorbed energy on a timescale small compared with lattice vibrations would result in Coulomb explosion tearing large holes (of the order of 10 nm) into the SLG, as we have observed for carbon nanomembranes[35,40]. Despite the possible self-healing of localized defects in graphene[41], such extended structural modifications should be detectable using transmission electron microscopy (TEM) or scanning transmission electron microscopy (STEM), yet careful investigation of the irradiated SLG does not reveal any nanometre-sized defect structures. Note that for freestanding SLG used in our study, in contrast to supported graphene layers, the defect formation because of a collision cascade in the substrate[42] is not operative. In our case, elastic collisions (nuclear stopping) may cause direct knockout of carbon atoms, but less than one carbon atom is sputtered on average by a 10–100 keV Xe ions according to Lehtinen *et al.*[43]. Even if point defects are produced, they will likely disappear due to dissociation of ubiquitous hydrocarbon molecules[41]. In Fig. 1d, a typical TEM image of a freestanding monolayer of graphene after irradiation with $Xe^{40+}$ ions with a kinetic energy of 180 keV is shown. The applied fluence of $10^{12}$ ions per $cm^2$ corresponds to approximately six ion impacts within this 25 nm × 25 nm frame. No rupture could be detected. This is in strong contrast to ultrathin polymeric carbon nanomembranes, where, because of low electron mobility, creation of pores with diameters of up to a few nanometre was observed after exposure to HCIs[35,40]. The absence of any traces of large-scale lattice deformations thus confirms the intrinsic ability of suspended SLG to locally sustain exceptionally high current densities, even though it cannot efficiently diffuse heat to a substrate[9,10].

**Local current density**. To illustrate the way the electronic processes take place, in Fig. 2, we show snapshots of the current density for a $q_{in} = 20$ projectile incident at graphene with velocity $v = 0.87\ nm\ fs^{-1}$. Results of the TDDFT calculations are

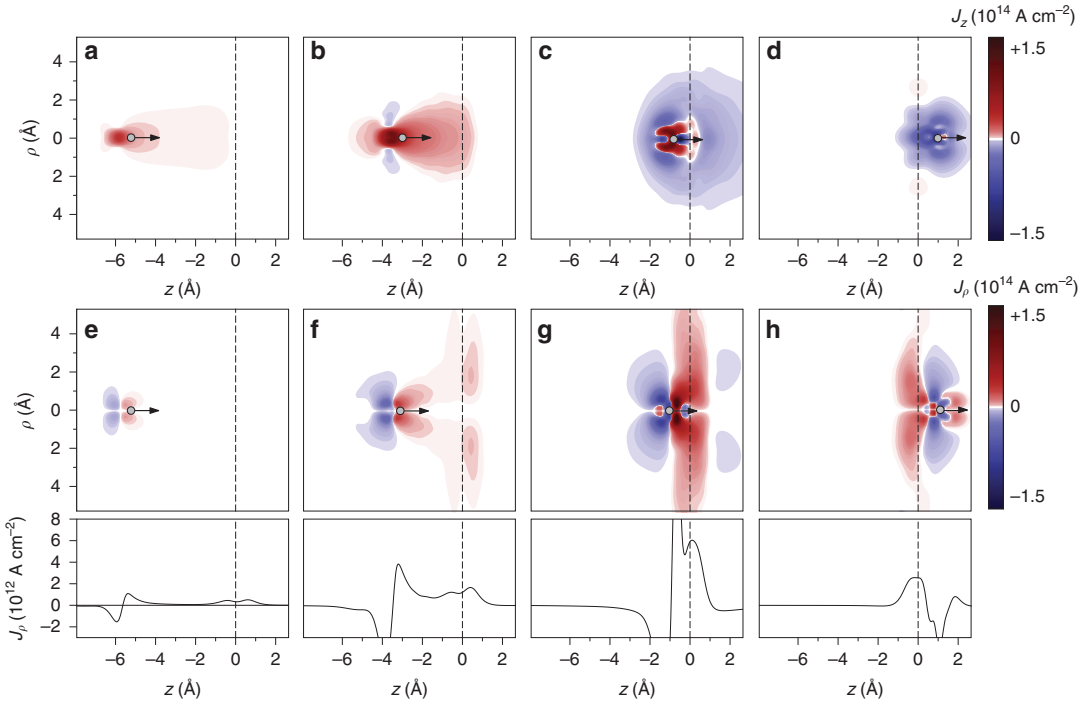


**Figure 2 | Perpendicular and radial current density obtained by TDDFT calculations.** Snapshots of the perpendicular $J_z$ (**a**–**d**) and radial $J_\rho$ (**e**–**h**) components of the current density for $q_{in} = 20$ at four different HCI–graphene distances obtained from TDDFT calculations performed in cylindrical (ρ,z) coordinates with z-axis set along the projectile trajectory perpendicular to the target surface. The figures show that already above the graphene layer electrons are transferred to the approaching HCI and the current density along the direction of motion explains the charge exchange of the HCI. Extremely high transverse current density (**f**–**h**) along the graphene layer is obtained. The corresponding profiles (lower panels) show the z-dependent transverse current density averaged over a circle of 10 Å in radius. Values exceeding $10^{12}$ A cm$^{-2}$ are obtained. The position of the HCI is indicated by a small circle, the position of the graphene layer by the vertical dashed line.

presented for four different HCI–graphene distances $z_{ion}$ along the ingoing trajectory path. We use cylindrical ($\rho$, $z$) coordinates, with the $z$ axis set along the projectile trajectory assuming normal incidence geometry. Note that because of the cylindrical symmetry in our calculations (see Supplementary Note 2 for details), there is no azimuthal angular dependence. Already at $z_{ion} \sim -6$ Å charge transfer from graphene to the HCI is sizable. For $z_{ion} \sim -3$ Å, the $J_z$ component of the current density along the direction of motion is further increased and a significant transverse current density along the graphene layer (located at $z = 0$) can be observed.

The current density along the direction of motion $J_z$ determines the charge exchange and energy loss of the HCI (see the section Energy loss), while the current density along the transverse direction $J_\rho$ shows the fast local response of graphene to the strong HCI perturbation. In fact, our calculations reproduce our experimental estimate since the transverse current densities in the proximity of the graphene layer reaches values as high as $10^{12}$ A cm$^{-2}$. This means that, transiently and locally, in the femtosecond and nanometre scale, graphene is able to sustain extremely high current densities. The positive charges created by electron capture and electron emission are spread over the entire layer[44].

**Energy loss**. As neutralization is incomplete in our measurements charge state effects on the energy loss become experimentally accessible. As observed earlier with thicker foils[31,34,45], the energy loss of a HCI passing through thin sheets strongly depends on the number of electrons transferred to the ion. The energy loss as experimentally deduced from the positions of the peaks for exit charge states $q_{out} = 2$ and $q_{out} = 4$ increases quadratically with the incident charge state (Fig. 3a). We observe keV energy losses, which are more than an order of magnitude larger than the result from a TRIM simulation (nuclear and electronic stopping) for neutral Xe transmitted through a layer with areal density of $3.82 \times 10^{15}$ at cm$^{-2}$ representing the target[46] (dashed line in Fig. 3a). This simulation predicts an energy loss of 228 eV taking into account our detector acceptance angle. The TRIM value is close to the energy loss expected from an extrapolation of our fit functions through our experimental data at $q_{in} = 0$ representing equilibrium stopping.

According to our TDDFT calculations, the non-adiabaticity of the charge-exchange and ionization processes introduced by the ion motion translates into an electronic energy loss of similar magnitude and charge state dependence as that observed in the measurements, although somewhat underestimated. The lower values in the theory as compared with the experiment are due to the fact that the used pseudo-potential description of the HCI does not include the full Coulomb singularity at distances $r$ smaller than a cutoff radius $R$. As discussed in the Supplementary Note 2 and shown in Supplementary Fig. 5, a simple change in the cutoff radius from $R = 0.53$ Å to $R = 0.26$ Å increases the value of the energy loss by a factor of two. Since the actual HCI would correspond to the value $R = 0$ and our aim is not to reproduce the data but to explain them, we consider our results rather satisfactory. In addition, the overestimation of the minimum excitation energy of graphene valence electrons in the jellium model is another reason for the underestimation of the energy loss, as it has been explicitly checked for helium

NATURE COMMUNICATIONS | DOI: 10.1038/ncomms13948 ARTICLE

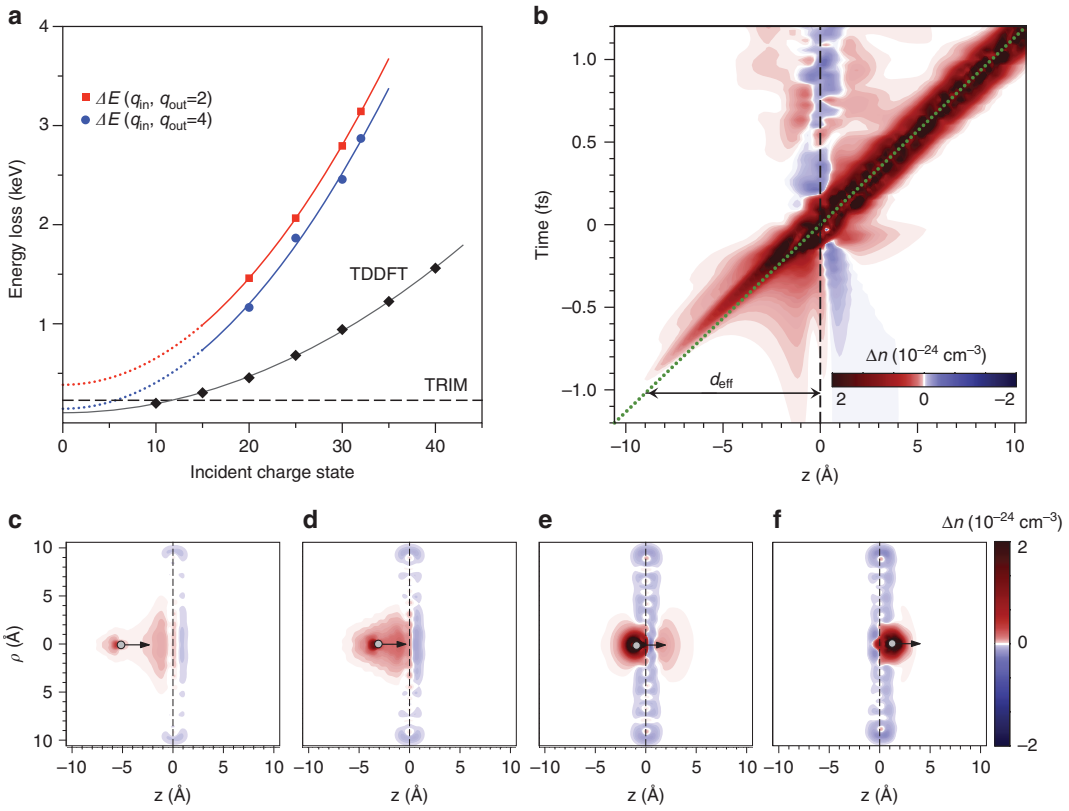


**Figure 3 | Ion energy loss results and a detailed view of the neutralization dynamics.** (**a**) Experimentally determined energy loss for ions with exit charge state $q_{out}=2$ and $q_{out}=4$ as a function of the incident charge state $q_{in}$. The energy of the projectiles was kept constant for all $q_{in}$ at $E=40$ keV. The data points are fitted by a quadratic function and the dashed line shows the result from a TRIM simulation (nuclear and electronic stopping) for a graphite layer of 3 Å thickness. The experimental data are compared with results from TDDFT calculations that reproduce the parabolic dependence with the initial charge state and the order of magnitude of the energy loss. (**b**) The induced charge density along the *z*-axis perpendicular to the surface and passing through the ion centre as function of time for $q_{in}=20$ at $v=0.87$ nm fs$^{-1}$ using the TDDFT description. It shows that already ~9 Å above the graphene layer the HCI starts to capture electrons. It is also visible that the induced charge is not centred at the HCI position but lacks behind (see green dashed line). By approaching the surface more and more electrons are captured. (**c**–**f**) Snapshots of the induced charge density in cylindrical (ρ,z) coordinates for four different position of the incoming HCI projectile. (Supplementary Movie 1). The polarization of the surface due to the approaching HCI and the excitation of the graphene layer while and after the crossing of the ion are clearly visible as well as the HCI neutralization.

ions (Supplementary Note 2; Supplementary Figs 2 and 3). Reproducing the $q_{in}^2$ dependence and the order of magnitude of measured energy losses by our TDDFT calculations shows again that electronic response of the simulated system is well described.

The fact that the measured projectile energy loss can be assigned to the electronic excitations agrees with results obtained in ab initio studies for low projectile charges[38]. It provides a consistent link between charge transfer and energy loss processes and allows to explain the absence of the induced damage despite the large energy deposition. Indeed, owing to the high electron mobility of graphene the positive charges created in the local surface area by electron capture and electron emission into vacuum are promptly screened thus reducing the local electronic temperature.

A detailed view on the neutralization dynamics is given in Fig. 3b, where we show a two-dimensional plot of the induced density along the direction of the ion motion at different ion positions from a simulation done for $q_{in}=20$ using our TDDFT description. The horizontal axis represents the distance to the graphene layer located at $z=0$ and the vertical axis corresponds to the timescale. The HCI starts capturing electrons from graphene already at 9 Å. The strong attractive potential accelerates electrons towards the HCI and, approximately, half of them end up captured by it along the incoming path before penetration into the graphene sheet. The induced electronic charge density as the HCI approaches the graphene layer has two components (Fig. 3c–f): one is formed by the convoy electrons around the HCI position, forming an asymmetric wake potential that slows down the ion, and the other one is located at the graphene layer due to the target polarization. Both components merge as the HCI gets closer to the target (Fig. 3e) and forward electron emission starts. Finally, after crossing the layer (Fig. 3f) the projectile is nearly neutralized and the corresponding induced electronic charge is centred around the HCI along its outgoing path. The actual HCI is probably not fully relaxed at the instant of crossing the graphene layer and, therefore, it still suffers a number of autoionization processes (not described in TDDFT) and subsequent de-excitation without a significant energy loss.

## Discussion

We have studied the electronic response of SLG to a large external field of an approaching HCI. We find an ultrafast neutralization within a few femtoseconds timescale leading to the capture and stabilization of almost (90%) all the missing electrons in the projectile. Our experiments and TDDFT calculations, both

suggest local current densities in the graphene plane exceeding $10^{12}$ A cm$^{-2}$, at least three orders of magnitude higher than previously established local breakdown currents, however, on a timescale of a few femtoseconds only. The exceptional electronic properties of graphene allow for a resupply of charge and distribution of the impact energy promptly enough to prevent Coulomb explosion in the electron-depleted region. In addition, the surprisingly large energy loss of the ion of a few keV, which is strongly connected with the charge-exchange process and depends on the incident and exit charge state, could be successfully explained. Our study revealed how graphene responds to extremely high fields and our results underline the exceptional properties of graphene for ultrafast electronic applications at high current densities.

## Methods

**Experimental set-up.** The measurements are performed at the Ion Beam Center of the Helmholtz-Zentrum Dresden-Rossendorf. Highly charged Xe ions are produced in a room temperature electron beam ion trap, charge state separated by an analysing magnet and then guided by several electrostatic lenses into the target chamber. Due to an electrostatic deceleration system, the kinetic energy of the extracted Xe ions can be varied between 0.1 and 4.4 $q$ keV corresponding to velocities between 0.13 and 0.5 nm fs$^{-1}$. The pressure in the experimental chamber is kept below $5 \times 10^{-9}$ mbar during measurements to prevent charge-exchange processes of the ions before interaction with the target.

The freestanding SLG sheets, which span over a regular array of holes in a TEM grid, are produced at the University Duisburg-Essen and transferred without the use of polymer coating (see Supplementary Note 1 and Supplementary Fig. 1 for details on the sample preparation and characterization). Before performing the transmission measurements, the graphene sheets are inspected by STEM to check the sample coverage and the grade of residual contamination. Contamination of the surface by water was either not present or does not affect the charge-exchange processes as the results of the experiments did not change when heating the samples up to 200 °C in ultra-high vacuum before and during the measurements. A heatable target holder and an electrostatic analyser are mounted in the target chamber (Fig. 1c). The electrostatic analyser is equipped with two channeltrons to analyse the charge state and energy of the transmitted ions and to count neutralized particles in forward direction. The analyser has an acceptance angle of 1.6°, the energy resolution was determined to be $\Delta E/E \approx 1.5 \times 10^{-3}$. The analyser's maximum operation voltage of 5,000 V limits the range of measurable charge states for projectiles with larger kinetic energies.

**TDDFT calculations.** Our TDDFT simulations are done following the time evolution of the Kohn–Sham orbitals (see Supplementary Note 2 for details) of the system defined by the constant velocity approach of a model pseudo-potential HCI (cutoff radius $R = 0.26$ Å, Coulomb tail $Q/r$) and a planar jellium disk with the correct work function value (4.6 eV)[13,47] representing the graphene layer. A non-uniform real space grid in cylindrical coordinates is used to treat properly the Coulomb singularity close to $r = R$. Finite size effects have been checked using jellium disks of different sizes containing 500, 1,004 and 2,000 electrons (Supplementary Figs 6 and 7). The Gunnarson and Lundqvist approximation[48] for the exchange correlation Kernel was used.

**Data availability.** The data that support the findings of this study are available from the corresponding author upon request.

## References


1. Banszerus, L. *et al.* Ultrahigh-mobility graphene devices from chemical vapor deposition on reusable copper. *Sci. Adv.* **1,** e1500222 (2015).
2. Reich, E. S. Graphene knock-offs probe ultrafast electronics. *Nature* **497,** 422–423 (2013).
3. Tielrooij, K.-J. *et al.* Generation of photovoltage in graphene on a femtosecond timescale through efficient carrier heating. *Nat. Nanotechnol.* **10,** 437–443 (2015).
4. Brenneis, A. *et al.* Ultrafast electronic readout of diamond nitrogen-vacancy centres coupled to graphene. *Nat. Nanotechnol.* **10,** 135–139 (2015).
5. Murali, R., Yang, Y., Brenner, K., Beck, T. & Meindl, J. D. Breakdown current density of graphene nanoribbons. *Appl. Phys. Lett.* **94,** 243114 (2009).
6. Behnam, A. *et al.* Transport in nanoribbon interconnects obtained from graphene grown by chemical vapor deposition. *Nano Lett.* **12,** 4424–4430 (2012).
7. Lee, K.-J., Chandrakasan, A. P. & Kong, J. Breakdown current density of CVD-grown multilayer graphene interconnects. *IEEE Electron Device Lett* **32,** 557–559 (2011).
8. Su, L. *et al.* Current-limiting challenges for all-spin logic devices. *Sci. Rep.* **5,** 14905 (2015).
9. Yu, J., Liu, G., Sumant, A. V., Goyal, V. & Balandin, A. A. Graphene-on-diamond devices with increased current-carrying capacity: Carbon sp$^2$-on-sp$^3$ technology. *Nano Lett.* **12,** 1603–1608 (2012).
10. Liao, A. D. *et al.* Thermally limited current carrying ability of graphene nanoribbons. *Phys. Rev. Lett.* **106,** 256801 (2011).
11. Tielrooij, K. *et al.* Photoexcitation cascade and multiple hot-carrier generation in graphene. *Nat. Phys.* **9,** 248–252 (2013).
12. Mittendorff, M. *et al.* Carrier dynamics in Landau-quantized graphene featuring strong Auger scattering. *Nat. Phys.* **11,** 75–81 (2015).
13. Yu, Y.-J. *et al.* Tuning the graphene work function by electric field effect. *Nano Lett.* **9,** 3430–3434 (2009).
14. Wang, X. *et al.* A spectrally tunable all-graphene-based flexible field-effect light-emitting device. *Nat. Commun.* **6,** 7767 (2015).
15. Krasheninnikov, A. V. & Nordlund, K. Ion and electron irradiation-induced effects in nanostructured materials. *J. Appl. Phys.* **107,** 071301 (2010).
16. Lucchese, M. M. *et al.* Quantifying ion-induced defects and Raman relaxation length in graphene. *Carbon* **48,** 1592–1597 (2010).
17. Cancado, L. G. *et al.* Quantifying defects in graphene via Raman spectroscopy at different excitation energies. *Nano Lett.* **11,** 3190–3196 (2011).
18. Banhart, F., Kotakoski, J. & Krasheninnikov, A. V. Structural defects in graphene. *ACS Nano* **5,** 26–41 (2011).
19. Åhlgren, E. H., Kotakoski, J. & Krasheninnikov, A. V. Atomistic simulations of the implantation of low-energy boron and nitrogen ions into graphene. *Phys. Rev. B* **83,** 115424 (2011).
20. Kalbac, M., Lehtinen, O., Krasheninnikov, A. V. & Keinonen, J. Ion-irradiation-induced defects in isotopically-labeled two layered graphene: enhanced *in-situ* annealing of the damage. *Adv. Mater.* **25,** 1004–1009 (2013).
21. Hopster, J. *et al.* Damage in graphene due to electronic excitation induced by highly charged ions. *2D Mater.* **1,** 011011 (2014).
22. Kotakoski, J. *et al.* Toward two-dimensional all-carbon heterostructures via ion beam patterning of single-layer graphene. *Nano Lett.* **15,** 5944–5949 (2015).
23. Ochedowski, O., Kleine Bussmann, B., Ban d'Etat, B., Lebius, H. & Schleberger, M. Manipulation of the graphene surface potential by ion irradiation. *Appl. Phys. Lett.* **102,** 153103 (2013).
24. Ochedowski, O. *et al.* Nanostructuring graphene by dense electronic excitation. *Nanotechnology* **26,** 465302 (2015).
25. Ahlberg, P. *et al.* Defect formation in graphene during low-energy ion bombardment. *APL Mater.* **4,** 046104 (2016).
26. Lupina, G. *et al.* Plasma-enhanced chemical vapor deposition of amorphous Si on graphene. *Appl. Phys. Lett.* **108,** 193105 (2016).
27. Buchheim, J., Wyss, R. M., Shorubalko, I. & Park, H. G. Understanding the interaction between energetic ions and freestanding graphene towards practical 2d perforation. *Nanoscale* **8,** 8345–8354 (2016).
28. Fox, D. S. *et al.* Nanopatterning and electrical tuning of $MoS_2$ layers with a subnanometer helium ion beam. *Nano Lett.* **15,** 5307–5313 (2015).
29. Herrmann, R. *et al.* Charge-state equilibration length of a highly charged ion inside a carbon solid. *Phys. Rev. A* **50,** 1435–1444 (1994).
30. Winecki, S., Cocke, C. L., Fry, D. & Stöckli, M. P. Neutralization and equilibration of highly charged argon ions at grazing incidence on a graphite surface. *Phys. Rev. A* **53,** 4228 (1996).
31. Schenkel, T. *et al.* Charge state dependent energy loss of slow heavy ions in solids. *Phys. Rev. Lett.* **79,** 2030–2033 (1997).
32. Hattass, M. *et al.* Charge equilibration time of slow, highly charged ions in solids. *Phys. Rev. Lett.* **82,** 4795–4798 (1999).
33. Martin, S., Brédy, R., Bernard, J., Désesquelles, J. & Chen, L. Very fast hollow-atom decay processes in $Xe^{30+}$-$C_{60}$ collisions. *Phys. Rev. Lett.* **89,** 183401 (2002).
34. Wilhelm, R. A. *et al.* Charge exchange and energy loss of slow highly charged ions in 1 nm thick carbon nanomembranes. *Phys. Rev. Lett.* **112,** 153201 (2014).
35. Wilhelm, R. A. *et al.* Threshold and efficiency for perforation of 1 nm thick carbon nanomembranes with slow highly charged ions. *2D Mater.* **2,** 035009 (2015).
36. Bohr, N. The penetration of atomic particles through matter. *Medd. Dan. Vid. Selsk* **18,** 1 (1948).
37. Burgdörfer, J., Lerner, P. & Meyer, F. W. Above-surface neutralization of highly charged ions: the classical over-the-barrier model. *Phys. Rev. A* **44,** 5674 (1991).
38. Ojanperä, A., Krasheninnikov, A. V. & Puska, M. Electronic stopping power from first-principles calculations with account for core electron excitations and projectile ionization. *Phys. Rev. B* **89,** 035120 (2014).
39. Aumayr, F. *et al.* Emission of electrons from a clean gold surface induced by slow, very highly charged ions at the image charge acceleration limit. *Phys. Rev. Lett.* **71,** 1943 (1993).
40. Ritter, R. *et al.* Fabrication of nanopores in 1 nm thick carbon nanomembranes with slow highly charged ions. *Appl. Phys. Lett.* **102,** 063112 (2013).
41. Zan, R., Ramasse, Q. M., Bangert, U. & Novoselov, K. S. Graphene reknits its holes. *Nano Lett.* **12,** 3936–3940 (2012).

42. Li, W. *et al.* Mechanism of the defect formation in supported graphene by energetic heavy ion irradiation: the substrate effect. *Sci. Rep.* **5,** 9935 (2015).
43. Lehtinen, O. *et al.* Effects of ion bombardment on a two-dimensional target: atomistic simulations of graphene irradiation. *Phys. Rev. B* **81,** 153401 (2010).
44. Miyamoto, Y. & Zhang, H. Electronic excitation in an $Ar^{7+}$ ion traversing a graphene sheet: Molecular dynamics simulations. *Phys. Rev. B* **77,** 161402 (2008).
45. Wilhelm, R. A., Gruber, E., Smejkal, V., Facsko, S. & Aumayr, F. Charge-state-dependent energy loss of slow ions. I experimental results on the transmission of highly charged ions. *Phys. Rev. A* **93,** 052708 (2016).
46. Ziegler, J. F., Biersack, J. P. & Ziegler, M. D. *The stopping and range of ions in matter*. Vol. 5 (SRIM Co., Chester, MD, USA, 2008).
47. Yuan, H. *et al.* Engineering ultra-low work function of graphene. *Nano Lett.* **15,** 6475–6480 (2015).
48. Gunnarsson, O. & Lundqvist, B. Exchange and correlation in atoms, molecules, and solids by the spin-density-functional formalism. *Phys. Rev. B* **13,** 4274 (1976).

## Acknowledgements

We acknowledge funding by Austrian Science Fund (FWF): project number: I1114-N20 and the German DFG (project number:WI 4691/1-1). We also acknowledge partial financial support from Gobierno Vasco project number IT-756-13 and MINECO project number FIS2013-48286-C2-1-P. We further acknowledge funding and fruitful discussions within the SPP 1495 'Graphene' and the collaborative research centre SFB 1242 'Non-equilibrium dynamics in condensed matter in the time domain' funded by the DFG. B.C.B. acknowledges funding from the European Union's Horizon 2020 research and innovation programme under the Marie Skłodowska-Curie grant agreement no. 656214-2DInterFOX. We are grateful for discussions with C. Lemell, J. Burgdörfer, P. Tiwald and I. Floss. We thank M. Heidelmann from the Interdisciplinary Center for Analytics on the Nanoscale (ICAN, core facility funded by the German Research Foundation, DFG) for support with the TEM Measurements.

## Author contributions

E.G., R.A.W. and V.S. performed the measurements, F.A. and S.F. were involved in planning and supervised the work, E.G. and R.A.W. processed the experimental data, performed the analysis, drafted the manuscript and designed the figures. R.P., I.A., A.K.K., A.A. and A.G.B. performed the TDDFT calculations. R.K., A.H. and M.S. manufactured the samples and characterized them with Raman spectroscopy and TEM, B.C.B. performed the STEM characterization. F.L. and A.V.K. aided in interpreting the results and worked on the manuscript. All authors discussed the results and commented on the manuscript.

## Additional information

**Supplementary Information** accompanies this paper at http://www.nature.com/naturecommunications

**Competing financial interests:** The authors declare no competing financial interests.

**Reprints and permission** information is available online at http://npg.nature.com/reprintsandpermissions/

**How to cite this article:** Gruber, E. *et al.* Ultrafast electronic response of graphene to a strong and localised electric field. *Nat. Commun.* **7,** 13948 doi: 10.1038/ncomms13948 (2016).

**Publisher's note**: Springer Nature remains neutral with regard to jurisdictional claims in published maps and institutional affiliations.

NANO LETTERS
Letter
pubs.acs.org/NanoLett

# Droplet-Confined Alternate Pulsed Epitaxy of GaAs Nanowires on Si Substrates down to CMOS-Compatible Temperatures

Leila Balaghi,[†,‡] Tina Tauchnitz,[†,‡] René Hübner,[†] Lothar Bischoff,[†] Harald Schneider,[†] Manfred Helm,[†,‡] and Emmanouil Dimakis[†,*]

[†]Institute of Ion Beam Physics and Materials Research, Helmholtz-Zentrum Dresden-Rossendorf, DE 01328 Dresden, Germany
[‡]cfaed, Technische Universität Dresden, DE 01062 Dresden, Germany

Supporting Information

**ABSTRACT:** We introduce droplet-confined alternate pulsed epitaxy for the self-catalyzed growth of GaAs nanowires on Si(111) substrates in the temperature range from 550 °C down to 450 °C. This unconventional growth mode is a modification of the migration-enhanced epitaxy, where alternating pulses of Ga and $As_4$ are employed instead of a continuous supply. The enhancement of the diffusion length of Ga adatoms on the {1$\bar{1}$0} nanowire sidewalls allows for their targeted delivery to the Ga droplets at the top of the nanowires and, thus, for a highly directional growth along the nanowire axis even at temperatures as low as 450 °C. We demonstrate that the axial growth can be simply and abruptly interrupted at any time without the formation of any defects, whereas the growth rate can be controlled with high accuracy down to the monolayer scale, being limited only by the stochastic nature of nucleation. Taking advantage of these unique possibilities, we were able to probe and describe quantitatively the population dynamics of As inside the Ga droplets in specially designed experiments. After all, our growth method combines all necessary elements for precise growth control, in-depth investigation of the growth mechanisms and compatibility with fully processed Si-CMOS substrates.

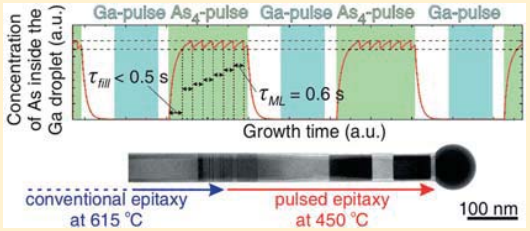


**KEYWORDS:** *nanowire, self-catalyzed, pulsed epitaxy, GaAs, Si substrate*

The self-catalyzed (or Ga-induced) growth of GaAs nanowires (NWs) on Si(111) by molecular beam epitaxy (MBE) has offered the opportunity to obtain vertical NWs with fairly good control on the structural polytypism (especially in favor of the zincblende phase),[1−5] without the risk of contamination by foreign elements like Au.[6] On those grounds, the plethora of exciting nanoscale phenomena already discovered in GaAs NWs[7−12] could eventually be integrated monolithically on Si circuit platforms.[13−15] The growth of NWs is typically performed close to the congruent sublimation temperature of GaAs (580−630 °C) in combination with relatively high V/III flux ratios.[16] These conditions ensure sufficiently high surface diffusion of Ga adatoms from the substrate and the NW sidewalls to the apex of the NWs, without thermal decomposition of the {1$\bar{1}$0} sidewalls. Nevertheless, the specific growth conditions impose several limitations: (1) the growth temperature exceeds largely the thermal budget limit of fully processed Si complementary metal−oxide−semiconductor (CMOS) circuits,[17] rendering the future integration of the two material technologies impossible; (2) the interruption of axial growth cannot be atomically abrupt due to the long shut-off transient of the As flux, which typically leads to an unintentional prolongation of the growth with a disturbed crystal phase being formed just below the Ga droplet;[3,18,19] (3) the composition or doping profiles in axial heterostructures cannot be atomically abrupt due to effects like interdiffusion, surface segregation, phase separation, or the reservoir effect, which are more prominent at high temperatures (where kinetic limitations are weak and solubility in liquid phase is higher).[20−23] Alternatively, metal−organic chemical vapor deposition (MOCVD) has been used for the self-catalyzed growth of GaAs NWs on Si(111) at 420−435 °C, but there is poor control of the shape (strong tapering) and the structural purity (rotational twin planes perpendicular to the growth direction) of the NWs.[24]

Aiming to surmount the aforementioned high-temperature limitations of the conventional MBE, we introduce an unconventional growth scheme called *droplet-confined alternate pulsed epitaxy* (DCAPE), where the Ga and $As_4$ beams are not supplied simultaneously, but alternately in short pulses. This mode resembles the so-called migration-enhanced epitaxy, which has been used in the past for the layer-by-layer growth of GaAs-based planar heterostructures at relatively low temperatures.[25] The success of the migration-enhanced epitaxy relies on the enhancement of the diffusion of Ga adatoms along the GaAs(001) surface when doses of Ga ($As_4$) comparable to the atom sheet-density of the growth interface are supplied in the absence of $As_4$ (Ga). In our case, though, the aim is not the layer-by-layer growth mode, but the minimization of the radial

**Received:** February 5, 2016
**Revised:** May 20, 2016
**Published:** June 28, 2016



DOI: 10.1021/acs.nanolett.6b00527
*Nano Lett.* 2016, 16, 4032−4039

NW growth and the enhancement of the axial one by transferring all the Ga adatoms from the sidewalls into the Ga droplet at the NW apex. This is possible due to the particular arrangement of the surface atoms on the GaAs{1$\bar{1}$0} sidewalls, where the diffusivity of Ga adatoms is high and the sticking coefficient of $As_4$ is low.[26,27] The alternate supply of Ga and $As_4$ has been used more recently for selective area growth of GaAs(111) pillars with {1$\bar{1}$0} sidewalls at a typical high temperature (590 °C),[28] whereas only one report deals with the self-catalyzed growth of GaAs(111) NWs with {1$\bar{1}$0} sidewalls in the temperature range of 540−580 °C.[29] The structural information, however, was limited to NWs grown at 580 °C, where a zincblende phase with a high density of (111) twin planes was observed, whereas the NW dimensions were found to be insensitive to the growth temperature in the investigated range.

In this work, we investigate the DCAPE of self-catalyzed GaAs NWs on Si(111) substrates in the temperature range of 450−550 °C. We study the dependence of the Ga adatom surface diffusivity on the growth conditions (namely, the growth temperature ($T_{gr}$) and the V/III flux ratio) and show that the directional character of the growth can be maintained even at the lowest temperature investigated here, in clear contrast to conventional MBE. Furthermore, we describe the correlation of the crystal structure of the NWs with the growth conditions used and demonstrate the possibility to obtain defect-free zincblende NWs. Finally, the possibility to employ very low growth rates and defect-free growth interruptions gave us a unique opportunity to design and conduct experiments dedicated to an insightful quantitative description of the growth mechanisms.

As this work did not concern the nucleation stage, GaAs NWs grown in the conventional mode at 615 °C were used as templates for all experiments reported here. The template NWs were 2 or 3 $\mu$m long and 25 or 40 nm thick, respectively, and a representative side-view (perpendicular to the substrate normal) scanning electron microscopy (SEM) image is shown in Figure 1a. The important role of the surface diffusivity of Ga adatoms is manifested by the fast axial growth rate of those NWs, which was approximately 50 times higher than what would be expected only from the direct Ga flux (i.e., the flux of Ga that impinged directly onto the Ga droplets at the apex of the NWs). That is, the amount of Ga adatoms that diffused from the substrate surface and the NW sidewalls to the Ga droplets was 50 times larger than the amount of Ga atoms that were deposited directly onto the Ga droplets. DCAPE follows the template growth and typically consists of a pulse sequence of *Ga pulse/interruption/$As_4$ pulse/interruption*, which is repeated numerous times. Comparing the dimensions and morphology of the NWs grown in DCAPE mode with those of the template by SEM (see Methods), we were able to study the growth mechanisms and to identify the optimal growth parameters.

First, we studied the DCAPE of self-catalyzed GaAs NWs at $T_{gr}$ = 550 °C, which was the highest temperature in the investigated range (DCAPE at 615 °C resulted in complete thermal decomposition of the GaAs template NWs, demonstrating the difficulty to interrupt the growth at such high temperatures). A series of samples grown with different V/III ratios was used for that purpose (the Ga flux or pulse duration was varied, while the $As_4$ flux and pulse duration were kept constant; see Methods). For DCAPE, we define V/III as the ratio between the supplied amount of $As_4$ per $As_4$ pulse and the

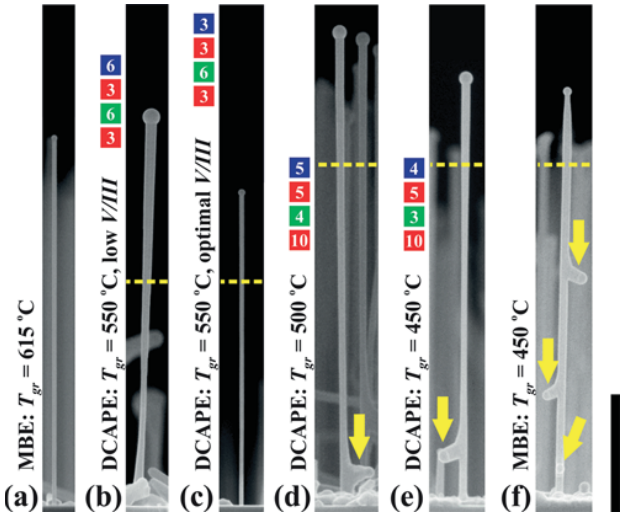


**Figure 1.** Side-view SEM images of GaAs NWs grown on Si(111). (a) Template NW grown in the conventional MBE mode at 615 °C. (b)−(e) NWs grown in DCAPE mode (on templates) at various V/III ratios or temperatures ($T_{gr}$) as indicated. The dashed yellow lines indicate the DCAPE/MBE interface. The yellow arrows indicate secondary Ga droplets on the NW sidewalls that formed during DCAPE. The pulse sequence of DCAPE is described with the colored boxes: the blue and green boxes indicate the pulse duration in seconds for Ga and $As_4$, respectively, while the red ones indicate the interruption time in seconds. The sequence reads from top to bottom and represents one period of an iterative process. (f) NW grown in the conventional MBE mode (on a template) at 450 °C. The yellow arrows indicate secondary Ga droplets on the NW sidewalls that formed during the growth at 450 °C. The scale bar corresponds to 1 $\mu$m for all images.

supplied amount of Ga per Ga pulse (each one is given by the product of beam flux × sticking coefficient at the given growth temperature × pulse duration). As depicted in Figure 1b, the NWs grow thicker at the top when a relatively low V/III ratio is used. The dashed yellow line indicates the position of the DCAPE/MBE interface, that is, the interface between the MBE template and the DCAPE segment. The NW morphology remains identical to that of the template NWs only when a high enough V/III ratio (11.5 in this case) is used as shown in Figure 1c. A further increase of the V/III ratio resulted in complete consumption of the Ga droplets (not shown here). The dependence of the NW morphology on the V/III ratio is attributed to the different arrival fluxes of Ga and As at the Ga droplets of the NWs (we refer to the amount of effective As rather than the total amount of As inside the Ga droplet). Those fluxes need to match in order to maintain a stable size of the Ga droplets and, thus, a homogeneous diameter along the NW axis. If this precondition is not fulfilled, but more Ga than As atoms arrive at the Ga droplets (V/III < 11.5), then the Ga droplets will grow larger and, consequently, the NWs will grow thicker than the template underneath. On the contrary, if less Ga than As atoms arrive at the droplets (V/III > 11.5), eventually the Ga droplets will be consumed and the self-catalyzed growth will be discontinued.

For a quantitative description of our observations, we measured the axial growth rate of the NWs during DCAPE ($GR_{NW}$; see Methods) and compared it with what would be expected only from the direct flux of Ga ($GR_{Ga}$) or $As_4$ ($GR_{As_4}$) at the Ga droplets (the contribution of the direct fluxes to the



DOI: 10.1021/acs.nanolett.6b00527
*Nano Lett.* 2016, 16, 4032−4039

axial growth rate was calculated following ref 30 for a droplet contact angle of 130°). This is plotted in Figure 2a as a function of V/III ratio for a constant $As_4$ flux (only Ga flux was varied). As expected for the self-catalyzed growth of GaAs NWs, where the axial growth rate is limited by the $As_4$ flux, the $GR_{NW}/GR_{As_4}$ ratio was found to be constant for V/III $\leq$ 11.5. In fact, it was found equal to 3.8 $\pm$ 0.5, suggesting that each Ga droplet is an efficient collector of the $As_4$ rebound flux, that is, the flux of $As_4$ that re-evaporates from the surrounding substrate surface or the sidewalls of the neighboring NWs.[31] Consequently, the linear decrease of the $GR_{NW}/GR_{Ga}$ ratio with decreasing the V/III ratio (or with increasing the Ga flux) must reflect the increasing deviation from the matching condition of the arriving Ga and As at the Ga droplet. Comparing the DCAPE growth under optimal conditions (V/III = 11.5) with the template NWs (star symbols in Figure 2a), we found very similar $GR_{NW}/GR_{As_4}$ and $GR_{NW}/GR_{Ga}$ values. This means that we were able to grow NWs by DCAPE at 65 °C lower than the conventional MBE without any significant change in their morphological characteristics. However, the DCAPE NWs have superior crystal quality as will be presented in a following section.

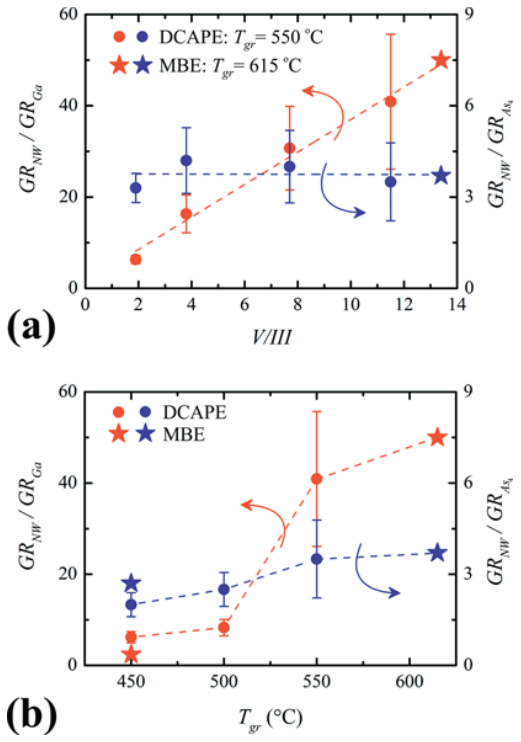


**Figure 2.** Plot of the $GR_{NW}/GR_{Ga}$ (left axis/red dots) and the $GR_{NW}/GR_{As_4}$ (right axis/blue dots) ratio for GaAs NWs grown in DCAPE mode as a function of (a) V/III ratio ($T_{gr}$ = 550 °C) and (b) $T_{gr}$ (with an optimized V/III at each $T_{gr}$). The star symbols correspond to NWs grown exclusively in the conventional MBE mode either at 615 or at 450 °C.

Next, we investigated the DCAPE of GaAs NWs at even lower $T_{gr}$, namely at 500 and 450 °C. Figure 1d,e illustrate representative SEM images from single NWs grown at the given temperatures. In both cases, a V/III ratio of approximately 3 was employed in order to achieve a good matching of the Ga and As arrival fluxes at the specific $T_{gr}$. Small deviations from a perfect matching were still present (this is a matter of fine-tuning of the V/III ratio), as evidenced by the slight increase of the diameter close to the top of the NWs, but this does not affect our analysis. Clear differences between the DCAPE NWs at 450 or 500 °C and those at 550 °C are the lower optimal value of V/III ratio, the formation of a secondary Ga droplet on the sidewalls near the base of the NWs (indicated by yellow arrows in Figure 1d,e), as well as the pronounced growth of polycrystalline GaAs islands on the substrate. All these findings suggest that the surface diffusivity of Ga adatoms is significantly reduced in the $T_{gr}$ range of 450−500 °C and less Ga adatoms arrive at the NW apex. The formation of secondary Ga droplets, in particular, implies that the diffusion length of Ga adatoms on the NW sidewalls is shorter than the length of the NWs, and thus, the Ga adatoms at the bottom of the NWs cannot diffuse to the NW apex. Nevertheless, the NW growth remained fairly directional for the particular total length of the NWs. For example, the axial growth rate was measured to be approximately 60 times faster than the radial growth rate at 450 °C (see Methods). For comparison, the corresponding factor for the conventional MBE at 615 °C was 170.

For a quantitative description of DCAPE at low temperatures, we plotted the ratios of $GR_{NW}/GR_{As_4}$ and $GR_{NW}/GR_{Ga}$ as a function of $T_{gr}$, as shown in Figure 2b. The monotonic decrease of $GR_{NW}/GR_{As_4}$ from 3.5 at 550 °C to 2.0 at 450 °C suggests that the rebound flux of $As_4$ is decreased at lower $T_{gr}$. Apparently, this is because more $As_4$ is incorporated into the polycrystalline GaAs islands that cover a larger surface area of the substrate at lower $T_{gr}$. If we assume a perfect matching of arriving Ga and As at the top NW droplets, then we can use the $GR_{NW}/GR_{Ga}$ ratio as an indicator of the surface diffusivity of Ga adatoms on the NW sidewalls (the higher the ratio, the higher the diffusivity). As it is implied from Figure 2b, the Ga adatom diffusivity is reduced at 450 or 500 °C by a factor of 7 or 5, respectively, as compared to 550 °C. The diffusion length of Ga adatoms was estimated by measuring the distance between the top and the secondary Ga droplet on every NW. In particular, the diffusion length was found to be approximately equal to 1.6 $\mu$m at 450 °C and 2.4 $\mu$m at 500 °C. Thus, the diffusion length at 550 °C is estimated to be approximately 12 $\mu$m. The aforementioned values for $T_{gr}$ of 450 and 500 °C correspond to the surface diffusivity of Ga adatoms along the NW $\{1\bar{1}0\}$ sidewalls (because the Ga adatoms on the substrate cannot diffuse to the NW apex), whereas the one at 550 °C corresponds to an overall value that includes both the NW sidewalls and the substrate surface.

The advantages of DCAPE are better highlighted by direct comparison with NWs grown in the conventional MBE mode at 450 °C. The conventional growth was performed on NW templates (like DCAPE) with very low fluxes of Ga and $As_4$, which maximized the surface diffusivity of Ga adatoms (see Methods). A V/III ratio as low as 0.9 had to be used to maintain the size of the Ga droplet at the NW apex (any higher value resulted in complete consumption of the Ga droplet), which is indicative of a reduced arrival rate of Ga adatoms diffusing from the NW sidewalls to the Ga droplet at the NW apex. The reduced diffusivity is also evidenced from the analysis of side-view SEM images as the one in Figure 1f. Namely, the axial growth rate was measured to be only 25 times faster than the radial one, while several secondary Ga droplets were formed along the sidewalls of each NW. The regular droplet spacing of 0.6 $\mu$m indicates a 3 times shorter diffusion length of Ga



DOI: 10.1021/acs.nanolett.6b00527
*Nano Lett.* 2016, 16, 4032−4039

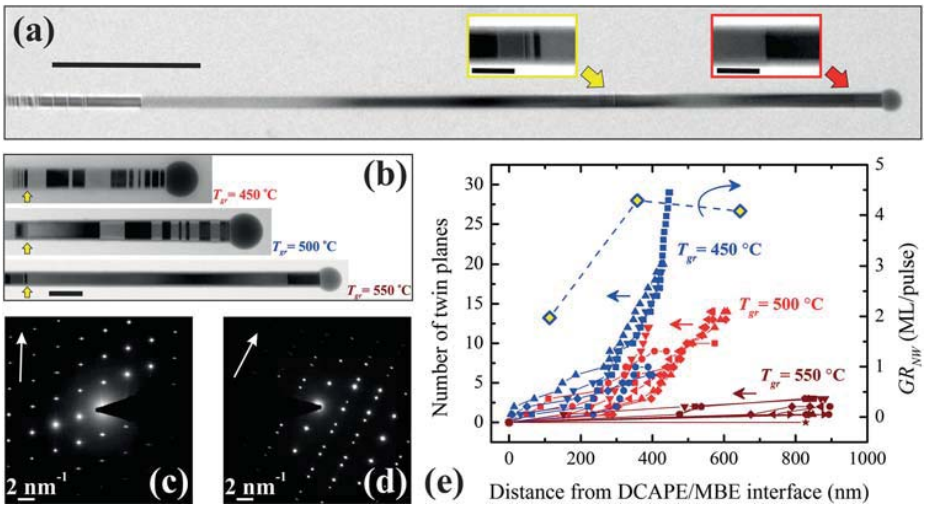


**Figure 3.** (a) Bright-field side-view TEM image of a GaAs NW grown in DCAPE mode at 550 °C. The yellow arrow indicates the defective segment at the DCAPE/MBE interface (shown magnified in the corresponding inset). The red arrow indicates the only twin plane found inside the DCAPE segment of the particular NW (shown magnified in the corresponding inset). The scale bars correspond to 0.5 $\mu$m (main image) and 50 nm (insets). (b) Bright-field side-view TEM images of GaAs NWs grown at three different temperatures in DCAPE mode. The images are close-ups of the DCAPE segment. The yellow arrows indicate the DCAPE/MBE interface. The scale bar corresponds to 100 nm. (c), (d) Representative SAED patterns from (c) pure and (d) twinned zincblende segments of GaAs NWs grown in the DCAPE mode. Both patterns were acquired along the [111] zone axis. The arrows indicate the growth direction. (e) Plot (left axis/single-colored symbols) of the total number of twin planes inside the DCAPE segment of GaAs NWs grown at three different temperatures as a function of the distance from the DCAPE/MBE interface. The axial growth rate of DCAPE GaAs NWs grown at 450 °C is also plotted (right axis/double-colored rhombus) as a function of the length of the DCAPE segment.

adatoms as compared to the DCAPE mode at the same temperature. In agreement with that, the $GR_{NW}/GR_{Ga}$ ratio was found to be 3 times lower than for DCAPE (Figure 2b).

The structural quality of the DCAPE NWs was evaluated by transmission electron microscopy (TEM). In Figure 3b, representative bright-field images are shown from the DCAPE segment of single NWs grown at different temperatures. The defective segment that is present on the left side of each image is attributed to a transient in the size of Ga droplets at the end of the template growth and the beginning of DCAPE (see Supporting Information for a detailed explanation). Thus, the defective segment serves as a marker of the DCAPE/MBE interface. The actual position of the interface is conventionally set at the top of the defective segment, as indicated by the yellow arrows. For completeness, the full length of one of the NWs ($T_{gr}$ = 550 °C) is shown in Figure 3a, where the yellow arrow shows the DCAPE/MBE interface (magnified in the corresponding inset), whereas the red arrow indicates the only twin plane inside the DCAPE segment (magnified in the corresponding inset) of the particular NW. The defective segment at the bottom of the NW is commonly found in conventionally grown NWs and attributed to local transients of the growth conditions in the beginning of the growth. The crystal structure of the DCAPE NW segments at any $T_{gr}$ was found to be zincblende, but twin planes were also present as evidenced by the sharp changes in the diffraction contrast along the NWs in Figure 3b (each contrast reversal corresponds to one twin plane). Representative selected area electron diffraction (SAED) patterns are shown in Figure 3c,d from DCAPE segments without and with twin planes, respectively.

In Figure 3b, we observe that the DCAPE NWs grown at 550 °C are almost defect-free and their top segment near the Ga droplet does not contain a distinctively higher number of defects, in contrast to what is typically found in conventional MBE. We also observe that the lower $T_{gr}$, the higher the total number of twin planes contained in each NW, but again, a distinctively higher number of defects was never detected near the Ga droplets. The spacing of the twin planes is irregular and, in any case, much larger than the NW elongation per $As_4$ pulse. Thus, the formation of twin planes cannot be attributed to the periodic variation of the growth conditions due to the alternate beam pulsing, which then would have been an inherent limitation of DCAPE.

The total number of twin planes was measured as a function of the distance from the DCAPE/MBE interface for several NWs grown at each temperature and the results are plotted in Figure 3e. The different symbols of the same color correspond to different NWs grown at the same temperature (from the same sample). As found for $T_{gr}$ = 450 and 500 °C, the total number of twin planes increased with the distance from the DCAPE/MBE interface in two modes, that is, with a slow rate during the first 300−400 nm of DCAPE and with a much faster rate afterward. This behavior suggests that the local conditions at the growth interface were not stable throughout the DCAPE stage, but some continuous or transient changes accelerated the twin plane formation. Interestingly, the two-mode increase of the twin plane number density at 450 °C correlates well with the evolution of $GR_{NW}$ at the same temperature, which is also plotted in Figure 3e ($GR_{NW}$ was measured for NWs grown under identical conditions at 450 °C, but with a different total number of identical pulses). The low formation rate of twin planes within the first 300 nm is accompanied by a relatively low $GR_{NW}$ that increases gradually, whereas the higher formation rate for the rest of the growth is accompanied by a higher $GR_{NW}$ that is stabilized at approximately 4 monolayers (MLs) per $As_4$ pulse (or equivalently 1.4 ML/s). The correlation between the twin plane formation rate and the axial growth rate was also confirmed for NWs grown at $T_{gr}$ =



DOI: 10.1021/acs.nanolett.6b00527
Nano Lett. 2016, 16, 4032−4039

Nano Letters Letter

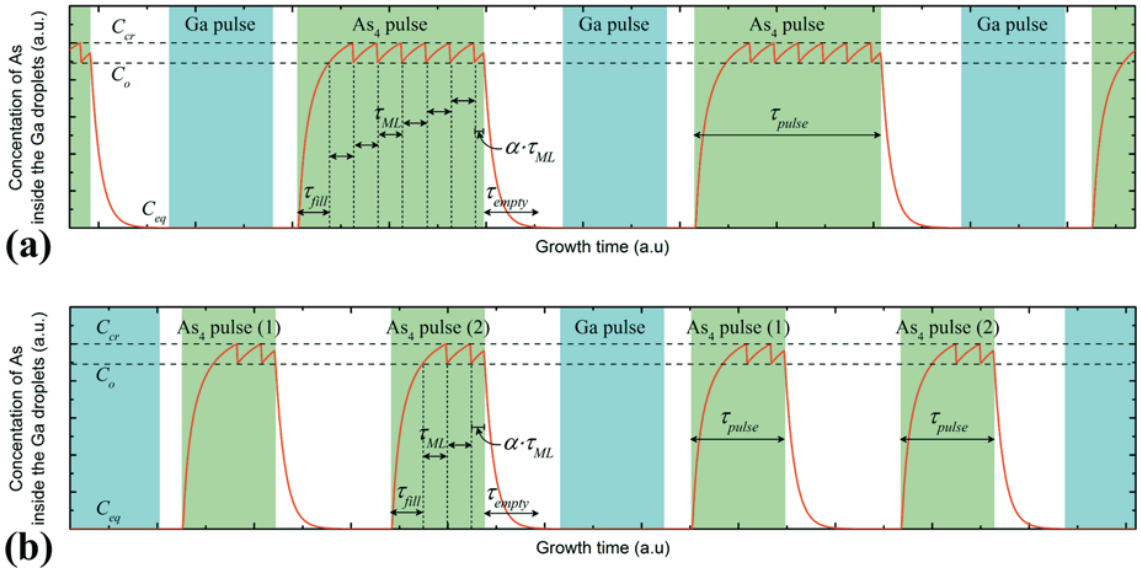


**Figure 4.** (a) Schematic plot of the As concentration inside the Ga droplets during the DCAPE pulse sequence. The characteristic time constants are indicated. (b) Same plot for an alternative pulse sequence, where each $As_4$ pulse in (a) has been split into two equal pulses of half duration. Constant $\alpha$ depends on the $As_4$ pulse duration ($\tau_{pulse}$); thus, it is different in (a) and (b).

500 °C, where the onset of the higher formation rate was shifted from 400 nm to more than 500 nm after decreasing the $GR_{NW}$ deliberately from 1.7 ML/s to 0.6 ML/s (see Supporting Information).

The initial increase and the subsequent stabilization of $GR_{NW}$ during the DCAPE stage (Figure 3e) can be understood as a result of the imperfect matching of the Ga and As arrival fluxes at the Ga droplet. That is, more Ga than As arrives at the Ga droplet, causing a gradual increase of the Ga droplet size with time. Being proportional to the droplet size (for fixed NW diameter and growth conditions), the axial growth rate also increases with time correspondingly. Eventually, the size of the Ga droplet and the axial growth rate will both reach a new equilibrium due to either the increasing diameter (tapering) of the NW or the increasing collection of the rebound flux of $As_4$ from the growing Ga droplet.[32,33] At this point, it is not conclusive whether the formation rate of twin planes is directly controlled by the axial growth rate or the Ga droplet size (or contact angle), but further investigations are currently in progress and the results will be published elsewhere. After all, the small number of twin planes at the beginning of the DCAPE clearly manifests the possibility to grow defect-free NWs at temperatures as low as 450 °C, if the Ga and $As_4$ fluxes are well-tuned.

The ability in DCAPE for defect-free growth interruptions in combination with very low axial growth rates (in the range of 1−10 MLs of GaAs per $As_4$ pulse) gave us the opportunity to design experiments dedicated to the investigation of the growth mechanisms. In specific, we designed a series of experiments to probe the dynamics of the As population inside the Ga droplets. As discussed in detail by ref 34, the concentration of As inside the Ga droplet fluctuates periodically during growth between two characteristic values. We adapt this picture for the case of DCAPE, as it is schematically plotted in Figure 4a. At this stage, we use it only as a deterministic approximation of the stochastic nucleation process. The high value $C_{cr}$ is the critical concentration that is needed to overcome the nucleation barrier at the top facet of the NW, whereas the low value $C_0$ is the reduced concentration after the growth of each ML of GaAs. Four characteristic time constants are employed to describe the dynamics of the As population inside the Ga droplet: $\tau_{fill}$ is the time needed to fill the Ga droplet with As to a concentration of $C_0$ at the onset of each $As_4$ pulse; $\tau_{ML}$ is the time needed to increase the As concentration from $C_0$ to $C_{cr}$ inside the Ga droplet after every single nucleation event; $\tau_{pulse}$ is the total time duration of each $As_4$ pulse; $\tau_{empty}$ is the time needed to evaporate the excess As from the Ga droplet and restore its equilibrium concentration $C_{eq}$ for the given temperature immediately after each $As_4$ pulse. For simplicity, we assume that $\tau_{empty}$ is shorter than the time-spacing between sequential $As_4$ pulses. The parameter $\alpha$ ($0 < \alpha < 1$) represents the time as a fraction of $\tau_{ML}$ from the completion of the last ML in a pulse until the end of that pulse ($\alpha$ depends on all the aforementioned time constants except $\tau_{empty}$). Even though a growth mode with single nucleation events (mononucleation mode) is generally considered,[35,36] our analysis is not bound to that because the definition of $\tau_{ML}$ also holds for any polynucleation mode.

A distinct feature of DCAPE is the filling of the Ga droplet with As up to a concentration of $C_0$ at the onset of every single $As_4$ pulse. The amount of $As_4$ used for that purpose does not contribute directly to the axial growth of the NWs, but rather re-evaporates from the droplet at the end of each $As_4$ pulse. Typically, the overall amount of $As_4$ ($N_{rf}$) used for the recurring filling of the droplets is considerably large because of the large number ($N_{pulse}$) of short $As_4$ pulses used for the growth ($N_{rf} = N_{pulse} \times \tau_{fill}/\tau_{ML}$, given in an equivalent number of GaAs MLs). This is unlike the conventional MBE, where only one filling of the droplets at the beginning of the growth is needed.

For the experimental determination of $\tau_{fill}$ and $\tau_{ML}$, we have designed a complex pulse sequence, where the $As_4$ pulses of a reference sequence are subdivided into multiple equal pulses, keeping the total time of $As_4$ supply ($N_{pulse} \times \tau_{pulse}$) always constant. By increasing $N_{pulse}$ and decreasing $\tau_{pulse}$ accordingly in different DCAPE experiments, we have been able to increase the number of recurring fillings of Ga droplets with As and,



DOI: 10.1021/acs.nanolett.6b00527
*Nano Lett.* 2016, 16, 4032−4039

consequently, increase $N_{rf}$. An example is shown in Figure 4, where each $As_4$ pulse of the reference sequence in (a) is subdivided into two pulses in (b) with half the duration of the reference pulse each. The number and duration of Ga pulses were kept unchanged in order to ensure identical growth conditions for all experiments (same V/III ratio and supplied Ga per pulse). The increase of $N_{rf}$ can be measured as a corresponding decrease of $GR_{NW}$ according to the following formula (expressed in MLs per unit of time; see derivation in Supporting Information)

$$GR_{NW} = \frac{1}{\tau_{ML}} - \left(\frac{\tau_{fill}}{\tau_{ML}} + \alpha\right)\frac{1}{\tau_{pulse}} \quad (1)$$

with the precondition that $N_{pulse} \times \tau_{pulse}$ = constant. The dependence of $GR_{NW}$ on $\tau_{pulse}$ was determined experimentally for $T_{gr}$ = 450 and 500 °C as plotted in Figure 5. In agreement

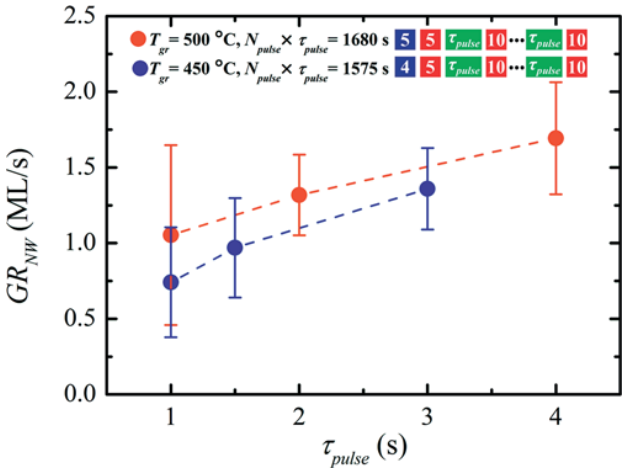


**Figure 5.** Plot of the axial growth rate of GaAs NWs during the DCAPE stage ($GR_{NW}$) as a function of the $As_4$ pulse duration ($\tau_{pulse}$). The total time of $As_4$ supply ($N_{pulse} \times \tau_{pulse}$) is constant at every growth temperature ($T_{gr}$). The differences between the two data sets are indicated. The pulse sequence is described with the colored boxes (see explanation in Figure 1) and reads from left to right.

with our expectations and eq 1, $GR_{NW}$ was found to decrease monotonically with decreasing $\tau_{pulse}$, confirming the depletion of As in the Ga droplets after every $As_4$ pulse. We presume that the equilibrium concentration of As inside the Ga droplets (which is in the order of 0.01−0.10% for solid GaAs in equilibrium with Ga-rich liquid at 450−500 °C[37]) is restored after every $As_4$ pulse.

Equation 1 contains three unknowns ($\tau_{fill}$, $\tau_{ML}$, and $\alpha$) and can be solved graphically. This is shown in Figure 6a,b for $T_{gr}$ = 450 and 500 °C, respectively, where $\tau_{fill}$ is plotted as a function of $\tau_{ML}$. Each gray-colored area corresponds to a different value of $\tau_{pulse}$, whereas $\alpha$ is allowed to take any value between 0 and 1. Because $\tau_{fill}$ and $\tau_{ML}$ should be independent of $\tau_{pulse}$, the set of all possible solutions is given by the purple-colored intersection. That is, $\tau_{ML}$ is found in the range of 0.5−0.7 s, whereas $\tau_{fill}$ is estimated with less accuracy (due to the dependence on the unknown $\alpha$) to be shorter than 0.5 s. Because $As_4$ flux was practically the same for all experiments, we believe that the slightly longer $\tau_{ML}$ at lower $T_{gr}$ is due to the lower rebound flux of $As_4$, as discussed previously. In any case, the relatively long $\tau_{ML}$ for the given Ga and $As_4$ fluxes in combination with the

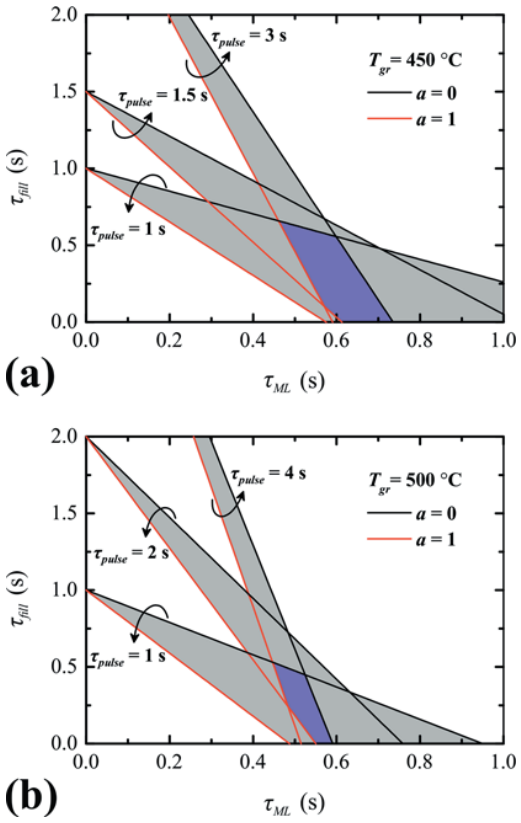


**Figure 6.** Plots of the characteristic filling time of the Ga droplet with As ($\tau_{fill}$) as a function of the characteristic time-spacing between sequential ML formations ($\tau_{ML}$) for any value of $\alpha$ and for three different $As_4$ pulse durations ($\tau_{pulse}$). The set of possible solutions is given by the purple-colored intersection of the gray-colored areas. The growth temperature ($T_{gr}$) was (a) 450 °C and (b) 500 °C.

negligible shut-off transient of $As_4$ flux in DCAPE makes it possible to control the axial NW growth with high accuracy.

Having good control over the axial growth of NWs is especially important for axial quantum heterostructures, where the length of the various NW segments need to be ultimately controlled in the single-monolayer scale. The resolution of our control is given by the shortest $As_4$ pulses in Figure 5 ($\tau_{pulse}$ = 1 s), which resulted in growth of 0.74 ± 0.36 MLs at 450 °C and 1.05 ± 0.59 MLs at 500 °C (the error bars represent the standard deviation of the $GR_{NW}$ measurements). Those values are in good agreement with the theoretical minimum and ultimate resolution of axial growth rate, that is, 1 ML per $As_4$ pulse. Definitely, we cannot rule out possible deviations (e.g., formation of 0, 2, or more MLs in some $As_4$ pulses) due to the stochastic nature of nucleation. However, the fact that the $GR_{NW}$ standard deviation is clearly lower than 1 ML per $As_4$ pulse suggests that the effect of stochasticity is limited and the nucleation can be well approximated by the deterministic model in Figure 4. In fact, it was possible to further reduce the $GR_{NW}$ standard deviation (to 0.10 MLs per $As_4$ pulse) by repeating the experiment with $\tau_{pulse}$ = 1 s at 500 °C using template NWs with an exceptionally narrow length distribution (±24 nm instead of ±107 nm for the experiments in Figure 5).

In conclusion, we have investigated the DCAPE of self-catalyzed GaAs NWs on Si(111) and demonstrated the possibility to obtain defect-free zincblende NWs at temperatures as low as 450 °C. Slow axial growth rates and defect-free



DOI: 10.1021/acs.nanolett.6b00527
Nano Lett. 2016, 16, 4032−4039

NWs in spite of growth interruptions were proven to be essential advantages of this growth technique. These features have enabled experiments allowing for a better understanding of the growth mechanisms. Therefore, we anticipate that DCAPE will lead to considerably improved epitaxial growth of axial heterostructures with the further advantage of compatibility with fully processed Si-CMOS platforms for monolithic integration. For the latter, dedicated investigations of the nucleation stage in DCAPE will be also needed.

**Methods.** *Growth and Analysis.* All samples were grown by solid source MBE using atomic Ga and molecular $As_4$ beams. The growth temperature $T_{gr}$ refers to the temperature measured on the Si(111) substrate by an optical pyrometer before the initiation of the growth. First, the template NWs were grown in conventional MBE mode (simultaneous supply of Ga and $As_4$ beams) at 615 °C with a V/III flux ratio of 13. At the end of the template growth, both Ga and $As_4$ beams were interrupted and the substrate temperature was decreased for the continuation of the growth in DCAPE mode (alternate pulsed supply of Ga and $As_4$ beams). Mechanical shutters were used for the creation of beam pulses, and a needle valve was employed in addition for the $As_4$ pulses. The background pressure in the growth chamber was in the $10^{-10}$ Torr range during the deposition of Ga. All length and diameter measurements were done by SEM. The diameter was measured at the middle of the NWs, that is, outside the DCAPE segment. Special care was taken to eliminate the image drift during the SEM measurements, allowing for a precise determination of NW lengths. The axial (radial) growth rate of NWs during DCAPE was determined by measuring the final NW length (diameter) after DCAPE, subtracting the measured length (diameter) of template NWs, and dividing by the total time of $As_4$ supply during DCAPE. For each data point in Figures 2 and 5, a statistical sample consisting of 40−80 NWs was analyzed. The plotted values and the error bars of $GR_{NW}$ correspond to the median value and the standard deviation, respectively.

*DCAPE Details.* The total amount of supplied Ga and $As_4$ was kept constant only in the sample series of Figure 2b and Figure 5. For the sample series in Figure 1, the $As_4$ (Ga) supply per pulse was 1.39 (0.72) ML in (b), 1.39 (0.12) ML in (c), 0.97 (0.30) ML in (d), 0.75 (0.24) ML in (e). For the NWs grown in conventional MBE mode, the $As_4$ (Ga) flux was equal to 1.61 (0.12) ML/s at 615 °C in (a) and 0.25 (0.28) ML/s at 450 °C in (f). At 450 °C, we chose to use the lowest possible $As_4$ flux within the practical limits of our experiments in order to maximize the surface diffusivity of Ga adatoms.[26] For the sample series in Figure 2a, the Ga supply was varied from 0.12 to 0.72 ML per pulse, with a constant $As_4$ supply of 1.39 ML per pulse. For the sample series in Figure 2b, the $As_4$ (Ga) supply per pulse was 0.75 (0.24) ML at 450 °C, 0.97 (0.30) ML at 500 °C, 1.39 (0.12) ML at 550 °C. For the sample series in Figure 5, the $As_4$ (Ga) flux was 0.25 (0.06) ML/s at 450 °C and 0.24 (0.06) ML/s at 500 °C.

## ■ ASSOCIATED CONTENT

### Supporting Information

The Supporting Information is available free of charge on the ACS Publications website at DOI: 10.1021/acs.nanolett.6b00527.

Analytical description of the defective segment at the DCAPE/MBE interface and comparison of the twin plane distribution (as measured by TEM) in DCAPE GaAs NWs grown at 500 °C with two different axial growth rates. Derivation of eq 1 for the axial growth rate during DCAPE. (PDF)

## ■ AUTHOR INFORMATION


### Corresponding Author

*E-mail: e.dimakis@hzdr.de. Phone: +49 (0351) 260 2765.


### Notes

The authors declare no competing financial interest.

## ■ ACKNOWLEDGMENTS

The authors thank Joachim Wagner for the technical maintenance of the molecular beam epitaxy laboratory. Support by the Structural Characterization Facilities Rossendorf at IBC is gratefully acknowledged.

## ■ REFERENCES


(1) Spirkoska, D.; Arbiol, J.; Gustafsson, A.; Conesa-Boj, S.; Glas, F.; Zardo, I.; Heigoldt, M.; Gass, M. H.; Bleloch, A. L.; Estrade, S.; et al. *Phys. Rev. B: Condens. Matter Mater. Phys.* **2009**, *80*, 245325.

(2) Krogstrup, P.; Popovitz-Biro, R.; Johnson, E.; Madsen, M. H.; Nygård, J.; Shtrikman, H. *Nano Lett.* **2010**, *10*, 4475−4482.

(3) Rieger, T.; Lepsa, M. I.; Schäpers, T.; Grützmacher, D. *J. Cryst. Growth* **2013**, *378*, 506−510.

(4) Gibson, S. J.; Boulanger, J. P.; Lapierre, R. R. *Semicond. Sci. Technol.* **2013**, *28*, 105025.

(5) Munshi, A. M.; Dheeraj, D. L.; Fauske, V. T.; Kim, D. C.; Huh, J.; Reinertsen, J. F.; Ahtapodov, L.; Lee, K. D.; Heidari, B.; van Helvoort, A. T.; Fimland, B. O.; Weman, H. *Nano Lett.* **2014**, *14*, 960−6.

(6) Bar-Sadan, M.; Barthel, J.; Shtrikman, H.; Houben, L. *Nano Lett.* **2012**, *12*, 2352−6.

(7) Jahn, U.; Lähnemann, J.; Pfüller, C.; Brandt, O.; Breuer, S.; Jenichen, B.; Ramsteiner, M.; Geelhaar, L.; Riechert, H. *Phys. Rev. B: Condens. Matter Mater. Phys.* **2012**, *85*, 045323.

(8) Heiss, M.; et al. *Nat. Mater.* **2013**, *12*, 439−444.

(9) Saxena, D.; Mokkapati, S.; Parkinson, P.; Jiang, N.; Gao, Q.; Tan, H. H.; Jagadish, C. *Nat. Photonics* **2013**, *7*, 963−968.

(10) Mayer, B.; Rudolph, D.; Schnell, J.; Morkötter, S.; Winnerl, J.; Treu, J.; Müller, K.; Bracher, G.; Abstreiter, G.; Koblmüller, G.; Finley, J. J. *Nat. Commun.* **2013**, *4*, 2931.

(11) Signorello, G.; Lortscher, E.; Khomyakov, P. A.; Karg, S.; Dheeraj, D. L.; Gotsmann, B.; Weman, H.; Riel, H. *Nat. Commun.* **2014**, *5*, 3655.

(12) Morkötter, S.; Jeon, N.; Rudolph, D.; Loitsch, B.; Spirkoska, D.; Hoffmann, E.; Döblinger, M.; Matich, S.; Finley, J. J.; Lauhon, L. J.; Abstreiter, G.; Koblmüller, G. *Nano Lett.* **2015**, *15*, 3295−3302.

(13) Dimakis, E.; Jahn, U.; Ramsteiner, M.; Tahraoui, A.; Grandal, J.; Kong, X.; Marquardt, O.; Trampert, A.; Riechert, H.; Geelhaar, L. *Nano Lett.* **2014**, *14*, 2604−9.

(14) Krogstrup, P.; Jørgensen, H. I.; Heiss, M.; Demichel, O.; Holm, J. V.; Aagesen, M.; Nygard, J.; Fontcuberta i Morral, A. *Nat. Photonics* **2013**, *7*, 306−310.

(15) Lin, Z.; Gendry, M.; Harmand, J. C.; Letartre, X. *26th International Conference on Indium Phosphide and Related Materials (Iprm)* **2014**, 1 DOI: 10.1109/ICIPRM.2014.6880585.

(16) Bastiman, F.; Küpers, H.; Somaschini, C.; Geelhaar, L. *Nanotechnology* **2016**, *27*, 095601.

(17) Thelander, C.; Agarwal, P.; Brongersma, S.; Eymery, J.; Feiner, L. F.; Forchel, A.; Scheffler, M.; Riess, W.; Ohlsson, B. J.; Gösele, U.; Samuelson, L. *Mater. Today* **2006**, *9*, 28−35.

(18) Cirlin, G. E.; Dubrovskii, V. G.; Samsonenko, Y. B.; Bouravleuv, A. D.; Durose, K.; Proskuryakov, Y. Y.; Mendes, B.; Bowen, L.; Kaliteevski, M. A.; Abram, R. A.; Zeze, D. *Phys. Rev. B: Condens. Matter Mater. Phys.* **2010**, *82*, 035302.

(19) Ambrosini, S.; Fanetti, M.; Grillo, V.; Franciosi, A.; Rubini, S. *AIP Adv.* **2011**, *1*, 042142.




DOI: 10.1021/acs.nanolett.6b00527
*Nano Lett.* 2016, 16, 4032−4039

(20) Cunningham, J. E.; Chiu, T. H.; Ourmazd, A.; Jan, W.; Kuo, T. Y. *J. Cryst. Growth* **1990**, *105*, 111−115.
(21) Lapierre, R. R.; Okada, T.; Robinson, B. J.; Thompson, D. A.; Weatherly, G. C. *J. Cryst. Growth* **1995**, *155*, 1−15.
(22) Dick, K. A.; Bolinsson, J.; Borg, B. M.; Johansson, J. *Nano Lett.* **2012**, *12*, 3200−3206.
(23) Priante, G.; Glas, F.; Patriarche, G.; Pantzas, K.; Oehler, F.; Harmand, J. C. *Nano Lett.* **2016**, *16*, 1917−1924.
(24) Ermez, S.; Jones, E. J.; Crawford, S. C.; Gradecak, S. *Cryst. Growth Des.* **2015**, *15*, 2768−2774.
(25) Horikoshi, Y. *J. Cryst. Growth* **1999**, *201-202*, 150−158.
(26) Lopez, M.; Nomura, Y. *J. Cryst. Growth* **1995**, *150*, 68−72.
(27) Tok, E. S.; Jones, T. S.; Neave, J. H.; Zhang, J.; Joyce, B. A. *Appl. Phys. Lett.* **1997**, *71*, 3278−3280.
(28) Iwai, T.; Toda, T.; Uehara, T.; Yoshiba, I.; Horikoshi, Y. *Jpn. J. Appl. Phys.* **2007**, *46*, 514−517.
(29) Kizu, R.; Yamaguchi, M.; Amano, H. *Phys. Status Solidi C* **2013**, *10*, 1365−1368.
(30) Glas, F.; Ramdani, M. R.; Patriarche, G.; Harmand, J.-C. *Phys. Rev. B: Condens. Matter Mater. Phys.* **2013**, *88*, 195304.
(31) Ramdani, M. R.; Harmand, J. C.; Glas, F.; Patriarche, G.; Travers, L. *Cryst. Growth Des.* **2013**, *13*, 91−96.
(32) Dubrovskii, V. G.; Xu, T.; Alvarez, A. D.; Plissard, S. R.; Caroff, P.; Glas, F.; Grandidier, B. *Nano Lett.* **2015**, *15*, 5580−5584.
(33) Tersoff, J. *Nano Lett.* **2015**, *15*, 6609.
(34) Krogstrup, P.; Jørgensen, H. I.; Johnson, E.; Madsen, M. H.; Sørensen, C. B.; Fontcuberta i Morral, A.; Aagesen, M.; Nygård, J.; Glas, F. *J. Phys. D: Appl. Phys.* **2013**, *46*, 313001.
(35) Kashchiev, D. *Cryst. Growth Des.* **2006**, *6*, 1154−1156.
(36) Glas, F.; Harmand, J. C.; Patriarche, G. *Phys. Rev. Lett.* **2010**, *104*, 135501.
(37) Rubenstein, M. *J. Electrochem. Soc.* **1966**, *113*, 752.



DOI: 10.1021/acs.nanolett.6b00527
*Nano Lett.* 2016, 16, 4032−4039

Nanoscale

PAPER

View Article Online
View Journal | View Issue



Cite this: *Nanoscale*, 2016, **8**, 14888

# Carbon : nickel nanocomposite templates – predefined stable catalysts for diameter-controlled growth of single-walled carbon nanotubes†

Svetlana Melkhanova,[a,b] Miro Haluska,[c] René Hübner,[a] Tim Kunze,‡[b] Adrian Keller,§[a] Gintautas Abrasonis,[a] Sibylle Gemming[a,b,d] and Matthias Krause*[a]

Received 8th October 2015,
Accepted 15th July 2016

DOI: 10.1039/c5nr06972f

www.rsc.org/nanoscale

Carbon : nickel (C : Ni) nanocomposite templates (NCTs) were used as catalyst precursors for diameter-controlled growth of single-walled carbon nanotubes (SWCNTs) by chemical vapor deposition (CVD). Two NCT types of 2 nm thickness were prepared by ion beam co-sputtering without (type I) or with assisting $Ar^+$ ion irradiation (type II). NCT type I comprised Ni-rich nanoparticles (NPs) with defined diameter in an amorphous carbon matrix, while NCT type II was a homogenous C : Ni film. Based on the Raman spectra of more than 600 individual SWCNTs, the diameter distribution obtained from both types of NCT was determined. SWCNTs with a selective, monomodal diameter distribution are obtained from NCT type I. About 50% of the SWCNTs have a diameter of (1.36 ± 0.10) nm. In contrast to NCT type I, SWCNTs with a non-selective, relatively homogeneous diameter distribution from 0.80 to 1.40 nm covering 88% of all SWCNTs are obtained from NCT type II. From both catalyst templates predominantly separated as-grown SWCNTs are obtained. They are free of solvents or surfactants, exhibit a low degree of bundling and contain negligible amounts of MWCNTs. The study demonstrates the advantage of predefined catalysts for diameter-controlled SWCNT synthesis in comparison to *in situ* formed catalysts.

## Introduction

Carbon nanotubes have been known for more than 20 years[1] and since the very first reports on their synthesis fascinating electronic properties of CNTs were predicted. It was expected that they will be used in many fields of molecular electronics, *viz.* in transistors,[2–4] medical devices,[5,6] chemical and biochemical sensors[7,8] *etc.* However, in currently commercialized applications CNTs are mainly used as additives to improve the mechanical, thermal, and electrical properties of bulk materials (resins, plastics, polymers).[9] Semiconducting SWCNTs are well suited for transistors because of their low electron scattering and small bandgap.[10] For "high-tech" applications, however, precisely-defined electronic properties are needed. This requires eventually one specific diameter and chiral angle of SWCNTs.[11,12] There are several methods of CNTs synthesis,[13–15] and among them CVD is the most versatile and most easily scalable one. The structural and morphological properties of CVD-grown CNTs are affected by many process parameters,[15] such as the carbon precursor nature and concentration, carrier gas pressure and composition, temperature, time, catalyst nature and size, *etc.* There are many reports that catalyst particles must have a suitable size in order to be active for CNT growth and that the control of the catalyst nanoparticles before and during CVD is very important in order to control CNT yield, diameter and chirality. The most used catalysts for CNT growth are Fe,[16–31] Co,[24,32–45] Ni[17,23,46–53] and their bimetallic alloys.[38,42,54–56] The CNT synthesis on these catalysts may produce SWCNTs with narrow diameter distribution and few chiralities depending on the catalyst nanoparticle size.[16,20,21,25,26,32,35,41,51,54]

In almost all studies, the catalysts are prepared *in situ* by an initial annealing step of the precursor prior to CVD or by precursor injection during the CVD process. The control of catalyst size and shape depends on many process parameters in a complex manner, whose optimization often requires numerous iterations.[27] The process could be simplified by introducing catalyst templates with predefined NP size and shape, which exhibit sufficient stability against coalescence and grain coarsening. Carbon : nickel nanocomposite (C : Ni NC) thin films of 10 nm to 100 nm thickness have been grown in a large variety of microstructures. This was achieved by variation of

[a]*Helmholtz-Zentrum Dresden-Rossendorf, Bautzner Landstraße 400, 01328 Dresden, Germany. E-mail: matthias.krause@hzdr.de*
[b]*Technische Universität Dresden, cfaed, 01062 Dresden, Germany*
[c]*Micro and Nanosystems, DMAVT ETH Zürich, 8092 Zürich, Switzerland*
[d]*Technische Universität Chemnitz, 09107 Chemnitz, Germany*
†Electronic supplementary information (ESI) available. See DOI: 10.1039/c5nr06972f
‡Present address: Fraunhofer-Institut für Werkstoff- und Strahltechnik, 01277 Dresden, Germany.
§Present address: Universität Paderborn, 33098 Paderborn, Germany.

 

deposition temperature (RT to 500 °C) and Ni concentration (5 to 30 at% Ni) during thin film growth without and with irradiation by an assisting low-energy $Ar^+$ beam. So far, C : Ni NCs were reported with NP diameters from 1.5 nm to 17 nm, spherical and columnar shapes, and in regular or stochastic three-dimensional particle arrangements.[57–59] In our previous work on SWCNT growth[48] we reported the successful growth of individual SWCNTs with a Gaussian-like, non-selective diameter distribution of (1.6 ± 0.4) nm from 10 nm thick templates consisting of columnar Ni NPs of (4.0 ± 1.0) nm diameter before the CVD growth process.

In this work, the SWCNT diameter distributions obtained by CVD from two 2 nm thick C : Ni NC template types are compared. NCT type I comprises predefined catalyst NPs, while for NCT type II the catalyst NPs are formed *in situ* during the CVD process. This approach enables a direct comparison of the SWCNT growth from pre-defined and *in situ* formed catalyst particles. Transmission electron microscopy (TEM) and scanning electron microscopy (SEM) were applied to characterize the NCTs before and after the CVD process and to determine the size distribution of the catalyst particles. SWCNT diameter distribution and the presence of multi-walled CNTs were analysed by SEM and Raman spectroscopy. It is demonstrated that SWCNT diameters strongly depend on the NCT type applied for CVD synthesis. Using NCT type I about 50% of the SWCNTs have a diameter of (1.36 ± 0.10) nm, while SWCNTs with a relatively homogeneous diameter distribution from 0.8 nm to 1.4 nm are obtained from NCT type II. Furthermore it is shown that MWCNT formation, SWCNT bundling, and catalyst NP coarsening are successfully suppressed. Finally, the possibilities and limits of SWCNT diameter control by defining the catalyst NP size are discussed.

## Experimental

The NCT type I (C : Ni, ~15 at% Ni) was deposited at 300 °C by ion beam co-sputtering of a graphite/Ni zone target onto a $Si/SiO_2$ (~0.5 μm, thermally oxidized) substrate. Template type II (C : Ni, ~8 at% Ni) was prepared at RT by irradiating the growing C : Ni film with an oblique incidence angle (~60°) assisting $Ar^+$ beam of 130 eV ion energy. The sputter ion source (Kaufmann type, IonTech Inc., Fort Collins, USA) was operated with an $Ar^+$ ion energy of 1 keV and a beam current of 40 mA, the assisting ion source (Kaufmann type, ISQ40KF, Ion-Tech GmbH, Wüstenbrand, Germany) with $Ar^+$ energies of 50 to 130 eV and a total beam current of 9 mA. The base pressure in the deposition chamber was $(1.3 \pm 0.3) \times 10^{-5}$ Pa, the working pressure was about $10^{-2}$ Pa, and the deposition time was 3 to 4 min. The given film composition was extrapolated from the Rutherford Backscattering analysis of our previous work.[57–59] Further deposition details are described *ibid*.

The subsequent CVD process consists of two consecutive steps: the NCT pre-treatment and the CNT growth. For this, the C : Ni templates were placed in the CVD oven (Black Magic, Aixtron) and exposed to flowing air (flow rate 200 sccm, pressure 2 to 3 mbar) for 10 min at 550 °C. After 10 min the reactor was evacuated, the temperature was increased to 735 °C, and the samples were exposed to a mixture of $C_2H_2/H_2/Ar$ (5/300/300 sccm; total pressure 5.1 mbar) for ~20 min.

Cross-sectional transmission electron microscopy images of C : Ni thin films were obtained using an image Cs-corrected Titan 80–300 (FEI) microscope operated at an acceleration voltage of 300 kV. TEM specimens of the C : Ni templates before CNT growth were prepared by sawing, grinding, dimpling, and final Ar ion milling. TEM lamella preparation of the C : Ni templates after pre-treatment and CNT growth was done by *in situ* lift-out using a Zeiss Crossbeam NVision 40 system. To protect the sensitive surface, a carbon cap layer was deposited beginning with electron beam assisted and subsequently followed by Ga focused ion beam (FIB) assisted precursor decomposition. Afterwards, the TEM lamella was prepared using a 30 keV Ga FIB with adapted currents. Its transfer to a 3 post copper lift-out grid (Omniprobe) was done with a Kleindiek micromanipulator. To minimize sidewall damage, Ga ions of only 5 keV energy were used for final thinning of the TEM lamella to electron transparency. SEM of the NCTs before and after CVD growth of the CNTs was performed by detecting secondary electrons using a S-4800 microscope (Hitachi) operated at an accelerating voltage of 10 kV. Raman maps of randomly selected sample areas of 20 × 20 $\mu m^2$ were recorded with a step width of 1.25 μm using a micro-Raman Labram HR spectrometer, which is equipped with a holographic 1800 lines per mm grating and a liquid nitrogen cooled CCD detector (Horiba-Jobin-Yvon). The laser wavelengths of 532 nm and 632.8 nm, corresponding to photon energies of 2.33 eV and 1.96 eV, respectively, were used for excitation. The obtained Raman spectra were fitted using an in-house software routine based on a Levenberg-Marquardt least-square algorithm. SWCNT diameter distributions were calculated by using the relation $d_{SWCNT} = 232\ cm^{-1}\ nm/\nu_{RBM}$,[60] wherein $\nu_{RBM}$ represents the Raman shift of the radial breathing mode of SWCNTs, and by sorting the obtained diameter values into diameter intervals of 0.05 nm width.

## Results

The microstructure of the original NCT type I is heterogeneous and consists of Ni-rich particles embedded in an amorphous carbon (a-C) matrix (Fig. 1). Cross-sectional TEM analysis gives a mean NP diameter of (2.0 ± 0.3) nm, which corresponds to the average NCT thickness. The NPs appear to be well-aligned with a mean NP center to center distance of (4.3 ± 0.3) nm. Lattice fringes were resolved for approximately 40% of 27 NPs analyzed in detail (Fig. 1b and c). Fast Fourier Transform (FFT) analysis gave lattice spacings grouped into (a) 0.22 nm to 0.24 nm and (b) 0.20 to 0.21 nm. In one case crossed lattice fringes with spacings of 0.21 nm and 0.15 nm enclosing an angle of 46° were observed. The latter values are in good agreement with reference data of the (006) and {116} planes of rhombohedral $Ni_3C$ (rh-$Ni_3C$), which are 0.215 nm, 0.156 nm,

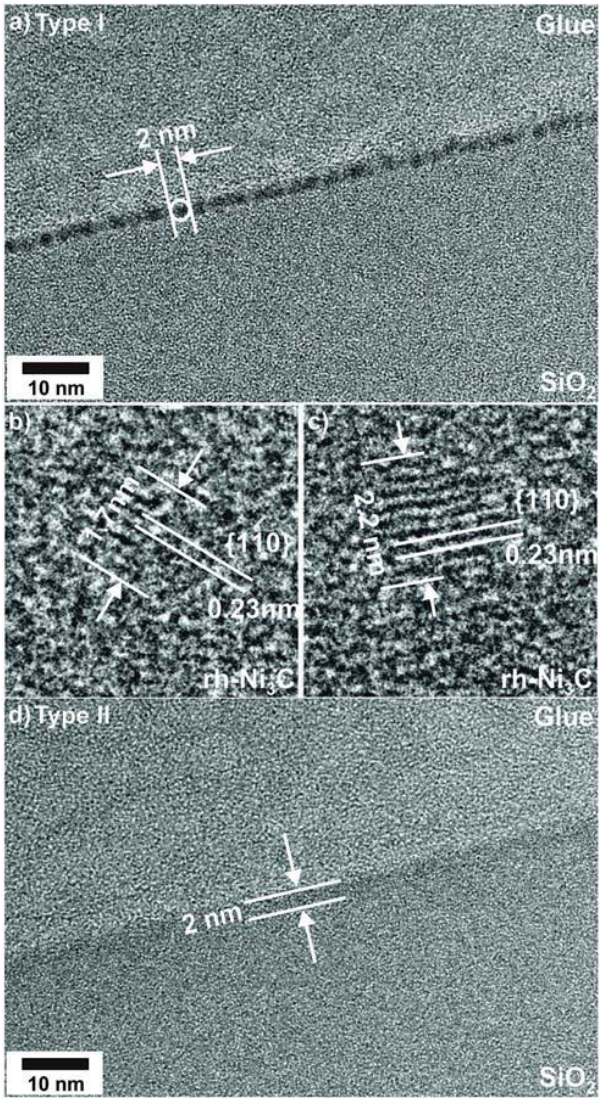


**Fig. 1** Cross-sectional TEM images of C : Ni templates before the CVD process of CNTs: (a)–(c) NCT type I; (d) NCT type II. Images (b) and (c) are enlarged views of micrograph (a) showing selected crystalline $Ni_3C$ NPs in NCT type I.

and 43.4°.[61] Moreover, the group (a) lattice fringe spacings are indicative for rh-$Ni_3C$, namely for its {110} planes.[61] Group (b) spacings could be assigned either to rh-$Ni_3C$ or to fcc-Ni. According to these findings, previous own work, and the literature on this material system, the initial Ni-rich phase of NCT type I is assigned to rh-$Ni_3C$.[57,62–64]

The cross-sectional TEM image of NCT type II (Fig. 1d) shows the formation of a Ni-enriched layer appearing darker than the $SiO_2$ substrate and the resin glue on top of the film, which is used for TEM specimen preparation. The layer thickness is 2 nm and hence the same as for the NCT type I. In contrast to NCT type I, no NP formation was detected for NCT type II (Fig. 1d). The homogenous microstructure of C : Ni NCT type II is attributed to the hyperthermal particle and energy flux of the irradiating $Ar^+$ ions. It causes ion-enhanced mixing and partial re-sputtering of Ni, which lead to a homogenous distribution of the metal in the a-C matrix.

After CVD growth of CNTs the morphology of NCT I consists of individual NPs as before the CVD process (Fig. 2).

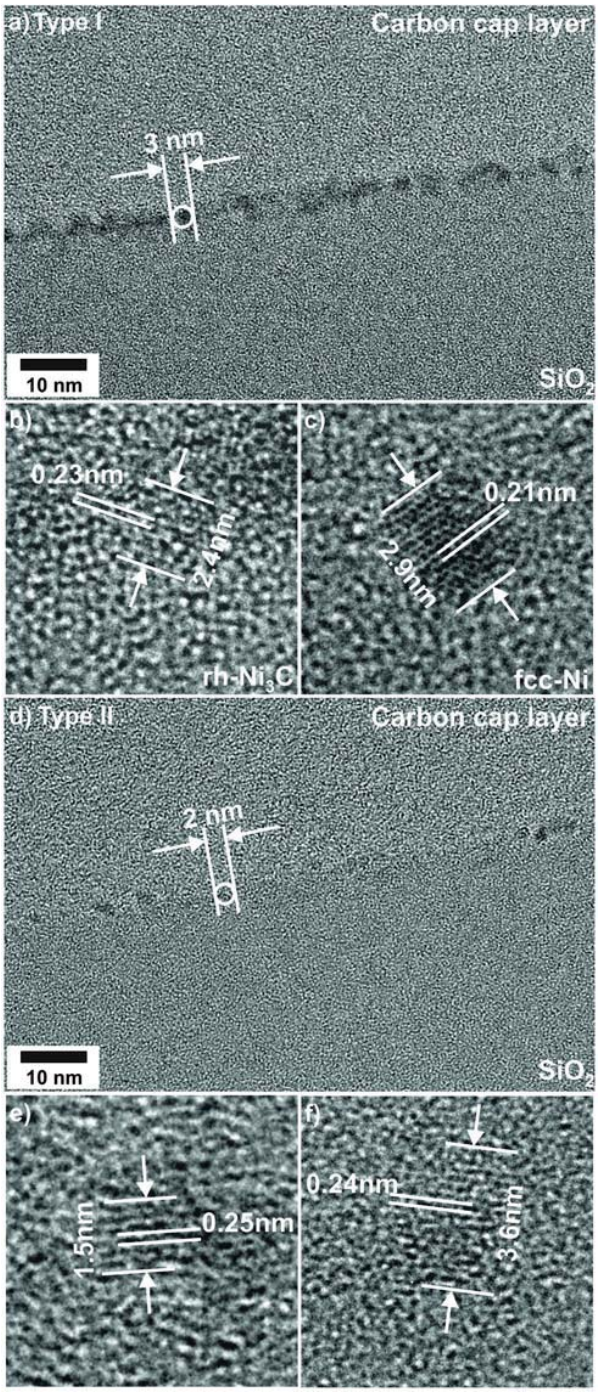


**Fig. 2** Cross-sectional TEM images of C : Ni templates after CVD growth of CNTs: (a)–(c) NCT type I; (d)–(f) NCT type II. Images (b) and (c) [(e) and (f)] show selected crystalline NPs in NCT type I [NCT type II].

 

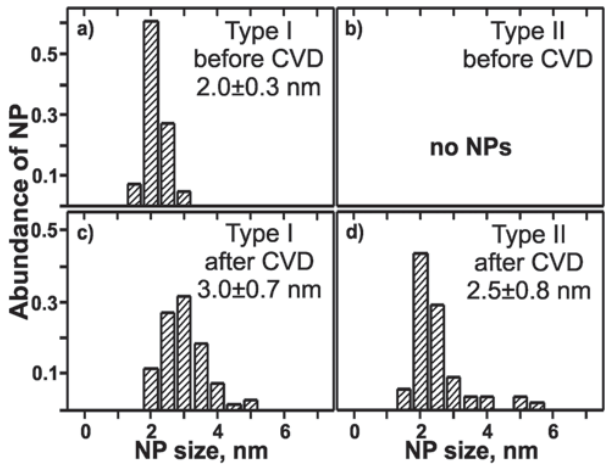


Fig. 3 Normalized size distributions of Ni-rich NPs measured by TEM before and after the CVD process, respectively. NCT type I, (a) and (c), NCT type II, (b) and (d).

Cross-sectional TEM revealed moderate NP coarsening accompanied by broadening of the diameter distribution from initially (2.0 ± 0.3) nm to (3.0 ± 0.7) nm (Fig. 3). The NPs are less aligned and the NCT surface appears rougher than before the CVD process. Lattice fringes were observed for 72% out of 29 NPs studied in detail. FFT analysis revealed the coexistence of Ni-rich NPs with hcp (Fig. 2b) and fcc (Fig. 2c) lattice structure in an approximately equal ratio. The details of this analysis are provided in the ESI.† The FFT of the nanocrystal in Fig. 2b corresponds very closely to a $[1\bar{2}1\bar{3}]$ zone axis image of hcp-Ni (for details see ESI, Fig. 1†).[65] It has the same Ni sublattice structure as rh-$Ni_3C$. The nanocrystal displayed in Fig. 2c has fcc crystal structure. Its FFT corresponds to a [011] zone axis image of fcc-Ni (for details see ESI, Fig. 2†).[65] One out of 29 FFT patterns showed lattice fringes with spacings of 0.22 nm and 0.25 nm enclosing an angle of 56°. One possible assignment would be fcc-NiO, although the observed spacings were enlarged by about 4% compared to the reference.[61] Alternatively, this FFT pattern might be described by $Ni_3C$ {110} and {014} lattice fringes, whose spacings are 0.22 nm and 0.25 nm with an interplanar angle of 56.7°.

In summary, approximately 50% of NCT type I NPs changed their lattice structure from rh-$Ni_3C$ to fcc-Ni. For another approximately 50% the observed hcp-Ni lattice structure points to the conservation of the initial rh-$Ni_3C$ phase structure. The formation of fcc-NiO could not be verified. Finally it should be noted that TEM analysis is not suitable to provide information about the structure of the a-C matrix.

The morphology of NCT type II, where initially only a contrast enhancement with respect to $SiO_2$ substrate and resin glue could be detected, was completely changed during the CVD process. The initial homogenous and 2 nm thick Ni-enriched layer was no more detected. Instead, NCT type II is characterized by the coexistence of ranges without (major fraction) and with (minor fraction) separated NPs after the CVD (Fig. 2d). Their average diameter is (2.5 ± 0.8) nm (Fig. 3). The smallest resolved NP had a diameter of 1.5 nm. Two dominant lattice spacings were identified by FFT analysis, namely 0.21 nm and 0.25 nm. Their assignment to rh-$Ni_3C$, fcc-Ni, or fcc-NiO is ambiguous as outlined in the previous sections, and supporting interplanar angles could not be determined. The NP formation from NCT type II can be considered as an example for the SWCNT growth using catalysts, which are formed *in situ* during the process of pre-treatment and CVD. The post-CVD NP diameter distribution of NCT type I is narrower than that of NCT type II. This difference can be expressed as relative deviation from the mean NP diameter values. It is 23% for NCT type I and 32% for NCT type II. Moreover, compared to NCT type II, a larger fraction of NCT type I NPs showed lattice fringes. This is a hint for a larger degree of NP crystallinity in NCT type I than in type II after the CVD growth of CNTs.

The TEM results show that the microstructure of the predefined NCT type I is largely preserved during the CNT growth process. Its mean NP diameter grew by about 1 nm (*ca.* 50%), and the fraction of crystalline NPs within the template increased. In contrast to that NCT type II underwent a complete re-structuring from a homogenous film into a film of NPs. The NP size distribution for NCT type II after CVD is sufficiently narrow and can be compared with the one obtained from metallic thin films. As an example, pre-annealing of a 0.22 nm-thin Ni film produced NPs with diameter of (4.4 ± 0.6) nm.[52]

In contrast to the featureless appearance before nanotube growth, SEM images of the NCT samples measured after the CVD process display three types of features: (i) randomly distributed spherical spots of less than 10 nm in diameter, (ii) bent objects of about 80 nm length, and (iii) blurred objects of up to 3 μm length (Fig. 4). These features are assigned to metallic nanoparticles, multi-walled CNTs (MWCNTs), and single-

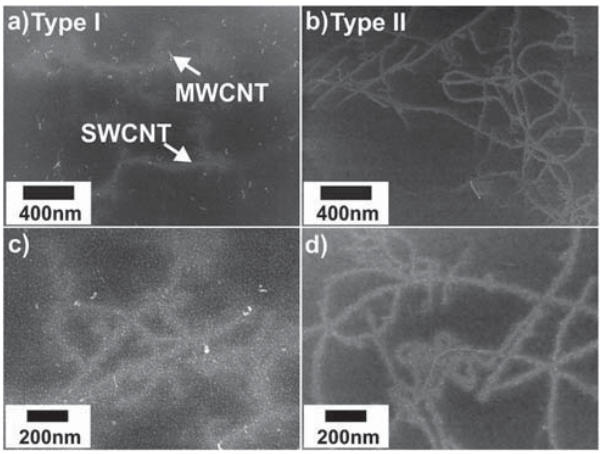


Fig. 4 SEM images of C : Ni templates after CVD growth of CNTs: (a), (c) NCT type I; (b), (d) NCT type II. Compared to the few MWCNTs the individual SWCNTs appear blurred and diffuse due to charging effects and probably also due to thermally-induced vibrations.

walled CNTs, respectively. The NP diameters are apparently larger for NCT type I than for type II. The amount of MWCNTs is generally very low. In NCT type II samples MWCNTs are virtually absent. The statistical analysis of the SEM images points to a similar efficiency of both types in catalyzing SWCNT growth with yields of ~5 to 7 tubes per $\mu m^2$.

Raman spectroscopy enables a non-destructive and simple determination of the SWCNT diameter because of the inverse proportionality of diameter and radial breathing mode (RBM) frequency. Hence, the diameter distribution of SWCNTs in the sample can be conveniently elucidated by measuring Raman spectra with two or more excitation laser wavelengths, for example, 532 nm and 632.8 nm. This approach allows detecting SWCNTs in the diameter range from 0.6 nm to 2.3 nm. The reliability of the SWCNT diameter distribution obtained by this method was confirmed by parallel Raman and High-Resolution TEM studies in the literature.[16,37]

Typical Raman spectra in the range of the RBM obtained during 2D Raman mapping with two excitation wavelengths for NCT types I and II are shown in Fig. 5a and b. The vast majority of the spectra contains only one single RBM line. In total, the Raman spectra of more than 600 individual SWCNTs were analysed in this study. The RBM line widths for SWCNTs grown with both template types cover the range of 4 $cm^{-1}$ to 8 $cm^{-1}$. They decrease with increasing RBM frequency, similar to the results reported previously in the literature.[66] The narrow line widths point to long lifetimes of the excited RBM modes, and indicate a high degree of structural order and a negligible contribution of defect-induced phonon decay processes. Such a behavior is consistent with the formation of individual SWCNTs with a low amount of structural defects.[67] In order to analyze the abundance of SWCNTs, the observed RBM frequencies were assigned to frequency intervals of 10 $cm^{-1}$ width and subsequently summed. The analysis shows a diameter-selective SWCNT formation for NCT type I: 50% of all observed tubes have RBM frequencies from 160 $cm^{-1}$ to 180 $cm^{-1}$ (Fig. 5c). In contrast to that, a broad distribution of RBM frequencies is found for NCT type II (Fig. 5d). The corresponding diameter distributions of SWCNTs (normalized to 1) are shown in Fig. 6. The SWCNT diameter distribution depends strongly on the template type. The diameter distribution of NCT type I reveals an astonishingly high selectivity for SWCNTs of the diameter interval centered at (1.360 ± 0.025) nm, which includes about 33% of the SWCNTs (Fig. 6a). Moreover, 51% of all synthesized SWCNTs fall into a narrow diameter range of 1.26 nm to 1.46 nm.

Applying the formula for the nanotube diameter $d$,

$$d = (a_0/\pi)\sqrt{n^2 + nm + m^2},$$

with the lattice constant $a_0$ = 0.246 nm and the chiral indices $n$ and $m$, in total 9 SWCNT chiralities can be expected in the diameter range of (1.360 ± 0.025) nm. Two of them are metallic, 7 are semiconducting. The analysis of the electronic transition energies of these 9 chiralities shows that only the $E_{33}$ electronic transition of semiconducting SWCNTs is in resonance with the laser energy of 2.33 eV.[68] This criterion requires that the difference between laser and electronic transition energy is $\Delta E \leq \pm 0.10$ eV.[69] The combination of these two informations reduces the chiralities preferentially observed in this study to three: (12,8), (17,1), and (16,3).

The proposed diameter selectivity is further supported by the following findings of the Raman analysis. The next thinner SWCNTs, which are expected to be in resonance with laser radiation of 532 nm, would be (13,6), (14,4) and (15,2) with diameters of 1.32 nm, 1.28 nm and 1.26 nm and RBM frequencies of 175 to 185 $cm^{-1}$, respectively. Their abundance is only of the order of 5% (Fig. 6). At slightly larger diameters than (1.360 ± 0.025) nm the SWCNTs (15,5), (11,10) and (14,7) with 1.41 nm, 1.43 nm and 1.45 nm should resonate with 532 nm laser excitation. The abundance of this fraction is about 7%. That means that the low and high limit of the SWCNT diameter distribution maximum is precisely defined for NCT type I.

It can be further concluded that semiconducting tubes with diameters of ~1.6 nm and RBM frequencies of around

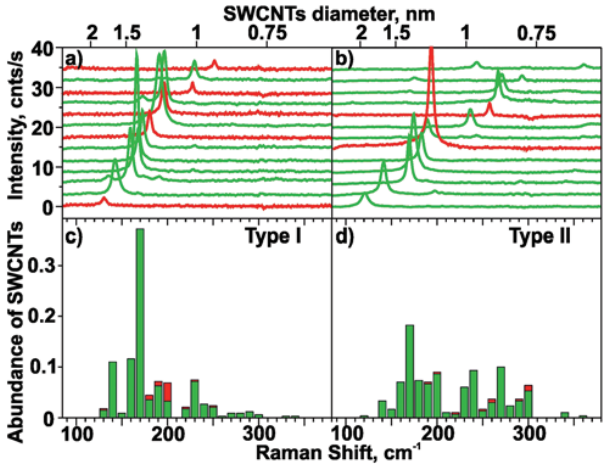


Fig. 5 Selected RBM range Raman spectra (a, b) and RBM distributions (c, d) of SWCNTs formed from C : Ni templates: (a), (c) NCT type I; (b), (d) NCT type II. The color code represents spectra measured with 532 nm (green) and 632.8 nm (red) laser excitation, respectively.

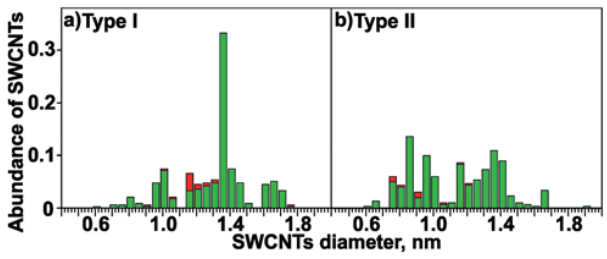


Fig. 6 Normalized diameter distributions of SWCNTs synthesized from C : Ni templates as derived from the abundance of observed RBM lines in the corresponding diameter intervals: (a) NCT type I; (b) NCT type II. The color code represents data obtained with 532 nm (green) and 632.8 nm (red) laser excitation, respectively.

 

140 $cm^{-1}$ contribute only to a minor extent to the observed diameter distribution (Fig. 6). Finally, for 632.8 nm laser excitation, the most abundant SWCNTs have RBM frequencies of around ~200 $cm^{-1}$ for NCT type I. They belong to metallic tubes with a diameter of 1.2 nm, whose $M_{11}$ transition is in resonance with the laser energy of 1.96 eV. These metallic tubes cause the local maximum in the diameter distribution for 632.8 nm laser excitation, but their contribution to the overall SWCNT diameter distribution is of the order of less than 5%.

In contrast to type I, NCT type II yields a relatively uniform distribution of SWCNT diameters from 0.8 to 1.4 nm (88% of all SWCNTs). The gap of the diameter distribution at about 1.15 nm, which is also observed for NCT type I, is explained by the missing resonance of such SWCNTs with 532 nm laser radiation. For this reason the diameter distribution is not described as bimodal but as uniform. The upper limit of the SWCNT diameter distribution obtained with NCT type II is defined by the very low amount of SWCNTs with an RBM frequency of about 140 $cm^{-1}$ (<5%) corresponding to diameters of about 1.7 nm. The high overall yield of SWCNT with small diameters (40% in the 0.6–1.0 nm range) is however remarkable.

Since NCT type I is apparently a very promising pre-defined and stable catalyst for diameter-selective SWCNT growth, its morphology after pre-treatment was investigated. For this purpose the growth process was terminated after the pre-treatment step (exposing the NCTs to flowing air at 550 °C for 10 min) and the pre-treated template was analyzed using cross-sectional TEM and Raman spectroscopy (Fig. 7). The Raman spectra of NCT type I show the typical $sp^2$-carbon ($sp^2$-C) Raman lines, *i.e.* the D line at around 1350 $cm^{-1}$ and the G line at around 1550 $cm^{-1}$, before and after pre-treatment (Fig. 7a). The intensity of the $sp^2$-C Raman lines decreased to 30% after the pre-treatment, and simultaneously the intensity of the Si-2TO lines at around 950 $cm^{-1}$ increased by approximately 40% (not shown). These observations point to a partial loss of a-C, presumably by oxidation to $CO_2$. Moreover, narrower line widths and G line up-shift indicate a higher degree of graphitization of the a-C matrix. Cross-sectional TEM analysis reveals a mean NP diameter of (2.2 ± 0.4) nm, which is the same as in the virgin NCT within the experimental accuracy. In conclusion, the pre-treatment step causes slight roughening of NCT type I due to partial removal of the embedding a-C matrix. These changes have apparently no effect on the NP morphology.

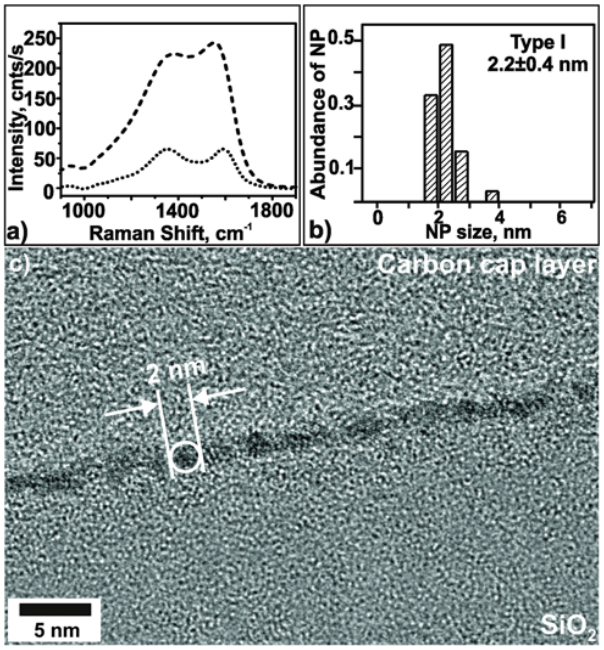


**Fig. 7** Characterization of NCT type I after the pre-treatment step: (a) Raman spectrum (dotted line) in comparison to that of the pristine template (dashed line), (b) normalized size distribution of Ni-rich NPs measured by TEM, (c) cross-sectional TEM image.

## Discussion

In the following section the conclusions from the presented results for CVD growth of SWCNTs using C : Ni NCTs with and without predefined NPs are discussed.

(a) NP stability of NCT type I.

Without stabilization, Ni thin films on $SiO_2$ surfaces undergo clustering *via* surface diffusion for temperatures larger than −173 °C.[70,71] Ni cluster diameters of 8 nm to 20 nm were reported for nominally 1 nm thick Ni films.[71,72] Bulk diffusion of Ni into a $SiO_2$ layer on Si and formation of $NiSi_2$ starts at elevated temperatures (≥425 °C), depending on $SiO_2$ thickness. The bulk diffusion onset temperature for a 2.5 nm thick $SiO_2$ layer was reported to be 800 °C.[70] These data demonstrate that without stabilization much larger Ni particles are formed at temperatures similar to those during catalyst pre-treatment and CVD growth in the present study.

In fact, our investigations have shown that a defined microstructure of Ni-rich NPs with narrow diameter distribution of (2.0 ± 0.3) nm can be stabilized up to temperatures of 735 °C and used to grow SWCNTs. This has been achieved by embedding the NPs in a protective matrix of a-C, forming a NCT of type I. The protective a-C is fully stable in ambient conditions and allows easy handling of the NCTs in air. Thus, the a-C matrix ensures the safe transport of the templates and their transfer into the CVD oven. During the pre-treatment step at 550 °C in air, the a-C matrix is partially conserved. This ensures that the Ni-rich NPs keep their initial positions, diameter distribution and spacing. In this way the NPs are prevented from coagulation and grain coarsening. This observation is attributed to the strong interaction between Ni and C, which is *e.g.* larger than that between Ni and $SiO_2$.[73] The rest of the a-C matrix presumably undergoes oxidation to $CO_2$. After pre-treatment, the NCT type I enters the CVD synthesis with pre-defined, almost unchanged diameter in activated form.

(b) Relation between SWCNT and catalyst properties.

It is obvious to explain the narrower and apparently selective SWCNT diameter distribution obtained by CVD growth using NCT type I by the pre-defined NP diameters and their demonstrated stability. As a consequence, the carbon precursors are exposed to almost equally-sized catalytically active NPs during the CVD process. In contrast to that situation, the initially homogenously distributed Ni in NCT type II undergoes a coarsening, the carbon precursor is exposed to catalytic particles of different size and as a consequence, the SWCNT distribution is broader and not selective. On the other hand the smaller SWCNT diameters obtained with NCT type II can be attributed to the fact that NPs grow from an initially homogenous Ni distribution to a size of (2.5 ± 0.8) nm. The behavior of NCT type II resembles catalysts whose catalytically active particles are formed *in situ* from metal thin films during the CVD process. The results presented here demonstrate that narrower SWCNT diameter distributions are accessible by the use of pre-defined, stable catalyst templates.

Apparently the best strategy to obtain SWCNTs with narrow diameter distribution is to use a catalyst with stable NPs of predefined size and to prevent them from coarsening during the CVD process. Several approaches to realize these preconditions were described in the literature. First, the catalyst NPs can be sparsely distributed over the inert substrate so that the large distance between the particles would prevent their aggregation.[21,23,44,53] For instance, Paillet *et al.*[53] studied the CVD synthesis of SWCNTs on Ni NPs with the mean size of (4.7 ± 1.4) nm using $C_2H_4$ as a carbon source. The narrow size distribution of SWCNTs was achieved at 850 °C when the density of NPs and the synthesized SWCNTs was small (40 and 100 NPs per $\mu m^2$ led to 0.1–0.2 and ~3 SWCNTs per $\mu m^2$, respectively). Importantly, for these conditions the Ni NPs had the same size before and after the CVD. An increase of the surface density to several hundred NPs per $\mu m^2$ led to aggregation of NPs and formation of amorphous carbon and big filamentous structures. An increase of the reaction temperature to 950 °C also resulted in larger Ni NPs with broader size distribution.[53] In our work, a narrow SWCNT diameter distribution was successfully obtained with a much higher density of catalyst NPs (*ca.* 20 000 NPs per $\mu m^2$) and synthesized SWCNTs (5–7 SWCNTs per $\mu m^2$).

So far, the most successful approach to obtain SWCNTs with a narrow diameter distribution is the use of an inert matrix, which protects NPs from coarsening or makes this process much slower than SWCNT nucleation. Well-defined Fe NPs were obtained *in situ* by a preliminary process step and stabilized during CVD by embedding them in an aluminum oxide matrix.[16,27,29,31] This method offers catalyst NPs of different size with narrow diameter distribution on the substrate surface, but the size of NPs is not constant over the reaction time. The other widely used supports for nano-scaled metal catalysts are porous materials like mesostructured silica,[32,33,36,39,40,45,74,75] porous magnesium oxide[24,34,47] and zeolites,[42,56,76] which offer SWCNTs with a selective chirality[32–34,36,39,45,74] and sufficient yield. Catalyst particles immobilized in the substrate pores retain their size over reaction time in a broad temperature range, however SWCNTs are formed not only on the surface but also in the bulk of the catalyst/matrix composite. As a result, they are bundled and inevitably mixed with the catalyst, which requires the use of laborious purification procedures.

In this work a new type of catalyst for diameter-selective SWCNT growth is presented. C : Ni nanocomposite template type I combines the following advantages: narrow catalyst diameter distribution, stability during the CVD process, potential for growing individual SWCNT with a significant length and yield. The study confirms the hypothesis that the diameter distribution of CVD-grown SWCNTs is determined by the catalyst morphology and the size of the catalyst particles at the initial point of the SWCNT nucleation.[44,77] In NCT type II, formation and growth of the catalyst NPs competes with the simultaneous SWCNT growth. Thus, the size distribution of the catalyst NPs is changing with time, and so does the diameter distribution of the nucleating SWCNTs. On the contrary, in NCT type I the catalyst NPs with narrow and weakly varying size distribution are available from the very beginning and during the whole time of the SWCNT growth. Hence, the diameter distribution of the synthesized SWCNTs is much narrower. Certainly, the study also shows that control of catalyst diameter is a necessary but not a sufficient condition for diameter-selective or even chirality-selective growth of SWCNTs. Further well-established parameters controlling the SWCNT diameter distribution are growth temperature, nature and concentration of precursors, and catalyst pre-treatment.

A final question that shall be briefly addressed is the chemical state of the catalytically active Ni-rich NPs. After the CVD process, fcc-Ni and $Ni_3C$ were identified by the TEM analysis (Fig. 3 and ESI†). It is reasonable to assume that these two Ni phases are catalytically active. Fcc-Ni is commonly considered as most suitable Ni based catalyst for CNT growth.[15,17,49,78] Recent papers also reported $Ni_3C$ as an active catalyst, at least for carbon nanofibers[64] and initial graphene layers of CNTs.[50] Moreover, indications for a minor fraction of NiO after the CVD process were obtained. A conclusion about its catalytic activity can however not be drawn on the basis of the presented results. *In situ* XPS and TEM studies could help to clarify the phase and chemical state of the catalytically active Ni species.

## Conclusions

A new type of pre-defined stable catalyst for diameter-controlled growth of SWCNTs was prepared and comprehensively characterized. It comprises dispersed catalytic particles, whose size is largely preserved during the CVD synthesis. This way, the problem of the Ostwald ripening is circumvented, and a new route for much better control over the diameter of CVD-grown SWCNTs is opened. Diameter-selectivity of NCT based SWCNT growth was demonstrated for the first time. A fraction of 50% of SWCNT diameters was confined to a range of (1.36 ± 0.10) nm. In comparison to the growth using the pre-defined

 

NPs, a non-selective SWCNT distribution, with 88% of all SWCNT in the diameter range of 0.80 nm to 1.40 nm was obtained using a NCT with a homogenous microstructure under otherwise identical conditions (NCT type II).

The as-grown SWCNTs themselves are ideal candidates for further comprehensive characterization, *e.g.* by coupling of Raman spectroscopy with atomic force or scanning tunneling microscopy. They consist predominantly of separated SWCNTs, are free of solvents or surfactants, exhibit a low degree of bundling, and contain negligible amounts of MWCNTs. Their length to diameter ratio was of the order of 200. The narrow RBM line widths of 4 $cm^{-1}$ to 8 $cm^{-1}$ show a high structural order of the as-grown SWCNTs and point to a low amount of intrinsic structural defects and negligible nanotube bundle formation.

The presented approach opens a new way to perform CVD synthesis of SWCNTs using catalyst particles with well-defined size distribution. Usually in CVD growth of SWCNTs, the metallic NPs are synthesized *in situ*, which severely limits the possibility to reliably ascertain their homogeneity and quality. The NCTs used in this study can be prepared prior to CNT synthesis, are not destroyed when exposed to air, and their properties can be characterized with a high degree of certainty as described above.

Further optimization of the size distribution, stability, and catalytic activity of metallic NPs in NCTs promises even better control over the size and diameter distribution of CVD-synthesized SWCNTs. The a-C matrix could be replaced by thermally stable oxides, which would improve the stability of the catalytic NPs during CVD growth of SWCNTs. Moreover, the catalytic activity and diameter selectivity can be improved by using nanocomposite templates with embedded NP alloys like FeNi or FeCo instead of pure metals.

## Funding sources

This work was funded by the EU, "European Regional Development Fund", Project ECEMP-D1 (no. 13857/2379), "Nanoskalige Funktionsschichten auf Kohlenstoffbasis", and LEI 100114022 "C-basierte Funktionsschichten für tribologische Anwendungen".

## Acknowledgements

Support by the Structural Characterization Facilities Dresden-Rossendorf at IBC is gratefully acknowledged. S.M. and S.G. acknowledge support of the Center of Advancing Electronics Dresden (CfAED). M.H. and M.K. thank NanoTP COST action for support. Additionally M.H. would like to acknowledge the operation team at the Binnig and Rohrer Nanotechnology Center for their support. Special thank by the authors is addressed to M. Missbach, A. Kunz, E. Christalle, A. Schneider, J. Wagner, B. Schreiber, L. Bischoff (all from HZDR) and T. Bayrak (Bilkent University Ankara) for technical assistance, and K.-H. Heinig, R. Wenisch, D. Janke, A. Erbe (all from HZDR), and A. Popov (IFW Dresden) for helpful discussions and careful proofreading of the manuscript.

## Notes and references

1 S. Iijima, *Nature*, 1991, **354**, 56.
2 A. Bachtold, P. Hadley, T. Nakanishi and C. Dekker, *Science*, 2001, **294**, 1317.
3 W. J. Yu and Y. H. Lee, *ChemSusChem*, 2011, **4**, 890.
4 B. Liu, C. Wang, J. Liu, Y. Che and C. Zhou, *Nanoscale*, 2013, **5**, 9483.
5 P. Wick, M. J. D. Clift, M. Rösslein and B. Rothen-Rutishauser, *ChemSusChem*, 2011, **4**, 905.
6 Z. Liu, W. Cai, L. He, N. Nakayama, K. Chen, X. Sun, X. Chen and H. Dai, *Nat. Nanotechnol.*, 2007, **2**, 47.
7 K. Besteman, J.-O. Lee, F. G. M. Wiertz, H. A. Heering and C. Dekker, *Nano Lett.*, 2003, **3**, 727.
8 K. Bradley, A. Davis, J.-C. P. Gabriel and G. Grüner, *Nano Lett.*, 2005, **5**, 841.
9 M. F. L. De Volder, S. H. Tawfick, R. H. Baughman and A. J. Hart, *Science*, 2013, **339**, 535.
10 A. M. Ionescu and H. Riel, *Nature*, 2011, **479**, 329.
11 R. Saito, M. Fujita, G. Dresselhaus and M. S. Dresselhaus, *Appl. Phys. Lett.*, 1992, **60**, 2204.
12 T. W. Odom, J.-L. Huang, P. Kim and C. M. Lieber, *Nature*, 1998, **391**, 62.
13 J.-P. Tessonnier and D. S. Su, *ChemSusChem*, 2011, **4**, 824.
14 J. Prasek, J. Drbohlavova, J. Chomoucka, J. Hubalek, O. Jasek, V. Adam and R. Kizek, *J. Mater. Chem.*, 2011, **21**, 15872.
15 C. Journet, M. Picher and V. Jourdain, *Nanotechnology*, 2012, **23**, 142001.
16 W. Song, C. Jeon, Y. S. Kim, Y. T. Kwon, D. S. Jung, S. W. Jang, W. C. Choi, J. S. Park, R. Saito and C.-Y. Park, *ACS Nano*, 2010, **4**, 1012.
17 S. Hofmann, R. Sharma, C. Ducati, G. Du, C. Mattevi, C. Cepek, M. Cantoro, S. Pisana, A. Parvez, F. Cervantes-Sodi, A. C. Ferrari, R. Dunin-Borkowski, S. Lizzit, L. Petaccia, A. Goldoni and J. Robertson, *Nano Lett.*, 2007, **7**, 602.
18 R. Rao, D. Liptak, T. Cherukuri, B. I. Yakobson and B. Maruyama, *Nat. Mater.*, 2012, **11**, 213.
19 A. R. Harutyunyan, G. Chen, T. M. Paronyan, E. M. Pigos, O. A. Kuznetsov, K. Hewaparakrama, S. M. Kim, D. Zakharov, E. A. Stach and G. U. Sumanasekera, *Science*, 2009, **326**, 116.
20 P. Petit, D. Salem, M. He, M. Paillet, R. Parret, J.-L. Sauvajol and A. Zahab, *J. Phys. Chem. C*, 2012, **116**, 24123.
21 L. Durrer, J. Greenwald, T. Helbling, M. Muoth, R. Riek and C. Hierold, *Nanotechnology*, 2009, **20**, 355601.
22 B. Zhao, D. N. Futaba, S. Yasuda, M. Akoshima, T. Yamada and K. Hata, *ACS Nano*, 2009, **3**, 108.
23 D. Takagi, Y. Homma, H. Hibino, S. Suzuki and Y. Kobayashi, *Nano Lett.*, 2006, **6**, 2642.

24 I. Abdullahi, N. Sakulchaicharoen and J. E. Herrera, *Diamond Relat. Mater.*, 2014, **41**, 84.
25 H. Ago, T. Ayagaki, Y. Ogawa and M. Tsuji, *J. Phys. Chem. C*, 2011, **115**, 13247.
26 C. L. Cheung, A. Kurtz, H. Park and C. M. Lieber, *J. Phys. Chem. B*, 2002, **106**, 2429.
27 S. Sakurai, M. Inaguma, D. N. Futaba, M. Yumura and K. Hata, *Small*, 2013, **9**, 3584.
28 H. Liu, D. Takagi, S. Chiashi and Y. Homma, *Nanotechnology*, 2009, **20**, 345604.
29 M. Cantoro, S. Hofmann, S. Pisana, V. Scardaci, A. Parvez, C. Ducati, A. C. Ferrari, A. M. Blackburn, K. Y. Wang and J. Robertson, *Nano Lett.*, 2006, **6**, 1107.
30 E. Suvacı, Y. Çelik, A. Weibel, A. Peigney and E. Flahaut, *Carbon*, 2012, **50**, 3092.
31 S. M. Kim, C. L. Pint, P. B. Amama, D. N. Zakharov, R. H. Hauge, B. Maruyama and E. A. Stach, *J. Phys. Chem. Lett.*, 2010, **1**, 918.
32 H. Wang, L. Wei, F. Ren, Q. Wang, L. D. Pfefferle, G. L. Haller and Y. Chen, *ACS Nano*, 2013, **7**, 614.
33 S. M. Bachilo, L. Balzano, J. E. Herrera, F. Pompeo, D. E. Resasco and R. B. Weisman, *J. Am. Chem. Soc.*, 2003, **125**, 11186.
34 M. He, H. Jiang, B. Liu, P. V. Fedotov, A. I. Chernov, E. D. Obraztsova, F. Cavalca, J. B. Wagner, T. W. Hansen, I. V. Anoshkin, E. A. Obraztsova, A. V. Belkin, E. Sairanen, A. G. Nasibulin, J. Lehtonen and E. I. Kauppinen, *Sci. Rep.*, 2013, **3**, 1460.
35 M. He, A. I. Chernov, P. V. Fedotov, E. D. Obraztsova, E. Rikkinen, Z. Zhu, J. Sainio, H. Jiang, A. G. Nasibulin, E. I. Kauppinen, M. Niemela and A. O. Krause, *Chem. Commun.*, 2011, **47**, 1219.
36 N. Li, X. Wang, F. Ren, G. L. Haller and L. D. Pfefferle, *J. Phys. Chem. C*, 2009, **113**, 10070.
37 M. Fouquet, B. C. Bayer, S. Esconjauregui, R. Blume, J. H. Warner, S. Hofmann, R. Schlögl, C. Thomsen and J. Robertson, *Phys. Rev. B: Condens. Matter*, 2012, **85**, 235411.
38 B. Liu, W. Ren, S. Li, C. Liu and H.-M. Cheng, *Chem. Commun.*, 2012, **48**, 2409.
39 L. Wei, S. Bai, W. Peng, Y. Yuan, R. Si, K. Goh, R. Jiang and Y. Chen, *Carbon*, 2014, **66**, 134.
40 H. Wang, K. Goh, R. Xue, D. Yu, W. Jiang, R. Lau and Y. Chen, *Chem. Commun.*, 2013, **49**, 2031.
41 S. Noda, Y. Tsuji, Y. Murakami and S. Maruyama, *Appl. Phys. Lett.*, 2005, **86**, 173106.
42 S. Maruyama, R. Kojima, Y. Miyauchi, S. Chiashi and M. Kohno, *Chem. Phys. Lett.*, 2002, **360**, 229.
43 K. Kakehi, S. Noda, S. Maruyama and Y. Yamaguchi, *Appl. Surf. Sci.*, 2008, **254**, 6710.
44 M. Fouquet, B. C. Bayer, S. Esconjauregui, C. Thomsen, S. Hofmann and J. Robertson, *J. Phys. Chem. C*, 2014, **118**, 5773.
45 H. Wang, B. Wang, X.-Y. Quek, L. Wei, J. Zhao, L.-J. Li, M. B. Chan-Park, Y. Yang and Y. Chen, *J. Am. Chem. Soc.*, 2010, **132**, 16747.
46 M. Picher, E. Anglaret, R. Arenal and V. Jourdain, *ACS Nano*, 2011, **5**, 2118.
47 H. J. Jeong, K. H. An, S. C. Lim, M.-S. Park, J.-S. Chang, S.-E. Park, S. J. Eum, C. W. Yang, C.-Y. Park and Y. H. Lee, *Chem. Phys. Lett.*, 2003, **380**, 263.
48 M. Krause, M. Haluška, G. Abrasonis and S. Gemming, *Phys. Status Solidi B*, 2012, **249**, 2357.
49 A. Achour, A. A. El Mel, N. Bouts, E. Gautron, E. Grigore, B. Angleraud, L. Le Brizoual, P. Y. Tessier and M. A. Djouadi, *Diamond Relat. Mater.*, 2013, **34**, 76.
50 N. T. Panagiotopoulos, E. K. Diamanti, L. E. Koutsokeras, M. Baikousi, E. Kordatos, T. E. Matikas, D. Gournis and P. Patsalas, *ACS Nano*, 2012, **6**, 10475.
51 H. Ago, Y. Nakamura, Y. Ogawa and M. Tsuji, *Carbon*, 2011, **49**, 176.
52 K. Kakehi, S. Noda, S. Chiashi and S. Maruyama, *Chem. Phys. Lett.*, 2006, **428**, 381.
53 M. Paillet, V. Jourdain, P. Poncharal, J.-L. Sauvajol, A. Zahab, J. C. Meyer, S. Roth, N. Cordente, C. Amiens and B. Chaudret, *J. Phys. Chem. B*, 2004, **108**, 17112.
54 W.-H. Chiang and R. Mohan Sankaran, *Nat. Mater.*, 2009, **8**, 882.
55 H. Sugime, S. Noda, S. Maruyama and Y. Yamaguchi, *Carbon*, 2009, **47**, 234.
56 Y. Miyauchi, S. Chiashi, Y. Murakami, Y. Hayashida and S. Maruyama, *Chem. Phys. Lett.*, 2004, **387**, 198.
57 G. Abrasonis, M. Krause, A. Mücklich, K. Sedlačková, G. Radnóczi, U. Kreissig, A. Kolitsch and W. Möller, *Carbon*, 2007, **45**, 2995.
58 M. Krause, A. Mücklich, T. W. H. Oates, M. Zschornak, S. Wintz, J. Luis Endrino, C. Baehtz, A. Shalimov, S. Gemming and G. Abrasonis, *Appl. Phys. Lett.*, 2012, **101**, 053112.
59 M. Krause, M. Buljan, A. Mücklich, W. Möller, M. Fritzsche, S. Facsko, R. Heller, M. Zschornak, S. Wintz, J. L. Endrino, C. Baehtz, A. Shalimov, S. Gemming and G. Abrasonis, *Phys. Rev. B: Condens. Matter*, 2014, **89**, 085418.
60 S. Reich, C. Thomsen and J. Maultzsch, *Carbon nanotubes: basic concepts and physical properties*, Wiley-vch, 2004.
61 International center for diffraction data, vol. card 00-004-0850 for fcc Ni, card 01-089-7129 for hexagonal Ni, card 04-007-3753 for rhombohedral nickel carbide, card 01-078-0429 for fcc NiO.
62 G. Abrasonis, A. C. Scheinost, S. Zhou, R. Torres, R. Gago, I. Jiménez, K. Kuepper, K. Potzger, M. Krause, A. Kolitsch, W. Möller, S. Bartkowski, M. Neumann and R. R. Gareev, *J. Phys. Chem. C*, 2008, **112**, 12628.
63 S. Uhlig, R. Struis, H. Schmid-Engel, J. Bock, A.-C. Probst, O. Freitag-Weber, I. Zizak, R. Chernikov and G. Schultes, *Diamond Relat. Mater.*, 2013, **34**, 25.
64 B. W. Yu, Q. K. Zhang, L. Z. Hou, S. L. Wang, M. Song, Y. H. He, H. Huang and J. Zou, *Carbon*, 2016, **96**, 904.
65 D. B. Williams and C. B. Carter, in *Transmission Electron Microscopy: A Textbook for Materials Science*, Springer, US,


 

Boston, MA, 2009, p. 283, DOI: 10.1007/978-0-387-76501-3_18.
66 A. Jorio, A. G. Souza, G. Dresselhaus, M. S. Dresselhaus, A. K. Swan, M. S. Unlu, B. B. Goldberg, M. A. Pimenta, J. H. Hafner, C. M. Lieber and R. Saito, *Phys. Rev. B: Condens. Matter*, 2002, **65**, 155142.
67 R. Pfeiffer, H. Kuzmany, C. Kramberger, C. Schaman, T. Pichler, H. Kataura, Y. Achiba, J. Kurti and V. Zolyomi, *Phys. Rev. Lett.*, 2003, **90**, 225501.
68 P. T. Araujo, S. K. Doorn, S. Kilina, S. Tretiak, E. Einarsson, S. Maruyama, H. Chacham, M. A. Pimenta and A. Jorio, *Phys. Rev. Lett.*, 2007, **98**, 067401.
69 J. Maultzsch, H. Telg, S. Reich and C. Thomsen, *Phys. Rev. B: Condens. Matter*, 2005, **72**, 205438.
70 J. T. Mayer, R. F. Lin and E. Garfunkel, *Surf. Sci.*, 1992, **265**, 102.
71 P. H. Lee and C. C. Chang, *Surf. Sci.*, 2007, **601**, 362.
72 J. B. Zhou, T. Gustafsson, R. F. Lin and E. Garfunkel, *Surf. Sci.*, 1993, **284**, 67.
73 M. Aral, T. Ishikawa and Y. Nishiyama, *J. Phys. Chem.*, 1982, **86**, 577.
74 A. Jorio, A. P. Santos, H. B. Ribeiro, C. Fantini, M. Souza, J. P. M. Vieira, C. A. Furtado, J. Jiang, R. Saito, L. Balzano, D. E. Resasco and M. A. Pimenta, *Phys. Rev. B: Condens. Matter*, 2005, **72**, 075207.
75 C. Zoican Loebick, R. Podila, J. Reppert, J. Chudow, F. Ren, G. L. Haller, A. M. Rao and L. D. Pfefferle, *J. Am. Chem. Soc.*, 2010, **132**, 11125.
76 T. Moteki, D. Nukaga, Y. Murakami, S. Maruyama and T. Okubo, *J. Phys. Chem. C*, 2014, **118**, 23664.
77 R. Sharma, P. Rez, M. M. J. Treacy and S. J. Stuart, *J. Electron Microsc.*, 2005, **54**, 231.
78 M. H. Kuang, Z. L. Wang, X. D. Bai, J. D. Guo and E. G. Wang, *Appl. Phys. Lett.*, 2000, **76**, 1255.



PRL 117, 087401 (2016) PHYSICAL REVIEW LETTERS week ending 19 AUGUST 2016

# Slow Noncollinear Coulomb Scattering in the Vicinity of the Dirac Point in Graphene

J. C. König-Otto,[1,2,*] M. Mittendorff,[3] T. Winzer,[4] F. Kadi,[4] E. Malic,[5] A. Knorr,[4] C. Berger,[6,7] W. A. de Heer,[6] A. Pashkin,[1] H. Schneider,[1] M. Helm,[1,2] and S. Winnerl[1]

[1]*Helmholtz-Zentrum Dresden-Rossendorf, P.O. Box 510119, 01314 Dresden, Germany*
[2]*Technische Universität Dresden, 01062 Dresden, Germany*
[3]*University of Maryland, College Park, Maryland 20742, USA*
[4]*Technische Universität Berlin, Hardenbergstraße 36, 10623 Berlin, Germany*
[5]*Chalmers University of Technology, SE-41296 Göteborg, Sweden*
[6]*Georgia Institute of Technology, Atlanta, Georgia 30332, USA*
[7]*Institut Néel, CNRS-Université Alpes, 38042 Grenoble, France*

(Received 13 November 2015; revised manuscript received 21 March 2016; published 15 August 2016)

The Coulomb scattering dynamics in graphene in energetic proximity to the Dirac point is investigated by polarization resolved pump-probe spectroscopy and microscopic theory. Collinear Coulomb scattering rapidly thermalizes the carrier distribution in $\boldsymbol{k}$ directions pointing radially away from the Dirac point. Our study reveals, however, that, in almost intrinsic graphene, full thermalization in all directions relying on noncollinear scattering is much slower. For low photon energies, carrier-optical-phonon processes are strongly suppressed and Coulomb mediated noncollinear scattering is remarkably slow, namely on a ps time scale. This effect is very promising for infrared and THz devices based on hot carrier effects.

DOI: 10.1103/PhysRevLett.117.087401

Coulomb scattering is a nonlinear many-body effect that transforms a nonequilibrium carrier distribution in a semiconductor into a hot Fermi-Dirac distribution [1]. In the gapless semiconductor graphene with linear energy dispersion, Coulomb scattering is known to be particularly strong [2–6]. A large number of both degenerate and multicolor pump-probe experiments, nonlinear THz spectroscopy, time-resolved photocurrent measurements, and time-resolved angle-resolved photoelectron emission spectroscopy (tr-ARPES) have provided detailed insights into the carrier dynamics of graphene [7–15]. Together with theoretical studies, they revealed that carriers typically thermalize on a sub-100 fs time scale [8,11,16]. This rapid transition from a nonequilibrium distribution to a hot thermalized distribution is mediated by both Coulomb scattering and scattering via optical phonons. These two processes have, so far, not been disentangled as they typically occur on the same time and energy scales [8,12,17]. However, when not just the electron energy, but also the angular distribution in $\boldsymbol{k}$ space is considered, it has been found that the distribution, in fact, thermalizes rapidly along all $\boldsymbol{k}$ directions radially pointing away from the Dirac point. In contrast, the thermalization between different $\boldsymbol{k}$ directions is considerably slower. This angular thermalization that is mediated mainly by efficient optical-phonon scattering is completed only after 150 fs [18–22]. In these studies, an initial anisotropic electron distribution is generated by pumping with linearly polarized radiation [2,21,23]. This anisotropy is linked to pseudospin flipping in interband transitions [24,25].

In this Letter, we utilize this anisotropy to trace the temporal and directional characteristics of pure Coulomb scattering in the vicinity of the Dirac point. To this end, we apply a photon energy of 88 meV that is well below the optical phonon energy (∼200 meV) so that scattering via optical phonons is strongly suppressed. In order to ensure that scattering of the thermalized carrier distribution with optical phonons is also negligible, the study is carried out at low temperature and low enough fluences. Acoustic phonon scattering takes place on a longer, 100 ps time scale. Both the experiments and the theory reveal that, in this regime, angular thermalization characterized by an isotropic distribution is approached remarkably slowly, namely on a ps time scale.

The pump-probe experiments presented here are carried out in transmission geometry on epitaxial multilayer graphene (∼50 layers), which was grown on the C face of 4H-SiC. Explicitly, the layers are rotationally stacked, so that each layer has the electronic structure of graphene [26,27]. The sample was kept at 20 K, and differential transmission signals (DTSs) were recorded. In our degenerate pump-probe experiments, the free-electron laser FELBE provides radiation at a photon energy of 88 meV (pulse duration 4 ps, repetition rate 13 MHz). At this photon energy, the measured signals stem predominantly from interband transitions in the almost intrinsic graphene layers ($|E_f| = 10$–$20$ meV), and only negligible contributions from intraband absorption are expected [28–30]. The probe-beam polarization is set to 45° with respect to the polarization of the pump beam by a grating polarizer on a polymer foil. Polarizers mounted in front of a mercury cadmium telluride detector, with orientation parallel or perpendicular to the pump beam polarization, allow one to measure the pump-induced transmission for

 

PRL 117, 087401 (2016) PHYSICAL REVIEW LETTERS week ending 19 AUGUST 2016

$\boldsymbol{E}_{\mathbf{probe}} \| \boldsymbol{E}_{\mathbf{pump}}$ and $\boldsymbol{E}_{\mathbf{probe}} \perp \boldsymbol{E}_{\mathbf{pump}}$, respectively. Normal incidence on the sample is used for the probe beam, while the pump beam is offset with respect to the probe beam by a small angle. We also performed a two-color experiment, where a Ti:sapphire laser synchronized to FELBE [31] with a jitter of 5 ps is employed for pumping at a photon energy of 1.5 eV (pulse duration 3 ps, repetition rate 78 MHz) while probing at 88 meV. Also, in this experiment, the response is dominated by interband transitions in the almost intrinsic graphene layers.

In our theoretical investigation, we solve the graphene Bloch equations based on the Heisenberg equation of motion in Born-Markov approximation [32–34]. By accounting for the semiclassical light-matter, carrier-carrier, and carrier-phonon interactions on a consistent microscopic footing, we are able to realistically model the carrier dynamics resolved in time, energy, and momentum angle without any adjustable parameter [2]. The screening of the Coulomb interaction is treated within the static limit of the Lindhard equation [1]. Dynamical screening [5,35] yields very similar results due to the induced broadening of the phase space for collinear scattering and the resulting softening of the strict energy conservation [36]. The latter has been included in a self-consistent procedure taking into account the finite lifetime of two-particle correlations for electrons or phonons [36,37].

In Fig. 1(a), we show schematically, the expected results for the angle-dependence of the optically induced population $\rho$ without scattering or saturation effects. It shows a clear anisotropy and follows a $\rho \sim |\sin(\Phi_k)|^2$ dependence featuring nodes at $\Phi_k = 0$ (and $\pi$), where $\Phi_k$ is the angle between the amplitude of the pump beam $\boldsymbol{E}_{\mathbf{pump}}$ and the $\boldsymbol{k}$ vector of electrons (defined as the relative momentum with respect to the Dirac point) [2]. In the following, the states around $\Phi_k = \pi/2$ (and $3\pi/2$) with respect to the pump beam will be referred to as antinode states and the states around $\Phi_k = 0$ (and $\pi$) as node states. Because of Pauli blocking, the $\boldsymbol{E}_{\mathbf{probe}} \| \boldsymbol{E}_{\mathbf{pump}}$ ($\boldsymbol{E}_{\mathbf{probe}} \perp \boldsymbol{E}_{\mathbf{pump}}$) configuration preferentially probes the antinode (node) states. Before discussing the experimental findings of the degenerate pump-probe experiments in detail, the main aspects of the involved physics are briefly highlighted. For energies below the optical phonon energy, Coulomb interaction is expected to be the main scattering mechanism. This involves both intraband and interband (Auger-type) processes [cf. Fig. 1(b)]. Coulomb scattering in graphene is predominantly collinear, as $|V|^2 \propto (1 + \cos\phi_1)(1 + \cos\phi_2)$, where $V$ is the intraband Coulomb matrix element and $\phi_i$ is the angle between the momenta of initial and final state of two scattering electrons $i = 1, 2$ [21,38]. That means the scattering cross section is maximal for collinear processes ($\phi_i = 0$), decreases with increasing scattering angle, and vanishes for back-scattering ($\phi_i = \pi$). In a degenerate pump-probe experiment at 88 meV, i.e. well below the optical phonon threshold,

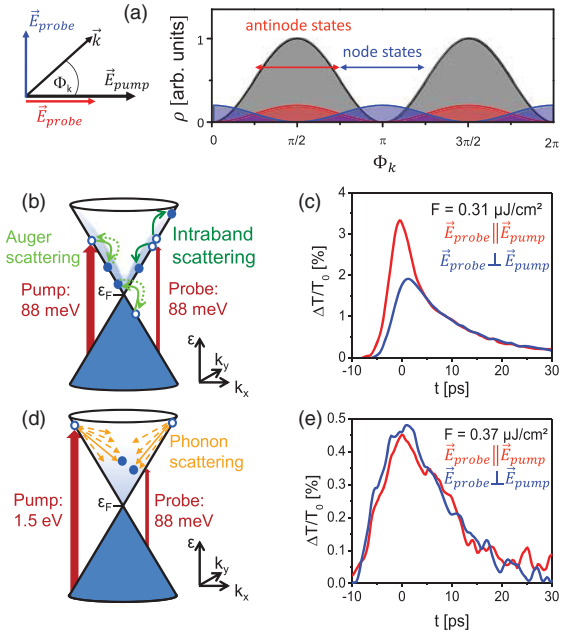


FIG. 1. (a) Schematic of the angular dependence of the occupation of optically excited carriers in the conduction band at the energy $\hbar\omega/2 = 44$ meV excited by the pump beam (black), a probe beam copolarized to the pump beam (red), and cross-polarized to the pump beam (blue). Schematic representation of the single-color (b) and two-color (d) experiments with important scattering mechanisms. Pump-induced transmission change for probing the antinode (red curves) and node states (blue curves), respectively, for the single-color (c) and two-color (e) experiments.

the different DTS for the two orthogonal probe pulse polarizations confirm that an anisotropic distribution persists for several ps [cf. Fig. 1(c)]. This is direct evidence that noncollinear scattering has not led to an angular thermalization. In contrast, pumping at 1.5 eV but with almost similar pulse duration and fluence enables scattering via optical phonons [cf. Fig. 1(d)]. As a result, the distribution probed at a photon energy of 88 meV is isotropic for all delay times [cf. Fig. 1(e)]. This comparison of single-color and two-color experimental results unambiguously shows that the dynamics in the vicinity of the Dirac point contains important aspects that are beyond the widely applied thermodynamic understanding of the carrier dynamics in graphene. The thermodynamic model implies thermalization on a sub-100 fs time scale and subsequent cooling (see, also, Supplemental Material [39]). Consequently, the induced transmission on time scales longer than 100 fs depends only on pump fluence, but not on pump photon energy. Many recent tr-ARPES and pump-probe experiments can be described very well by the thermodynamic model [11,15,17,49]. In these experiments, ultrafast thermalization is ensured by the excitation conditions, leading to both strong Coulomb and electron-phonon scattering. Our experiments show, however, that this is

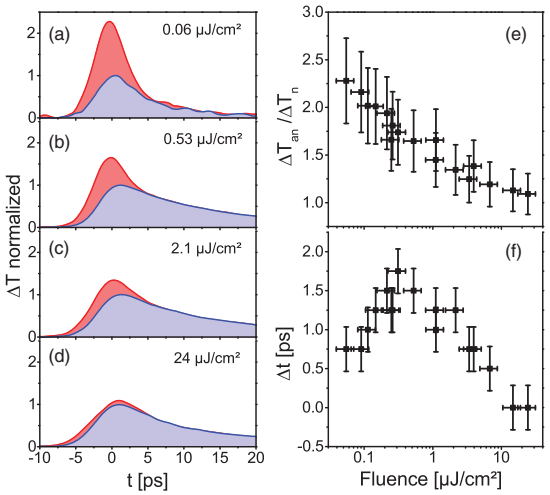


FIG. 2. (a)–(d) Single-color differential transmission for probing the antinode (red curves) and node (blue curves) states, respectively, normalized to the peak value obtained for probing the node states for different pump fluences. (e) Fluence dependence of the maximal induced transmission change for probing the antinode states divided by the maximal induced transmission change for probing the node states. (f) Fluence dependence of the temporal shift of the maximum induced transmission for probing the node states with respect to the maximum obtained for probing the antinode states.

not a general case. Comparably long time scales (few ps) for Coulomb scattering and a strong angular dependence of Coulomb scattering have also been predicted in a study on the impact-excitation of extrinsic electrons in graphene [38].

Next, for low-energy excitations, the carrier dynamics is investigated in a wide range of fluences. At low fluences, the induced maximum transmission change for probing the antinode states is about 2.3 times larger than for probing the node states, as shown in Figs. 2(a) and 2(e). In the absence of scattering, or for purely collinear scattering, one would expect a factor of 3 [18]. With increasing fluence, the ratio between the maximum transmission obtained for probing the antinode and node states $\Delta T_{an}/\Delta T_n$ asymptotically approaches the value 1, corresponding to a completely angularly thermalized distribution. Apart from the signal amplitudes, the temporal positions of the signal maxima for the two probing conditions also feature a pronounced fluence dependence [see Figs. 2(a)–2(d) and 2(f)]. The peaks for the two probe polarizations occur almost at the same time when low and high fluences are applied. At intermediate fluences ($\sim 0.3\ \mu J/cm^2$), the signal probing the node states is delayed by about 1.6 ps with respect to the signal probing the antinode states. To understand this phenomenon, it is instructive to discuss three different fluence regimes: low, intermediate, and high. The Coulomb scattering rate scales with the number of available scattering partners, which, in turn, scales with the applied pump fluence. For low fluences, noncollinear Coulomb scattering is most inefficient resulting in $\Delta T_{an}/\Delta T_n \approx 3$. In the absence of noncollinear scattering, the signal for probing the node states stems from optically excited carriers around $\Phi_k = \pi/4$ [and $3\pi/4$, $5\pi/4$, … cf. Fig. 1(a)]; consequently, there is no time delay between the signals for probing the node and antinode states. At intermediate fluences, noncollinear scattering becomes relevant, resulting in reduced values for $\Delta T_{an}/\Delta T_n$ and in a delayed maximum for probing the node states. This delay indicates the transfer of carriers from antinode states to node states. Finally, in the high-fluences regime, full thermalization occurs on time scales beyond the resolution of the experiment. This results in basically identical DTSs for probing antinode and node states, respectively. Naturally, these curves feature similar amplitudes and similar temporal positions of the maxima.

Note that saturation of pump-probe signals due to phase space filling can also affect the amplitude and temporal position of the induced transmission maxima. However, while the latter effect can qualitatively explain the reduction of the anisotropy with increasing fluence, it cannot explain the peculiar shift of the maximum for probing the node states. We have also performed polarization-resolved experiments at elevated temperatures up to room temperature. For temperatures above 100 K, the decay of the signal becomes fast and the amplitude drops rapidly (see, also, [29]) resulting in a decreased signal-to-noise ratio that does not allow one to trace the noncollinear scattering contribution over a large range of fluences. Nevertheless, we could not find any indication that the dynamics of the noncollinear Coulomb scattering are influenced by the substrate temperature up to 300 K (for more details, see the Supplemental Material [39]).

For a detailed insight into the relaxation dynamics and, also, for a clear separation of the saturation effect from noncollinear scattering, microscopic modeling is applied. The modeling is performed for an intrinsic graphene monolayer, nevertheless, the results are still valid for the more complex sample structure used in the experiment. For more information, see the Supplemental Material [39]. For directly visualizing the carrier dynamics, the carrier occupations along the direction of the center of the antinodes (center of the nodes) corresponding to $\boldsymbol{k} \perp \boldsymbol{E}_{\mathbf{pump}}$ ($\boldsymbol{k} \| \boldsymbol{E}_{\mathbf{pump}}$) are depicted in Fig. 3 for two fluences in a range where the largest qualitative differences are found. At low fluences and early times, the optically generated carriers at an energy of $\hbar\omega/2 = 44$ meV are clearly visible in the occupation along $\Phi_k = \pi/2$. However, a hot distribution is reached rapidly along the respective $\Phi_{\mathbf{k}}$ direction due to efficient collinear scattering. As noncollinear scattering is less efficient, the distribution remains anisotropic on a time scale of several ps. For higher pump fluences, cf. Figs. 3(d)–3(f), both collinear and noncollinear Coulomb scattering becomes more efficient. As a result, thermalization along a particular $\Phi_{\mathbf{k}}$ direction is considerably faster, and an almost isotropic

PRL 117, 087401 (2016) PHYSICAL REVIEW LETTERS week ending 19 AUGUST 2016

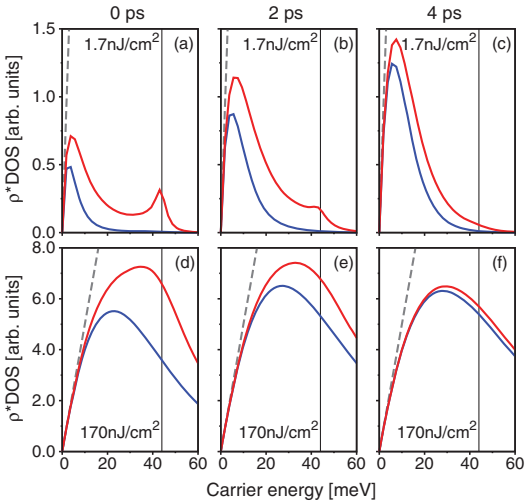


FIG. 3. (a)–(f) Carrier occupation multiplied by the density of states for three different times (time zero corresponds to maximum intensity of the pump pulse) and two different pump fluences. Red curves correspond to the $\boldsymbol{k}$ direction $\boldsymbol{k}\perp\boldsymbol{E}_{\mathbf{pump}}$ ($\Phi_k = \pi/2$), blue curves to $\boldsymbol{k}\|\boldsymbol{E}_{\mathbf{pump}}$ ($\Phi_k = 0$). The solid line denotes the energy $\hbar\omega/2$, the dashed line half-filling of the available states.

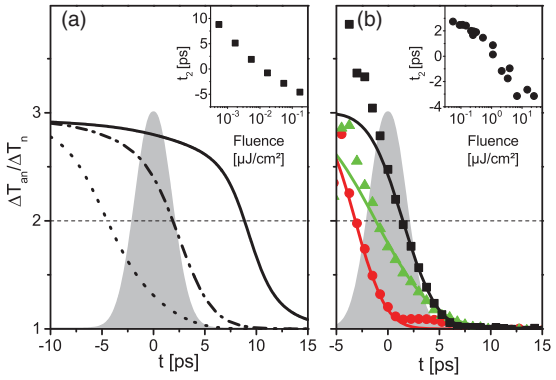


FIG. 4. The decay of the ratio $\Delta T_{an}/\Delta T_n$ is depicted for different fluences. (a) theoretical data: 171 nJ/cm$^2$ dotted line; 5.4 nJ/cm$^2$ dotted-dashed line; 0.54 nJ/cm$^2$ solid line. (b) experimental data: 24 $\mu$J/cm$^2$ circle; 2.1 $\mu$J/cm$^2$ triangle; 0.5 $\mu$J/cm$^2$ square. The gray shaded areas indicate the pump pulse. For the experimental data in (b), fit curves based on an error function that were used to extract the value of $t_2$ are shown. In the insets, the time $t_2$ ascribed to the half-way decay of the optically induced anisotropy is shown over the fluence.

distribution is reached within ~4 ps. Note that, even for high fluences, the occupation numbers at the probe energy of 44 meV are well below half-filling of available states. Therefore, saturation effects can be ruled out as the main mechanism of the observed dynamics.

With increasing pump fluence, the temperature of the thermalized electrons increases. Consequently, electronic states above 200 meV also eventually become populated and, thus, emission of optical phonons may contribute to the relaxation dynamics [29]. To investigate the strength of this effect, the DTS curves are calculated for the full dynamics and for the dynamics without phonons. The differences are negligible, a detailed comparison is shown in the Supplemental Material [39]. In summary, those calculations, together with the extraordinary lifetime of the anisotropy compared to experiments in the near infrared [18,20] and the comparison of the two color and the degenerate pump probe experiment [cf. Figs. 2(c) and 2(e)], prove that noncollinear Coulomb scattering is the only remaining relaxation channel to reduce the anisotropy. This channel can be effectively controlled and studied by the variation of the pump fluence.

Finally, we quantitatively investigate the decay of the anisotropic carrier distribution into a thermalized distribution and compare experiment and theory. To this end, the temporal evolution of the ratio between the induced transmissions for probing the antinode and node states, respectively, $\Delta T_{an}/\Delta T_n$ is evaluated for both experimental and theoretical data (see Fig. 4). Starting from a value of 3, corresponding to the optically excited nonequilibrium distribution, the ratio $\Delta T_{an}/\Delta T_n$ drops to the value of 1, characterizing the isotropic thermalized distribution. While the overall shape of this ratio as a function of time depends only weakly on fluence, the point in time at which the distribution loses its anisotropic character depends strongly on fluence. For low fluences, the anisotropic distribution persists until the pump pulse has vanished, while for high fluences, a significant loss in anisotropy occurs already during the rising edge of the pulse [cf. Fig. 4(a)]. The experimental dynamics [cf. Fig. 4(b)] is qualitatively very similar to the theoretically predicted one. Since, for early times, the signal is small compared to the noise, the ratio $\Delta T_{an}/\Delta T_n$ at those times is instable as one essentially divides by zero. Note that a significant part of the dynamics occurs during the pump pulse; hence, there is a balance of refreshing the anisotropic distribution by optical pumping and a decay of the anisotropy by noncollinear scattering. For a quantitative comparison, the time $t_2$ at which the distribution is half-way angularly thermalized (i.e., $\Delta T_{an}/\Delta T_n = 2$), is extracted from both the theoretical and experimental data [cf. insets of Figs. 4(a) and 4(b)]. In both experiment and theory, $t_2$ is positive for small fluences, reflecting a pronounced anisotropic distribution after the excitation pulse maximum. Increasing noncollinear Coulomb scattering by applying higher fluences results in a reduction of $t_2$ down to values corresponding to the very front of the excitation pulse ($\sim -4$ ps). However, there is a notable offset between the theoretical and the experimental data; i.e., higher fluences are required in the experiment to achieve similar effects. This might be ascribed to an overestimation of the fluence in the experiment since the fluence is reduced for the layers underneath the top layer. Furthermore, there is an uncertainty in the determination of the temporal position of the pump-pulse

maximum. Last, but not least, it has to be considered that no adjustable parameters are used in the comparison.

The comparably long time for angular thermalization is expected to be advantageous for infrared and THz device applications based on hot carriers such as fast detectors and modulators [50–52]. To improve the efficiency of such devices, the higher electron temperature in the direction perpendicular to the direction of the polarization can be exploited by applying appropriate electrode geometries. The relaxation time on the ps time scale is attractive as it is long enough to result in a significant contribution to the extractable signal of such devices. On the other hand, the ps time scale is fast enough to prevent a deterioration of the operation speed of the device, resulting in a high temporal resolution. Anisotropic photoconductive effects have been observed for excitation with visible radiation [53]. Our study suggests that this effect should be much larger for photon energies below the optical phonon energy. Besides its fundamental importance, the present study is of particular relevance for gated devices, where the Fermi level is shifted to the charge neutrality point [54,55]. Furthermore, our calculations predict that an anisotropic carrier distribution on a ps time scale can also be observed in doped graphene; however, in this case, the pump-induced change in transmission is much smaller (see Supplemental Material [39]). These preliminary results suggest that our main findings may also be relevant for devices employing doped graphene. For all the mentioned device applications, it is highly attractive that anisotropic carrier distribution also persists at room temperature.

In conclusion, our study has revealed that low energy Coulomb scattering in almost intrinsic graphene exhibits an unusual twofold nature: It rapidly thermalizes the distribution along all $\boldsymbol{k}$ directions pointing radially away from the Dirac point, while preserving the optically induced anisotropy on a ps time scale. This effect is attractive for optoelectronic devices based on hot carriers.

We thank P. Michel and the ELBE-team for their dedicated support. This work was financially supported by the SPP 1459 (S. W., E. M.) and SfB 910 (A. K.) of the DFG. E. M. and C. B. also acknowledge financial support from the EU Graphene Flagship and E. M. from the Swedish Research Council (Grant No. 604391). W. d. H. acknowledges support from the AFOSR. We thank H. Mittenzwey, who acknowledges support from GRK 1558 of the DFG, for his help.

*j.koenig-otto@hzdr.de

[1] R. Binder, D. Scott, A. E. Paul, M. Lindberg, K. Henneberger, and S. W. Koch, Phys. Rev. B **45**, 1107 (1992).
[2] E. Malic, T. Winzer, E. Bobkin, and A. Knorr, Phys. Rev. B **84**, 205406 (2011).
[3] T. Plötzing, T. Winzer, E. Malic, D. Neumaier, A. Knorr, and H. Kurz, Nano Lett. **14**, 5371 (2014).
[4] B. Y. Sun, Y. Zhou, and M. W. Wu, Phys. Rev. B **85**, 125413 (2012).
[5] A. Tomadin, D. Brida, G. Cerullo, A. C. Ferrari, and M. Polini, Phys. Rev. B **88**, 035430 (2013).
[6] M. Mittendorff, F. Wendler, E. Malic, A. Knorr, M. Orlita, M. Potemski, C. Berger, W. A. de Heer, H. Schneider, M. Helm, and S. Winnerl, Nat. Phys. **11**, 75 (2015).
[7] J. M. Dawlaty, S. Shivaraman, M. Chandrashekhar, F. Rana, and M. G. Spencer, Appl. Phys. Lett. **92**, 042116 (2008).
[8] M. Breusing, S. Kuehn, T. Winzer, E. Malic, F. Milde, N. Severin, J. P. Rabe, C. Ropers, A. Knorr, and T. Elsaesser, Phys. Rev. B **83**, 153410 (2011).
[9] P. A. Obraztsov, M. G. Rybin, A. V. Tyurnina, S. V. Garnov, E. D. Obraztsova, A. N. Obraztsov, and Y. P. Svirko, Nano Lett. **11**, 1540 (2011).
[10] K. J. Tielrooij, J. C. W. Song, S. A. Jensen, A. Centeno, A. Pesquera, A. Zurutuza Elorza, M. Bonn, L. S. Levitov, and F. H. L. Koppens, Nat. Phys. **9**, 248 (2013).
[11] Z. Mics, K.-J. Tielrooij, K. Parvez, S. A. Jensen, I. Ivanov, X. Feng, K. Müllen, M. Bonn, and D. Turchinovich, Nat. Commun. **6**, 7655 (2015).
[12] S. A. Jensen, Z. Mics, I. Ivanov, H. S. Varol, D. Turchinovich, F. H. L. Koppens, M. Bonn, and K. J. Tielrooij, Nano Lett. **14**, 5839 (2014).
[13] K. J. Tielrooij, L. Piatkowski, M. Massicotte, A. Woessner, Q. Ma, Y. Lee, K. S. Myhro, C. N. Lau, P. Jarillo-Herrero, N. F. van Hulst, and F. H. L. Koppens, Nat. Nanotechnol. **10**, 437 (2015).
[14] J. C. Johannsen, S. Ulstrup, F. Cilento, A. Crepaldi, M. Zacchigna, C. Cacho, I. C. E. Turcu, E. Springate, F. Fromm, C. Raidel, T. Seyller, F. Parmigiani, M. Grioni, and P. Hofmann, Phys. Rev. Lett. **111**, 027403 (2013).
[15] I. Gierz, J. C. Petersen, M. Mitrano, C. Cacho, I. C. E. Turcu, E. Springate, A. Stöhr, A. Köhler, U. Starke, and A. Cavalleri, Nat. Mater. **12**, 1119 (2013).
[16] I. Gierz, F. Calegari, S. Aeschlimann, M. Chávez Cervantes, C. Cacho, R. T. Chapman, E. Springate, S. Link, U. Starke, C. R. Ast, and A. Cavalleri, Phys. Rev. Lett. **115**, 086803 (2015).
[17] I. Gierz, S. Link, U. Starke, and A. Cavalleri, Faraday Discuss. **171**, 311 (2014).
[18] M. Mittendorff, T. Winzer, E. Malic, A. Knorr, C. Berger, W. A. de Heer, H. Schneider, M. Helm, and S. Winnerl, Nano Lett. **14**, 1504 (2014).
[19] X.-Q. Yan, J. Yao, Z.-B. Liu, X. Zhao, X.-D. Chen, C. Gao, W. Xin, Y. Chen, and J.-G. Tian, Phys. Rev. B **90**, 134308 (2014).
[20] M. Trushin, A. Grupp, G. Soavi, A. Budweg, D. De Fazio, U. Sassi, A. Lombardo, A. C. Ferrari, W. Belzig, A. Leitenstorfer, and D. Brida, Phys. Rev. B **92**, 165429 (2015).
[21] E. Malic, T. Winzer, and A. Knorr, Appl. Phys. Lett. **101**, 213110 (2012).
[22] A. Satou, V. Ryzhii, and T. Otsuji, J. Phys. Conf. Ser. **584**, 012018 (2015).
[23] A. Grüneis, R. Saito, G. G. Samsonidze, T. Kimura, M. A. Pimenta, A. Jorio, A. G. Souza Filho, G. Dresselhaus, and M. S. Dresselhaus, Phys. Rev. B **67**, 165402 (2003).

[24] M. Trushin and J. Schliemann, Europhys. Lett. **96**, 37006 (2011).

[25] T. J. Echtermeyer, P. S. Nene, M. Trushin, R. V. Gorbachev, A. L. Eiden, S. Milana, Z. Sun, J. Schliemann, E. Lidorikis, K. S. Novoselov, and A. C. Ferrari, Nano Lett. **14**, 3733 (2014).

[26] C. Berger, Z. Song, X. Li, X. Wu, N. Brown, C. Naud, D. Mayou, T. Li, J. Hass, A. N. Marchenkov, E. H. Conrad, P. N. First, and W. A. de Heer, Science **312**, 1191 (2006).

[27] M. Sprinkle, D. Siegel, Y. Hu, J. Hicks, A. Tejeda, A. Taleb-Ibrahimi, P. Le Fèvre, F. Bertran, S. Vizzini, H. Enriquez, S. Chiang, P. Soukiassian, C. Berger, W. A. de Heer, A. Lanzara, and E. H. Conrad, Phys. Rev. Lett. **103**, 226803 (2009).

[28] D. Sun, Z.-K. Wu, C. Divin, X. Li, C. Berger, W. A. de Heer, P. N. First, and T. B. Norris, Phys. Rev. Lett. **101**, 157402 (2008).

[29] S. Winnerl, M. Orlita, P. Plochocka, P. Kossacki, M. Potemski, T. Winzer, E. Malic, A. Knorr, M. Sprinkle, C. Berger, W. A. de Heer, H. Schneider, and M. Helm, Phys. Rev. Lett. **107**, 237401 (2011).

[30] F. Kadi, T. Winzer, E. Malic, A. Knorr, F. Göttfert, M. Mittendorff, S. Winnerl, and M. Helm, Phys. Rev. Lett. **113**, 035502 (2014).

[31] J. Bhattacharyya, M. Wagner, S. Zybell, S. Winnerl, D. Stehr, M. Helm, and H. Schneider, Rev. Sci. Instrum. **82**, 103107 (2011).

[32] M. Lindberg and S. W. Koch, Phys. Rev. B **38**, 3342 (1988).

[33] A. Knorr, S. Hughes, T. Stroucken, and S. W. Koch, Chem. Phys. **210**, 27 (1996).

[34] E. Malic and A. Knorr, *Graphene and Carbon Nanotubes: Ultrafast Optics and Relaxation Dynamics*, 1st ed. (Wiley-VCH, Weinheim, Germany, 2013).

[35] F. Kadi, T. Winzer, A. Knorr, and E. Malic, Sci. Rep. **5**, 16841 (2015).

[36] T. Winzer and E. Malic, J. Phys. Condens. Matter **25**, 054201 (2013).

[37] J. Schilp, T. Kuhn, and G. Mahler, Phys. Rev. B **50**, 5435 (1994).

[38] J. C. W. Song, K. J. Tielrooij, F. H. L. Koppens, and L. S. Levitov, Phys. Rev. B **87**, 155429 (2013).

[39] See Supplemental Material at http://link.aps.org/supplemental/10.1103/PhysRevLett.117.087401 for a discussion about substrate temperature, doping, role of optical phonons, sample geometry and a comparison of our results to a thermodynamic model, which includes Refs. [40–48].

[40] H. Choi, F. Borondics, D. A. Siegel, S. Y. Zhou, M. C. Martin, A. Lanzara, and R. A. Kaindl, Appl. Phys. Lett. **94**, 172102 (2009).

[41] M. Orlita, C. Faugeras, P. Plochocka, P. Neugebauer, G. Martinez, D. K. Maude, A.-L. Barra, M. Sprinkle, C. Berger, W. A. de Heer, and M. Potemski, Phys. Rev. Lett. **101**, 267601 (2008).

[42] A. Matkovic, A. Beltaos, M. Milicevic, U. Ralevic, B. Vasic, D. Jovanovic, and R. Gajic, J. Appl. Phys. **112**, 123523 (2012).

[43] S.-F. Shi, T.-T. Tang, B. Zeng, L. Ju, Q. Zhou, A. Zettl, and F. Wang, Nano Lett. **14**, 1578 (2014).

[44] C. B. McKitterick, D. E. Prober, and M. J. Rooks, Phys. Rev. B **93**, 075410 (2016).

[45] S. Bae, H. Kim, Y. Lee, X. Xu, J.-S. Park, Y. Zheng, J. Balakrishnan, T. Lei, H. Ri Kim, Y. I. Song, Y.-J. Kim, K. S. Kim, B. Özyilmaz, J.-H. Ahn, B. H. Hong, and S. Iijima, Nat. Nanotechnol. **5**, 574 (2010).

[46] S. Mammadov, J. Ristein, R. J. Koch, M. Ostler, C. Raidel, M. Wanke, R. Vasiliauskas, R. Yakimova, and T. Seyller, 2D Mater. **1**, 035003 (2014).

[47] T. Stroucken, A. Knorr, P. Thomas, and S. W. Koch, Phys. Rev. B **53**, 2026 (1996).

[48] M. T. Mihnev, J. R. Tolsma, C. J. Divin, D. Sun, R. Asgari, M. Polini, C. Berger, W. A. de Heer, A. H. MacDonald, and T. B. Norris, Nat. Commun. **6**, 8105 (2015).

[49] I. Ivanov, M. Bonn, Z. Mics, and D. Turchinovich, Europhys. Lett. **111**, 67001 (2015).

[50] B. Sensale-Rodriguez, R. Yan, M. M. Kelly, T. Fang, K. Tahy, W. S. Hwang, D. Jena, L. Liu, and H. G. Xing, Nat. Commun. **3**, 780 (2012).

[51] M. Mittendorff, J. Kamann, J. Eroms, D. Weiss, C. Drexler, S. D. Ganichev, J. Kerbusch, A. Erbe, R. J. Suess, T. E. Murphy, S. Chatterjee, K. Kolata, J. Ohser, J. C. König-Otto, H. Schneider, M. Helm, and S. Winnerl, Opt. Express **23**, 28728 (2015).

[52] K. J. Tielrooij, M. Massicotte, L. Piatkowski, A. Woessner, Q. Ma, P. Jarillo-Herrero, N. F. van Hulst, and F. H. L. Koppens, J. Phys. Condens. Matter **27**, 164207 (2015).

[53] M. Kim, H. Ang Yoon, S. Woo, D. Yoon, S. Wook Lee, and H. Cheong, Appl. Phys. Lett. **101**, 073103 (2012).

[54] J. Tong, M. Muthee, S.-Y. Chen, S. K. Yngvesson, and J. Yan, Nano Lett. **15**, 5295 (2015).

[55] F. H. L. Koppens, T. Mueller, P. Avouris, A. C. Ferrari, M. S. Vitiello, and M. Polini, Nat. Nanotechnol. **9**, 780 (2014).

# Statistics

Image: HZDR/N. Klingner

# Publications

## Books and chapters

1. Hlawacek, G.; Gölzhäuser, A. (Eds.)
**Helium Ion Microscopy (NanoScience and Technology)**
Springer Berlin Heidelberg (2016), ISBN 978-3-319-41988-6, 526 pages

2. Cybart, S. A.; Bali, R.; Hlawacek, G.; Röder, F.; Fassbender, J.
**Focused Helium and Neon Ion Beam Modification of High-Tc Superconductors and Magnetic Materials**
Hlawacek, G.; Gölzhäuser, A. (Eds.): Helium Ion Microscopy (NanoScience and Technology), Springer Berlin Heidelberg (2016), ISBN 978-3-319-41988-6, pp. 415-445

3. Makarov, D.; Krone, P.; Albrecht, M.
**Bit-Patterned Magnetic Recording**
Varvaro, G.; Casoli, F. (Eds.): Ultrahigh-Density Magnetic Recording: Storage Materials and Media Designs, Singapore: Pan Stanford Publishing Pte. Ltd. (2016), ISBN 978-9-814-66958-0, pp. 327-384

4. Montoya, E.; Sebastian, T.; Schultheiss, H.; Heinrich, B.; Camley, R. E.; Celinski, Z.
**Magnetization Dynamics**
Camley. R. E.; Celinski, Z.; Stamps, R. L. (Eds.): Magnetism of Surfaces, Interfaces, and Nanoscale Materials, Netherlands: Elsevier (2016), ISBN 978-0-444-62634-9, pp. 113-168

5. Semisalova, A. S.; Orlov, A.; Smekhova, A.; Gan'Shina, E.; Perov, N.; Anwand, W.; Potzger, K.; Lähderanta, E.; Granovsky, A.
**Above Room Temperature Ferromagnetism in Dilute Magnetic Oxide Semiconductors**
Zhukov, A. (Ed.): Novel Functional Magnetic Materials. Fundamentals and Applications. Springer Series in Materials Science **231**, Switzerland: Springer International Publishing (2016), ISBN 978-3-319-26104-1, pp. 187-219

## Publications in journals

### *Magnetism*

1. Aleksandrov, Y.; Fowley, C.; Kowalska, E.; Sluka, V.; Yildirim, O.; Lindner, J.; Ocker, B.; Fassbender, J.; Deac, A. M.
**Evolution of the interfacial magnetic anisotropy in MgO/CoFeB/Ta/Ru based multilayers as a function of annealing temperature**
AIP Advances **6**, 065321 (2016)

2. Arora, M.; Fowley, C.; Mckinnon, T.; Kowalska, E.; Sluka, V.; Deac, A. M.; Heinrich, B.; Girt, E.
**Spin torque switching in nanopillars with antiferromagnetic reference layer**
IEEE Magnetics Letters **8**, 3100605 (2016)

3. Awari, N.; Kovalev, S.; Fowley, C.; Rode, K.; Gallardo, R. A.; Lau, Y.-C.; Betto, D.; Thiyagarajah, N.; Green, B.; Yildrim, O.; Lindner, J.; Fassbender, J.; Coey, J. M. D.; Deac, A. M.; Gensch, M.
**Narrow-band tunable terahertz emission from ferrimagnetic $Mn_{3-x}Ga$ thin films**
Applied Physics Letters **109**, 032403 (2016)

4. Borisov, K.; Betto, D.; Lau, Y. C.; Fowley, C.; Titova, A.; Thiyagarajah, N.; Atcheson, G.; Lindner, J.; Deac, A. M.; Coey, J. M. D.; Stamenov, P.; Rode, K.
**Tunnelling magnetoresistance of the half-metallic compensated ferrimagnet $Mn_2Ru_xGa$**
Applied Physics Letters **108**, 19240 (2016)

5. Bouzerar, R.; May, D.; Löw, U.; Machon, D.; Melinon, P.; Zhou, S.; Bouzerar, G.
**Carrier-induced ferromagnetism in the insulating Mn-doped III-V semiconductor InP**
Physical Review B **94**, 094437 (2016)

6. Kravchuk, V. P.; Rößler, U. K.; Volkov, O. M.; Sheka, D. D.; van den Brink, J.; Makarov, D.; Fangohr, H.; Gaididei, Y.
**Topologically stable magnetization states on a spherical shell: curvature stabilized skyrmion**
Physical Review B **94**, 144402 (2016)

7. Langer, M.; Wagner, K.; Sebastian, T.; Hübner, R.; Grenzer, J.; Wang, Y.; Kubota, T.; Schneider, T.; Stienen, S.; Linder, J.; Lenz, K.; Linder, J.; Takanashi, K.; Arias, R.; Fassender, J.
**Parameter-free determination of the exchange constant in thin films using magnonic patterning**
Applied Physics Letters **108**, 102402 (2016)

8. Lin, G.; Karnaushenko, D. D.; Canon Bermudez, G. S.; Schmidt, O. G.; Makarov, D.
**Magnetic Suspension Arrays Technology: Controlled Synthesis and Screening in Microfluidic Networks**
Small **12**, 4553 (2016)

9. Makarov, D.; Melzer, M.; Karnaushenko, D.; Schmidt, O. G.
**Shapeable magnetoelectronics**
Applied Physics Reviews **3**, 011101 (2016)

10. Münzenrieder, N.; Karnaushenko, D.; Petti, L.; Cantarella, G.; Vogt, C.; Büthe, L.; Karnaushen, D. D.; Schmidt, O. G.; Makarov, D.; Tröster, G.
**Entirely flexible on-site conditioned magnetic sensorics**
Advanced Electronic Materials **2**, 1600188 (2016)

11. Otálora, A. S.; Yan, M.; Schultheiss, H.; Hertel, R.; Kákay, A.
**Curvature-Induced Asymmetric Spin-Wave Dispersion**
Physical Review Letters **117**, 227203 (2016)

12. Pylypovskyi, O. V.; Sheka, D. D.; Kravchuk, V. P.; Yershov, K. V.; Makarov, D.; Gaididei, Y.
**Rashba Torque Driven Domain Wall Motion in Magnetic Helices**
Scientific Reports **6**, 23316 (2016)

13. Streubel, R.; Fischer, P.; Kronast, F.; Kravchuk, V. P.; Sheka, D. D.; Gaididei, Y.; Schmidt, O. G.; Makarov, D.
**Magnetism in curved geometries**
Journal of Physics D: Applied Physics **49**, 363001 (2016)

14. Takahashi, Y. K.; Medapalli, R.; Kasai, S.; Wang, J.; Ishioka, K.; Wee, S. H.; Hellwig, O.; Hono, K.; Fullerton, E. E.
**Accumulative Magnetic Switching of Ultrahigh-Density Recording Media by Circularly Polarized Light**
Physical Review Applied **6**, 054004 (2016)

15. Tsema, Y.; Kichin, G.; Hellwig, O.; Mehta, V.; Kimel, A. V.; Kirilyuk, A.; Rasing, T.
**Helicity and field dependent magnetization dynamics of ferromagnetic Co/Pt multilayers**
Applied Physics Letters **109**, 072405 (2016)

16. Ueltzhöffer, T.; Streubel, R.; Koch, I.; Holzinger, D.; Makarov, D.; Schmidt, O. G.; Ehresmann, A.
**Magnetically patterned rolled-up exchange bias tubes: A paternoster for superparamagnetic beads**
ACS Nano **10**, 8491 (2016)

17. Wagner, K.; Kakay, A.; Schultheiss, K.; Henschke, A.; Sebastian, T.; Schultheiss, H.
**Magnetic domain walls as reconfigurable spin-wave nanochannels**
Nature Nanotechnology **11**, 432 (2016)

18. Wintz, S.; Tiberkevych, V.; Weigand, M.; Raabe, J.; Lindner, J.; Erbe, A.; Slavin, A.; Fassbender, J.
**Magnetic vortex cores as tunable spin wave emitters**
Nature Nanotechnology **11**, 948 (2016)

19. Yuan, Y.; Hübner, R.; Liu, F.; Sawicki, M.; Gordan, O.; Salvan, G.; Zahn, D. R. T.; Banerjee, D.; Baehtz, C.; Helm, M.; Zhou, S.
**Ferromagnetic Mn-Implanted GaP: Microstructures vs Magnetic Properties**
ACS Applied Materials and Interfaces **8**, 3912 (2016)

20. Yildirim, O.; Cornelius, S.; Smekhova, A.; Butterling, M.; Anwand, W.; Wagner, A.; Baehtz, C.; Böttger, R.; Potzger, K.
**Threshold concentration for ion implantation-induced Co nanocluster formation in $TiO_2$:Co thin films**
Nuclear Instruments and Methods in Physics Research B **389-390**, 13 (2016)

21. Zhou, S.; Li, L.; Yuan, Y.; Rushforth, A. W.; Chen, L.; Wang, Y.; Boettger, R.; Heller, R.; Zhao, J.; Edmonds, K. W.; Campion, R. P.; Gallagher, B. L.; Timm, C.; Helm, M.
**Precise tuning of the Curie temperature of (Ga,Mn)As-based magnetic semiconductors by hole compensation: Support for valence-band ferromagnetism**
Physical Review B **95**, 075205 (2016)

### *Nanoscience and materials for information technologies*

22. Bischoff, L.; Mazarov, P.; Bruchhaus, L.; Gierak, J.
**Liquid Metal Alloy Ion Sources - an Alternative for Focused Ion Beam Technology**
Applied Physics Reviews **3**, 021101 (2016)

23. Björkman, T.; Skakalova, V.; Kurasch, S.; Kaiser, U.; Meyer, J. C.; Smet, J. H.; Krasheninnikov, A. V.
**Vibrational properties of a two-dimensional silica Kagome lattice**
ACS Nano **10**, 10929 (2016)

24. Bogusz, A.; Bürger, D.; Skorupa, I.; Schmidt, O. G.; Schmidt, H.
**Bipolar resistive switching in $YMnO_3$/Nb:$SrTiO_3$ pn-heterojunctions**
Nanotechnology **27**, 455201 (2016)

25. Bogusz, A.; Choudhary, O. S.; Skorupa, I.; Bürger, D.; Lawerenz, A.; Lei, Y.; Zeng, H.; Abendroth, B.; Stäcker, H.; Schmidt, O. G.; Schmidt, H.
**Photocapacitive light sensor based on metal-$YMnO_3$-insulator-semiconductor structures**
Applied Physics Letters **108**, 052103 (2016)

26. Dimakis, E.; Balaghi, L.; Tauchnitz, T.; Hübner, R.; Bischoff, L.; Schneider, H.; Helm, M.
**Droplet-confined alternate pulsed epitaxy of GaAs nanowires on Si substrates down to CMOS-compatible temperatures**
Nano Letters **16**, 4032 (2016)

27. El-Said, A. S.; Wilhelm, R. A.; Heller, R.; Akhmadaliev, S.; Schumann, E.; Sorokin, M.; Facsko, S.; Trautmann, C.
**Modifications of gallium phosphide single crystals using slow highly charged ions and swift heavy ions**
Nuclear Instruments and Methods in Physics Research B **382**, 86 (2016)

28. El-Said, A. S.; Wilhelm, R. A.; Heller, R.; Sorokin, M.; Facsko, S.; Aumayr, F.
**Tuning the fabrication of nanostructures by low-energy highly charged ions**
Physical Review Letters **117**, 126101 (2016)

29. Engler, M.; Michely, T.
**Amorphous to crystalline phase transition: onset of pattern formation during ion erosion of Si(001)**
Physical Review B **93**, 085423 (2016)

30. Eßer, F.; Winnerl, S.; Patanè, A.; Helm, M.; Schneider, H.
**Excitonic mobility edge and ultra-short photoluminescence decay time in n-type GaAsN**
Applied Physics Letters **109**, 182113 (2016)

31. Glaser, M.; Kitzler, A.; Johannes, A.; Prucnal, S.; Potts, H.; Conesa-Boj, S.; Filipovic, L.; Kosina, H.; Skorupa, W.; Bertagnolli, E.; Ronning, C.; Fontcuberta I. Morral, A.; Lugstein, A.
**Synthesis, Morphological, and Electro-optical Characterizations of Metal/Semiconductor Nanowire Heterostructures**
Nano Letters **16**, 3507 (2016)

32. Gruber, E.; Wilhelm, R. A.; Petuya, R.; Smejkal, V.; Kozubek, R.; Hierzenberger, A.; Bayer, B. C.; Aldazabal, I.; Kazansky, A. K.; Libisch, F.; Krasheninnikov, A. V.; Schleberger, M.; Facsko, S.; Borisov, A. G.; Arnau, A.; Aumayr, F.
**Ultrafast electronic response of graphene to a strong and localized electric field**
Nature Communications **7**, 13948 (2016)

33. Günther, F.; Gemming, S.; Seifert, G.
**Hopping Based Charge Transfer in Diketopyrrolopyrrole Based Donor-Acceptor Polymers: A Theoretical Study**
Journal of Physical Chemistry C **120**, 9581 (2016)

34. Heera, V.; Fiedler, J.; Skorupa, W.
**Large magnetoresistance of insulating silicon films with superconducting nanoprecipitates**
AIP Advances **6**, 105203 (2016)

35. Hlawacek, G.; Jankovski, M.; Wormeester, H.; van Gastel, R.; Zandvliet, H. J. W.; Poelsema, B.
**Visualization of steps and surface reconstructions in Helium Ion Microscopy with atomic precision**
Ultramicroscopy **162**, 17 (2016)

36. Ilday, S.; Ilday, F. O.; Hübner, R.; Prosa, T. J.; Martin, I.; Nogay, G.; Kabacelik, I.; Mics, Z.; Bonn, M.; Turchinovich, D.; Toffoli, H.; Toffoli, D.; Friedrich, D.; Schmidt, B.; Heinig, K.-H.; Turan, R.
**Multiscale Self-Assembly of Silicon Quantum Dots into an Anisotropic Three-Dimensional Random Network**
Nano Letters **16**, 1942 (2016)

37. Jadidi, M. M.; König-Otto, J. C.; Winnerl, S.; Sushkov, A. B.; Drew, H. D.; Murphy, T. E.; Mittendorff, M.
**Nonlinear Terahertz Absorption of Graphene Plasmons**
Nano Letters **16**, 2734 (2016)

38. Kaltenecker, K. J.; König-Otto, J. C.; Mittendorff, M.; Winnerl, S.; Schneider, H.; Helm, M.; Helm, H.; Walther, M.; Fischer, B. M.
**Gouy phase shift of a tightly focused, radially polarized beam**
Optica **3**, 35 (2016)

39. Kehr, S. C.; Mcquaid, R. G. P.; Ortmann, L.; Kämpfe, T.; Kuschewski, F.; Lang, D.; Döring, J.; Gregg, J. M.; Eng, L. M.
**A Local Superlens**
ACS Photonics **3**, 20 (2016)

40. Kelling, J.; Ódor, G.; Gemming, S.
**Universality of (2+1)-dimensional restricted solid-on-solid models**
Physical Review E **94**, 022107 (2016)

41. Klingner, N.; Heller, R.; Hlawacek, G.; von Borany, J.; Notte, J.; Huang, J.; Facsko, S.
**Nanometer scale elemental analysis in the helium ion microscope using time of flight spectrometry**
Ultramicroscopy **162**, 91 (2016)

42. König-Otto, J.; Mittendorff, M.; Winzer, T.; Kadi, F.; Malic, E.; Knorr, A.; Berger, C.; de Heer, W. A.; Pashkin, A.; Schneider, H.; Helm, M.; Winnerl, S.
**Slow noncollinear Coulomb scattering in the vicinity of the Dirac point in graphene**
Physical Review Letters **117**, 087401 (2016)

43. Kuschewski, F.; von Ribbeck, H.-G.; Döring, J.; Winnerl, S.; Eng, L. M.; Kehr, S. C.
**Narrow-band near-field nanoscopy in the spectral range from 1.3 to 8.5 THz**
Applied Physics Letters **108**, 113102 (2016)

44. Kvashnin, D. G.; Ghorbani-Asl, M.; Shtansky, D. V.; Golberg, D.; Krasheninnikov, A. V.; Sorokin, P. B.
**Mechanical properties and current-carrying capacity of Al reinforced with graphene/BN nanoribbons: a computational study**
Nanoscale **8**, 20080 (2016)

45. Kvashnin, D. G.; Krasheninnikov, A. V.; Shtansky, D.; Golberg, P. B. Sorokin D.
**Nanostructured BN–Mg composites: features of interface bonding and mechanical properties**
Physical Chemistry Chemical Physics **18**, 965 (2016)

46. Liu, F.; Prucnal, S.; Hübner, R.; Yuan, Y.; Skorupa, W.; Helm, M.; Zhou, S.
**Suppressing the cellular breakdown in silicon supersaturated with titanium**
Journal of Physics D: Applied Physics **49**, 245104 (2016)

47. Liu, Y.; Chen, L.; Hilliard, D.; Huang, Q.-S.; Liu, F.; Wang, M.; Böttger, R.; Hübner, R.; N'Diaye, A. T.; Arenholz, E.; Heera, V.; Skorupa, W.; Zhou, S.
**Controllable growth of vertically aligned graphene on C-face SiC**
Scientific Reports **6**, 34814 (2016)

48. Liu, Y.; Li, Z.; Guo, L.; Chen, X.; Yuan, Y.; Liu, F.; Prucnal, S.; Helm, M.; Zhou, S.
**Intrinsic diamagnetism in the Weyl semimetal TaAs**
Journal of Magnetism and Magnetic Materials **408**, 73 (2016)

49. Liu, Y.; Pan, R.; Zhang, X.; Han, J.; Yuan, Q.; Tian, Y.; Yuan, Y.; Liu, F.; Wang, Y.; N'Diaye, A. T.; Arenholz, E.; Chen, X.; Sun, Y.; Song, B.; Zhou, S.
**Vacancy Defect Complexes in Silicon: Charge and Spin Order**
Physical Review B **94**, 195204 (2016)

50. Luka-Guth, K.; Hambsch, S.; Bloch, A.; Ehrenreich, P.; Briechle, B. M.; Kilibarda, F.; Sendler, T.; Sysoiev, D.; Huhn, T.; Erbe, A.; Scheer, E.
**Role of solvents in the electronic transport properties of single-molecule junctions**
Beilstein Journal of Nanotechnology **7**, 1055 (2016)

51. Melkhanova, S.; Kunze, T.; Haluska, M.; Hübner, R.; Keller, A.; Abrasonis, G.; Gemming, S.; Krause, M.
**Carbon:nickel nanocomposite templates - predefined stable catalysts for diameter-controlled growth of single-walled carbon nanotubes**
Nanoscale **8**, 14888 (2016)

52. Möller, W.; Johannes, A.; Ronning, C.
**Shaping and compositional modification of zinc oxide nanowires under energetic manganese ion irradiation**
Nanotechnology **27**, 175301 (2016)

53. Nawroth, J. F.; Neisser, C.; Erbe, A.; Jordan, R.
**Nanopatterned Polymer Brushes by Reactive Writing**
Nanoscale **8**, 7513 (2016)

54. Prucnal, S.; Liu, F.; Berencén, Y.; Vines, L.; Bischoff, L.; Grenzer, J.; Andric, S.; Tiagulskyi, S.; Pyszniak, K.; Turek, M.; Drozdziel, A.; Helm, M.; Zhou, S.; Skorupa, W.
**Enhancement of carrier mobility in thin Ge layer by Sn co-doping**
Semiconductor Science and Technology **31**, 105012 (2016)

55. Prucnal, S.; Liu, F.; Voelskow, M.; Vines, L.; Rebohle, L.; Lang, D.; Berencén, Y.; Andric, S.; Boettger, R.; Helm, M.; Zhou, S.; Skorupa, W.
**Ultra-doped n-type germanium thin films for sensing in the mid-infrared**
Scientific Reports **6**, 27643 (2016)

56. Rebohle, L.; Prucnal, S.; Skorupa, W.
**A review of thermal processing in the subsecond range: semiconductors and beyond**
Semiconductor Science and Technology **31**, 103001 (2016)

57. Sabbagh, D.; Schmidt, J.; Winnerl, S.; Helm, M.; Di Gaspare, L.; de Seta, M.; Virgilio, M.; Ortolani, M.
**Electron Dynamics in Silicon−Germanium Terahertz Quantum Fountain Structures**
ACS Photonics **3**, 403 (2016)

58. Singh, A.; Winnerl, S.; König-Otto, J. C.; Stephan, D. R.; Helm, M.; Schneider, H.
**Plasmonic efficiency enhancement at the anode of strip line photoconductive terahertz emitters**
Optics Express **24**, 22628 (2016)

59. Smejkal, V.; Gruber, E.; Wilhelm, R. A.; Brandl, L.; Heller, R.; Facsko, S.; Aumayr, F.
**A setup for transmission measurements of low energy multiply charged ions through free-standing few atomic layer films**
Nuclear Instruments and Methods in Physics Research B **382**, 119 (2016)

60. Stephan, D.; Bhattacharyya, J.; Huo, Y. H.; Schmidt, O. G.; Rastelli, A.; Helm, M.; Schneider, H.
**Inter-sublevel dynamics in single InAs/GaAs quantum dots induced by strong terahertz excitation**
Applied Physics Letters **108**, 082107 (2016)

61. Steinbach, G.; Gemming, S.; Erbe, A.
**Non-equilibrium dynamics of magnetically anisotropic particles under oscillating fields**
European Physical Journal E **39**, 69 (2016)

62. Steinbach, G.; Gemming, S.; Erbe, A.
**Rotational friction of dipolar colloids measured by driven torsional oscillations**
Scientific Reports **6**, 34193 (2016)

63. Steinbach, G.; Nissen, D.; Albrecht, M.; Novak, E.; Sanchez, P. A.; Kantorovich, S. S.; Gemming, S.; Erbe, A.
**Bistable self-assembly in homogeneous colloidal systems for flexible modular architectures**
Soft Matter **12**, 2737 (2016)

64. Suess, R. J.; Winnerl, S.; Schneider, H.; Helm, M.; Berger, C.; de Heer, W. A.; Murphy, T. E.; Mittendorff, M.
**Role of Transient Reflection in Graphene Nonlinear Infrared Optics**
ACS Photonics **3**, 1069 (2016)

65. Sutter, E.; Huang, Y.; Komsa, H.-P.; Ghorbani-Asl, M.; Krasheninnikov, A. V.; Sutter, P.
**Electron-beam induced transformations of layered tin dichalcogenides**
Nano Letters **16**, 4410 (2016)

66. Teschome, B.; Facsko, S.; Schönherr, T.; Kerbusch, J.; Keller, A.; Erbe, A.
**Temperature-Dependent Charge Transport through Individually Contacted DNA Origami-Based Au Nanowires**
Langmuir **32**, 10159 (2016)

67. Vierimaa, V. V.; Krasheninnikov, A. V.; Komsa, H.-P.
**Phosphorene under electron beam: from monolayer to one-dimensional chains**
Nanoscale **8**, 7949 (2016)

68. Wenisch, R.; Hübner, R.; Munnik, F.; Gemming, S.; Abrasonis, G.; Krause, M.
**Nickel-Enhanced Graphitic Ordering of Carbon Ad-Atoms During Physical Vapor Deposition**
Carbon **100**, 656 (2016)

69. Wilhelm, R. A.; Heller, R.; Facsko, S.
**Slow highly charged ion induced nanopit formation on the KCl(001) surface**
EPL - Europhysics Letters **115**, 43001 (2016)

70. Wilhelm, R.; Gruber, E.; Smejkal, V.; Facsko, S.; Aumayr, F.
**Charge-state-dependent energy loss of slow ions. I. Experimental results on the transmission of highly charged ions**
Physical Review A **93**, 052708 (2016)

71. Wilhelm, R.; Möller, W.
**Charge-state-dependent energy loss of slow ions. II. Statistical atom model**
Physical Review A **93**, 052709 (2016)

72. Wutzler, R.; Rebohle, L.; Prucnal, S.; Hübner, R.; Facsko, S.; Böttger, R.; Helm, M.; Skorupa, W.
**III-V nanocrystal formation in ion-implanted Ge and Si via liquid phase epitaxy during short-time flash lamp annealing**
Materials Science in Semiconductor Processing **42**, 166 (2016)

73. Xu, M.; Gao, K.; Wu, J.; Cai, H.; Yuan, Y.; Prucnal, S.; Hübner, R.; Skorupa, W.; Helm, M.; Zhou, S.
**Polycrystalline ZnTe thin film on silicon synthesized by pulsed laser deposition and subsequent pulsed laser melting**
Materials Research Express **3**, 036403 (2016)

74. Zhu, J.; Liu, F.; Zhou, S.; Franke, C.; Wimmer, S.; Volobuev, V. V.; Springholz, G.; Pashkin, A.; Schneider, H.; Helm, M.
**Lattice vibrations and electrical transport in $(Bi_{1-x}In_x)_2Se_3$ films**
Applied Physics Letters **109**, 202103 (2016)

### *Materials for energy and transport technologies*

75. Al-Motasem, A. T.; Mai, N. T.; Choi, S. T.; Posselt, M.
**Atomistic study on mixed-mode fracture mechanisms of ferrite iron interacting with coherent copper and nickel nanoclusters**
Journal of Nuclear Materials **472**, 20 (2016)

76. Altstadt, E.; Ge, H. E.; Kuksenko, V.; Serrano, M.; Houska, M.; Lasan, M.; Bruchhausen, M.; Lapetite, J.-M.; Dai, Y.
**Critical evaluation of the small punch test as a screening procedure for mechanical properties**
Journal of Nuclear Materials **472**, 186 (2016)

77. Altstadt, E.; Serrano, M.; Houska, M.; Garcia-Junceda, A.
**Effect of anisotropic microstructure of a 12Cr-ODS steel on the fracture behaviour in the small punch test**
Materials Science and Engineering A **654**, 309 (2016)

78. Bergner, F.; Hilger, I.; Virta, J.; Lagerbom, J.; Gerbeth, G.; Connolly, S.; Hong, Z.; Grant, P. S.; Weissgärber, T.
**Alternative fabrication routes toward oxide dispersion strengthened steels and model alloys**
Metallurgical and Materials Transactions A **47**, 5313 (2016)

79. Cornelius, S.; Vinnichenko, M.
**Al in ZnO - From doping to alloying: An investigation of Al electrical activation in relation to structure and charge transport limits**
Thin Solid Films **605**, 20 (2016)

80. Heintze, C.; Bergner, F.; Hernandez-Mayoral, M.; Kögler, R.; Müller, G.; Ulbricht, A.
**Irradiation hardening of Fe-9Cr-based alloys and ODS Eurofer: Effect of helium implantation and iron-ion irradiation at 300 °C including sequence effects**
Journal of Nuclear Materials **470**, 258 (2016)

81. Heintze, C.; Bergner, F.; Akhmadaliev, S.; Altstadt, E.
**Ion irradiation combined with nanoindentation as a screening test procedure for irradiation hardening**
Journal of Nuclear Materials **472**, 196 (2016)

82. Heras, I.; Krause, M.; Abrasonis, G.; Pardo, A.; Endrino, J. L.; Guillén, E.; Escobar-Galindo, R.
**Advanced characterization and optical simulation for the design of solar selective coatings based on carbon:transition metal carbide nanocomposites**
Solar Energy Materials & Solar Cells **157**, 580 (2016)

83. Hernández-Mayoral, M.; Heintze, C.; Onorbe, E.
**Transmission electron microscopy investigation of the microstructure of Fe-Cr alloys induced by neutron and ion irradiation at 300 ºC**
Journal of Nuclear Materials **474**, 88 (2016)

84. Hilger, I.; Bergner, F.; Ulbricht, A.; Wagner, A.; Weißgärber, T.; Kieback, B.; Heintze, C.; Dewhurst, C. D.
**Investigation of spark plasma sintered oxide-dispersion strengthened steels by means of small-angle neutron scattering**
Journal of Alloys and Compounds **685**, 927 (2016)

85. Hilger, I.; Boulnat, X.; Hoffmann, J.; Testani, C.; Bergner, F.; de Carlan, Y.; Ferraro, F.; Ulbricht, A.
**Fabrication and characterization of oxide dispersion strengthened (ODS) 14Cr steels consolidated by means of hot isostatic pressing, hot extrusion and spark plasma sintering**
Journal of Nuclear Materials **472**, 206 (2016)

86. Posselt, M.; Devaraj, M.; Schiwarth, M.
**Influence of phonon and electron excitations on the free energy of defect clusters in solids: A first-principles study**
Computational Materials Science **127**, 284 (2016)

87. Wagner, A.; Bergner, F.; Chaouadi, R.; Hein, H.; Hernández-Mayoral, M.; Serrano, M.; Ulbricht, A.; Altstadt, E.
**Effect of neutron flux on the characteristics of irradiation-induced nanofeatures and hardening in pressure vessel steels**
Acta Materialia **104**, 131 (2016)

### *Other topics and external users of ion beam center and free-electron laser*

88. Alishahi, M.; Mahboubi, F.; Mousavi Khoie, S. M.; Aparicio, M.; Hübner, R.; Soldera, F.; Gago, R.
**Electrochemical behavior of nanocrystalline Ta/TaN multilayer on 316L stainless steel: Novel bipolar plates for proton exchange membrane fuel-cells**
Journal of Power Sources **322**, 1 (2016)

89. Al-Kuhaili, M. F.; Durrani, S. M. A.; El-Said, A. S.; Heller, R.
**Influence of iron doping on the structural, chemical, and optoelectronic properties of sputtered zinc oxide thin films**
Journal of Materials Research **31**, 3230 (2016)

90. Al-Kuhaili, M. F.; Durrani, S. M. A.; El-Said, A. S.; Heller, R.
**Enhancement of the refractive index of sputtered zinc oxide thin films through doping with $Fe_2O_3$**
Journal of Alloys and Compounds **690**, 453 (2016)

91. Amekura, H.; Akhmadaliev, S.; Zhou, S.; Chen, F.
**A possible new origin of long absorption tail in Nd-doped yttrium aluminum garnet induced by 15 MeV gold-ion irradiation and heat treatment**
Journal of Applied Physics **119**, 173104 (2016)

92. Baradas, N. P.; Kosmata, M.; Hanf, D.; Munnik, F.
**The influence of the beam charge state on the analytical calculation of RBS and ERDA spectra**
Nuclear Instruments and Methods in Physics Research B **371**, 121 (2016)

93. Bayer, B. C.; Bosworth, D. A.; Michaelis, F. B.; Blume, R.; Habler, G.; Abart, R.; Weatherup, R. S.; Kidambi, P. R.; Baumberg, J. J.; Knop-Gericke, A.; Schloegl, R.; Baehtz, C.; Barber, Z. H.; Meyer, J. C.; Hofmann, S.
**In Situ Observations of Phase Transitions in Metastable Nickel (Carbide)/Carbon Nanocomposites**
Journal of Physical Chemistry C **120**, 22571 (2016)

94. Berencén, Y.; Illera, S.; Rebohle, L.; Ramírez, J. M.; Wutzler, R.; Cirera, A.; Hiller, D.; Rodríguez, J. A., Skorupa, W.; Garrido, B.
**Luminescence mechanism for $Er^{3+}$ ions in a silicon-rich nitride host under electrical pumping**
Journal of Physics D: Applied Physics **49**, 085106 (2016)

95. Berencén, Y.; Mundet, B.; Rodríguez, J. A.; Montserrat, J.; Domínguez, C.; Garrido, B.
**Hot electron engineering for boosting electroluminescence efficiencies of silicon-rich nitride light emitting devices**
Journal of Luminescence **183**, 26 (2017)

96. Berova, M.; Sandulov, M.; Tsvetkova, T.; Avramova, I.; Boettger, I.; Bischoff, L.
**X-Ray Photoelectron Study of Ion Implanted Tetrahedral Carbon**
Przeglad Elektrotechniczny **92**, 59 (2016)

97. Berova, M.; Sandulov, M.; Tsvetkova, T.; Bischoff, L.; Boettger, R.; Abrashev, M.
**Vibrational spectroscopy of $Ga^+$ ion implanted ta-C films**
Journal of Physics: Conference Series **682**, 012020 (2016)

98. Berova, M.; Sandulov, M.; Tsvetkova, T.; Karashanova, D.; Boettger, R.; Bischoff, L.
**Structural modification of $Ga^+$ and $N^+$ ion implanted ta-C films**
Journal of Physics: Conference Series **700**, 12035 (2016)

99. Bogdanović Radović, I.; Buljan, M.; Karlušić, M.; Jerčinović, M.; Dražič, G.; Bernstorff, S.; Boettger, R.
**Modification of semiconductor or metal nanoparticle lattices in amorphous alumina by MeV heavy ions**
New Journal of Physics **18**, 093032 (2016)

100. Boichot, R.; Tian, L.; Richard, M.-I.; Crisci, A.; Chaker, A.; Cantelli, V.; Coindeau, S.; Lay, S.; Ouled, T.; Guichet, C.; Chu, M. H.; Aubert, N.; Ciatto, G.; Blanquet, E.; Thomas, O.; Deschanvres, J.-L.; Fong, D. D.; Renevier, H.
**Evolution of Crystal Structure During the Initial Stages of ZnO Atomic Layer Deposition**
Chemistry of Materials **28**, 592 (2016)

101. Caneva, S.; Weatherup, R. S.; Bayer, B. C.; Blume, R.; Cabrero-Vilatela, A.; Braeuninger-Weimer, P.; Martin, M. B.; Wang, R.; Baehtz, C.; Schloegl, R.; Meyer, J. C.; Hofmann, S.
**Controlling Catalyst Bulk Reservoir Effects for Monolayer Hexagonal Boron Nitride CVD**
Nano Letters **16**, 1250 (2016)

102. Chen, C.; He, R.; Tan, Y.; Wang, B.; Akhmadaliev, Sh.; Zhou, S.; de Aldana, J. R. V.; Hu, L.; Chen, F.
**Optical ridge waveguides in $Er^{3+}$/$Yb^{3+}$ co-doped phosphate glass produced by ion irradiation combined with femtosecond laser ablation for guided-wave green and red upconversion emissions**
Optical Materials **51**, 185 (2016)

103. Chen, C.; Rüter, C.; Volk, M.; Chen, C.; Shang, Z.; Lu, Q.; Akhmadaliev, S.; Zhou, S.; Chen, F.; Kip, D.
**Second harmonic generation of diamond-blade diced $KTiOPO_4$ ridge waveguides**
Optics Express **24**, 16434 (2016)

104. Chen, L. L.; Liu, Y.; Zhao, Y.; Chen, N.; Qu, L. T.
**Graphene-based fibers for supercapacitor applications**
Nanotechnology **27**, 032001 (2016)

105. Cheng, Y.; Lv, J.; Akhmadaliev, S.; Zhou, S.; Chen, F.
**Optical ridge waveguides in Nd:LGS crystal produced by combination of swift $C^{5+}$ ion irradiation and precise diamond blade dicing**
Optics and Laser Technology **81**, 122 (2016)

106. Chernoglazov, K. Y.; Nikolaev, S. N.; Rylkov, V. V.; Semisalova, A. S.; Zenkevich, A. V.; Tugushev, V. V.; Vasil'Ev, A. L.; Chesnokov, Y. M.; Pashaev, E. M.; Matveev, Y. A.; Granovskii, A. B.; Novodvorskii, O. A.; Vedeneev, A. S.; Bugaev, A. S.; Drachenko, O.; Zhou, S.
**Anomalous Hall Effect in Polycrystalline $Mn_xSi_{1-x}$ ($x \approx 0.5$) Films with the Self-Organized Distribution of Crystallites over Their Shapes and Sizes**
JETP Letters **103**, 476 (2016)

107. Dankwort, T.; Hansen, A.-L.; Winkler, M.; Schürmann, U.; König, J. D.; Johnson, D. C.; Hinsche, N. F.; Zahn, P.; Mertig, I.; Bensch, W.; Kienle, L.
**Nanostructure, thermoelectric properties, and transport theory of $V_2VI_3$ and $V_2VI_3$ / IV-VI based superlattices and nanomaterials**
Physica Status Solidi A **213**, 662 (2016)

108. Dell'Anna, R.; Giubertoni, D.; Iacob, E.; Demenev, E.; Secchi, M.; Böttger, R.; Pepponi, G.
**Nanofabrication of self-organized periodic ripples by ion beam sputtering**
Microelectronic Engineering **155**, 50 (2016)

109. Drovosekov, A. B.; Kreines, N. M.; Savitsky, A. O.; Kapelnitsky, S. V.; Rylkov, V. V.; Tugushev, V. V.; Prutskov, G. V.; Novodvorskii, O. A.; Cherebilo, E. A.; Kulatov, E. T.; Wang, Y.; Zhou, S.
**Magnetic anisotropy peculiarities of high-temperature ferromagnetic $Mn_xSi_{1-x}$ ($x \approx 0.5$) alloy films**
Europhysics Letters **115**, 37008 (2016)

110. Finizio, S.; Wintz, S.; Kirk, E.; Raabe, J.
**In-situ membrane bending setup for strain-dependent scanning transmission x-ray microscopy investigations**
Review of Scientific Instruments **87**, 123703 (2016)

111. Förster, A.; Wagner, C.; Schuster, J.; Gemming, S.
**Theoretical investigation of in situ k-restore processes for damaged ultra-low-k dielectrics**
Microelectronic Engineering **156**, 121 (2016)

112. Gago, R.; Vinnichenko, M.; Hübner, R.; Redondo-Cubero, A.
**Bonding structure and morphology of chromium oxide films grown by pulsed-DC reactive magnetron sputter deposition**
Journal of Alloys and Compounds **672**, 529 (2016)

113. Gan'Shina, E.; Golik, L.; Kun'Kova, Z.; Bykov, I.; Novikov, A.; Rukovishnikov, A.; Yuan, Y.; Zykov, G.; Böttger, R.; Zhou, S.
**Transversal Kerr effect of $In_{1-x}Mn_xAs$ layers prepared by ion implantation followed by pulsed laser annealing**
Japanese Journal of Applied Physics **55**, 07MF02 (2016)

114. Ghorbani-Asl, M.; Bristowe, P. D.; Koziol, K.; Heine, T.; Kuc, A.
**Effect of compression on the electronic, optical and transport properties of $MoS_2$/graphene-based junctions**
2D Materials **3**, 025018 (2016)

115. Giri, A.; Hunwee, S.; Jain, S.; Hellwig, O.; Hopkins, P. E.
**Influence of chemical ordering on the thermal conductivity and electronic relaxation in FePt thin films in heat assisted magnetic recording applications**
Scientific Reports **6**, 32077 (2016)

116. Gkogkou, D.; Schreiber, B.; Shaykhutdinov, T.; Ly, H.; Kuhlmann, U.; Gernert, U.; Facsko, S.; Hildebrandt, P.; Esser, N.; Hinrichs, K.; Weidinger, I.; Oates, T.
**Polarization- and Wavelength-Dependent Surface-Enhanced Raman Spectroscopy Using Optically Anisotropic Rippled Substrates for Sensing**
ACS Sensors **1**, 318 (2016)

117. Green, B.; Kovalev, S.; Asgekar, V.; Geloni, G.; Lehnert, U.; Golz, T.; Kuntzsch, M.; Bauer, C.; Hauser, J.; Voigtlaender, J.; Wustmann, B.; Koesterke, I.; Schwarz, M.; Freitag, M.; Arnold, A.; Teichert, J.; Justus, M.; Seidel, W.; Ilgner, C.; Awari, N.; Nicoletti, D.; Kaiser, S.; Laplace, Y.; Rajasekaran, S.; Zhang, L.; Winnerl, S.; Schneider, H.; Schay, G.; Lorenzc, I.; Rauscher, A.; Radu, I.; Mährlein, S.; Kampfrath, T.; Wall, S.; Heberle, J.; Malnasi, A.; Cavalleri, A.; Steiger, A.; Müller, A. S.; Helm, M.; Schramm, U.; Cowan, T.; Michel, P.; Fisher, A. S.; Stojanovic, N.; Gensch, M.
**High-field High-Repetition-rate sources for the Coherent THz Control of Matter**
Scientific Reports **6**, 22256 (2016)

118. Gros, K.; Słaby, E.; Förster, H.-J.; Michalak, P. P.; Munnik, F.; Götze, J.; Rhede, D.
**Visualization of trace-element zoning in apatite using BSE and CL imaging and EPMA and particle-induced X-ray/gamma-ray emission mapping**
Mineralogy and Petrology **110**, 809 (2016)

119. Gruber, W.; Baehtz, C.; Horisberger, M.; Ratschinski, I.; Schmidt, H.
**Microstructure and strain relaxation in thin nanocrystalline platinumfilms produced via different sputtering techniques**
Applied Surface Science **368**, 341 (2016)

120. Gushchina, N. V.; Ovchinnikov, V. V.; Mücklich, A.
**Acceleration of volume decomposition of supersaturated Al + 4 wt.% Cu solid solution under irradiation with $Ar^+$ ions**
Physica Status Solidi B **253**, 770 (2016)

121. Hanf, D.; Buchriegler, J.; Merchel, S.; Munnik, F.; Renno, A.; Ziegenrücker, R.; Scharf, O.; Nowak, S. H.; von Borany, J.
**A new Particle-Induced X-ray Emission set-up for laterally resolved analysis over wide areas**
Nuclear Instruments and Methods in Physics Research B **377**, 17 (2016)

122. Hardie, C. D.; Odette, G. R.; Wu, Y.; Akhmadaliev, S.; Roberts, S. G.
**Mechanical properties and plasticity size effect of Fe-6%Cr irradiated by Fe ions and by neutrons**
Journal of Nuclear Materials **482**, 236 (2016)

123. Hinsche, N. F.; Rittweger, F.; Hölzer, M.; Zahn, P.; Ernst, A.; Mertig, I.
**Ab initio description of the thermoelectric properties of heterostructures in the diffusive limit of transport**
Physica Status Solidi A **213**, 672 (2016)

124. Jagielski, J.; Ostaszewska, U.; Bielinski, D.; Grambole, D.; Romaniec, M.; Jozwik, I.; Kozinski, R.; Kosinska, A.
**Hydrogen release from irradiated elastomers measured by Nuclear Reaction Analysis**
Nuclear Instruments and Methods in Physics Research B **371**, 216 (2016)

125. Jagielski, J.; Ostaszewska, U.; Kozinski, R.; Hassa-Zaloba, A.; Romaniec, M.; Kurpaska, L.; Kosinska, A.; Grambole, D.; Jozwik, I.
**Structural and functional properties of ion-irradiated graphene-reinforced elastomers**
Surface & Coatings Technology **306**, 176 (2016)

126. Jain, R.; Dominic, D.; Jordan, N.; Rene, E. R.; Weiss, S.; van Hullebusch, E. D.; Hübner, R.; Lens, P. N. L.
**Higher Cd adsorption on biogenic elemental selenium nanoparticles**
Environmental Chemistry Letters **14**, 381 (2016)

127. Joseph, A.; Tetzlaff, D.; Schmidt, J.; Böttger, R.; Wietler, T. F.; Osten, H. J.
**Formation and properties of high-dose nitrogen implanted epitaxially grown $Gd_2O_3$ on silicon**
Journal of Applied Physics **120**, 144103 (2016)

128. Karpov, Y.; Erdmann, T.; Raguzin, I.; Al-Hussein, M.; Binner, M.; Lappan, U.; Stamm, M.; Gerasimov, K. L.; Beryozkina, T.; Bakulev, V.; Anokhin, D. V.; Ivanov, D. A.; Günther, F.; Gemming, S.; Seifert, G.; Voit, B.; Kiriy, A.
**High Conductivity in Molecularly p-doped Diketopyrrolopyrrole–Based Polymer: the Impact of a High Dopant Strength and Good Structural Order**
Advanced Materials **28**, 6003 (2016)

129. Landgraf, A.; Dzhumabaeva, A.; Abdrakhmatov, K. E.; Strecker, M.; Macaulay, Euan A.; Arrowsmith, J. R.; Preusser, F.; Sudhaus, H.; Rugel, G.; Merchel, S.
**Repeated large-magnitude earthquakes in a tectonically active, low-strain continental interior: the northern Tien Shan, Kyrgyzstan**
Journal of Geophysical Research B - Solid Earth **121**, 3888 (2016)

130. Li, R.; Nie, W.; Shang, Z.; Cheng, C.; Akhmadaliev, S.; Zhou, S.; Lu, Q.; Chen, F.
**Guided-wave second harmonics in Nd:YCOB ridge waveguides produced by combination of carbon ion irradiation and precise diamond blade dicing**
Optical Materials **57**, 153 (2016)

131. Lindberg, P. F.; Lipp Bregolin, F.; Wiesenhütter, K.; Wiesenhütter, U.; Riise, H. N.; Vines, L.; Prucnal, S.; Skorupa, W.; Svensson, B. G.; Monakhov, E. V.
**The effect of millisecond flash lamp annealing on electrical and structural properties of ZnO:Al/Si structures**
Journal of Applied Physics **119**, 185305 (2016)

132. Liu, G.; Dong, N.; Wang, J.; Akhmadaliev, Sh.; Zhou, S.; Chen, F.
**Optical waveguides in Yb:SBN crystals fabricated by swift C ion irradiation**
Optical Materials **51**, 31 (2016)

133. Liu, W.; Haubold, D.; Rutkowski, B.; Oschatz, M.; Hübner, R.; Werheid, M.; Ziegler, C.; Sonntag, L.; Liu, S.; Zheng, Z.; Herrmann, A.-K.; Geiger, D.; Terlan, B.; Gemming, T.; Borchardt, L.; Kaskel, S.; Czyrska-Filemonowicz, A.; Eychmüller, A.
**Self-Supporting Hierarchical Porous PtAg Alloy Nanotubular Aerogels as Highly Active and Durable Electrocatalysts**
Chemistry of Materials **28**, 6477 (2016)

134. Lorinčík, J.; Veselá, D.; Vytykáčová, S.; Švecová, B.; Nekvindová, P.; Macková, A.; Mikšová, R.; Malinský, P.; Böttger, R.
**Comparison of SIMS and RBS for depth profiling of silica glasses implanted with metal ions**
Journal of Vacuum Science & Technology B **34**, 03H129 (2016)

135. Lu, N.-Y.; Yu, X.-J.; Wan, J.-W.; Weng, Y.-Y.; Guo, J.-H.; Liu, Y.
**Surface plasmon resonance coupling effect of micro-patterned gold film**
Acta Physica Sinica **65**, 208102 (2016)

136. Ludwig, P.; Bishop, S.; Egli, R.; Chernenko, V.; Deneva, B.; Faestermann, T.; Famulok, N.; Fimiani, L.; Gómez-Guzmán, J.; Hain, K.; Korschinek, G.; Hanzlik, M.; Merchel, S.; Rugel, G.
**Time-Resolved Two Million Year Old Supernova Activity Discovered in the Earth's Microfossil Record**
Proceedings of the National Academy of Sciences (PNAS) **113**, 9232 (2016)

137. Ma, L.; Tan, Y.; Akhmadaliev, S.; Zhou, S.; Chen, F.
**Electrically Tunable Nd:YAG waveguide laser based on Graphene**
Scientific Reports **6**, 36785 (2016)

138. Macková, A.; Malinský, P.; Sofer, Z.; Šimek, P.; Sedmidubský, D.; Veselý, M.; Böttger, R.
**The structural and optical properties of metal ion-implanted GaN**
Nuclear Instruments and Methods in Physics Research B **371**, 254 (2016)

139. Mai, A.; Bunce, C.; Hübner, R.; Pahner, D.; Dauderstädt, U.
**In situ bow change of Al-alloy MEMS micromirrors during 248-nm laser irradiation**
Journal of Micro-Nanolithography, MEMS, and MOEMS **15**, 035502 (2016)

140. Markwitz, A.; Gupta, P.; Mohr, B.; Hübner, R.; Leveneur, J.; Zondervan, A.; Becker, H.-W.
**Near-surface hydrogen depletion of diamond-like carbon films produced by direct ion deposition**
Nuclear Instruments and Methods in Physics Research B **371**, 230 (2016)

141. Meng, L.; Xu, C.; Yuan, Y.; Qi, Y.; Zhou, S.; Li, L.
**Magnetic properties and giant reversible magnetocaloric effect in the $GdCoC_2$ compound**
RSC Advances **6**, 74765 (2016)

142. Miller, T.; Gensch, M.; Wall, S.
**Light control of Orbital Domains: case of the prototypical manganite $La_{0.5}Sr_{1.5}MnO_4$**
Physica Scripta **91**, 124002 (2016)

143. Montoya, E.; Omelchenko, P.; Coutts, C.; Lee-Hone, N. R.; Hübner, R.; Broun, D.; Heinrich, B.; Girt, E.
**Spin transport in tantalum studied using magnetic single and double layers**
Physical Review B **94**, 054416 (2016)

144. Müller, T.; Osenbrueck, K.; Strauch, G.; Pavetich, S.; Al-Mashikhi, K.-S.; Herb, C.; Merchel, S.; Rugel, G.; Aeschbach, W.; Sanford, W.
**Use of multiple age tracers to estimate groundwater residence times and long-term recharge rates in arid southern Oman**
Applied Geochemistry **74**, 67 (2016)

145. Nikolaev, S.; Semisalova, A.; Rylkov, V.; Tugushev, V.; Zenkevich, A.; Vasiliev, A.; Pashaev, E.; Chernoglazov, K.; Chesnokov, Y.; Likhachev, I.; Perov, N.; Matveyev, Yu.; Novodvorskii, O.; Kulatov, E.; Bugaev, A.; Wang, Y.; Zhou, S.
**Ferromagnetism of $Mn_xSi_{1-x}$ (x~0.5) films grown in the shadow geometry by pulsed laser deposition method**
AIP Advances **6**, 015020 (2016)

146. Nord, M.; Krajnak, M.; Bali, R.; Hlawacek, G.; Liersch, V.; Fassbender, J.; Mcvitie, S.; Paterson, G. W.; Maclaren, I.; Mcgrouther, D.
**Developing Rapid and Advanced Visualisation of Magnetic Structures Using 2-D Pixelated STEM Detectors**
Microscopy and Microanalysis **22**, 530 (2016)

147. Pan, X.; Shuai, Y.; Wu, C.; Luo, W.; Sun, X.; Zeng, H.; Zhou, S.; Böttger, R.; Ou, X.; Mikolajick, T.; Zhang, W.; Schmidt, H.
**Rectifying filamentary resistive switching in ion-exfoliated $LiNbO_3$ thin films**
Applied Physics Letters **108**, 032904 (2016)

148. Pavlov, S. G.; Deßmann, N.; Pohl, A.; Shuman, V. B.; Portsel, L. M.; Lodygin, A. N.; Astrov, Y. A.; Winnerl, S.; Schneider, H.; Stavrias, N.; van der Meer, A. F. G.; Tsyplenkov, V. V.; Kovalesky, K. A.; Zhukavin, R. K.; Shastin, V. N.; Abrosimov, N. V.; Hübers, H.-W.
**Dynamics of nonequilibrium electrons on neutral center states of interstitial magnesium donors in silicon**
Physical Review B **94**, 075208 (2016)

149. Pelizzo, M. G.; Corso, A. J.; Tessarolo, E.; Zuppella, P.; Böttger, R.; Hübner, R.; Della Corte, V.; Palumbo, P.; Taglioni, G.; Preti, G.; Foggetta, L.; Valente, P.; Rancoita, P.; Martucci, A.; Napolitani, E.
**Optical components in harsh space environment**
Proceedings of SPIE **9981**, 99810G (2016)

150. Pelliccia, D.; Rack, A.; Scheel, M.; Cantelli, V.; Paganin, D. M.
**Experimental x-ray ghost imaging**
Physical Review Letters **117**, 113902 (2016)

151. Pettinari, G.; Drachenko, O.; Lewis, R. B.; Tiedje, T.
**Electron effective mass enhancement in Ga(AsBi) alloys probed by cyclotron resonance spectroscopy**
Physical Review B **94**, 235204 (2016)

152. Pombo-García, K.; Weiss, S.; Zarschler, K.; Ang, C.-S.; Hübner, R.; Pufe, J.; Meister, S.; Seidel, J.; Pietzsch, J.; Spiccia, L.; Stephan, H.; Graham, B.
**Zwitterionic polymer-coated ultrasmall superparamagnetic iron oxide nanoparticles with low protein interaction and high biocompatibility**
ChemNanoMat **2**, 959 (2016)

153. Putero, M.; Coulet, M. V.; Muller, C.; Baehtz, C.; Raoux, S.; Cheng, H. Y.
**Ge-doped GaSb thin films with zero mass density change upon crystallization for applications in phase change memories**
Applied Physics Letters **108**, 1019091 (2016)

154. Radek, M.; Bracht, M.; Liedke, B.; Böttger, R.; Posselt, M.
**Ion-beam induced atomic mixing in isotopically controlled silicon multilayers**
Journal of Applied Physics **120**, 185701 (2016)

155. Rafaja, D.; Wüstefeld, C.; Abrasonis, G.; Braeunig, S.; Baehtz, C.; Hanzig, F.; Dopita, M.; Krause, M.; Gemming, S.
**Thermally induced formation of metastable nanocomposites in amorphous Cr-Zr-O thin films deposited using reactive ion beam sputtering**
Thin Solid Films **612**, 430 (2016)

156. Reinhardt, T. P.; Akhmadaliev, S.; Bemmerer, D.; Stöckel, K.; Wagner, L.
**Absolute hydrogen depth profiling using the resonant $^{1}H(^{15}N,\alpha\gamma)^{12}C$ nuclear reaction**
Nuclear Instruments and Methods in Physics Research B **381**, 58 (2016)

157. Rensberg, J.; Zhang, S.; Zhou, Y.; Mcleod, A. S.; Schwarz, C.; Goldflam, M.; Liu, M.; Kerbusch, Jochen; Nawrodt, R.; Ramanathan, S.; Basov, D. N.; Capasso, F.; Ronning, C.; Kats, M.
**Active optical metasurfaces based on defect-engineered phase-transition materials**
Nano Letters **16**, 1050 (2016)

158. Riedl, H.; Koller, C. M.; Munnik, F.; Hutter, H.; Mendez Martin, F.; Rachbauer, R.; Kolozsvári, S.; Bartosik, M.; Mayrhofer, P. H.
**Influence of oxygen impurities on growth morphology, structure and mechanical properties of Ti-Al-N thin films**
Thin Solid Films **603**, 39 (2016)

159. Rugel, G.; Pavetich, S.; Akhmadaliev, S.; Enamorado Baez, S. M.; Scharf, A.; Ziegenrücker, R.; Merchel, S.
**The first four years of the AMS-facility DREAMS: Status and developments for more accurate radionuclide data**
Nuclear Instruments and Methods in Physics Research B **370**, 94 (2016)

160. Sakamaki, M.; Amemiya, K.; Sveklo, I.; Mazalski, P.; Liedke, M. O.; Fassbender, J.; Kurant, Z.; Wawro, A.; Maziewski, A.
**Formation of Co nanodisc with enhanced perpendicular magnetic anisotropy driven by $Ga^+$ ion irradiation on Pt/Co/Pt films**
Physical Review B **94**, 174422 (2016)

161. Satyarthi, P.; Ghosh, S.; Sekhar, B. R.; Wang, Y.; Zhou, S.; Skorupa, I.; Bürger, D.; Schmidt, H.; Srivastava, P.
**Unraveling carrier's kinetics in tuning the ferromagnetism of transparent $Zn_{0.95}Co_{0.05}O$ epitaxial films**
Journal of Alloys and Compounds **687**, 28 (2016)

162. Satyarthi, P.; Ghosh, S.; Wang, Y.; Zhou, S.; Bürger, D.; Skorupa, I.; Schmidt, H.; Olivi, L.; Srivastava, P.
**Direct evidence of defect coordination and magnetic interaction in local structure of wurtzite type $Zn_{1-x}Co_xO$ thin films**
Journal of Alloys and Compounds **670**, 113 (2016)

163. Schmidt, C.; Bühler, J.; Mayer, B.; Pashkin, A.; Leitenstorfer, A.; Seletskiy, D.
**Controlled polar asymmetry of few-cycle and intense mid-infrared pulses**
Journal of Optics **18**, 05LT01 (2016)

164. Schneider, M.; Lämmel, C.; Hübner, R.; Gierth, U.; Michaelis, A.
**TEM investigation of barrier-like anodic oxide films on aluminum**
Surface and Interface Analysis **48**, 906 (2016)

165. Schwanghart, W.; Bernhardt, A.; Stolle, A.; Hoelzmann, P.; Adhikari, Basanta R.; Andermann, C.; Tofelde, S.; Merchel, S.; Rugel, G.; Fort, M.; Korup, O.
**Repeated catastrophic valley infill following medieval earthquakes in the Nepal Himalaya**
Science **351**, 147 (2016)

166. Slugen, V.; Gokhman, O.; Pecko, S.; Sojak, S.; Bergner, F.
**JRQ and JPA irradiated and annealed reactor pressure vessel steels studied by positron annihilation**
Radiation Effects and Defects in Solids **171**, 231 (2016)

167. Tan, Y.; Chen, L.; Wang, D.; Chen, Y.; Akhmadaliev, S.; Zhou, S.; Hong, M.; Chen, F.
**Tunable Picosecond Laser Pulses via the Contrast of Two Reverse Saturable Absorption Phases in a Waveguide Platform**
Scientific Reports **6**, 26176 (2016)

168. Tan, Y.; Guo, Z.; Ma, L.; Zhang, H.; Akhmadaliev, Sh.; Zhou, S.; Chen, F.
**Q-switched waveguide laser based on two-dimensional semiconducting materials: tungsten disulfide and black phosphorous**
Optics Express **24**, 2858 (2016)

169. Tan, Y.; Guo, Z.; Shang, Z.; Liu, F.; Böttger, R.; Zhou, S.; Shao, J.; Yu, X.; Zhang, H.; Chen, F.
**Tailoring nonlinear optical properties of $Bi_2Se_3$ through ion irradiation**
Scientific Reports **6**, 21799 (2016)

170. Tan, Y.; Ma, L.; Akhmadaliev, Sh.; Zhou, S.; Chen, F.
**Ion irradiated Er:YAG ceramic cladding waveguide amplifier in C and L bands**
Optical Materials Express **6**, 711 (2016)

171. Temnov, V. V.; Razdolski, I.; Pezeril, T.; Makarov, D.; Seletskiy, D.; Melnikov, A.; Nelson, K. A.
**Towards the nonlinear acousto-magneto-plasmonics**
Journal of Optics **18**, 093002 (2016)

172. Tropf, L.; Kunert, G.; Jakieła, R.; Wilhelm, R. A.; Figge, S.; Grenzer, J.; Hommel, D.
**Polarity dependence of Mn incorporation in (Ga,Mn)N superlattices**
Journal of Crystal Growth **437**, 49 (2016)

173. Tsvetkova, T.; Berova, M.; Sandulov, M.; Kitova, S.; Avramov, L.; Boettger, R.; Bischoff, L.
**Focused ion beam optical patterning of ta-C films**
Surface & Coatings Technology **306**, 341 (2016)

174. Vytykacova, S.; Svecova, B.; Nekvindova, P.; Spirkova, J.; Mackova, A.; Miksova, R.; Böttger, R.
**The formation of silver metal nanoparticles by ion implantation in silicate glasses**
Nuclear Instruments and Methods in Physics Research B **371**, 245 (2016)

175. Wallner, A.; Feige, J.; Kinoshita, N.; Paul, M.; Fifield, L. Keith; Golser, R.; Honda, M.; Linnemann, U.; Matsuzaki, H.; Merchel, S.; Rugel, G.; Tims, S.; Steier, P.; Yamagata, T.; Winkler, S. R.
**Recent near-Earth supernovae probed by global deposition of interstellar radioactive $^{60}$Fe**
Nature **532**, 69 (2016)

176. Weiss, C.; Schnabel, M.; Prucnal, S.; Hofmann, J.; Reichert, A.; Fehrenbach, T.; Skorupa, W.; Janz, S.
**Formation of silicon nanocrystals in silicon carbide using flash lamp annealing**
Journal of Applied Physics **120**, 105103 (2016)

177. Werner, Z.; Barlak, M.; Ratajczak, R.; Konarski, P.; Markov, A. M.; Heller, R.
**Electron-beam pulse annealed Ti-implanted GaP**
Journal of Applied Physics **120**, 085103 (2016)

178. Wetterskog, E.; Klapper, A.; Disch, S.; Josten, E.; Hermann, R.; Rücker, U.; Brückel, T.; Bergström, L.; Alvarez, G.-S.
**Tuning the structure and crystal habit of mesocrystals using magnetic fields**
Nanoscale **8**, 15571 (2016)

179. Xie, Y.; Chen, X.; Zhang, Z.; Song, W.; Zhou, S.; Yang, Z.
**Magnetocapacitance in $CdCr_{1.8}In_{0.2}S_4$ Single Crystal Annealed in Cadmium Vapor**
IEEE Transactions on Magnetics **52**, 2501404 (2016)

180. You, T.; Selvaraj, L. P.; Zeng, H.; Luo, W.; Du, N.; Buerger, D.; Skorupa, I.; Prucnal, S.; Lawerenz, A.; Mikolajick, T.; Schmidt, O. G.; Schmidt, H.
**An Energy-Efficient, $BiFeO_3$-Coated Capacitive Switch with Integrated Memory and Demodulation Functions**
Advanced Electronic Materials **2**, 1500352 (2016)

181. Yu, H.; Kopach, A.; Misko, V. R.; Vasylenko, A. A.; Makarov, D.; Marchesoni, F.; Nori, F.; Baraban, L.; Cuniberti, G.
**Confined catalytic Janus swimmers in a crowded channel: geometry-driven rectification transients and directional locking**
Small **12**, 5882 (2016)

182. Zipf, L.; Merchel, S.; Bohleber, P.; Rugel, G.; Scharf, A.
**Exploring ice core drilling chips from a cold Alpine glacier for cosmogenic radionuclide ($^{10}$Be) analysis**
Results in Physics **6**, 78 (2016)

### *Popular-science publications*

183. Helm, M.; Michel, P.; Gensch, M.; Wagner, A.
**Alles im Fluss**
Physik Journal **15**(1), 29-34 (2016)

184. Merchel, S.; DREAMS-Team; DREAMS-Users
**Bestimmung langlebiger Radionuklide mittels Beschleunigermassenspektrometrie (AMS) für archäometrische Fragestellungen**
Metalla **8** (Special Issue), 30-33 (2016)

185. Schultheiß, H.
**Optik einmal anders**
Physik Journal **15**(10), 16-17 (2016)

# Concluded scientific degrees

## PhD theses

1. Eßer, F.
   **Cyclotron resonance and photoluminescence studies of dilute GaAsN in magnetic fields up to 62 Tesla**
   *TU Dresden, 18.08.2016*
2. Fehrenbacher, M.
   **Terahertz near-field investigation of a plasmonic GaAs superlens**
   *TU Dresden, 03.03.2016*
3. Heidarian, A.
   **Study of the static and dynamic magnetization across the first order phase transition in FeRh thin films**
   *TU Dresden, 22.01.2016*
4. Kosub, T.
   **Ferromagnet-free magnetoelectric thin film elements**
   *TU Chemnitz, 25.11.2016*
5. Neubert, M.
   **Die Rolle des Sauerstoffanteils in Titandioxid bei Tantal-Dotierung zur Verwendung als transparentes leitfähiges Oxid**
   *TU Dresden, 01.02.2016*
6. Steinbach, G.
   **Ferromagnetic colloidal particles with anisotropic magnetization distribution: self-assembly and response to magnetic fields**
   *TU Chemnitz, 10.05.2016*
7. Stephan, D.
   **Inter-sublevel dynamics in single InAs/GaAs quantum dots probed by strong terahertz excitation**
   *TU Dresden, 12.09.2016*
8. Teschome, B.
   **Functional DNA origami nanostructures for nanoelectronics**
   *TU Dresden, 13.12.2016*
9. Yildirim, O.
   **Effect of microstructure on the magnetic properties of transition metal implanted $TiO_2$**
   *TU Dresden, 24.02.2016*

## Master/Diploma theses

1. Abdou, J.
   **Thermodynamics and kinetics of Y-Ti-O nanoclusters in bcc-Fe**
   *RWTH Aachen, 30.06.2016*

2. Agha, C.
   **Investigations on the dependence of the Sticking Coefficient of Silver (Ag) on the topography of Silicon (Si) surfaces using in-situ Rutherford Backscattering Spectrometry**
   *TU Dresden, 18.08.2016*

3. Braun, M.
   **Elektrische und optische Eigenschaften von dotierten ZnO Dünnfilmschichten nach Temperung mit spektral modifizierten Blitzlampen**
   *Westsächsische Hochschule Zwickau, 15.11.2016*

4. Iseke, H.
   **Charakterisierung von graphenbasierten Detektoren im NIR–UV Bereich**
   *TU Dresden, 19.09.2016*

5. Khan, M. B.
   **Fabrication of sub-20 nm Silicon Nanowires**
   *TU Dresden, 07.07.2016*

6. Körber, L.
   **Phasenverschiebung und Transmission von Spinwellen durch magnetische Domänenwände**
   *TU Dresden, 12.12.2016*

7. Strobel, A. T.
   **Verwendung einer stromdurchflossenen Spule zur Simulation der Wechselwirkung von magnetischen Januskugeln**
   *TU Chemnitz, 12.04.2016*

# Appointments and honors

## Appointments

1. **Schultheiß, Helmut**

   Head of the Emmy Noether Junior Research Group “Magnonics: Spin waves bridging Spintronics and Photonics” was appointed as **Associate Editor** of the journal Magnetic Letters of the IEEE Magnetics Society.

## Awards and honors

1. **Schultheiß, Helmut**

   Head of the Emmy Noether Junior Research Group “Magnonics: Spin waves bridging Spintronics and Photonics” was announced as the **Walter Schottky Prize 2017** laureate for „his fundamental research about understanding spin wave propagation in nanostructures and their application in new functional devices for transport and logic processing of information“.

2. **Arora, Himani**

   PhD student in the division “Scaling Phenomena” and fellow of the International Research School NanoNet won a **Cfaed Inspire Grant** by the Center for Advancing Electronics Dresden (cfaed) to collaborate with Prof. James Hone at Columbia University, N.Y., USA for a 3-months stay in the field of heterostructures of 2-dimensional materials. In addition, she received the **Best Student Paper Award** for her contribution "Building electronics based on two-dimensional materials" at the IEEE RADIO 2016 conference.

3. **Ehrler, Jonathan**

   PhD student in the division “Magnetism” obtained an **IEEE Travel Grant** to attend the IEEE Summer School in Sendai, Japan, July 10 – 16, 2016.

4. **Günther, Florian**

   PhD student in the division “Scaling Phenomena”, fellow of the Center for Advancing Electronics Dresden (cfaed), and member of the International Research School NANONET acquired a **DAAD PhD Student Grant** to collaborate with the group of Prof. Ubirajara Rodrigues Filho at the University Sao Paolo, Campus Sao Carlos, Brazil on semiconducting and dielectric materials for polymer electronics for one year starting October 2016.

5. **Kilibarda, Filip**

   PhD student in the division “Scaling Phenomena” and fellow of the International Research IHRS NANONET won the **2nd Poster Prize** for his contribution ”Single molecule level measurements” at the NANONET International Workshop 2016, Prague, Czech Republic, August 30 – September 02, 2016.

6. **Trinh, Thu Trang**

   PhD student in the division “Magnetism” received a **DAAD Congress Grant** to participate at the International Hydrogen Conference in Grand Teton, USA, September 11 – 14, 2016.

7. **Wang, Mao**

PhD candidate in the Helmholtz Young Investigator Group "Functional Materials" of the division "Semiconductor Materials" received the **Best Student Poster Award** with her presentation "Electrical conduction and negative magnetoresistance in tellurium-hyperdoped silicon" at the 33rd International Conference on the Physics of Semiconductors, Beijing, China, July 31 – August 08, 2016.

8. **Yuan, Ye**

PhD candidate in the Helmholtz Young Investigator Group "Functional Materials" of the division "Semiconductor Materials" won the **1st Prize** at the **Young Scientist Contest** with his oral presentation "Ferromagnetic Mn-implanted GaP: Microstructures vs. magnetic properties" at the 11th International Conference: Ion Implantation and Other Applications of Ions and Electrons, Kazimierz Dolny, Poland, June 13 – 16, 2016.

# Invited conference contributions, colloquia, lectures and talks

## Invited conference talks

1. Bali, R.; Hlawacek, G.; Liersch, V.; Röder, F.; Wintz, S.; Semisalova, A.; Fassbender, J.
**Positive magnetic patterning using ion beams – principles and device applications**
603. WE-Heraeus-Seminar: Magnonics – Spin Waves Connecting Charges, Spins and Photons, 06. – 08.01.2016, Bad Honnef, Germany

2. Berencén, Y.; Prucnal, S.; Liu, F.; Wang, M.; Zhou, S.; Helm, M.; Rebohle, L.; Skorupa, W.
**Non-equilibrium thermal processing for hyperdoping Si**
11th International Conference of ion implantation and other applications of ions and electrons – ION 2016, 13. – 16.06.2016, Kazimierz Dolny, Poland

3. Bernert, K.; Sluka, V.; Fowley, C.; Lindner, J.; Deac, A. M.; Fassbender, J.
**General switching voltages for magnetic tunnel junctions with in-plane and/or perpendicular-to-plane anisotropy free layers**
New Horizons for Memory Storage: Advancing Non-volatile Memory with Atomistic Simulations, 29.06. – 01.07.2016, Dublin, Ireland

4. Bishop, S.; Ludwig, P.; Egli, R.; Chernenko, V.; Deveva, B.; Faestermann, T.; Famulok, N.; Fimiani, L.; Gomez, J.; Hain, K.; Korschinek, G.; Hanzlik, M.; Merchel, S.; Rugel, G.
**Time-Resolved Two Million Year Old Supernova Activity Discovered in the Earth's Microfossil Record**
Carpathian Summer School of Physics 2016, 26.06. – 09.07.2016, Sinaia, Romania

5. Bishop, S.; Ludwig, P.; Egli, R.; Chernenko, V.; Deveva, B.; Faestermann, T.; Famulok, N.; Fimiani, L.; Gomez, J.; Hain, K.; Korschinek, G.; Hanzlik, M.; Merchel, S.; Rugel, G.
**Time-Resolved Two Million Year Old Supernova Activity Discovered in the Earth's Microfossil Record**
Max-Planck-Institute for Physics (MPP) Colloquium, 17.05.2016, Munich, Germany

6. Böttger, R.; Heinig, K.-H.; Bischoff, L.; Huebner, R.
**Self-organized Ge & Si nanostructures by heavy-ion irradiation**
24th International Conference on the Application of Accelerators in Research and Industry CAARI, 30.10. – 04.11.2016, Fort Worth, TX, USA

7. Buljan, M.; Nekic, N.; Sancho Paramon, J.; Jercinovic, M.; Bogdanovic-Radovic, I.; Grenzer, J.; Hübner, R.; Bernstorff, S.
**Self-ordered Ge-based core/shell quantum dots in glass matrix**
20th International Vacuum Congress (IVC-20), 21. – 26.08.2016, Busan, Korea

8. Dimakis, E.
**The role of Ga droplets in the epitaxy of GaAs nanowires on Si substrates**
FemtoTera Workshop, 29.09.2016, Óbuda University, Budapest, Hungary

9. Engler, M.; Ou, X.; Facsko, S.
**"Reverse Epitaxy" on semiconductor surfaces by low energy ion irradiation**
11th International Conference on Ion Implantation and other Applications of Ions and Electrons – ION 2016, 13. – 16.06.2016, Kazimierz Dolny, Polska

10. Erb, D.; Engler, M.; Ou, X.; Facsko, S.
**Reverse epitaxy: Nanopattern formation by vacancy self-assembly upon low energy ion irradiation of crystalline semiconductor surfaces**
24th International Conference on the Application of Accelerators in Research and Industry CAARI, 30.10. – 04.11.2016, Fort Worth, TX, USA

11. Facsko, S.; Ou, X.; Engler, M.; Erb, D.; Lenz, K.
**Properties of Metallic Thin Films Grown On Periodically Corrugated Surfaces**
18th International Conference on Solid Films and Surfaces (ICSFS 18), 28.08. – 02.09.2016, Chemnitz, Germany

12. Fassbender, J.
**Ion beam modification of magnetic materials – revisited**
DPG Spring Meeting, 06. – 11.03.2016, Regensburg, Germany

13. Georgiev, Y.
**Novel Nanoelectronic Devices and Technologies for Their Fabrication**
IEEE 25th International Scientific Conference Electronics – ET 2016, 12. – 14.09.2016, Sozopol, Bulgaria

14. Heinig, K. H.; Facsko, S.; Stegemann, K. H.; Pruefer, T.; Xu, X.; Hlawacek, G.; Huebner, R.; Wolf, D.; Bischoff, L.; Moeller, W.; Borany, J.
**Ion Irradiation Assisted Fabrication of Si Quantum Dots for Ultra-Low Power Electronics**
20th International Conference on Ion Beam Modification of Materials (IBMM 2016), 30.10. – 4.11.2016, Wellington, New Zealand

15. Helm, M.
**Solid state spectroscopy with THz free electron lasers**
Laser Optics 2016, 27.06. – 01.07.2016, St. Petersburg, Russland

16. Helm, M.
**MIR and THz spectroscopy of condensed matter**
Summer School NanoTech Tera-Mir, 29.08. – 01.09.2016, Porquerolles, Hyeres, France

17. Helm, M.; König-Otto, J. C.; Mittendorff, M.; Pashkin, A.; Schneider, H.; Winnerl, S.; Wendler, F.; Winzer, T.; Malic, E.; Knorr, A.
**Surprising effects of electron-electron scattering in graphene revealed by THz pump-probe spectroscopy**
Teranano VII, 02. – 07.10.2016, Porquerolles, France

18. Helm, M.; König-Otto, J. C.; Mittendorff, M.; Pashkin, A.; Schneider, H.; Winnerl, S.; Wendler, F.; Winzer, T.; Malic, E.; Knorr, A.
**Surprising effects of electron-electron scattering in graphene revealed by THz pump-probe spectroscopy**
International Workshop on Terahertz Science, Nanotechnologies and Applications, 16. – 22.07.2016, Erice, Italy

19. Helm, M.; König-Otto, J. C.; Mittendorff, M.; Pashkin, A.; Schneider, H.; Winnerl, S.; Wendler, F.; Winzer, T.; Malic, E.; Knorr, A.
**The strange implications of electron-electron scattering in graphene**
International Conference on Terahertz Emission, Metamaterials and Nanophotonics (TERAMETANANO 2016), 03. – 10.04.2016, Cartagena, Colombia

20. Helm, M.; König-Otto, J.; Mittendorff, M.; Pashkin, A.; Schneider, H.; Wendler, F.; Winzer, T.; Malic, E.; Knorr, A.; Winnerl, S.
**Surprising effects of electron-electron scattering in graphene**
5th Russia-Japan-USA-Europe Symposium on Fundamental & Applied Problems of Terahertz Devices & Technologies (RJUSE TeraTech-2016), 31.10. – 04.11.2016, Sendai, Japan

21. Hlawacek, G.; Veligura, V.; Bali, R.
**Application of Helium Ion Microscopy to study radiation damage**
24th International Conference on the Application of Accelerators in Research and Industry CAARI, 30.10. – 04.11.2016, Fort Worth, TX, USA

22. Kaltenecker, K. J.; König-Otto, J. C.; Mittendorff, M.; Winnerl, S.; Schneider, H.; Helm, M.; Helm, H.; Walther, M.; Fischer, B. M.
**Tracing the Gouy phase shift of focused, radially polarized THz pulses**
41st International Conference on Infrared, Millimeter and Terahertz Waves, 25. – 30.09.2016, Kopenhagen, Denmark

23. Kelling, J.; Ódor, G.; Heinig, K. H.; Weigel, M.; Gemming, S.
**Pushing the Limits of Lattice Monte-Carlo Simulations using GPUs**
Perspectives of GPU computing in Science, 26. – 28.09.2016, Roma, Italia

24. Krause, M.
**Introduction into Raman spectroscopy**
Friends$^2$-Workshop: Advanced coating and characterization techniques, 19. – 20.09.2016, Dresden-Rossendorf, Germany

25. Krause-Rehberg, R.; John, M.; Akhmadaliev, S.; Böttger, R.; Anwand, W.; Wagner, A.
**Improvement of Depth Resolution of VEPAS by Sputtering Techniques**
14$^{th}$ International Workshop on Slow Positron Beam Techniques & Applications, 22. – 27.05.2016, Matsue, Japan

26. Lenz, K.; Narkowicz, R.; Reiche, C. F.; Kákay, A.; Mühl, T.; Büchner, B.; Suter, D.; Lindner, J.; Fassbender, J.
**Magnetization dynamics of a single Fe-filled carbon nanotube detected by ferromagnetic resonance**
5$^{th}$ International Conference on Microwave Magnetics, 05. – 08.06.2016, Tuscaloosa, USA

27. Makarov, D.
**Magnetic functionalities for flexible interactive electronics**
61$^{st}$ Annual Conference on Magnetism and Magnetic Materials (MMM 2016), 31.10. – 04.11.2016, New Orleans, USA

28. Makarov, D.
**Shapeable magnetic sensorics**
Brazilian-German Frontiers of Science & Technology Symposium, 20. – 23.09.2016, Campinas, Brazil

29. Makarov, D.
**Curvilinear magnetism**
7$^{th}$ International Conference on Metamaterials, Photonic Crystals and Plasmonics (META 2016), 25. – 28.07.2016, Malaga, Spain

30. Makarov, D.
**Active and passive electronics for smart implants**
MRS Fall Meeting 2016, 27.11. – 02.12.2016, Boston, USA

31. Makarov, D.
**Magnetism in curved geometries**
8$^{th}$ Joint European Magnetic Symposia (JEMS 2016), 21. – 26.08.2016, Glasgow, United Kingdom

32. Makarov, D.; Streubel, R.; Perez Rodriguez, N.; Pierce, D. T.; Unguris, J.; Pofahl, S.; Schäfer, R.; Schmidt, M.; Baenitz, M.; Kronast, F.; Wilhelm, H.; Rößler, U. K.
**Observations on surface magnetic order in FeGe and FeSi**
MRS Fall Meeting 2016, 27.11. – 02.12.2016, Boston, USA

33. Markwitz, A.; Williams, G.; Osipowicz, T.; Hübner, R.; Saumitra, V.; Gupta, P.
**Self Assembly of Magnetic Nanoclusters in Diamond-Like Carbon: A Diffusion Enhanced Process Activated by Collision Cascades**
International Union of Materials Research Societies – International Conference on Electronic Materials (IUMRS-ICEM) 2016, 04. – 08.07.2016, Singapore, Singapore

34. Merchel, S.; Khojasteh Mohammadi, Nasrin B.; Pavetich, S.; Rugel, G.; Scharf, A.; Dreams-Users; Dreams-Friends
**Determination of long-lived cosmogenic radionuclides by accelerator mass spectrometry**
International Conference on Radioanalytical and Nuclear Chemistry (RANC-2016), 10. – 15.04.2016, Budapest, Hungary

35. Osten, J.; Greene, P.; Lenz, K.; Fassbender, J.; Jenkins, C.; Arenholz, E.; Endo, T.; Iwata, N.; Liu, K.
**Use of ion irradiation to tune magnetic anisotropy**
Ion Beams in Materials Engineering and Characterization (IBMEC), 28.09. – 01.10.2016, New Dehli, Indien

36. Otalora, J. A.; Yan, M.; Lindner, J.; Fassbender, J.; Hertel, R.; Kakay, A.
**Spin waves going 3D – chiral effects in curved magnetic nanowires**
603. WE-Heraeus-Seminar: Magnonics – Spin Waves Connecting Charges, Spins and Photons, 06. – 08.01.2016, Bad Honnef, Deutschland

37. Pashkin, A.
**Nonlinear Multi-Terahertz Excitation of Strongly Correlated Materials**
Gordon Research Conference "Ultrafast Phenomena in Cooperative Systems", 14. – 19.02.2016, Lucca (Barga), Italy

38. Pashkin, A.
**FEL-based nonlinear THz spectroscopy at the ELBE accelerator**
Workshop on an accelerator based source for nonlinear THz science, 03. – 04.10.2016, SwissFEL, Windisch, Switzerland

39. Pelizzo, M. G.; Corso, A. J.; Zuppella, P.; Böttger, R.; Tessarolo, E.
**Optical components in harsh space environment**
SPIE Meeting – Planetary Defense and Space Environment Applications (Conference OP410), 28.08. – 01.09.2016, San Diego, United States

40. Prucnal, S.
**Ge comeback – new properties of an old material**
11th International Conference on Ion Implantation and other Applications of Ions and Electrons – ION 2016, 13. – 16.06.2016, Kazimierz Dolny, Polska

41. Rebohle, L.; Schumann, T.; Prucnal, S.; Skorupa, W.
**Ultra-fast Thermal Processing**
The International Conference on Coatings on Glass and Plastics, 12. – 16.06.2016, Braunschweig, Germany

42. Rebohle, L.; Schumann, T.; Prucnal, S.; Skorupa, W.
**Ultra-fast thermal processing of TCO and other thin films**
6. Workshop Transparente leitfähige Materialien, 22. – 23.11.2016, Erfurt, Germany

43. Schneider, H.
**Terahertz free-electron laser spectroscopy of semiconductor nanostructures**
8th International Symposium on Ultrafast Phenomena and Terahertz Waves (ISUPTW 2016), 10. – 12.10.2016, Chongqing, China

44. Schneider, H.
**Semiconductor spectroscopy with infrared and THz free-electron lasers**
International Conference on "Synchrotron and Free electron laser Radiation: generation and application" (SFR-2016), 04. – 07.07.2016, Novosibirsk, Russia

45. Schneider, H.; Stephan, D.; Zybell, S.; Winnerl, S.; Bhattacharyya, J.; Eßer, F.; Helm, M.
**Exciton dynamics in semiconductor quantum wells and single quantum dots studied with a THz free-electron laser**
International Workshop on "Terahertz Science, Nanotechnologies and Applications", 16. – 22.07.2016, Erice, Italien

46. Schneider, H.; Stephan, D.; Zybell, S.; Winnerl, S.; Bhattacharyya, J.; Eßer, F.; Helm, M.
**Terahertz free-electron laser spectroscopy of excitons in III-V semiconductor quantum wells and single quantum dots**
SPIE Photonics Asia, Symposium on "Infrared, Millimeter Wave, and Terahertz Technologies", 12. – 14.10.2016, Beijing, China

47. Schumann, E.; Lungwitz, F.
**UV-vis-NIR spectroscopic Ellipsometry and Photospectrometry of thin films**
Friends2-Workshop: Advanced coating and characterization techniques, 19. – 20.09.2016, Dresden-Rossendorf, Germany

48. Skorupa, W.
**Subsecond thermal processing for the advancement of thin layers and functional coatings**
SVC (Society of Vacuum Coaters), 59th Annual Technical Conference (TechCon), 09. – 13.05.2016, Indianapolis, IN, USA

49. Skorupa, W.
**Engineering for NEMS with ion beams & flash annealing**
Workshop on “Ion Implantation – improving the MEMS processes?”, 03.03.2016, Erfurt, Germany

50. Sluka, V.; Weigand, M.; Kakay, A.; Schultheiß, K.; Warnatz, T.; Erbe, A.; Tiberkevych, V.; Slavin, A.; Deac, A.; Lindner, J.; Fassbender, J.; Raabe, J.; Wintz, S.
**Directional Spin Wave Emission From Topological Spin Textures**
1st Baltic Spin conference, 09. – 13.08.2016, Jurmala, Lettland

51. Smekhova, A.; Eggert, B.; Cöster, B.; La Torre, E.; Szyjka, T.; Ollefs, K.; Bali, R.; Potzger, K.; Cornelius, S.; Liedke, M. O.; Lindner, J.; Salamon, S.; Rogalev, A.; Wende, H.
**Ferromagnetism of $Fe_{60}Al_{40}$ thin films under a magnifying glass of hard X-rays**
50th PNPI School on condensed matter physics, 14. – 19.03.2016, St. Petersberg, Russian Federation

52. Wagner, A.; Anwand, W.; Ehrler, J.; Krause-Rehberg, R.; Liedke, M. O.; Potzger, K.; Trinh, T. T.
**Positron Annihilation Lifetime Spectroscopy at a Superconducting Electron Accelerator**
14th International Workshop on Slow Positron Beam Techniques & Applications, 22. – 27.05.2016, Matsue, Japan

53. Wagner, K.; Kakay, A.; Schultheiß, K.; Henschke, A.; Sebastian, T.; Schultheiß, H.
**Magnetic domain walls as reconfigurable spin-wave nanochannels**
61st Annual Conference on Magnetism and Magnetic Materials (MMM 2016), 31.10. – 04.11.2016, New Orleans, USA

54. Wagner, K.; Kakay, A.; Schultheiß, K.; Henschke, A.; Sebastian, T.; Schultheiß, H.
**Magnetic domain walls as reconfigurable spin-wave nanochannels**
SPIE Optics and Photonics Conference, Spintronics IX Symposium, 28.08. – 01.09.2016, San Diego, USA

55. Wilhelm, R. A.; Gruber, E.; Smejkal, V.; Schwestka, J.; Kozubek, R.; Hierzenberger, A.; Schleberger, M.; Facsko, S.; Aumayr, F.
**Highly charged ion interaction with graphene**
12th European Conference on Atoms, Molecules and Photons (ECAMP), 05. – 09.09.2016, Frankfurt., Germany

56. Wilhelm, R. A.; Gruber, E.; Smejkal, V.; Schwestka, J.; Kozubek, R.; Hierzenberger, A.; Schleberger, M.; Facsko, S.; Aumayr, F.
**Charge equilibration and energy loss of slow highly charged ions in single layer graphene**
27th International Conference on Atomic Collisions in Solid (ICACS), 24. – 29.07.2016, Lanzhou, China

57. Winnerl, S.; Fehrenbacher, M.; Kuschewski, F.; von Ribbeck, H.-G.; Döring, J.; Kehr, S.; Eng, L. M.; Schneider, H.; Helm, M.
**Plasmonic superlens based on doped GaAs**
Samller and Faster: Infrared and Terahertz Spectral-Imaging at the Nanoscale with Synchrotron and Free Electron Laser Sources (SAFE), 01. – 02.12.2016, Trieste, Italy

58. Winnerl, S.; König-Otto, J. C.; Mittendorff, M.; Pashkin, A.; Schneider, H.; Helm, M.; Winzer, T.; Wendler, F.; Malic, E.; Knorr, A.
**Surprising Coulomb-scattering effects in graphene revealed by polarization–resolved THz spectroscopy**
5th EOS Topical Meeting on Terahertz Science & Technology, 08. – 11.05.2016, Pecs, Hungary

59. Winnerl, S.; Mittendorff, M.; König-Otto, J. C.; Wendler, F.; Malic, E.; Knorr, A.; Pashkin, A.; Schneider, H.; Helm, M.
**Population and polarization dynamics in Landau-quantized graphene – evidence for strong Auger scattering**
22nd International Conference on High Magnetic Fields in Semiconductor Physics (HMF-22), 24. – 29.07.2016, Sapporo, Japan

60. Wintz, S.; Sluka, V.; Weigand, M.; Kakay, A.; Schultheiß, K.; Erbe, A.; Tiberkevych, V.; Slavin, A.; Deac, A.; Lindner, J.; Raabe, J.; Fassbender, J.
**Spin Wave Emission From Topological Spin Textures**
SPIE Optics and Photonics Conference, Spintronics IX Symposium, 28.08. – 01.09.2016, San Diego, USA

61. Zhou, S.
**Application of Ion Beams to Fabricate and Tune Properties of Dilute Ferromagnetic Semiconductors**
24th International Conference on the Application of Accelerators in Research and Industry CAARI, 30.10. – 04.11.2016, Fort Worth, TX, USA

62. Zhou, S.
**Ion implantation + sub-second annealing: a route towards hyperdoped semiconductors**
26th annual meeting of MRS-J, 19. – 22.12.2016, Yokohama, Japan

## Colloquia, lectures and talks (without conference talks)

63. Dimakis, E.
**Growth and applications of III–V nanowires on Si substrates**
Seminar, Institute of Electronic Structure and Laser, Foundation for Research and Technology-Hellas (FORTH), 05.08.2016, Heraklion, Greece

64. Dimakis, E.
**Growth and applications of III-V nanowires on Si substrates**
Seminar, ANKA - Karlsruhe Institute of Technology (KIT), 15.09.2016, Eggenstein-Leopoldshafen, Germany

65. Fassbender, J.
**Nanomagnets – created and tailored by ions**
Colloquium, 07.07.2016, Leipzig, Germany

66. Fassbender, J.
**Nanomagnets – created and tailored by ions**
Colloquium, 17.05.2016, Krakow, Polen

67. Fassbender, J.
**Ion Beam Modification of Magnetic Materials**
Colloquium CIC Nanogune San Sebastian, 16.02.2016, San Sebastian, Spanien

68. Fassbender, J.
**Magnetic storage technology and spintronic applications**
Invited talk at ICT/Applied Materials, 09.03.2016, Munich, Germany

69. Georgiev, Y.
**Top-down fabrication of silicon nanowires**
Seminar SENTECH "Plasma Process Technology", 07.04.2016, Berlin, Germany

70. Hlawacek, G.
**Towards an analytic ion microscope**
HZB Seminar, 09.02.2016, Berlin, Germany

71. Liu, Y.
**Defect-induced magnetism in SiC: The new opportunity in spintronics**
Seminar in Shanghai Institute of Ceramics, Chinese Academy of Sciences, 25.01.2016, Shanghai, China

72. Makarov, D.
**Curved magnetic nanomembranes**
Seminar at Argonne National Laboratory, 28.11.2016, Lemont, USA

73. Makarov, D.
**Magnetic functionalities for flexible interactive electronics**
Special seminar, Institute of Physics, Johannes Gutenberg-Universität Mainz, 29.08.2016, Mainz, Germany

74. Rebohle, L.; Schumann, T.; Prucnal, S.; Skorupa, W.
**Ultra-fast thermal processing for thin metallic films**
FLA Seminar, CERN, 19.10.2016, Geneva, Switzerland

75. Schneider, H.
**Terahertz spectroscopy of semiconductor nanostructures with a free-electron laser**
Seminar, Chinese Academy of Engineering Physics, 18.10.2016, Chengdu, China

76. Schneider, H.
**Terahertz spectroscopy of semiconductor nanostructures with a free-electron laser**
Seminar, Ecole Normale Superieure, Laboratoire Pierre Aigrain, 23.09.2016, Paris, France

77. Winnerl, S.
**Unusual Coulomb Effects in Graphene**
Seminar lecture in graduate college Electronic Properties of Carbon Based Nanostructures, 22.01.2016, Regensburg, Germany

78. Zhou, S.
**Ion implantation + sub-second annealing: a route towards hyperdoped semiconductors**
Invited lecture at Shanghai Institute of Microsystem and Information Technology, 05.07.2016, Shanghai, China

79. Zhou, S.
**Application of Ion Beams to Fabricate and Tune Properties of Dilute Ferromagnetic Semiconductors**
Invited lecture at Shanghai University, 07.07.2016, Shanghai, China

80. Zhou, S.
**Ion implantation + sub-second annealing: a route towards hyperdoped semiconductors**
Invited lecture at University of Electronic Science and Technology of China, 18.07.2016, Chengdu, China

81. Zhou, S.
**Precisely doping semiconductors by ion implantation**
Invited seminar at University of Warsaw, 22.09.2016, Warsaw, Poland

# Conferences, workshops, colloquia and seminars

## Organization of conferences and workshops

1. Arie, A.; Dunin-Borkowski, R.; Gemming, S.
**620. Wilhelm and Else Heraeus Seminar: Interaction of shaped electron wavefunctions with light and matter**
*19. – 23.06.2016, Bad Honnef, Germany*

2. Erbe, A.; Honolka, J.; Zahn, P.
**NANONET International Workshop 2016**
*30.08. – 02.09.2016, Prague, Czech Republic*

3. Faßbender, J.; Helm, M.
**Institute Retreat (Off-site Seminar)**
*01./02.06.2016, Altenberg, Germany*

4. Gemming, S.; Zahn, P.
**MEMRIOX International Workshop 2016**
*25. – 27.09.2016, Lohmen, Germany*

5. Heintze, C.; Hilger, I.; Bergner, F.; Posselt, M.
**3rd International Workshop on ODS Materials**
*21./22.04.2016, Dresden, Germany*

6. Hilger, I.; Heintze, C.
**3rd ODISSEUS Workshop of the Oxide Dispersion Strengthened Steels group of young European Scientists**
*19./20.04.2016, Dresden, Germany*

7. Krasheninnikov, A.V.; Skakalova, V.; Tapaszto, L.
**EMRS Spring Meeting, Symposium Y: Graphene and related materials**
*02. – 06.05.2016, Lille, France*

8. Krasheninnikov, A.V.; Foster, A.S.
**International Physics Boat Workshop: Atomic structure of nanosystems from first-principles simulations and microscopy experiments**
*31.05 – 02.06.2016, Helsinki, Finland – Stockholm, Sweden*

9. Krause, M.; Gemming, S.
**FRIENDS$^2$-Workshop: Advanced coating and characterization techniques**
*19./20.09.2016, Dresden, Germany*

10. Makarov, D.; Gentile, P.; Ortix, C.; Ivan Vera-Marun, I.
**TOP-SPIN 2: Spin and Topological phenomena in nanostructures**
*26./27.05.2016, Groningen, The Netherlands*

11. Posselt, M.; Smith, R.; Uberuaga, B.
**International Focus Workshop: Bridging-Time Scale Techniques and their Applications in Atomistic Computational Science**
*12. – 15.09.2016, Dresden, Germany*

12. Schultheiß, H.; Chumak, A.
**603. Wilhelm and Else Heraeus Seminar: Magnonics – Spin waves connecting charges, spins and photons**
*06. – 08.01.2016, Bad Honnef, Germany*

13. Zhou, S.; von Bardeleben, J.; Gali, A.
**International Workshop on Defect engineering in SiC for quantum technology**
*8./9.12.2016, Dresden, Germany*

## Colloquia

1. Back, Christian H.
   University of Regensburg/Institute of Experimental and Applied Physics, Germany
   **Spin orbit fields at the Fe/GaAs(001) interface**
   *24.11.2016*
2. Carman, Greg P.
   University of California, Los Angeles, USA
   **Magnetics + Mechanics + Nanoscale = Electromagnetics Future**
   *05.12.2016*
3. Ensslin, Klaus
   ETH Zurich, Switzerland
   **Fermionic cavities in high-mobility electron gases**
   *06.06.2016*
4. Hono, Kazuhiro
   University of Tsukuba/National Institue for Materials Science, Japan
   **Materials challenges for next-generation, high-density magnetic recording – media and read heads**
   *02.09.2016*
5. Lerch, Wilfried
   centrotherm AG, Blaubeuren, Germany
   **Advanced thermal processing: Milli, nano, atto... and then?**
   *09.09.2016*
6. Rauschenbach, Stephan
   Max-Planck-Institute for Solid State Research, Stuttgart, Germany
   **Electrospray ion beam deposition – Preparative mass spectrometry for the surface science of individual nonvolatile molecules and functional thin films**
   *21.04.2016*
7. Repp, Jascha
   University of Regensburg/Institute of Experimental and Applied Physics, Germany
   **Scanning probe microscopy of individual molecules**
   *30.05.2016*
8. Sadowski, Janusz
   Lund University, Sweden and Polish Academy of Sciences/Institute of Physics, Poland
   **Segregation of magnetic MnAs nanocrystals in GaMnAs layers, superlattices and nanowires**
   *17.11.2016*
9. Svensson, Bengt
   University of Oslo, Norway
   **Ion implantation and defects: More fun... or graveyard?**
   *09.09.2016*
10. Vandervorst, Wilfried
    IMEC and KU Leuven, Belgium
    **Advances in metrology for complex systems embedded in small volumes**
    *21.01.2016*
11. Wallner, Anton
    Australian National University/Department of Nuclear Physics, Canberra, Australia
    **Long-lived radionuclides – unique signatures for astrophysical and environmental applications**
    *19.10.2016*
12. Zichner, Ralf
    Fraunhofer Institute for Electronic Nano Systems (ENAS), Chemnitz, Germany
    **From basics via application to innovation: Facts, fiction… or fancy?**
    *09.09.2016*
13. Züttel, Andreas
    École polytechnique fédérale de Lausanne (EPFL), Switzerland
    **From renewable energy to hydrogen and synfuels**
    *17.03.2016*

## Seminars

1. Asano, Kohta
National Institute of Advanced Industrial Science and Technology (AIST), Tsukuba, Japan
**Nanometer-sized metal clusters embedded in immiscible matrix induced by hydrogenation**
*26.01.2016*

2. Avasthi, Devesh K.
Amity University Noida, India
**Synthesis and engineering of nanostructures by ion beams**
*02.05.2016*

3. Barsukov, Igor
University of California, Riverside, USA
**Magnonic condensates and nonlinear dynamics due to spin-currents in nanomagnets**
*11.08.2016*

4. Bradley, Mark
Colorado State University/Departments of Physics and Mathematics, USA
**Virtually defect-free ripples and terraced topographies produced by ion sputtering**
*17.06.2016*

5. Chen, Wei
ETH Zurich/Institute of Theoretical Physics, Switzerland
**Quantum tunneling of spin and its application in spectroscopy**
*14.07.2016*

6. Fallarino, Lorenzo
CIC nanoGUNE, San Sebastian, Spain
**Depth dependent magnetic correlation in metallic and oxide films and multilayers**
*28.11.2016*

7. George, Antony
University of Jena/Institut für Physikalische Chemie, Germany
**Atomically thin 2D materials for ultrathin device applications**
*16.06.2016*

8. Guimarães, Filipe
Forschungszentrum Jülich, Germany
**Dynamical current-induced spin excitations and their impact on magnetoresistance and Hall effects**
*12.10.2016*

9. Jadidi, Mehdi
University of Maryland, USA
**Graphene plasmonics for tunable Terahertz technology**
*04.05.2016*

10. Jariwala, Deep
California Institute of Technology (CalTech), Pasadena, USA
**Photocurrent microscopy and spectroscopy in atomically-thin semiconductor devices**
*05.09.2016*

11. Johne, Robert
Max-Planck-Institut für die Physik komplexer Systeme, Dresden, Germany
**Controlling the light-matter interaction in semiconductor microcavities**
*22.09.2016*

12. Julin, Jaako
JAMK University of Applied Sciences, Jyväskylä, Finland
**Advances and challenges in instrumentation for time-of-flight ERDA: gas ionization chambers and digitizing data acquisition**
*14.04.2016*

13. Kieschnick, Michael
BAD Gesundheitsvorsorge und Sicherheitstechnik GmbH., München, Germany
**Combinatorial material science with ion beams**
*08.04.2016*

14. Liu, Enke
Max Planck Institute Chemical Physics of Solids Dresden and Chinese Academy of Sciences/Institute of Physics, Beijing, China
**Magnetostructural phase transformations and new magnetic states in shape memory alloys**
*07.12.2016*

15. López-Vidrier, Julian
Albert-Ludwigs-Universität Freiburg/Institut für Mikrosystemtechnik (IMTEK)
**Silicon nanocrystal superlattices: From materials to devices**
*11.08.2016*

16. Mantañez Huamán, Liz
Pontificia Universidad Católica del Perú, Lima and Technische Universität Ilmenau, Germany
**Synthesis and characterization of wide bandgap semiconductors doped with terbium for electroluminescent devices**
*19.01.2016*

17. Mazzinghi, Anna
LABEC, Florence, Italy
**A window on cultural heritage applications at LABEC laboratory**
*10.08.2016*

18. Mchedlidze, Teimuraz
Technische Universität Dresden, Germany
**Smart light-induced crystallization of silicon**
*07.01.2016*

19. Münzenrieder, Niko
University of Sussex, UK
**Properties, characterisation and application of flexible oxide transistors**
*07.07.2016*

20. Perov, Nikolai
Lomonosov Moscow State University, Russia
**Functional magnetic materials and recent activities at Moscow State University Magnetism Department**
*23.02.2016*

21. Prüfer, Thomas
Justus-Liebig-Universität Gießen, Germany
**Open circuit voltage of lithium-ion-cells**
*26.01.2016*

22. Rack, Alexander
European Synchrotron Radiation Facility (ESRF), Grenoble, France
**Full-field X-ray imaging using hard synchrotron radiation: 4D microtomography and real-time imaging of fast processes**
*18.03.2016*

23. Raschke, Markus B.
University of Colorado, Boulder, USA
**Nano-focused multimodal imaging, control, and interaction dynamics: Ultrafast spectroscopy reaching the single molecule limit**
*12.12.2016*

24. Sato, Nana
Keio University/Department of Physics, Tokyo, Japan
**Current induced frequency shift of backward volume spin waves**
*25.02.2016*

25. Sawicki, Maciej
Polish Academy of Sciences/Institute of Physics, Warsaw, Poland
**On the critical behavior near the Curie Point in dilute ferromagnetic semiconductors**
*14.03.2016*

26. Scheunert, Gunther
Weizmann Institute of Science, Rehovot, Israel
**Scanning probe lithography – Heat assisted magnetic recording in the lab**
*12.09.2016*

27. Secchi, Maria
University of Trento, Italy
**Nanostructure formation on Germanium by ion irradiation**
*26.01.2016*

28. Shields, Brendan; Appel, Patrick
University of Basel, Switzerland
**Nanoscale magnetic imaging with a single crystalline diamond probe**
*05.07.2016*

29. Shipman, Patrick
Colorado State University, Fort Collins, USA
**Topological measures of order for pattern-forming systems**
*15.06.2016*

30. Tamaru, Shingo
National Institute of Advanced Industrial Science and Technology (AIST), Tsukuba, Japan
**Challenges and strategies for using spin torque oscillators for practical microwave applications**
*13.05.2016*

31. Tanyeli, Irem
Eindhoven University of Technology, The Netherlands
**Low energy helium ion irradiation induced surface modification of metals**
*08.04.2016*

32. Titova, Aleksandra
Lomonosov Moscow State University/Department of Physics, Russia
**Soft magnetic properties of Fe-based nanocrystalline films**
*25.02.2016*

33. van Delft, Falco
Nanovalk, Valkenswaard, The Netherlands
**Nano-patterning for manipulation of bio-molecules and cells**
*05.10.2016*

34. Venanzi, Tommaso
Sapienza - Università di Roma, Italy
**Near-field investigation of nanoantennas made of metallic Germanium**
*24.06.2016*

35. Vert, Matthieu
Université Pierre-et-Marie-Curie Paris, France
**Modeling a stochastic process: Conversion of Schelling's segregation model into Markov chains**
*26.01.2016*

36. Wawro, Andrzej
Polish Academy of Sciences/Institute of Physics, Warsaw, Poland
**Co/Mo(Au) multilayers: structure influence on magnetic anisotropy and interlayer coupling**
*05.10.2016*

37. Wolf, Daniel
Technische Universität Dresden, Germanz
**Electron tomography – 3D reconstruction of nanoscale materials**
*27.01.2016*

# Exchange of researchers

## Guests at our Institute

1. Azad, F.
   *The University of Hong Kong; 01.12. – 16.12.2016*
2. Bergen, L.
   *Technische Unversität Wien, Austria; 14.11. – 31.12.2016*
3. Bohovicova, J.
   *University of Technology Bratislava, Slovakia; 27.11. – 09.12.2016*
4. Bradley, M.
   *Colorado State University, USA; 13.06. – 24.06.2016*
5. Canpolat, C.
   *Ankara University, Turkey; 15.04. – 15.07.2016*
6. Cheng, F.
   *Beijing Normal University, China; 01.01. – 29.08.2016*
7. Clifford, E.
   *Dublin Institute of Technology, Ireland; 01.02. – 12.08.2016*
8. Devaraj, M.
   *Indian Institute of Technology Madras, India; 10.09. – 09.10.2016*
9. Drovosenko, A.
   *Moscow University, Russia; 23.11. – 30.11.2016*
10. Edgecombe, M.
    *Ohio State University, USA; 17.05. – 17.08.2016*
11. El-Said, A. S.
    *Mansoura University, Egypt; 07.01. – 15.01.; 02.06. – 23.06.2016*
12. Garcia Hemme, E.
    *Universidad Complutense de Madrid, Spain; 01.09. – 01.12.2016*
13. Gas, K.
    *University Wroclaw, Poland; 09.03.-15.03.; 09.09. – 18.09.2016*
14. Gregor-Pawlowski, J.
    *Krakow University of Technology, Poland; 06.11. – 13.11.2016*
15. Holybee,B.
    *University of Illinois at Urbana Champaign, USA; 17.09. – 02.10.2016*
16. Hoy, C. G.
    *Imperial College London, U. K.; 04.06. – 28.07.2016*
17. Huang, K.
    *Shanghai Institute of Microsystem and Information Technology (SIMIT), Shanghai, China; 19.09. – 25.10.2016*
18. Jia, Q.
    *Shanghai Institute of Microsystem and Information Technology (SIMIT), Shanghai, China; 19.09. – 19.10.2016*
19. Krupinski, M.
    *Institute of Nuclear Physics, Krakow, Poland; 20.07. – 31.07.2016*
20. Madeira, T.
    *Universidade de Lisboa, Portugal; 01.03. – 31.12.2016*

21. Marynowska, A.
*Institute of Physics, Warsaw, Poland; 01.05. – 07.05.2016*

22. Mesko, M.
*University of Technology Bratislava, Slovakia; 27.11. – 09.12.2016*

23. Mirek, R.
*University of Warsaw, Poland; 04.07. – 14.08.2016*

24. Nazarov, A.
*University of Kyiv, Ukraine; 17.04. – 23.04.2016*

25. Nekic, N.
*Ruder Boskovic Institute Zagreb, Croatia; 20.06. – 02.07.2016*

26. Perzanowski, M.
*Institute of Nuclear Physics, Krakow, Poland; 20.07 – 31.07.; 06.11. – 13.11.2016*

27. Otalóra, J. A.
*Universidad Valparaiso, Chile; 26.08. – 11.09.2016*

28. Ou, X.
*Shanghai Institute of Microsystem and Information Technology (SIMIT), Shanghai, China; 17.10. – 25.10.2016*

29. Sheka, D.
*University of Kyiv, Ukraine; 25.01. – 21.02.2016*

30. Smith, R.
*Loughborough University, U. K.; 17.04. – 23.04.2016*

31. Soroka, W.
*Lublin University, Poland; 17.10. – 28.10.2016*

32. Turek, M.
*Lublin University, Poland; 24.04. – 30.04.2016*

33. Vasin, A.
*University of Kyiv, Ukraine; 17.04. – 23.04.2016*

34. Volkov, O.
*University of Kyiv, Ukraine; 15.01. – 15.03.2016*

35. Yershov, K.
*Institute for Theoretical Physics, Kyiv, Ukraine; 02.07. – 28.09.2016*

36. Younas, M.
*The University of Hong Kong; 11.01. – 25.01.2016*

37. Yu, Y.
*Harbin Institute of Technology, China; 01.01. – 12.09.2016*

38. Zabila, Y.
*Institute of Nuclear Physics, Krakow, Poland; 13.11. – 19.11.2016*

39. Zhang, Z.
*Hefei University, China; 01.04. – 31.12.2016*

40. Zhu, J.
*Shanghai Institute of Technical Physics (SITP), Shanghai, China; 01.01. – 31.12.2016*

41. Zuk, J.
*Lublin University, Poland; 24.04. – 30.04.2016*

# Projects

The projects are listed by funding institution and project starting date. In addition, the institute has several bilateral service collaborations with industrial partners and research institutions. These activities are not included in the following overview.

## European Projects

1. 01/2013 – 12/2016 European Union EU
**SPRITE – Supporting postgraduate research**
*Dr. J. v. Borany Phone: 0351 260 3378 j.v.borany@hzdr.de*

2. 11/2013 – 10/2017 European Union EU
**MatISSE – Materials' Innovations for a Safe and Sustainable nuclear in Europe**
*Dr. E. Altstadt Phone: 0351 260 2276 e.altstadt@hzdr.de*

3. 01/2015 – 12/2018 European Union EU
**FRIENDS$^2$ – Engineering of New Durable Solar Surfaces**
*Prof. S. Gemming Phone: 0351 260 2470 s.gemming@hzdr.de*

4. 06/2015 – 05/2016 European Union EU
**SlovakION – Supporting of Slovak Ion Beam Centre**
*Dr. J. v. Borany Phone: 0351 260 3378 j.v.borany@hzdr.de*

5. 09/2015 – 08/2019 European Union EU
**SOTERIA – Safe Long Term Operation of Light Water Reactors**
*Dr. E. Altstadt Phone: 0351 260 2276 e.altstadt@hzdr.de*

6. 10/2015 – 12/2017 European Union EU
**SMaRT (ERC Starting Grant) – Shapeable Magnetoelectronics**
*Dr. D. Makarov Phone: 0351 260 3273 d.makarov@hzdr.de*

7. 02/2016 – 01/2020 European Union EU
**IONS4SET – Single Electron Transistor**
*Dr. J. v. Borany Phone: 0351 260 3378 j.v.borany@hzdr.de*

## Helmholtz Association Projects

1. 03/2011 – 02/2016 Helmholtz-Gemeinschaft HGF
**Functional Materials – Helmholtz Young Investigator Group**
*Dr. Shengqiang Zhou Phone: 0351 260 2484 s.zhou@hzdr.de*

2. 07/2011 – 09/2018 Helmholtz-Gemeinschaft HGF
**NANONET – International Helmholtz Research School on Nanoelectronics**
*Dr. A. Erbe Phone: 0351 260 2366 a.erbe@hzdr.de*

3. 10/2011 – 09/2016 Helmholtz-Gemeinschaft HGF
**MEMRIOX – Virtual Institute – Memory Effects in Resistive Ion-beam Modified Oxides**
*Dr. P. Zahn Phone: 0351 260 3121 p.zahn@hzdr.de*

4. 01/2013 – 12/2017 Helmholtz-Gemeinschaft HGF
**W3-Professorship TU Chemnitz**
*Prof. S. Gemming Phone: 0351 260 2470 s.gemming@hzdr.de*

5. 01/2014 – 12/2018 Helmholtz-Gemeinschaft HGF
**Spintronics – Helmholtz Young Investigator Group**
*Dr. A.M. Deac Phone: 0351 260 3709 a.deac@hzdr.de*

6. 03/2014 – 02/2017 Helmholtz-Gemeinschaft HGF
**Functional Materials – HGF Postdoc Dr. Yu Liu**
*Prof. M. Helm Phone: 0351 260 2260 m.helm@hzdr.de*

7. 11/2014 – 10/2017 Helmholtz-Gemeinschaft HGF
**Magnetism – HGF Postdoc Dr. K. Schultheiß**
*Prof. J. Faßbender Phone: 0351 260 3096 j.fassbender@hzdr.de*

8. 04/2016 – 03/2017 Helmholtz-Gemeinschaft HGF
**Helmholtz-Enterprise-Fonds – GridLab**
*Dr. H. Schultheiß Phone: 0351 260 3243 h.schultheiss@hzdr.de*

9. 05/2016 – 04/2019 Helmholtz-Gemeinschaft HGF
**THz Spectroscopy – HGF Postdoc Dr. A. Singh**
*Prof. M. Helm Phone: 0351 260 2260 m.helm@hzdr.de*

10. 10/2016 – 09/2017 Helmholtz-Gemeinschaft HGF
**Helmholtz Exzellenznetzwerk – cfaed**
*Dr. A. Erbe Phone: 0351 260 2366 a.erbe@hzdr.de*

## German Science Foundation Projects

1. 11/2010 – 12/2016 Deutsche Forschungsgemeinschaft DFG
**Relaxation dynamics in graphene**
*Dr. S. Winnerl Phone: 0351 260 3522 s.winnerl@hzdr.de*

2. 09/2012 – 06/2017 Deutsche Forschungsgemeinschaft DFG
**ATOMIX – Atomic mixing in semiconductor layers**
*Dr. M. Posselt Phone: 0351 260 3279 m.posselt@hzdr.de*

3. 01/2013 – 12/2016 Deutsche Forschungsgemeinschaft DFG
**MWN – Magnetization dynamics in nanostructures**
*Dr. J. Lindner Phone: 0351 260 3221 j.lindner@hzdr.de*

4. 01/2013 – 10/2017 Deutsche Forschungsgemeinschaft DFG
**Cluster of Excellence – Center for Advancing Electronics Dresden (cfaed)**
*Prof. M. Helm Phone: 0351 260 2260 m.helm@hzdr.de*

5. 02/2013 – 01/2016 Deutsche Forschungsgemeinschaft DFG
**Nanostructured thermoelectrics**
*Dr. P. Zahn Phone: 0351 260 3121 p.zahn@hzdr.de*

6. 04/2014 – 03/2016 Deutsche Forschungsgemeinschaft DFG
**Dynano – Spin wave excitations in periodic nanostructures**
*Dr. K. Lenz Phone: 0351 260 2435 k.lenz@hzdr.de*

7. 05/2014 – 04/2019 Deutsche Forschungsgemeinschaft DFG
**Emmy Noether Junior Research Group – Magnonics**
*Dr. H. Schultheiß Phone: 0351 260 3243 h.schultheiss@hzdr.de*

8. 11/2014 – 10/2017 Deutsche Forschungsgemeinschaft DFG
**Thermal spin-transfer torques**
*Dr. J. Lindner Phone: 0351 260 3221 j.lindner@hzdr.de ,*
*Dr. A. M. Deac Phone: 0351 260 3709 a.deac@hzdr.de*

9. 11/2014 – 10/2017 Deutsche Forschungsgemeinschaft DFG
**All Optical Switching**
*Dr. H. Schultheiß Phone: 0351 260 3243 h.schultheiss@hzdr.de*

10. 10/2015 – 09/2018 Deutsche Forschungsgemeinschaft DFG
**Ferromagnetic Silicon**
*Dr. Shengqiang Zhou Phone: 0351 260 2484 s.zhou@hzdr.de*

## Federally and Saxony State Funded Projects

1. 01/2014 – 06/2017 PT Jülich BMBF
**In-situ TEM**
*Prof. J. Fassbender* *Phone: 0351 260 3096* *j.fassbender@hzdr.de*

2. 10/2014 – 09/2017 PT Jülich BMBF
**InTerFEL – High-Field Spectroscopy in the THz Regime**
*Dr. H. Schneider* *Phone: 0351 260 2065* *h.schneider@hzdr.de*

3. 02/2016 – 12/2018 Sächsische Aufbaubank SAB
**PolCarr-Sens – Electrically Polarizable Materials**
*Dr. K. Wiesenhütter* *Phone: 0351 260 2065* *k.wiesenhuetter@hzdr.de*

## Personnel Exchange Projects and Society Chairs

1. 01/2012 – 12/2018 Institute of Electrical and Electronics Engineers IEEE
**Magnetics Society German Chapter Chair**
*Prof. J. Fassbender* *Phone: 0351 260 3096* *j.fassbender@hzdr.de*

2. 04/2015 – 03/2017 Deutscher Akademischer Austauschdienst DAAD
**Personnel exchange with Chile – ChileConMagnon**
*Dr. K. Lenz* *Phone: 0351 260 2435* *k.lenz@hzdr.de*

3. 11/2015 – 04/2017 Deutscher Akademischer Austauschdienst DAAD
**Visit of Dr. Zhu**
*Prof. M. Helm* *Phone: 0351 260 2260* *m.helm@hzdr.de*

4. 01/2016 – 12/2017 Deutscher Akademischer Austauschdienst DAAD
**Personnel exchange with Poland – Magnetic Anisotropy**
*Dr. K. Potzger* *Phone: 0351 260 3244* *k.potzger@hzdr.de*

5. 01/2016 – 12/2017 Deutscher Akademischer Austauschdienst DAAD
**Personnel exchange with Poland – BEGIN**
*Dr. S. Prucnal* *Phone: 0351 260 2065* *s.prucnal@hzdr.de*

6. 01/2016 – 12/2017 Deutscher Akademischer Austauschdienst DAAD
**Personnel exchange with China – Semicondcutors**
*Dr. S. Facsko* *Phone: 0351 260 2987* *s.facsko@hzdr.de*

7. 06/2016 – 09/2016 Deutscher Akademischer Austauschdienst DAAD
**Research visit Dr. K.V. Yershov**
*Dr. D. Makarov* *Phone: 0351 260 3273* *d.makarov@hzdr.de*

8. 06/2016 – 05/2018 Alexander-von-Humboldt-Stiftung AvH
**Humboldt fellowship Dr. Y. Berencen**
*Dr. L. Rebohle* *Phone: 0351 260 3368* *l.rebohle@hzdr.de*

## Bilateral Projects

1. 10/2012 – 12/2016 Carl-Zeiss Microscopy Industry
**Collaboration on analytical ion microscopy**
*Dr. J. v. Borany* *Phone: 0351 260 3378* *j.v.borany@hzdr.de*

2. 11/2015 – 01/2019 TU Hamburg-Harburg University
**ZETA Membrane**
*Dr. J. v. Borany* *Phone: 0351 260 3378* *j.v.borany@hzdr.de*

3. 11/2015 – 01/2016 Robert-Bosch GmbH Industry
**Ion Beam Analysis**
*Dr. J. v. Borany* *Phone: 0351 260 3378* *j.v.borany@hzdr.de*

4. 09/2016 – 11/2016 FEP Fraunhofer
**Flash Lamp Annealing**
*Dr. W. Skorupa* *Phone: 0351 260 3612* *w.skorupa@hzdr.de*

# Doctoral training programme

## International Helmholtz Research School NANONET

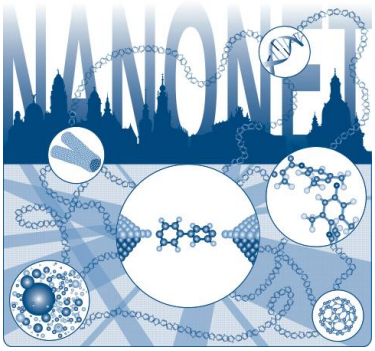


The Institute of Ion Beam Physics and Materials Research is coordinating the International Helmholtz Research School for Nanoelectronic Networks (IHRS NANONET) supported by the Initiative and Networking Fund of the Helmholtz Association. The project started in October 2012. The total funding is 1.2 Mio. € for a period of six years.

The IHRS NANONET is an international, interdisciplinary and thematically focused doctoral programme in the field of molecular electronics. The research school aims at attracting and promoting excellence by educating promising doctoral candidates with backgrounds in physics, chemistry, materials science and electrical engineering. During a period of three years PhD candidates benefit from well-structured, comprehensive training curricula and multiple mentorship, while performing cutting edge research projects within one of the 15 NANONET research groups. Under the supervision of outstanding scientists leading the field of nanoelectronics, the doctoral candidates have the unique opportunity to contribute to the advancement of molecular electronics by developing strategies for the integration of single nano-sized building blocks into large interconnected networks.

The IHRS NANONET fosters not only professional qualification but also personal development by equipping young graduates with competencies for successful careers in a wide variety of positions in academia and industry. The NANONET International Workshop 2016 was conducted in the Czech capital Prague and was attended by about 60 participants from 9 countries. In 2016 we attracted new students: Türkan Bayrak, Jingjing Ye, Filip Kilibarda, Bilal Khan, Alexander Strobel and Hagen Sekulla who are from Turkey, China, Serbia, Pakistan, and Germany, respectively. Three senior students concluded their PhD degree at the TU Dresden: Congratulations to Drs. Mimi Hetti, Banu Iyisan, and Bezu Teschome.

**The consortium**

- Helmholtz-Zentrum Dresden-Rossendorf (HZDR)
- Technische Universität (TU) Dresden
- Leibniz Institute of Polymer Research (IPF) Dresden
- Fraunhofer Institute for Ceramic Technologies and Systems (IKTS) Dresden
- Nanoelectronic Materials Laboratory (NaMLab) gGmbH Dresden

For further information please contact the NANONET coordinator, Dr. Peter Zahn (nanonet@hzdr.de) or visit the IHRS NANONET website: www.hzdr.de/nanonet.

# Experimental equipment

## Accelerators, ion implanters and other ion processing tools

| | | |
|---|---|---|
| Van de Graaff Accelerator (VdG) | 2 MV | *TuR Dresden, DE* |
| Tandetron Accelerator (T1) | 3 MV | *HVEE, NL* |
| Tandetron Accelerator (T2) | 6 MV | *HVEE, NL* |
| Low-Energy Ion Implanter | 0.1 – 40 kV | *Danfysik, DK* |
| High-Current Ion Implanter | 20 – 200 kV | *Danfysik, DK* |
| High-Energy Ion Implanter | 20 – 500 kV | *HVEE, NL* |
| Plasma Immersion Ion Implantation | 5 – 30 kV | *UK, DE;Home-built* |
| Mass-Separated Focused Ion Beam (FIB)<br>(15 nm, variable ions) | 10 – 30 keV<br>>10 A/cm$^2$ | *Orsay Physics, FR* |
| ORION NanoFab FIB Tool<br>(Including GIS and Nanopatterning) | He, Ne ions,<br>10 – 35 kV,<br>Resolution < 2 nm | *Carl Zeiss Microscopy, DE* |
| Highly-Charged Ion Facility | 25 eV – 25 keV × Q<br>Q = 1 … 40 (Xe) | *Home-built* |
| Ion-Beam Sputtering | 200 – 2000 V | *Home-built* |
| UHV Ion Irradiation (Ar, He, etc.) | 0 – 5 kV<br>Scan 10 × 10 mm$^2$ | *Cremer, DE;VG, USA* |

## Ion beam analysis (IBA)

A wide variety of advanced IBA techniques are available at the MV accelerators (see figure).

| | | | |
|---|---|---|---|
| RBS | Rutherford Backscattering Spectrometry | (1), (10), (11), (12) | *VdG, T1, T2, HIM* |
| RBS/C | RBS + Channelling | (1), (11), (12) | *VdG, T1, T2* |
| HR-RBS | High-Resolution RBS | (10), (14) | *T1* |
| ERDA | Elastic Recoil Detection Analysis | (1), (4) | *VdG, T2* |
| PIXE | Particle-Induced X-ray Emission | (1), (5), (6), (12) | *VdG, T1, T2* |
| PIGE | Particle-Induced $\gamma$ Emission | (6), (12) | *T1, T2* |
| NRA | Nuclear Reaction Analysis | (3), (7), (11), (12) | *T1, T2* |
| NRRA | Nuclear Resonance Reaction Analysis | (3), (7), (11) | *T1, T2* |
| NMP | Nuclear Microprobe | (12) | *T1* |
| AMS | Accelerator Mass Spectrometry<br>(focused to long-lived radionuclides: $^{10}$Be, $^{26}$Al, $^{36}$Cl, $^{41}$Ca, $^{129}$I) | (15) | *T2* |

Some stations are equipped with additional process facilities enabling *in-situ* IBA investigations during ion irradiation, sputtering, deposition, annealing etc.

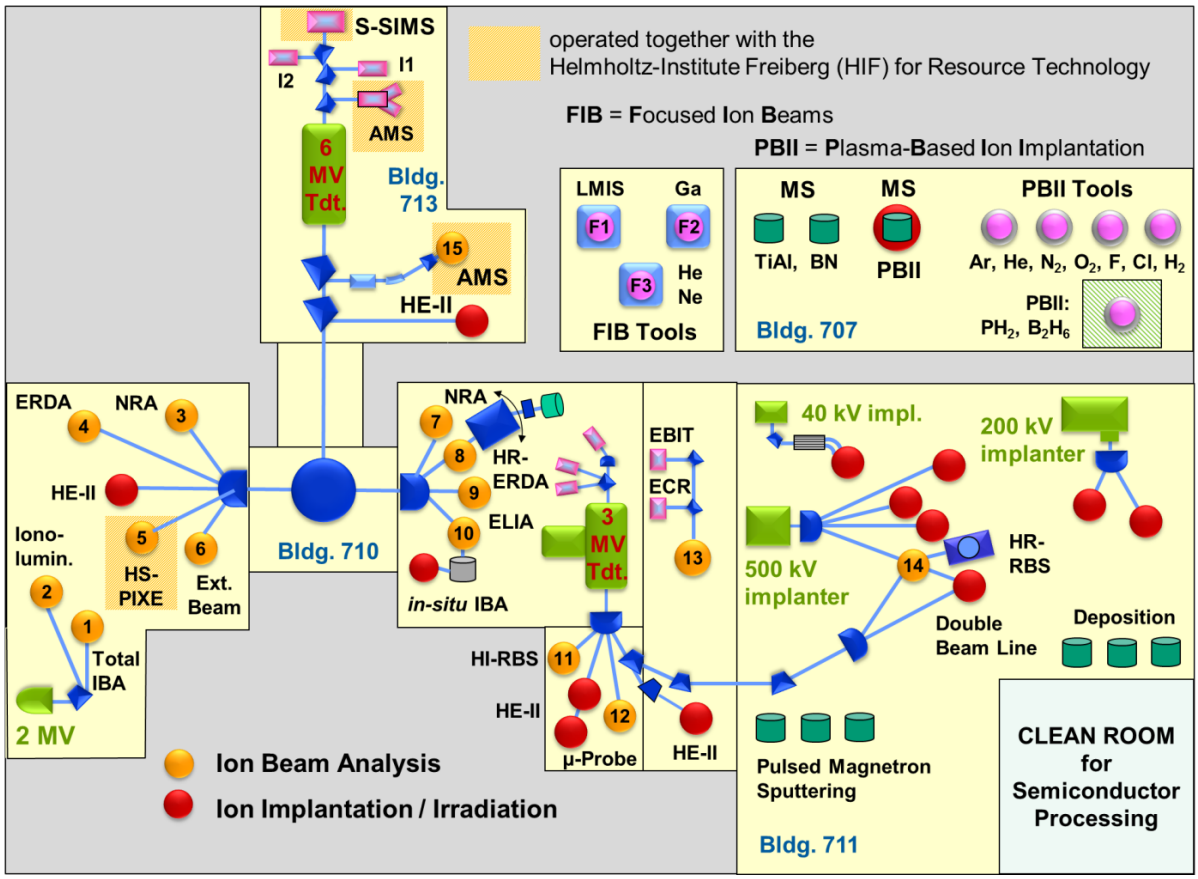


*Schematic overview of the HZDR Ion Beam Center*

## Other particle-based analytical techniques

| | | | |
|---|---|---|---|
| SEM | Scanning Electron Microscope (S4800 II) | 1 – 30 keV<br>+ EDX | *Hitachi, JP* |
| TEM | Transmission Electron Microscope<br>(Titan 80-300 with Image Corrector) | 80 – 300 keV<br>+ EDX, EELS | *FEI, NL* |
| TEM | Transmission Electron Microscope<br>(Talos F200X) | 20 – 200 keV<br>+ SuperX EDX | *FEI, NL* |
| HIM | Scanning Ion Microscope<br>(ORION NanoFab with He, Ne ions) | He, Ne ions<br>10 – 35 kV<br>+ RBS, SIMS | *Carl Zeiss Microscopy, DE* |
| FIB/SEM | Focused Ion/Electron Cross Beam<br>(NVision 40 with Elphy Plus Litho) | 0.5 – 30 keV<br>+ EDX, EBSD | *Carl Zeiss Microscopy, DE* |
| AES | Auger Electron Spectroscopy | + XPS | *Thermo Fisher Scientific, UK* |
| LEEM | Low-Energy Electron Microscope<br>(Spec-LEEM-III) | 0 eV – 4.5 keV<br>Resolution < 6 nm<br>+ AES | *Elmitec, DE* |
| CEMS | Mössbauer Spectroscopy | $^{57}$Fe source | *Home-built* |

## Photon-based analytical techniques

| | | | |
|---|---|---|---|
| XRD/XRR | X-Ray Diffractometers | Cu-Kα | |
| | θ-θ Powder D8 | | *Bruker, DE* |
| | θ-2θ 4-Circle D5005 | | *Siemens, DE* |
| | θ-θ 4-Circle Empyrean | | *PANalytical, NL* |
| | θ-2θ 4+2-Circle SEIFERT XRD3003-HR | | *General Electric, US* |
| SE | Spectroscopic Ellipsometry | 250 – 1700 nm | *Woollam, US* |
| UV-Vis | Solid Spec 3700 DUV | 190 – 3300 nm | *Shimadzu, JP* |
| FTIR | Fourier-Transform Infrared Spectrometer | 600 – 7000 $cm^{-1}$ | *Nicolet, US* |
| FTIR | Fourier-Transform Infrared Spectrometer | 50 – 15000 $cm^{-1}$ | *Bruker, DE* |
| | Ti:Sapphire Femtosecond Laser | 78 MHz | *Spectra Physics, US* |
| | Femtosecond Optical Parametric Osci. | | *APE, DE* |
| | Ti:Sapphire Femtosecond Amplifier | 1 kHz, 250 kHz | *Coherent, US* |
| | Femtosecond Optical Parametric Amplifier | | *Light Conversion, LT* |
| THz-TDS | Terahertz Time-Domain Spectroscopy | 0.1 – 4 THz | *Home-built* |
| Raman | Raman Spectroscopy | > 45 $cm^{-1}$ | *Jobin-Yvon-Horiba, FR* |
| | In-situ Raman Spectroscopy | > 100 $cm^{-1}$ | *Jobin-Yvon-Horiba, FR* |
| PL | Photoluminescence (10 – 300 K) | 300 – 1600 nm | *Jobin-Yvon-Horiba, FR* |
| TRPL | Time-Resolved Photoluminescence | $\tau$ = 3 ps – 2 ns<br>$\tau$ > 5 ns | *Hamamatsu Phot., JP*<br>*Stanford Research, US* |
| EL | Electroluminescence | 300 – 1600 nm | *Jobin-Yvon-Horiba, FR* |
| | Optical Split-Coil Supercond. Magnet | 7 T | *Oxford Instr., UK* |
| PR | Photomodulated Reflectivity | 300 – 1600 nm | *Jobin-Yvon-Horiba, FR* |
| PLE | Photoluminescence Excitation | 300 – 1600 nm | *Jobin-Yvon-Horiba, FR* |
| OES | Optical Emission Spectroscopy | 250 – 800 nm | *Jobin-Yvon-Horiba, FR* |

## Magnetic thin film deposition and analysis

| | | | |
|---|---|---|---|
| PLD | Pulsed Laser Deposition | | *SURFACE, DE* |
| MFM | Magnetic Force Microscope | ~ 50 nm resol. | *VEECO;DI, US* |
| SQUID MPSM | Supercond. Quantum Interference Device | ± 7 T | *Quantum Design, US* |
| SQUID VSM | Vibrating Sample Magnetometer | ± 7 T | *Quantum Design, US* |
| MOKE | Magneto-Optic Kerr Effect (in-plane) | ± 0.35 T | *Home-built* |
| MOKE | Magneto-Optic Kerr Effect (perpend.) | ± 2 T | *Home-built* |
| FR-MOKE | Frequency-Resolved Magneto-Optic KE | ± 1.1 T | *Home-built* |
| SKM | Scanning Kerr Microscope | | *Home-built* |
| | Kerr Microscope | | *Evico Magnetics, DE* |
| TR-MOKE | Time-Resolved MOKE (Pump-Probe) | | *Home-built* |
| VNA-FMR | Vector Network Analyzer Ferromagnetic Resonance | 50 GHz | *Agilent, DE;*<br>*Home-built* |
| Cryo-FMR | Variable-Temperature Ferromagnetic Resonance | 3 – 300 K | *Attocube, DE;*<br>*Home-built* |

| | | | |
|---|---|---|---|
| ME | Magnetoellipsometer | | *LOT, DE; AMAC, US* |
| µBLS | Brillouin Light Scattering Microscope | ± 0.8 T, 532 nm & 491 nm | *Home-built* |
| SKM | Scanning Kerr Microscope with RF Detection (Spectrum Analyzer) | ± 0.5 T, 40 GHz | *Home-built* |
| MT-50G | High Frequency Magneto-transport Setup | ± 1.5 T, 50 GHz 250 ps | *Home-built* |

## Other analytical and measuring techniques

| | | | |
|---|---|---|---|
| STM/AFM | UHV Scanning Probe Microscope (variable T) | | *Omicron, DE* |
| AFM | Atomic Force Microscope (Contact, Tapping, Spreading) | | *Bruker, US* |
| AFM | Atomic Force Microscope (with c-AFM, SCM-Module) | | *Bruker, US* |
| | Dektak Surface Profilometer | | *Bruker, US* |
| | Micro Indenter/Scratch Tester | | *Shimatsu, JP* |
| MPMS | Mechanical Properties Measurement System – Stretcher | | *Home-built* |
| MS | Mass Spectrometers (EQP-300, HPR-30) | | *HIDEN, DE/US* |
| | Wear Tester (pin-on disc) | | *Home-built* |
| LP | Automated Langmuir Probe | | *Impedans, IE* |
| HMS | Hall Measurement System | 2 – 400 K, ≤ 9 T | *LakeShore, US* |
| | Van-der-Pauw HMS Ecopia | 300 K & LNT, 0.5 T | *Bridge Technol., US* |
| MTD | Magneto-Transport Device | 300 K, ≤ 3 T | *Home-built* |
| RS | Sheet-Rho-Scanner | | *AIT, KOR* |
| DLTS | Deep Level Transient Spectroscopy | + I-U/C-V 10 – 300 K, 1 MHz | *PhysTech, DE* |
| IV / CV | Photocapacitance (+I-V/G-V) | 250 – 2500 nm | *Home-built* |
| IV / CV | I-V and C-V Analyzer | | *Keithley, US* |
| IV / CV | I-V and C-V Semi-Automatic Prober | -60 – 300 °C | *Süss, DE; Keithley, US* |
| IV | I-V Prober | 4.2 – 600 K | *LakeShore, Agilent, US* |

## Deposition and processing techniques

| | | |
|---|---|---|
| Physical Deposition | Sputtering DC/RF, Evaporation | *Nordiko, UK* |
| | Electron Beam Evaporation System | *Leybold Optics, DE* |
| | Thermal Evaporation | *Bal-Tec, LI* |
| | High Power Impulse Magnetron Sputtering | *Melec, DE* |
| Molecular Beam Epitaxy | III-V Semiconductors | *Riber, FR* |
| Chemical Vapour Deposition | Plasma Enhanced CVD (for a-Si, a-Ge, $SiO_2$, SiON, $Si_3N_4$) | *Oxford Instr., UK* |
| Atomic Layer Deposition | $Al_2O_3$, $HfO_2$, $SiO_2$ | *Ultratech, US* |
| Dry Etching | ICP-RIE, $CF_4$, $SF_6$, $C_4F_8$ | *Sentech, DE* |
| | RIBE, ∅ 6”, Ar, $CF_4$ | *Roth & Rau, DE* |

| | | |
|---|---|---|
| Etching/Cleaning | incl. Anisotropic Selective KOH Etching | |
| Photolithography | Mask-Aligner, 2 µm-Level | *Süss, DE* |
| | Direct Laser Writer DWL 66FS | *Heidelberg Instr., DE* |
| | MicroWriter | *LOT QD, DE* |
| Electron Beam Lithography | Raith 150-TWO: ∅ 6”, 10 nm resol. | *Raith, DE* |
| | e-Line Plus: ∅ 4”, 10 nm resol. | *Raith, DE* |
| Thermal Treatment | Room Temperature – 2000 °C | |
| Furnace | | *InnoTherm, DE* |
| Rapid Thermal Annealing JETFIRST 100 | | *JIPELEC, FR* |
| Rapid Thermal Annealing AW 610 | | *Allwin21, USA* |
| Flash-Lamp Units (0.5 – 20 ms) | | *Home-built;FHR/DTF, DE* |
| RF Heating (Vacuum) | | *JIPELEC, FR* |
| Laser Annealing (CW, 808 nm, 450 W)<br>Laser Annealing (30 ns pulse,10 Hz, 308 nm, 500 mJ) | | *LIMO, DE;*<br>*COHERENT, USA* |
| Bonding Techniques | Ultrasonic Wire Bonding | *Kulicke & Soffa, US* |
| Cutting, Grinding, Polishing | | *Bühler, DE* |
| TEM Sample Preparation | Plan View and Cross Section<br>incl. Ion Milling Equipment | *Gatan, US* |

## Hot cells laboratory

| | | |
|---|---|---|
| Mechanical testing of neutron irradiated structural materials | Max. Total Activity 5 TBq ($^{60}$Co),<br>-150 ... +315 °C | |
| Fracture mechanics testing | Max. Load ±50 kN | *MTS, US* |
| Charpy impact testing | 300 J | *WPM Leipzig, DE* |
| Small punch test | 10 kN | *Hegewald & Peschke, DE* |
| Specimen preparation | Electrical Discharge Machining | *AGIE, DE* |
| Depth sensing nanoindentation/ AFM | UNAT, Load Range 1 – 500 mN | *ASMEC, DE* |

# User facilities and services

## Ion Beam Center (IBC)

The Ion Beam Center (IBC) at HZDR combines various machines (electrostatic accelerators, ion implanters, plasma-based equipment) into a unique facility primarily used for ion beam modification and ion beam analysis of materials. The available energy range spans from a few eV to almost 100 MeV with a respective interaction depth in solids between 0.1 nm to 10 µm. In addition to standard broad beams also focused (down to 1 nm) and highly-charged (charge state up to +45) ion beams are available. In addition to these ion beam facilities, structural analysis (electron microscopy and spectroscopy, X-ray scattering techniques) and sample or device processing under clean-room conditions can be utilized at IBC to provide a "complete" user service. As a part of the IBC, the IBC together with the Helmholtz Institute Freiberg for Resource Technology (HIF, www.hzdr.de/HIF) operates the DREAMS (DREsden AMS = accelerator mass spectrometry) facility which is used for the determination of long-lived radionuclides ($^{10}$Be, $^{26}$Al, $^{35}$Cl, $^{41}$Ca and others) with ultimate sensitivity. A schematic overview of the IBC including the description of the main beam lines and experimental stations is given on page 97 of this Annual Report. In 2016 about 13.300 beam time hours were delivered for about 450 users from 22 countries worldwide performing experiments at IBC or using the capabilities for ion beam services.

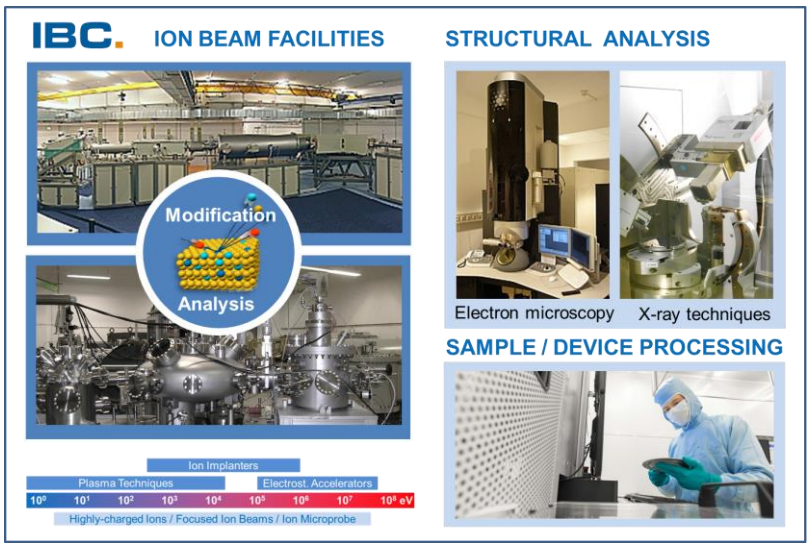


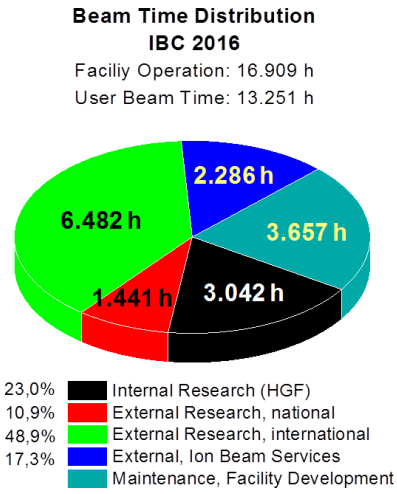


IBC activities are efficiently integrated into various Helmholtz programmes within the research field "Matter", but also in the Helmholtz cross-programme activities "Mineral Resources", "Materials Research for Energy Technologies", and "Helmholtz Energy Materials Foundry". From 2013 the IBC has been recognized as a large-scale facility within the "BMBF Verbundforschung" programme promoting long-term collaborations with universities. In addition, from 2015 the IBC has the status of a Helmholtz LK–II user facility.

The IBC demonstrates its outstanding status within the international community of ion beam facilities by the following features:

- the IBC has provided ion beam technology as a user and competence centre for ion beam applications for more than 30 years. With respect to user beam time hours the IBC is internationally leading and has been supported by numerous national and European grants and by industry.
- the IBC activities cover both ion beam modification as well as ion beam analysis (IBA). Experienced staff is present to support IBC users and to enhance the experimental capabilities to their needs.

• the operation of IBC is accompanied by a strong in-house research at the affiliated host “Institute of Ion Beam Physics and Materials Research”, both in experiment and theory. This allows in-depth research in targeted research areas as well as the exploration of new application fields for ion beam technology.

Following the rules of a European and national user facility, access for scientific experiments to IBC is provided on the basis of a proposal procedure (www.hzdr.de/IBC) via the common HZDR user facility portal **HZDR-GATE** (gate.hzdr.de). Due to the availability of multiple machines and versatile instrumentation, continuous submission of IBC proposals can be offered (no deadline). The scientific quality of the proposals is steadily evaluated and ranked by an external international User Selection Panel. For successfully evaluated proposals, users get free access to IBC facilities for their experiments which can be often realized within three months after proposal submission. The use of the IBC facilities includes the scientific and technical support during planning, execution and evaluation of the experiments. For AMS samples preparation two chemical laboratories are available.

The IBC strongly supports the commercial exploitation of ion beam technology of partners from industry which is essential for materials science applications. For ion beam services the HZDR Innovation GmbH (spin-off of the HZDR) – www.hzdr-innovation.de – provides a direct and fast access to the IBC facilities based on individual contracts. The close collaboration between IBC and HZDR Innovation GmbH is considered as a Helmholtz reference model aiming to develop innovative strategies for an effective contribution of large-scale facilities for economic innovation. Currently, about 18% of the total IBC beam time is provided for commercial ion beam services.

The IBC pursues two strategic objectives for further development. On one hand, it is focused on the successful operation as an international user facility to sustain its position as a leading European ion beam center in the fields of materials and interdisciplinary research. This requires the continuous development and extension of ion beam technologies. Special emphasis is directed towards new R&D areas and communities which so far have not been aware of the advantages of ion technology. On the other hand, cutting edge scientific challenges, in particular for the modification and understanding of the function of materials at the nanoscale down to the atomic level, is addressed in order to achieve new functionalities and to design novel materials. These challenges comprise:

• the extended application of low-energy ions for modification and analysis of ultra-thin films, surfaces, 2D materials and molecular layers based on a new low-energy ion nano-engineering technology platform which has recently started with the installation of first tools,

• the investigation of material states and modifications far from equilibrium induced by high-energy density excitations with cluster and highly-charged ions,

• the exploration of new IBA approaches with unprecedented lateral resolution, ultimate detection limit and high sample throughput, e.g. for resource technology. With projects like “PIXE-Camera” and “Super-SIMS”, both in close collaboration with the HIF, the interdisciplinary work of IBC will be substantially extended towards the application of ion beam analysis methods in geosciences and resource technology.

Recently, some new ion beam tools or end-stations have been commissioned which will attract new users by cutting-edge experimental instrumentation. The ion microscope *ORION NanoFab* (He/Ne ions, 10 – 40 keV) is now in routine operation with unique possibilities for surface imaging, nano-fabrication and, for the first time, elemental analysis using ion beam analysis methods. The cluster tool at the 6 MV accelerator – in operation since 2015 – allows *in situ* deposition and analysis investigations at temperature of up to 800 °C. Analytical techniques comprise Rutherford backscattering spectrometry, Raman spectroscopy and Vis-NIR spectroscopic ellipsometry. In 2016, the ion microprobe at HZDR at the 3 MV tandetron has been basically upgraded (electronics, control software etc.) which now delivers the possibility to use – in parallel or sequential – several IBA techniques with a spatial resolution of about 3 µm and a user friendly operation mode. Results of DREAMS work contributed to outstanding publications in *Nature* and *Science* related to geomorphology and cosmogenic events.

For more detailed information please contact Dr. Johannes von Borany (j.v.borany@hzdr.de) or Dr. Stefan Facsko (s.facsko@hzdr.de) and visit the IBC webpage: www.hzdr.de/IBC.

# Free Electron Laser FELBE

ELBE is an acronym for the free-electron laser (FEL) at the Electron Linear accelerator with high Brilliance and low Emittance (ELBE) located at the Helmholtz-Zentrum Dresden-Rossendorf, Germany. The heart of ELBE is a superconducting linear accelerator operating in cw mode with a pulse repetition rate of 13 MHz. The electron beam (40 MeV, 1 mA max.) is guided to several laboratories where secondary beams (particle and electromagnetic) are generated. Two free-electron lasers (U27-FEL and U100-FEL) produce intense, coherent electromagnetic radiation in the mid and far infrared, which is tunable over a wide wavelength range (4 – 250 µm) by changing the electron energy or the undulator magnetic field. Main parameters of the infrared radiation produced by FELBE are as follows:

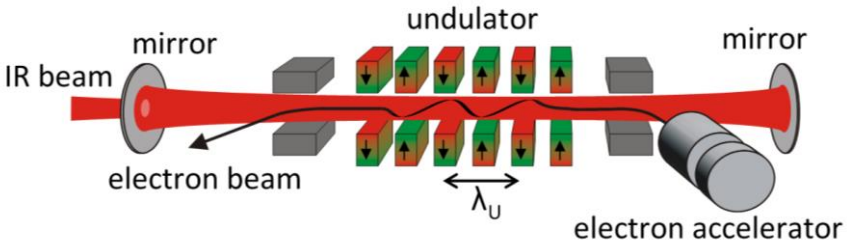


| | | |
|---|---|---|
| Wavelength λ | 4 – 22 µm<br>18 – 250 µm | FEL with undulator U27<br>FEL with undulator U100 |
| Pulse energy | 0.01 – 2 µJ | depends on wavelength |
| Pulse length | 1 – 25 ps | depends on wavelength |
| Repetition rate | 13 MHz | 3 modes: • cw<br>• macropulsed (> 100 µs, < 25 Hz)<br>• single pulsed (Hz … kHz) |

The free electron laser is a user facility. Applications for beam time can be submitted twice a year, typically by April 15 and October 15.

Typical applications are picosecond pump-probe spectroscopy (also in combination with several other femtosecond lasers, which are synchronized to the FEL), near-field microscopy and nonlinear optics. The FELBE facility also serves as a far-infrared source for experiments at the High-Field Laboratory Dresden (HLD) involving pulsed magnetic fields up to 70 T.

The statistics shows that the FEL used 1255 hours beam time of the ELBE accelerator. This corresponds to 21 % of total beam time, which is again distributed among internal and external users.

For further information please contact:
Prof. Manfred Helm (m.helm@hzdr.de)
or visit the FELBE webpage
www.hzdr.de/FELBE.

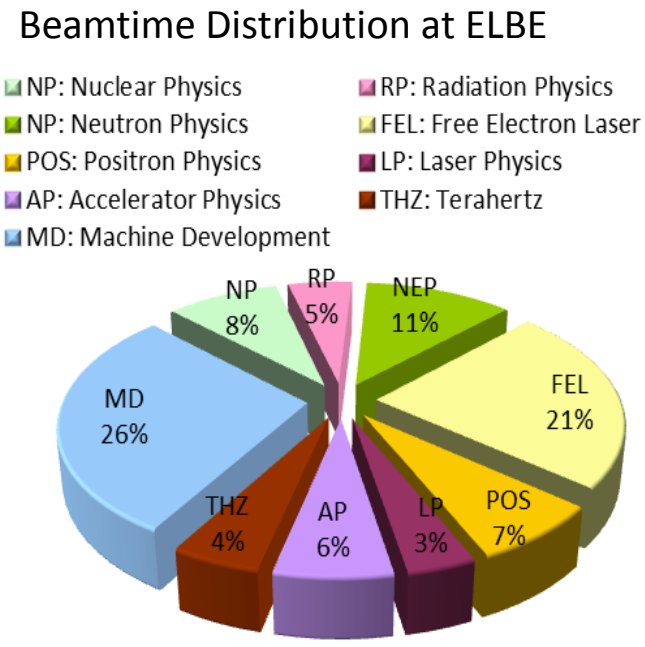

# Organization chart

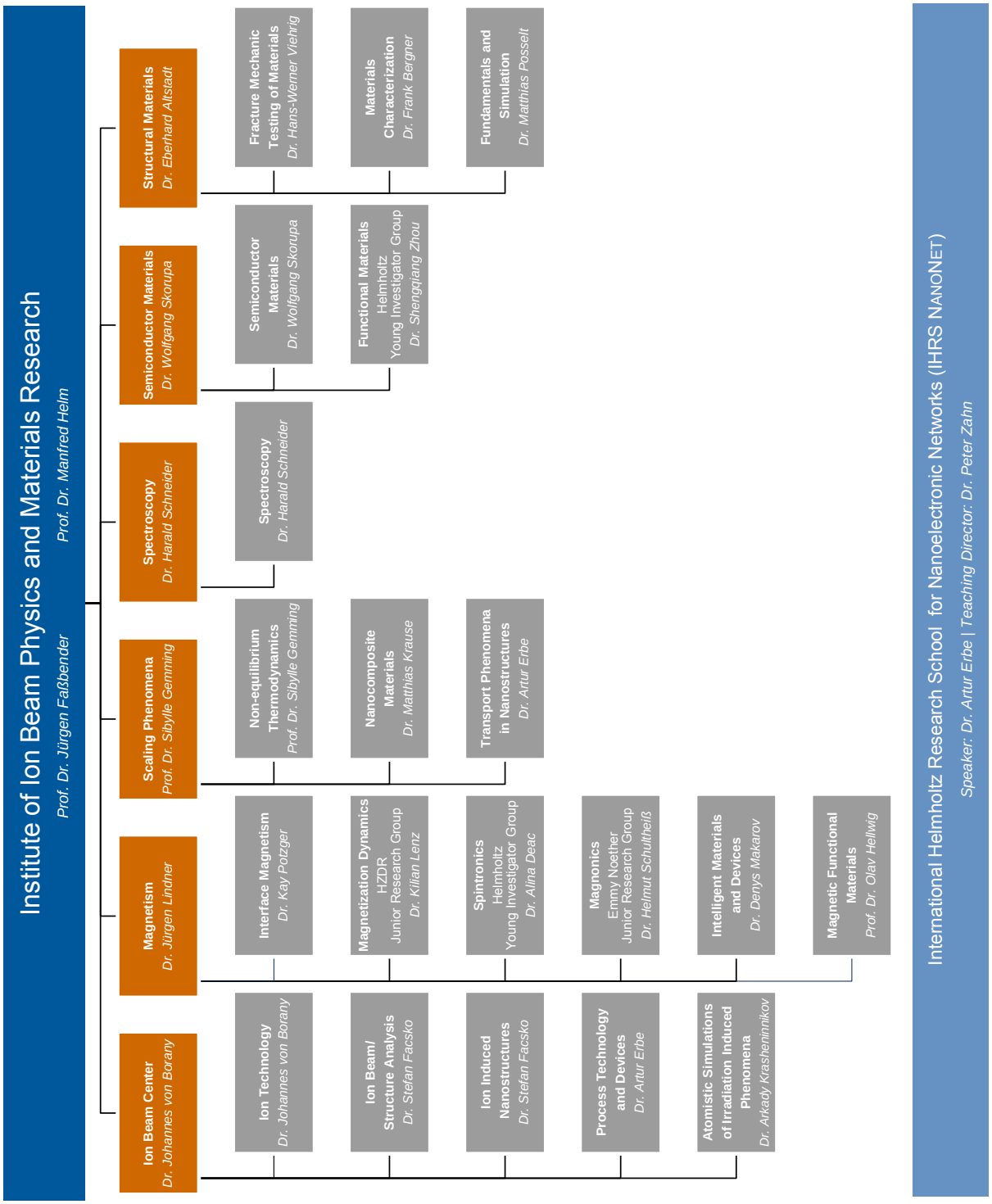

# List of personnel 2016

## DIRECTORS
**Prof. Dr. M. Helm, Prof. Dr. J. Faßbender**

## OFFICE
**S. Gebel, S. Kirch**

### SCIENTIFIC STAFF

#### Permanent staff

Dr. C. Akhmadaliev
Dr. E. Altstadt
Dr. F. Bergner
Dr. L. Bischoff
Dr. J. von Borany
Dr. E. Dimakis
Dr. A. Erbe
Dr. S. Facsko
Prof. Dr. S. Gemming
Dr. J. Grenzer
Dr. V. Heera
Dr. R. Hübner
Dr. M. Krause
Dr. J. Lindner
Dr. G. Müller
Dr. F. Munnik
Dr. M. Posselt
Dr. K. Potzger
Dr. L. Rebohle
Dr. H. Schneider
Dr. W. Skorupa
Dr. A. Ulbricht
Dr. H.-W. Viehrig
Dr. M. Voelskow
Dr. S. Winnerl
Dr. P. Zahn
Dr. S. Zhou

#### Non-permanent

Dr. R. Bali
Dr. Y. Berencén (P)
Dr. R. Böttger
Dr. V. Cantelli
Dr. A. Deac
Dr. M. Engler
Dr. D. Erb
Dr. C. Fowley
Dr. J. Ge (P)
Dr. Y. Georgiev
Dr. M. Ghorbani Asl
Dr. K.-H. Heinig (P)
Dr. C. Heintze
Dr. R. Heller
Prof. Dr. O. Hellwig
Dr. G. Hlawacek (P)
M. Houska
Dr. E. Josten
Dr. J. Julin
Dr. A. Kákay
R. Kaltofen (P)
Dr. T. Kosub
Dr. A. Krasheninnikov
Dr. K. Lenz
Dr. M. Lenz
Dr. K. Li (P)
Dr. B. Liedke
Dr. Y. Liu (P)
Dr. D. Makarov
Prof. Dr. W. Möller (P)
Dr. I. Mönch (P)
Dr. M. Neubert (P)
Dr. N. Nishida (P)
Dr. J. Osten (P)
Dr. P. Pandey (P)
Dr. A. Pashkin
Dr. S. Prucnal
Dr. R. Rana
Dr. F. Röder (P)
Dr. A. Scharf
Dr. H. Schultheiß (P)
Dr. K. Schultheiß (P)
Dr. T. Sebastian (P)
Dr. A. Semisalova
Dr. A. Singh
Dr. S. Stienen
Dr. O. Volkov (P)
Dr. X. Wang (P)
Dr. K. Wiesenhütter (P)
Dr. R. Wilhelm
Dr. D. Wolf (P)
Dr. R. Yankov (P)
Dr. O. Yildirim (P)

## TECHNICAL STAFF

### Permanent staff

Rb. Aniol
Ry. Aniol
E. Christalle
S. Eisenwinder
B. Gebauer
H. Gude
D. Hanf
J. Haufe
A. Henschke
H. Hilliges
S. Klare
J. Kreher
A. Kunz
H. Lange
U. Lucchesi
F. Ludewig
R. Mester
Dr. R. Narkovic
C. Neisser
F. Nierobisch
J. Pietzsch
T. Putzke
A. Reichel
H. Richter
M. Roßner
S. Rott
B. Scheumann
G. Schnabel
A. Schneider
A. Scholz
T. Schumann
I. Skorupa
U. Skorupa
M. Steinert
A. Thiel
K. Thiemig
J. Wagner
W. Webersinke
A. Weise
R. Weiss
J. Winkelmann
L. Zimmermann
J. Zscharschuch

### Non-permanent

A. Gerner
S. Klengel
T. Schönherr (P)
A. Weißig (P)
G. Winkler
I. Winkler
A. Vetter

(P) Projects

## PhD STUDENTS

Y. Aleksandrov
H. Arora
A. W. Awan
L. Balaghi
T. Bayrak
J. Braun
A. Bogusz
J. Buchriegler
G.S. Canon Bermudez
H. Cansever
A. Das
D. Deb
B. Duan
J. Ehrler
F. Eßer
F. Fuchs
F. Günther
I. Hilger
D. Janke
M. B. Khan
F. Kilibarda
N. Klingner
J. König-Otto
M. Kopte
E. Kowalska
S. Kretschmer
D. Lang
M. Langer
F. Liu
Lokamani
F. Lungwitz
T. Prüfer
J. Schmidt
E. Schumann
D. Stephan
A. Strobel
T. Tauchnitz
A. Titova
B. Teschome
M. Vallinayagam
T. Venanzi
T. Voitsekhivska
K. Wagner
C. Wang
M. Wang
X. Wang
R. Wutzler
C. Xu
X. Xu
Y. Yuan

## **STUDENTS** (Diploma / MSc / BSc)

J. Abdou
C. Agha
O. Ahmed
M. Braun
H. Iseke
H. Isim
L. Koch
V. Koladi Mootheri
L. Körber
J. Leipoldt
V. Liersch
M. Neumann
T. Nurmamytov
L. Ramasubramanian
R. Seifert
N. Srinivasan
A. Strobel
T. Strunck
J. Vinayakrishna

HZDR
HELMHOLTZ ZENTRUM DRESDEN ROSSENDORF

Institute of Ion Beam Physics and Materials Research
P.O. Box 51 01 19 · 01314 Dresden/Germany
Phone +49 351 260-2345
Fax +49 351 260-3285
http://www.hzdr.de

Member of the Helmholtz Association